UNIVERSITÉ DE MONTRÉAL

ISOTOPE ENGINEERING AND LATTICE DISORDER IN GROUP IV NANOSCALE AND QUANTUM SEMICONDUCTORS

SAMIK MUKHERJEE

DÉPARTEMENT DE GÉNIE PHYSIQUE

ÉCOLE POLYTECHNIQUE DE MONTRÉAL

THÈSE PRÉSENTÉE EN VUE DE L'OBTENTION

DU DIPLÔME DE PHILOSOPHIAE DOCTOR

(GÉNIE PHYSIQUE)

JUILLET 2017

UNIVERSITÉ DE MONTRÉAL

ÉCOLE POLYTECHNIQUE DE MONTRÉAL

Cette thèse intitulée:

ISOTOPE ENGINEERING AND LATTICE DISORDER IN GROUP IV NANOSCALE AND QUANTUM SEMICONDUCTORS

présentée par : MUKHERJEE Samik

en vue de l'obtention du diplôme de : Philosophiae Doctor

a été dûment acceptée par le jury d'examen constitué de :

M. MÉNARD David, Ph. D., président

M. MOUTANABBIR Oussama, Ph. D., membre et directeur de recherche

M. ROCHEFORT Alain, Doctorat., membre

M. JAGADISH Chennupati, Ph. D., membre externe

DEDICATION

আমার বাবা, মা, জ্যেঠু, ও স্বর্গীয় দাদু ঠাকুমা কে

To my father, my mother,
my uncle, and
my late grandparents

ACKNOWLEDGEMENTS

I am grateful for all the support and guidance I have received over the last four and half years at Polytechnique Montreal. First and foremost, I am immensely grateful to my advisor Prof. Oussama Moutanabbir, for giving me the opportunity to work in his research group. It has been an honor to share the title along with Dany, of being his first Ph.D. student at Polytechnique Montreal. I appreciate all his wonderful insights, the contributions of time, ideas, laboratory freedom, and the fundings to make my Ph.D. experience a productive and joyous one. The enthusiasm and passion he has for research are very contagious and have motivated me through the difficult patches in pursuit of my Ph.D..

I am also grateful to my Ph.D. committee members: Prof. Chennupati Jagadish, Prof. David Ménard, and Prof. Alain Rochefort for their precious time and interest in evaluating my thesis and providing me with valuable suggestions. I will forever be thankful to my former research advisors Prof. Nikhil Ranjan Das and Prof. Elizabeth Boer-Duchemin. They were immensely helpful in providing advice many times during my graduate school career.

I thank all our collaborators for their help and assistance on several research projects: Prof. K. Itoh and Dr. T. Sekiguchi (Keio University, Japan), Dr. M. de la Mata and Prof. J. Arbiol (ICN2 and ICMAB, Barcelona, Spain), Dr. U. Givan and Dr. S. Senz (Max Planck Institute, Halle, Germany), Prof. S. Francoeur, N. Kodali, and A. Bergeron (Polytechnique Montreal), Dr. H. Watanabe (AIST, Ibaraki, Japan), Dr. S. Wirths and Dr. D. Buca (Peter Grünberg Institute, Juelich, Germany), and Dr. J. Hartmann (CEA-LETI, Minatec, Grenoble, France). I am especially grateful to the Northwestern University Center for Atom Probe Tomography (NUCAPT) for hosting me for the atom probe experiments and to Dr. D. Isheim and Prof. D. Seidman for the time spent together at their lab at Northwestern University and for sharing with me their vast knowledge and experience on atom probe tomography.

I gratefully acknowledge the various funding agencies like the Natural Sciences and Engineering Research Council of Canada (NSERC), Fondation de l'Ecole Polytechnique de Montréal, Canada Research Chair, Canada Foundation For Innovation, MRIF-Québec, Regroupement Québécois Matériaux de Pointe (RQMP), and Max Planck Society for funding this research.

My special gratitude goes to Joël Bouchard, Christophe Clément, Marie-Helene Bernier, and Samir Eloutik for their technical assistance. I also thank the wonderful staff in the Department of Engineering Physics for always being so helpful and friendly. People here are genuinely nice and want to help out. Special thanks go out to Adèle, Lyne, and Joanne.

Throughout all the time I spent at Polytechnique Montreal, my friends and colleagues became a part of my life. My heartiest thanks go to all of them: Dany, Anis, Simone, Olga, Marc, Zeinab, Matthieu, Jerome, Julien, Etienne, Aashis and all the past members of the Moutanabbir group. It was a pleasure to work, do sports, and spend time with them. Best wishes to Dany as he finishes up. Special thanks to Simone, Olga, and Anis for all the camping, hiking trips, the peak-productivity Wednesdays, and the numerous other memories which I can never forget. I also thank my friends Prajwal, Suchakra, Tanushree, Alice, Francis, Anna, Emma, Daniel, Leigh, Dennis, Roksana, Sara, Emily, Debashis, Deboshree, Kaustav (apologies if I have missed someone!) for the support and friendship that I needed.

My special thanks go out to my cousins and friends back in India: Sayak, Butai, Joy, Partho, Gopal, Debjit, Riu, Raja, Pritha, Keya, Anik, Syam, Biswarup, Debayan, Saion, Abhinaba, Pushpargha, Sandeep, Sumanta, Alak, Pratik, Mrinmoy, Soham, Sandip (too many in the list but you know who you are!) for keeping me smiling, happy and relaxed and for making my every trip back home really memorable. I extend my gratitude to my former teachers at my school and college who had the biggest influence on me: Mr. K.P. Mukherjee, Fr. J. Pathickal, Fr. T.S. Gomes, Prof. A. Dasgupta, Prof. D. Sengupta, Prof. A. Lahiri, Prof. A.C. Gomes, Prof. B. Bandhopadhay, Prof. P.C Rakshit, Prof. A.D. Burman. They not only remain my role model as ideal teachers and mentors but are also the reason I took up research as a career.

Finally, through all this I received unyielding love, support and encouragement of my entire family. I am out of words to express my gratitude to my uncle Bholanath Mukherjee, who has been like a father-figure to me since my childhood days. I dearly miss my late grandparents Rohininandan and Jaminibala Mukherjee, but their blessings are always with me. I wished they lived a few more years to see me graduate. I especially thank my mom and dad. My hard-working parents have sacrificed their lives for me and provided unconditional love and care. I love them so much, and I would not have made it this far without them.

RÉSUMÉ

L'ingénierie des isotopes stables est la manipulation artificielle de la composition et de la distribution des isotopes stables d'un élément dans la maille cristalline d'un matériau donné. Au cours des deux dernières décennies, de nombreuses études conduites sur des semi-conducteurs monocristallins ont montré que de telles modifications peuvent altérer considérablement leurs propriétés fondamentales comme les propriétés nucléaires, le comportement des phonons, le diagramme des bandes d'énergie et le paramètre de maille. Ces développements ont permis un nouvel élan d'innovation et d'applications potentielles exploitant l'ingénierie isotopique dans le transport thermique et thermoélectrique, dans l'optoélectronique, et dans le traitement quantique de l'information, parmi tant d'autres.

L'essentiel de la littérature relative à l'ingénierie des isotopes à l'échelle quantique ou nanoscopique se concentre principalement sur des investigations théoriques. A ce jour, les études expérimentales demeurent absentes malgré leur importance dans l'élucidation d'un vaste éventail de phénomènes quantiques et nanoscopiques. Dans cette thèse, nous explorons ce paradigme méconnu en concentrant nos expérimentations sur les propriétés de base des structures dont la composition isotopique est contrôlée à l'échelle nanoscopique. Des nanofils isotopiquement pures de ^{29}Si ou d'alliage isotopique $^{28}Si_x{}^{30}Si_{1-x}$ ont été synthétisés à l'aide de la méthode vapeur-liquide-solide et leurs propriétés de transport des phonons ont été étudiées en utilisant la nanothermométrie Raman. La composition et la distribution isotopiques des nanofils individuels ont été déterminées à l'aide de la sonde atomique tomographique assistée par laser. Cependant, avant que la sonde atomique tomographique ne soit appliquée pour imager les isotopes dans un nanofil, l'utilisation de cette technique unique, mais néanmoins extrêmement délicate, a été d'abord optimisée grâce à deux systèmes additionnels. Le premier système de matériaux consiste en un super réseau isotopique de diamant, et le deuxième est une série d'alliages ternaires métastables de silicium-germanium-étain. Ces recherches nous ont permis non seulement de développer nos connaissances et notre maîtrise de la sonde atomique tomographique, mais également de faire des nouvelles découvertes intéressantes.

En exploitant l'imagerie tridimensionnelle atomique d'alliages ternaires métastables, nous avons obtenu des preuves solides que ces alliages sont parfaitement monocristallins et croissent sans agrégats d'étain même pour des concentrations supérieures à la composition attendue de

l'équilibre thermodynamique. Cependant, en augmentant la quantité d'étain, nous avons montré que la distribution du silicium dans ces alliages s'éloigne de la distribution théorique idéale. La principale cause de cet ordre atomique à courte portée est la présence d'une interaction répulsive entre les atomes de silicium et les atomes d'étain. L'étude menée sur le super réseau isotopique de diamant à l'aide de la sonde atomique tomographique a montré pour la première fois qu'il est en effet possible de contrôler le phénomène d'évaporation par effet de champ, un seul atome à la fois, d'un matériau comme le diamant, possédant le plus haut champ d'évaporation connu. Afin d'expliquer la physique sous-jacente de ce résultat, nous proposons un mécanisme détaillé de l'évaporation par effet de champ assistée par laser de nanofils de diamant.

Toute l'expertise acquise de ces mesures tomographiques fut mobilisée pour l'analyse des nanofils d'alliage isotopique $^{28}Si_x{}^{30}Si_{1-x}$. Les expériences ont révélé que les deux isotopes du silicium sont distribués de manière non uniforme dans un nanofil $^{28}Si_x{}^{30}Si_{1-x}$, avec l'isotope ^{28}Si plus léger proche de la surface et l'isotope ^{30}Si plus lourd au cœur du nanofil. Ces observations révèlent des nouveaux détails sur le comportement des atomes de silicium à l'interface liquide-solide pendant la croissance vapeur-liquide-solide via un catalyseur métallique. En fait, nous observons que la cristallisation des nanofils met en jeu des mécanismes qui paraissent sensibles à la masse atomique, amenant ainsi de nouvelles connaissances fondamentales sur la dynamique de croissance épitaxiale à l'échelle nanométrique. Les mesures de nanothermométrie Raman sur ces nanofils à la composition isotopique contrôlée ont révélé que la conductivité thermique des nanofils isotopiquement désordonnés $^{28}Si_x{}^{30}Si_{1-x}$ est réduite de $\sim 25-30\%$ au voisinage de la température ambiante par rapport à celle des nanofils isotopiquement purs en ^{29}Si. Le comportement des phonons a été également étudié dans une série supplémentaire d'alliages isotopiques $^{28}Si_x{}^{30}Si_{1-x}$ avec des inclusions polytypiques de segments lamellaires hexagonaux selon l'axe longitudinal des nanofils. Nous avons montré que ces segments hexagonaux à l'intérieur des nanofils voient leur température augmenter plus rapidement en comparaison aux segments de maille cubique de type diamant dans le même nanofils. Nous avons aussi observé que la conductivité thermique globale de ces nanofils d'alliage isotopique avec polytypes est réduite de ~10% par rapport à son équivalent à maille cubique de type diamant, proche de la température ambiante.

Au cœur de cette thèse se trouve la première démonstration expérimentale de la synthèse, de la caractérisation et de l'étude des effets du désordre cristallin dans des nanofils de silicium à la composition isotopique contrôlée. L'impact de ce travail réside dans la rigoureuse démonstration

expérimentale de la manipulation de la composition isotopique et de la distribution des éléments lors de la croissance de nanostructures ainsi que dans la caractérisation précise des effets des isotopes sur leurs propriétés fondamentales. Par conséquent, ce travail prépare le terrain pour le développement d'une famille complètement nouvelle de structures nanoscopiques et quantiques à la composition isotopique contrôlée visant des applications dans le transport de chaleur à l'échelle nanoscopique, les dispositifs thermiques quantiques, et le traitement quantique de l'information, pour en nommer quelques-uns. Cette thèse soulève également de nouvelles questions fondamentales ainsi présentant des opportunités pour des études futures.

ABSTRACT

Stable isotope engineering refers to the artificial manipulation of the content and distribution of the stable isotopes of an element within the lattice of a material. Over the last two decades, numerous studies conducted on bulk semiconductors have shown that exercising such a control can significantly alter the fundamental behavior of a material such as the nuclear properties, phonon behavior, electronic energy gaps, and lattice constant. Consequently, a myriad of opportunities emerged from this isotopic engineering of semiconductors enabling a variety of novel and potential applications such as thermal transport and thermoelectric, optoelectronics, and quantum information processing, to name a few.

The body of literature related to isotope engineering in nanoscale materials is made primarily of theoretical investigations. Till date, the experimental investigations remain conspicuously missing, despite the fact that the combination of mass-related effects and size-related effects can provide a rich playground to uncover and harness a wide range of new nanoscale and quantum phenomena. In this thesis, we unfold this unexplored paradigm by focusing our experimental investigations on the basic lattice properties of isotopically programmed nanoscale structures. The isotopically pure ^{29}Si and mixed $^{28}Si_x{}^{30}Si_{1-x}$ nanowires were synthesized using the metal catalysed vapor-liquid-solid method and the phonon transport in these nanowires was studied using Raman nanothermometry. The isotopic composition and distribution within an individual nanowire was investigated using laser-assisted atom probe tomography. However, before the atom probe tomography could be implemented to map the isotopes within a nanowire, the experimental capabilities of this unique yet extremely challenging technique were first optimized in two additional systems. The first material system consists of diamond isotopic superlattice and the second, a set of ternary metastable silicon-germanium-tin alloys. These investigations not only equipped us with the science and the practice of atom probe tomography, but also had some interesting revelations of their own.

Based on the atom-by-atom three-dimensional mapping of ternary metastable alloys, we obtained clear evidence that these alloys grew without any tin clustering even at contents larger than the equilibrium composition. However, with the increase in tin content, the silicon distribution within these alloys was found to deviate from the ideal theoretical distribution. The root cause of this short-range atomic ordering is the presence of a repulsive interaction between silicon and tin

atoms. The atom probe investigations of the isotopic diamond superlattice showed for the first time that it is indeed possible to control the process of field evaporation in an atom-by-atom fashion from a material like diamond with the highest known evaporation field. To explain the underlying physics of this achievement, we proposed a detailed mechanism of the laser-assisted field evaporation of diamond nanotips.

All the expertise gained from these atom probe measurements were summoned in for analysing a single isotopically mixed $^{28}Si_x{}^{30}Si_{1-x}$ nanowire. The investigations revealed that the two silicon isotopes are non-uniformly distributed within a $^{28}Si_x{}^{30}Si_{1-x}$ nanowire with the lighter ^{28}Si isotope rich near the surface and the heavier ^{30}Si isotope rich at the core of a nanowire. This revelation sheds a new light on the atomistic-level behavior of silicon atoms at the liquid-solid interface during the metal catalyzed vapor-liquid-solid growth. In fact, we observed that the nanowire crystallization involves processes that are seemingly mass-sensitive thus providing new fundamental insights on the dynamics of the nanowire growth. The Raman nanothermometric measurements on these isotopically engineered nanowires revealed that the lattice thermal conductivity of the isotopically mixed $^{28}Si_x{}^{30}Si_{1-x}$ nanowires is reduced by a $\sim 25-30\%$ relative to the isotopically pure ^{29}Si nanowires around the room temperature. The phonon behavior was also studied on a different set of isotopically mixed $^{28}Si_x{}^{30}Si_{1-x}$ nanowires with polytypic inclusions of lamellar hexagonal segments along their long axis. The hexagonal segments in these nanowires were found to heat up more *rapidly* compared to the diamond cubic segments and the overall lattice thermal conductivity of these polytypic isotopically mixed nanowires to be reduced by $\sim 10\%$ relative to its diamond cubic counterpart, close to room temperature.

At the core of this thesis is the first experimental demonstration of the synthesis, characterization, and the investigations of the lattice disorder effect in isotopically engineered silicon nanowires. Its impact lies in providing clear experimental demonstration of the manipulation of the isotopic content and distribution during the growth of nanostructures and a precise characterization of the effects of isotopes on their fundamental properties. Hence, this thesis lays the groundwork for the development of an entirely new family of isotopically engineered nano and quantum structures relevant for applications in nanoscale heat transport, quantum thermal devices, and quantum information processing, to name a few. The thesis also raises some new fundamental questions creating a wealth of opportunities for future studies.

TABLE OF CONTENTS

LIST OF TABLES

LIST OF FIGURES

LIST OF ABBREVIATIONS

amu	Atomic mass unit
APT	Atom probe tomography
APFIM	Atom probe field ion microscope
ATDC	Amplifier time-to-digital conversion
CCD	Charge couple device
CL	Cathodoluminesence
CVD	Chemical vapor deposition
Da	Dalton
DFT	Density functional theory
EBSD	Electron backscattered diffraction
E-P	Electron-phonon
EXAFS	Extended X-ray absorption fine structure
FD	Frequency distribution
FE	Free exciton
FET	Field effect transistor
FIB	Focused ion beam
FIM	Field ion microscope
FWHM	Full width at half maxima
HOMO	Highest occupied molecular orbital
HPHT	High pressure high temperature
HRTEM	High-resolution transmission electron microscope
HV	High-voltage
HWP	Half-wave plate
IAP	Imaging atom probe
IVAS	Integrated visualization and analysis software
LA	Longitudinal acoustic
LE	Local electrode
LEAP	Local electrode atom probe
LO	Longitudinal optic
LUMO	Lowest unoccupied molecular orbital
LVM	Local vibrational mode
LVS	Local vibrational spectra
MBE	Molecular beam epitaxy
MD	Molecular dynamics
MCP	Microchannel plate
MOS	Metal-oxide-semiconductor

NA	Numerical aperture
NN	Nearest neighbor
NP	No-phonon
NS	Nuclear spin
NW	Nanowire
NV	Nitrogen vacancy
PL	Photoluminescence
ppm.	Parts per million
p-RDF	Partial radial distribution function
PoSAP	Position sensitive atom probe
QIP	Quantum information processing
ROI	Region of interest
SAD	Selected area diffraction
SAP	Scanning atom probe
sccm.	Standard cubic centimeter per minute
SEM	Scanning electron microscope
SiGeSn	Silicon-germanium-tin
SIMS	Secondary ion mass spectrometer
STEM	Scanning transmission electron microscope
TA	Transverse acoustic
TBP	Triple phase boundary
TEM	Transmission electron microscope
TO	Transverse optic
TOF-MS	Time-of-flight mass spectrometer
UV	Ultraviolet
VCA	Virtual crystal approximation
VLS	Vapor-liquid-solid

LIST OF SYMBOLS

A	Arbitrary constant
a	Lattice constant
α	Scattering angle of an electron
$\alpha_{\rho\sigma}$	(ρ, σ) components of the atomic polarizability tensor
α_0	Atomic polarizability at the equilibrium position of a vibrating atom
$\alpha_{free-hole}$	Free hole absorption coefficient
B	Magnetic field
$\mathscr{b}$	Arbitrary constant
$\mathcal{B}$	Isothermal bulk modulus
β	Arbitrary constant
Λ	Binding energy of an atom at the surface of an atom probe tip
$\gamma_{q,j}$	Grüneisen parameter
$\mathcal{C}$	Arbitrary constant
$C(T)$	Specific heat at a temperature T
$C_{I/V}^{eq}$	Fraction of atoms undergoing self-interstitial (I) and self-vacancy (V) diffusion
c	Velocity of light
c_i	Fractional composition of the i^{th} isotope
c_{th}	Threshold concentration for defining an iso-concentration surface
D	Arbitrary constant
$\mathfrak{D}$	Diameter of an aperture associated with a magnetic lens
D_{SD}	Coefficient of self-diffusion
$D_{I/V}$	Coefficient of self-interstitial (I) and self-vacancy (V) diffusion
$D_{28/30}$	Coefficient of self-diffusion for ^{28}Si atoms and ^{30}Si atoms
D_{ex}	Exchange factor in interstitial and vacancy mediated self-diffusion
Δ	Imaginary part of phonon self-energy (Width of a Raman line)
Δ_0	Spin-orbit splitting
ΔH_{mix}	Mixing enthalpy of an alloy
ΔH_{Ch}	Contribution of chemical interaction to the total enthalpy of an alloy
δ_a	Anomalous skin-depth in metals
δ_T	Constant coupling the laser intensity to the rise in temperature of an atom probe tip
E_g^i	Indirect band gap
E_0	Direct band gap
E_{Pulse}	Laser pulse energy
E_1	Electric field of light
E_1^σ	σ^{th} component of the electric field of light
e	Electronic charge
ε_0	Free space permittivity

$\mathcal{E}_\eta$	Energy of the quantized vibrational levels
F	DC electric field at the apex of an atom probe tip
F_t	Total Helmholtz free energy of a crystal
F_{ph}	Phonon free energy
F_{ev}	Evaporation field
F_{OR}	Electric field generated by optical-rectification
f	Final vibrational state of an atom
f_m	Focal length of a magnetic lens
$f_{I,V}$	Correlation factor for interstitial (I) and vacancy (V) mediated self-diffusion
G_e, G_h	Electron (e) and hole (h) generation rate within diamond from impact ionization
g_2	Degree of mass-disorder or second order moment of mass fluctuation
H_{SD}	Enthalpy of self-diffusion
H_{alloy}	Enthalpy of an alloy
H_{Si}, H_{Ge}, H_{Sn}	Enthalpy of the pure element: silicon, germanium, and tin
h	Planck's constant
$\hbar$	Reduced Planck's constant
i	Initial vibrational state of an atom
I_i	Energy of the i^{th} ionization state of a cation
I_s	Intensity of scattered light
I_{Stokes}	Intensity of Raman Stokes scattered light
$I_{Anti-Stokes}$	Intensity of Raman Anti-Stokes scattered light
J	Laser pulse intensity
j	Branch of phonon dispersion relation
θ	Angle of dispersion of light from a diffraction grating
θ_D	Debye temperature
k	Electron wave vector
k_1	Wave vector of incident light
k_s	Wave vector of scattered light
k_B	Boltzmann constant
κ	Lattice or phononic thermal conductivity
κ_{max}	Maximum value of lattice thermal conductivity
$k_{\bar{\upsilon}}$	Constant connecting light scattered at wavenumber $\bar{\upsilon}_s$ to its intensity
$\mathscr{k}$	Arbitrary constant depending on the shape of an atom probe tip
L	Separation between an atom probe tip and position-sensitive detector
$\mathfrak{L}$	Length of an atom probe tip
l	Total path length of the *x*-coordinate delay-line detector
$\mathcal{L}$	Width of the $^{13}C/^{12}C$ homointerfaces
ℓ	Diffusion length of atoms across the $^{13}C/^{12}C$ homointerfaces
ℓ_e	Electron mean free path

λ_1	Light wavelength
λ_{ph}	Phonon mean free path
λ_{el}	Electron de-Broglie wavelength
m	Mass of a particle
$\mathfrak{m}$	Number of monolayers in a superlattice
$\mathcal{M}$	Magnification factor of a magnetic lens
m_i	Atomic mass of the i^{th} isotope
m_0	Rest mass of an electron
$\langle m \rangle$	Average atomic mass
μ_e	Permeability
N	Number of kink sites at the surface of an atom probe tip
N'	Groove density of a diffraction grating
$\mathcal{N}$	Number of silicon-tin bonds in an alloy
N_{Stokes}	Population of the vibrational level that initiates the Raman Stokes scattering
$N_{Anti-Stokes}$	Population of the vibrational level that initiates the Raman Anti-Stokes scattering
n	Branch of an electron dispersion relation
$\mathfrak{n}$	Order of a diffraction spectrum
n'	Number of photons
n_B	Bose-Einstein factor
n_h	Free hole concentration at the surface of an atom probe tip
$\mathcal{n}$	Charge state of an evaporated cation
η	Vibrational quantum number
P_{ev}	Probability of evaporation of a cation from an atom probe tip
$P_i^{(2)}$	Second order polarization
$P_k(r, C)$	Probability of finding a nearest neighbor at r of the k^{th} atom-type with conc. C
$\Pi(\omega)$	Phonon self-energy
$\Pi'(T)$	Shift in Raman peak position at a temperature T relative to that at 0K
p	Electron momentum
p_o	Amplitude of induced electric dipole moment in an atom
p_ρ	ρ^{th} component of electric dipole moment vector
σ_e	Electronic conductivity
Q_0	Evaporation barrier for a cation at $\mathcal{n}^{\text{th}}$ charge-state, under no-field
Q_k	Displacement of the k^{th} atom from its equilibrium position
Q_k^0	Vibrational amplitude of the k^{th} atom
$Q_n(F)$	Evaporation barrier for a cation at $\mathcal{n}^{\text{th}}$ charge-state, under a field F
q	Phonon wave vector
$\mathcal{q}$	Charge of a particle
R	Reflectivity of light from an atom probe tip
$\mathcal{R}^2$	Coefficient of determination

r_{apex}	Apex radius of an atom probe tip
S_{SD}	Entropy of self-diffusion
σ_{spot}	Laser spot diameter
S_{res}	Residual sum of squares
S_{tot}	Total sum of squares
T	Absolute temperature
T_{max}	The temperature at which the maxima of lattice thermal conductivity occurs
T'_{max}	Maximum temperature rise of an atom probe tip
T_2	Coherence time
t	Time
t_{flight}	Time-of-flight of an evaporated cation
t_x	Total charge traverse time along the *x*-coordinate delay-line detector
t_{x1}	Charge traverse time to the terminal-1 of the *x*-coordinate delay-line detector
t_{x2}	Charge traverse time to the terminal-2 of the *x*-coordinate delay-line detector
Γ	Real part of phonon self-energy (Position of a Raman line)
Γ_{ev}	Evaporation rate of cations from an atom probe tip
τ_{ph}	Phonon decay-time
τ_p	Laser pulse duration
$\tau_{cooling}$	Effective cooling time of the surface of an atom probe tip
τ_{Ev}	Effective evaporation time for a cation from the surface of an atom probe tip
τ_{Anh}	Phonon decay-time due to anharmonic scattering
τ_{Dis}	Phonon decay-time due to scattering from mass-disorder
U_0	Crystal binding energy
u^2	Squared vibrational amplitude of atoms
V	Crystal volume
V_{dc}	DC voltage applied to an atom probe tip
V_p	Pulsed voltage applied to a local electrode
V_{tip}	Voltage at the apex of an atom probe tip
v	Velocity of a particle
$\mathcal{v}$	Normal component of vibration of an atom at the surface of an atom probe tip
v_{el}	Velocity of an electron
$\upsilon_1, \upsilon_2, \upsilon_3$	Localized vibrational modes of impurity oxygen in silicon
$\bar{\upsilon}_s$	Wave number of scattered light
v_{ion}	Final velocity of an evaporated cation from an atom probe tip
$\langle v_{ph} \rangle$	Average phonon group velocity
ϕ_{e}	Work function of the atom probe specimen
$\omega_{q,j}$	Phonon energy at a wave vector q and j^{th} branch of dispersion relation
ω_1	Frequency of incident light
ω_0	Raman peak position (average phonon energy) at 0K

ω_s	Frequency of scattered light
ω_{vib}	Frequency of atomic vibration
ω_{fi}	Difference in frequency between the final and initial vibrational state of an atom
ω_{Stokes}	Frequency of Raman Stokes scattered light
$\omega_{Anti-Stokes}$	Frequency of Raman Anti-Stokes scattered light
$\omega_{3C/9R}$	Raman peak position for the diamond cubic (3C) and hexagonal (9R) phases
Ω_{Si-Sn}	Silicon-tin interaction parameter
$\Omega(T)$	Raman peak position (average phonon energy) at a temperature T

LIST OF APPENDICES

CHAPTER 1 INTRODUCTION

We begin this introductory chapter with a brief overview of the core elements of this thesis. The overview puts this thesis in perspective and outline its broad scientific context. This introductory chapter also identifies the important scientific questions that has been tackled as we highlight the main motivations, the key objectives, as well as the methodologies adapted to achieve these objectives. We end this chapter by describing the organization of this document.

1.1 Overview

As realized by Fredrick Soddy in 1911 [1], isotopes are atomic nuclei of an element which have the same number of electrons (the same atomic number), the same number of protons but different number of neutrons (different mass number). Stable semiconductor isotopes differ in their atomic mass, nuclear spin, and the thermal neutron capture cross-section during a nuclear reaction. Table 1.1 lists the stable isotopes of the group IV semiconductors along with their established atomic masses, natural abundances, nuclear spin, and thermal neutron capture cross-section. By engineering the concentration and distribution of stable isotopes of an element within a nanoscale material, we essentially introduce an additional degree of freedom to manipulate some of its fundamental properties. This has two main benefits: first, it paves the way to fabricate a novel class of semiconductor devices with targeted application in nano-thermoelectric, nano-optoelectronic, and quantum information processing. Second, it stimulates the development of new techniques of precise metrology capable of detecting and quantifying the subtle isotope effects. However, before we can harness any of these benefits in nanostructures, two major challenges need to be overcome. The synthesis of nanostructures is in itself a more challenging process as compared to their bulk counterparts. The first challenge involves tailoring the content and the distribution of different isotopes during the growth of a nanostructure. Once that is achieved comes the next hurdle, which is to characterize the same within the grown nanomaterial.

The entire field of stable isotope engineering in nanostructures are based on these two pillars: the ability to control and characterize the isotopic content at nanoscale. In this thesis, we have addressed these two challenges as we report the first demonstration of the synthesis of isotopically engineered silicon (Si) nanowires (NWs), their atomistic level characterization, and

the measurement of their thermal properties. The phonon behavior in the monoisotopic and isotopically mixed NWs was studied in realm of the precise isotopic concentration and distribution, as revealed by the atom probe tomography (APT). APT is the only known analytical technique, with supreme mass resolving power that can spatially resolve even the two isotopes of an element, within nanoscale materials. However, the technique, especially when it comes to the analysis of nanoscale materials like the NWs, is far from being simple. To expose ourselves to the scope, technicalities, and the limitations associated with this technique we performed atom probe analysis on two other materials, each came with its own challenges, questions to address, and revelations.

Table 1.1: *Stable isotopes of C, Si, and Ge, along with their natural abundances, atomic mass, nuclear spin, and neutron capture cross-section*

Element	Stable isotopes	Natural abundances (at. %) [2]	Atomic mass (Dalton)	Nuclear spin	Neutron capture cross-section (barn) [$1\text{barn} = 10^{-24}\text{cm}^2$] [3]
Carbon	^{12}C	98.93	12.000	0	0.0034
	^{13}C	1.07	13.003	1/2	0.0009
Silicon	^{28}Si	92.24	27.9769	0	0.17
	^{29}Si	4.68	28.9764	1/2	0.10
	^{30}Si	3.08	29.9737	0	0.11
Germanium	^{70}Ge	20.84	69.9242	0	3.25
	^{72}Ge	27.54	71.9220	0	1.0
	^{73}Ge	7.73	72.9234	9/2	15.0
	^{74}Ge	36.28	73.9211	0	0.36
	^{76}Ge	7.61	75.9214	0	0.16

The first of the two system is an isotopic diamond ^{12}C/^{13}C superlattice. APT was employed to map the distribution of the two diamond isotopes within the superlattice structure and evaluate interfacial properties. Diamond, with the highest evaporation field among all materials, is always known to be a non-cooperative material for field evaporation and has eluded all previous attempts of being imaged in an atom probe. It therefore requires an in-depth knowledge of the science of

field evaporation process to achieve an optimal control the key parameters during an atom probe experiment. 3D atomistic maps of the diamond isotopes could become crucial to the ultimate performance of future diamond based quantum sensing and quantum information processing devices. Such devices and applications call for the knowledge of the location of the various defect-centers and/or the isotopes, precise to a scale of few atomic distances, which only APT can provide. The second of the two material systems analyzed in the APT is a set of ternary non-equilibrium group IV alloys of Si, germanium (Ge), and tin (Sn). These Sn-rich alloys have been in the limelight for quite sometime now for the bright prospect that they hold as future building-blocks for on-chip optical communication on an industry compatible group-IV platform. APT was employed to look for Sn aggregates and investigate the atomic distribution of the three constituent atomic species within the alloys. With Ge and Sn having five and ten stable natural isotopes respectively, it required the full potential of the mass sensitivity and spatial resolution of an atom probe to resolve all the isotopes of all the three elements and an in-depth knowledge of the atom probe data analysis tools to evaluate their spatial distribution within nanoscopic volumes of the alloys. Such maps could point out limitations that are inherent to the metastable nature of these alloys and never envisioned before. Side-by-side the information can be used as guidelines to optimize the synthesis of such alloys which can eventually broaden their scope and applicability.

1.2 Motivation

Isotope engineering in semiconductors is a powerful paradigm to manipulate some of their important physical parameters and exploit them in form of novel device structures. Earlier works mainly focused on isotopically engineered bulk semiconductors [4]–[7]. Nanoscale materials can provide a unique platform where the size related effects (like the surface effects and confinement) can be combined with the atomic mass related effect coming from the isotopes. A striking example of the same was set by demonstrating carrier confinement in nanoscopic ^{12}C layers of a $^{12}C/^{13}C$ isotopic superlattice, using only the isotope effect on the electronic gap [8]. Of all the material properties, the isotopic effect on phonon transport is the most prominent and much easily observable compared to the other subtle effects. Consequently, the phonon spectra of isotopically engineered semiconductors generate tremendous amount of interest. The theoretical studies on the transport properties indicate a myriad of possibilities by which the isotope effect in Si NWs can be exploited to tune the lattice thermal conductivity and the thermoelectric figure of merit [9], [10].

However, no experimental investigations related to the isotope effect on the transport properties were ever reported. We have therefore undertaken the growth of isotopically engineered Si NWs and study their phonon behavior. Through these studies, we looked to unravel as to how the isotopic composition affect the phonon behavior in a nanoscale material and provide a test-ground to the proposed theoretical models of the phonon transport in isotopically engineered Si NWs.

No such study is complete without correlating it with the concentration and the distribution of the isotopes within the material being studied. Apart from the time-of-flight instruments, most of the conventional characterization techniques rely on the difference in electronic properties between different elements (like the electron microscopes, where the image contrast depends on the atomic number of an element) and are therefore incapable in probing the isotopic distribution. Secondary ion mass spectrometry (SIMS) requires a large area for sputtering materials and is therefore unfit for application to nanoscale materials. The decision to use APT is rather unambiguous, motivated by its near atomic scale spatial resolution coupled with an unparallel mass resolving power. However, before we can exploit its full potential, grasping a complete knowledge of the underlying science and practice of an atom probe is indispensable for the ultimate success of these investigations. Although the use of this technique is rather straight-forward in the case of metals, probing non-metallic specimen and that too with unusual geometries like a nanowire, is still fraught with uncertainties. We have therefore carried out atom probe investigations on two other systems. This will provide us with a first-hand experience as how to make specimen for an atom probe, control the key parameters during an atom probe experiment on complex nanoscale samples, and how to analyze the atom probe data. The choice of these two material systems were not random, but rather handpicked in a way that they would push the capabilities of an atom probe to its limit. By this process we look to build up a concrete base comprising of a sound knowledge of the fundamentals and technicalities of an atom probe, before we apply it to carry out atomistic studies of the isotopically programmed Si NWs.

The first of the two systems is an isotopic diamond superlattice. The field evaporation of diamond in an atom probe has always been a major challenge. There are no earlier reports of a controlled atom-by-atom field evaporation of diamond, with earlier attempts leading to the evaporation of atomic clusters [11]. Meteoritic nanodiamonds although successfully evaporated, the volume of the nanodiamonds embedded within a platinum matrix were extremely small [12]. Defect and isotope engineering has shown great promises in recent years in the field of diamond

based quantum sensing and quantum information processing [13]–[15]. It is often imperative to know the precise distribution of defects centers, like the nitrogen vacancy (NV) centers, the spin full ^{13}C isotopes within a spin free ^{12}C matrix in determining the ultimate device performance. For example, when an electron spin of a NV centers is being used as a quantum bit, its close proximity to a ^{13}C isotope could be detrimental due to electron-spin nuclear-spin hyperfine interaction [14]. In another scenario, the electron-spin of a NV center could be used to initialize the nuclear spin of ^{13}C, the latter can serve as a quantum bit [15]. In this case, the proximity of a NV center to a ^{13}C isotope is desired. Here, we are talking of proximities that could well be on a scale of one or few nearest neighbor distances. The examples show that each time, depending on the boundary conditions, a different order or distribution of defect centers and ^{13}C, the degree of isotope enrichment of the ^{12}C matrix may be required. A proper quantification of the same requires generating atomistic maps with the utmost spatial resolution. APT was employed on a diamond superlattice not just to map the distribution of different diamond isotopes but at the same time to answer a more pertinent fundamental question: if at all a material like diamond with the highest known evaporation field, can be field evaporated in a controlled manner. In the quest for this answer, we look to develop the necessary skill-set to be able to understand the fundamentals of the field-evaporation process and achieve its control in an atom-by-atom fashion.

The second of these two material systems is a set of silicon-germanium-tin (SiGeSn) non-equilibrium ternary alloys. These emerging alloys are of paramount importance to the semiconductor industry as they present us with a unique opportunity to achieve a direct gap using only the group IV elements. There is an overwhelming number of possible optoelectronic and photonic devices that can be engineered on a Si platform, using these alloys. However, one stumbling block that these alloys could encounter has to do with their metastable nature. Indeed, relevant SiGeSn semiconductors require a sizable incorporation of Sn, orders of magnitude above the equilibrium concentration in Si and Ge. It has been shown, albeit indirectly, that the distribution of the constituents in some mainstream III-V semiconductors is not always perfectly random [16], [17], forcing us to reconsider weather something similar can happen in these emerging group IV alloys as well. As often happens with novel material, the spot light shifts so much towards applications that we often tend to overlook such minute details regarding the fundamental aspects of the material itself. Perhaps, this is the reason that the wide body of peer reviewed publications that exists on these metastable alloys are pertinently application-oriented and do not contain any

systematic investigation of the basic properties of such alloys. Unlike, the previous x-ray and the photoluminescence based investigations on III-V alloys [17], [18], the atom probe data will allow us to see the atomic distribution in real space. However, finding out the actual distribution of the constituent atoms on a near-atomic scale requires a mastery of the atom probe data analysis. At the end of this phase of the journey, we hope not only to achieve this mastery but also as a bonus, find out the extent to which the actual distribution of the atoms in these alloys match the expected distribution and outline the root causes of any anomalies that are found.

1.3 Objectives and Methodology

The thesis has one main objective which is to develop isotopically engineered nanoscale materials and elucidate their basic properties. More specifically, studying the effect of isotopic composition on the phonon transport properties in Si NWs. A combination of the mass related effect coming from the isotopes and the size related effect coming from the quasi-one dimensional geometry of a NWs should make this investigation first of its kind. A part of the objective is also to quantify and isolate the effects on phonon behavior coming from the isotopes and the nanoscale size. In the following we highlight the methodologies (details provided in chapters 4-6) that we shall follow in order to meet the aforementioned objective. The methodologies are:

1) Synthesis of Si NWs with controlled isotopic compositions. The metal catalyzed vapor-liquid-solid (VLS) growth with gaseous silane as precursor in a chemical vapor deposition (CVD) chamber, is one of the easiest ways to grow Si NWs. Instead of natural silane, isotopically enriched silane gases are used as the precursors. To create the mass-disorder, $^{28}Si_x{}^{30}Si_{1-x}$ NWs are synthesized wherein the two stable isotopes of Si are mixed. The disorder is maximized when the ratio of the two isotopes are equal, that is *x* is 0.5. Next, a different set of NWs with no isotopic disorder is synthesized. For this, we choose the isotopically pure ^{29}Si NWs with the same morphology as the isotopically mixed ones. The mass-disorder is the only difference between the two sets of NWs.

2) Raman nanothermometry is employed to study the phonon behavior in the two sets of NWs and compare the effect of mass-disorder on the phonon behavior and the lattice thermal conductivity.

3) 3D atomistic maps of a single $^{28}Si_x{}^{30}Si_{1-x}$ NWs are achieved using APT in order to obtain an accurate picture of the concentration and the distribution of the two isotopes within a NW.

4) But before we can proceed with the atomistic investigation of the isotopically disorder (mixed) NWs, the APT is carried out on other relevant material systems to equip ourselves with its science and practice.

   4a) An isotopically modulated diamond superlattice. For this the data analysis is relatively simple but the atom probe experiment is not. A trial and error approach is undertaken to control the field evaporation of atoms from a diamond tip during the atom probe runs. As we shall outline in the following chapters, there are a few input parameters at the disposal of a user that can be tuned in order to control the evaporation mechanism of atoms in a laser-assisted atom probe. By control, we mean that atoms are evaporated as single or bi or tri-cations and not as clusters of many atoms or as carbon-hydrogen, carbon-oxygen complexes. Also, atom probe tips are prone to fractures, especially during wide variations of the user controlled parameters. A proper control ascertains that a significant number of atoms, enough to perform data analysis with the set, are collected before any fracture events can occur. A mere collection of atoms from the first few atomic layers of the sample do not signify a good control.

   4b) Ternary non-equilibrium SiGeSn alloys grown by the chemical vapour deposition process. The atom probe experiment on such alloys is relatively straightforward, but the data analysis is not. Sn being incorporated in amounts much higher than the equilibrium concentration, is the most likely element to form aggregates. APT is employed to look for the Sn precipitates and clusters and investigate the distribution of each atomic species on a scale of few nearest neighbouring distances. Finally, the distribution is compared to an ideal theoretical distribution. For this, several statistical tools, inbuild within an atom probe software is implemented. Attempts are made to dig deep into the growth dynamics of such alloys and understand the basic underlying cause of variations from an ideal solid solution.

1.4 Thesis Organization

This thesis is organized into nine chapters. Chapter 2, contains a detailed literature review on the isotope effects on the properties of semiconductors as well as the current understanding of the impact of isotope engineering on semiconductor physics. The chapter also highlights the literature

on the techniques of sample preparation and the atom probe investigations on nanoscale materials. A detailed discussion on the most important instruments used in this thesis is provided in chapter 3. This includes atom probe tomograph, Raman spectrometer, and transmission electron microscope (TEM). The underlying physics associated with the atom probe and the Raman spectrometer have also been discussed in brief to highlight their working principles. Chapter 4, 5, and 6 are composed of three articles. Chapter 4 (S. Mukherjee et *al*., Nano Letters 16(2), 1335 (2016)) discusses the underlying physics of diamond atom-by-atom mapping using laser-assisted atom probe tomography. Chapter 5 (S. Mukherjee et *al*., Physical Review B Rapid Comm. 95, 161402 (2017)) addresses short-range atomic ordering in group IV non-equilibrium semiconductors. Chapter 6 (S. Mukherjee et *al*., Nano Letters 15(6), 3885 (2015)) highlights the role of mass disorder in heat transport in Si nanowires. These three chapters are organized in the following sequence: authors, abstract, introduction, experiment, results and discussions, summary, and the acknowledgements. In chapter 7, we show some of the recent results on the combined effect of mass disorder and crystal phase on nanoscale heat transport, yet to be formulated in the form of a journal article. A general discussion of the key results is presented in chapter 8, wherein we highlight the originality and the significance of our findings. Finally, conclusions to the thesis are drawn and perspectives on future work are given in Chapter 9. This is followed by the bibliographical references and the appendices. The appendices A, B, and C contain the supplementary information to chapters 4, 5, and 6, respectively.

CHAPTER 2 LITERATURE REVIEW

In this chapter, we present a survey on the literature that exists on the two key components of this thesis: stable isotope engineering in semiconductors and APT. First, we discuss the various methods known for isotope separation and enrichment. The literature survey on the isotope effect on semiconductor fundamental properties and the impact of stable isotope engineering on semiconductor physics follows next. The literature survey on atom probe begins with a roadmap, from the early predecessors leading up to the modern state-of-the-art atom probes. This is followed by the different methods of atom probe specimen (tip) fabrication using nanoscale samples. The section ends as we discuss some important results in literature pertaining to atom probe investigations on a variety of nanoscale materials.

2.1 Stable Isotope Engineering in Group IV Semiconductors

This section contains the literature review on the conventional methods of isotope separation, the isotopic effect on the fundamental properties of bulk semiconductors, and the impact that isotope engineering had on semiconductor science and devices in the past few decades.

2.1.1 Isotope Separation

One of the most popular methods of isotope enrichment is the centrifuge setup. It essentially consists of a cylinder (containing a gaseous mixture of isotopes of an element. For Uranium (U), it is UF_6 while for Si it is SiF_4 and so on), spinning on its vertical axis. It is based on the principle that the centrifugal force acting on a particle is proportional to its mass – forcing the heavier isotope to accumulate near the periphery of the spinning cylinder and the lighter isotope towards the center. Normally there is a cascade of centrifuges which eventually produces the enriched isotopes. Initial centrifuge designs though looked promising, the Manhattan project failed to produce a workable model for U enrichment (primarily due to the excessive energy requirements of the high-speed centrifuges which could only sustain short runs before breaking down) and the project scientists eventually moved on to gaseous diffusion and electromagnetic based enrichment methods. Isotope enrichment by gaseous diffusion is based on the principle that lighter isotopes of an element can cross a diffusion barrier quicker than the heavier isotope [19], [20]. It too needs to be repeated several times, through a sequential cascade of diffusion setups, to obtain an enriched isotope at the end. Early works on isotope enrichment by gaseous diffusion started in Great Britain. But after

President Roosevelt and Prime Minister Churchill signed the Quebec-agreement in 1943 (agreeing on a full exchange of intelligence and information between the Great Britain and the US), it became an integral part of the Manhattan project. The electromagnetic separation setup sends a flux of charged particles through a crossed magnetic field [21], [22]. It is based on the principle that moving charged particles (of velocity v and charge q) in a crossed magnetic field (B) experiences a Lorentz force ($qv \times B$), which provides the centripetal force needed to bend the trajectory of a particle (of mass m) in a circular path. The radius of the circular path (mv/qB) of a charged particle is a function of its mass and hence the different isotopes can be collected by different receivers. With the centrifuge systems failing the expectations during the Manhattan project, the first industrial scale project undertaken to separate isotope by electromagnetic means took place at the Y-12 plant at Oak Ridge, Tennessee.

The centrifuge problem was later tackled by several scientists. During and after the war, several German scientists and intellectuals were kidnapped to the Soviet Union, some of whom worked in the Soviet nuclear program. Among them, Gernot Zippe and Max Steenbeck made several improvements to the centrifuge design and managed to eliminate the frictional losses encountered by earlier designs. Later, as Zippe migrated to Virginia, he reconstructed the design (primarily based on his memory) and it soon gained popularity. Till today, the Zippe-centrifuge largely remains one of the most commonly used method of isotope enrichment. For a brief period in the 1940s, isotope enrichment by liquid thermal diffusion was also taken into consideration. Unlike a gaseous centrifuge, which uses a gaseous mixture of the isotopes of an element, this process uses the pressurized liquid mixture (liquid UF_6 for example) of isotopes. The liquid mixture is put into the space between two concentric cylinders with the outer wall cooled by running cold water and the inner wall heated by steam. This would eventually set up a convection current carrying the lighter isotope to the top wherefrom it could be separated and after several repetitions, an enriched isotope could be obtained [23], [24]. While the Zippe-centrifuge method is still in extensive use today, the other process became nearly obsolete after the war. A more recent technique, the laser isotope separation came into the picture in the 1970's. It uses the shift induced in the molecular spectra by the isotope effect to selectively photoionize or photodissociate a particular isotope of an element using a properly tuned laser beam. The photoionized or photodissociated isotope can then be separated electrostatically or by means of chemical reactions [25]–[28].

2.1.2 Stable Isotope Effect on Fundamental Properties of Semiconductors

2.1.2.1 Phonon Properties: Energy and Scattering Rates

One of the most drastic isotope related effects is found in the vibrational behavior of a crystal. Within the realm of a harmonic approximation, atoms in a crystal within a periodic lattice, behave like harmonic oscillators with the atomic vibrational frequency depending inversely on the square root of the average atomic mass as $\omega_{q,j} \propto \langle m \rangle^{-1/2}$ (q is the vibrational wave vector corresponding to the j^{th} branch of the dispersion relation). The concept of average atomic mass comes from the virtual crystal approximation (VCA)[29], which assumes each lattice site to be occupied by an atom of average mass $\langle m \rangle = \sum_i c_i m_i$, where c_i is the fractional composition of the i^{th} isotope of mass m_i. In a real crystal, the presence of mass-disorder and the anharmonic phonon interaction perturbs this pure harmonic picture of atomic vibrations. Raman spectroscopy is the most commonly employed method to investigate the vibrational waves or phonons in isotopically engineered bulk crystals [30]–[34]. It probes only the phonons located near the center of the Brillouin zone. For measurements done at room temperature and lower, the phonon spectrum is often analyzed in realm of a *quasi-harmonic approximation*, wherein it is assumed that the anharmonic perturbations although present, are small compared to the harmonic effect and the harmonic approximation is still valid. Figure 2.1(a) shows the evolution of the measured phonon frequency with varying $\langle m \rangle$ in several isotopically engineered bulk Si samples [30].

Quantum perturbation theory is often employed [35]–[37] to investigate the anharmonic self-energy $\left(\Pi_{Anhrm}(\omega)\right)$ and the isotopic disorder induced self-energy $\left(\Pi_{Isotope}(\omega)\right)$ of phonons. The two are additive in nature and contribute to the total phonon self-energy as $\Pi(\omega) = \Pi_{Anhrm}(\omega) + \Pi_{Isotope}(\omega)$. $\Pi(\omega)$ is complex in nature $\{\Pi(\omega) = \Gamma(q, j, \omega) - i\Delta(q, j, \omega)\}$, the real and the imaginary part of which gives the frequency shift and broadening of a Raman spectral line, respectively. Theoretically, the imaginary part of the self-energy (Δ), which depends on the amplitudes of the scattering phonons, the temperature (T), and the density of states into which the Raman phonon can scatter into, is first calculated and then the real part (Γ) is obtained by applying the Hilbert-Kramer-Kroning relation on Δ. Both $-\Delta^{(3)}_{Anhrm}$ and $\Gamma^{(3)}_{Anhrm}$ terms coming from the three phonon anharmonic interaction can be shown to have a $\langle m \rangle^{-1}$ dependence at $T > 0K$ [38]. At very high temperatures, this $\langle m \rangle^{-1}$ dependence is lost into a $T/\langle m \rangle^{1/2}$

dependence. $-\Delta_{Isotope}$ and $\Gamma_{Isotope}$ and coming from the isotopic fluctuation can be shown to be independent of $\langle m \rangle$ and T, but rather depend on the second order moment of mass fluctuation

$$g_2 = \sum_i c_i \left(\frac{m_i - \langle m \rangle}{m_i} \right)^2 \quad (2.1.1)$$

where c_i is the fractional composition of the isotope of mass m_i [35]. The dotted black line in Figure 2.1(a) is the fit to the experimentally measured Raman frequencies while the continuous black line represents the contribution of the bare harmonic ($\sim \langle m \rangle^{-1/2}$) and the anharmonic ($\sim \langle m \rangle^{-1}$) terms. The difference between the two lines represent the contribution of mass-disorder, which is maximum for the sample with equal (~50.0 at.% of each) concentration of the two isotopes (hence the maximum g_2).

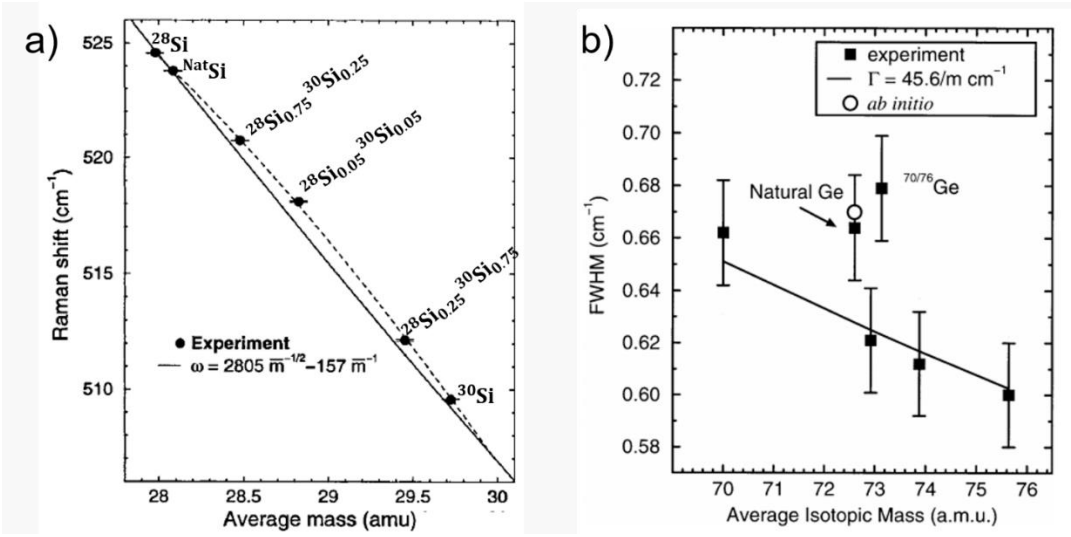

Figure 2.1: *(a) The evolution of the phonon energies (Raman frequencies) of different isotopically engineered Si samples with* $\langle m \rangle$*. (Reproduced with permission from Widulle et al. [30]). (b) The evolution of the Raman line width of the different isotopically engineered Ge samples with* $\langle m \rangle$*. (Reproduced with permission from Zhang et al. [33]).*

If the interaction between the phonons in a crystal had been purely harmonic, a precise determination of phonon frequency would have been possible. The Raman spectra should have been a δ-function located at the bare harmonic frequency $\omega_{0,j}$ (the suffix '0' denoting the center

of the Brillouin zone or $q = 0$). Uncertainties in precise determination of phonon frequency appears due to scattering of phonons and is reflected in the finite width (FWHM or full width at half maxima) of a Raman line. Stronger the phonon scattering rate, greater the uncertainty and greater is the width of the Raman line. Different mechanisms can affect the phonon scattering rate in a crystal, for example the normal anharmonic phonon scattering, the Umklapp anharmonic scattering of a Raman phonon outside the first Brillouin zone (typically above θ_D, the Debye temperature of a material), and the scattering of phonons from mass disorder. In nanostructures when the dimension of the crystal becomes comparable to the phonon mean free path, an additional boundary or surface scattering comes into play. While the anharmonic and the Umklapp scattering rates depend inversely on $\langle m \rangle$, the scattering rate from mass disorder depend only on g_2. Figure 2.1(b) shows the evolution of Raman FWHM of different isotopically engineered Ge crystals as a function of $\langle m \rangle$ [33]. The Raman FWHM after correcting for the instrumental broadening can be broken into [32]:

$$FWHM = \frac{A}{\langle m \rangle} + g_2 C = \frac{1}{2\pi c \tau_{ph}} \quad (2.1.2)$$

c being the velocity of light. Where several phonon scattering mechanisms are simultaneously present, the decay time (τ_{ph}) of phonons in a crystal can be expanded by Matthiessen's rule under the assumption that different phonon scattering processes are independent of each other. The FWHM in Figure 2.1(b) can therefore be broken into

$$FWHM = \frac{1}{2\pi c}\left[\frac{1}{\tau_{Anhrm}} + \frac{1}{\tau_{Isotope}}\right] \quad (2.1.3)$$

Umklapp scattering and boundary scattering are absent for bulk semiconductors at temperatures lower than θ_D. The thick black line in Figure 2.1(b) represents the contribution of the anharmonic effect to the total line broadening. The departure in the measured widths shown by the ^{Nat}Ge and $^{70/76}$Ge samples from this line is due to the contribution of mass-disorder which is more for $^{70/76}$Ge owing to its higher g_2. The deconvolution of the total FWHM enabled measuring the decay time of phonons due to anharmonic scattering, which in ^{70}Ge, ^{76}Ge and ^{Nat}Ge was found to be $6.4(\pm 0.1)$ps, $5.9(\pm 0.1)$ps, and $6.1(\pm 0.1)$ps respectively [32]. The phonon decay time due to isotope scattering was found to be two orders of magnitude higher. The Raman spectra of isotopically modulated superlattices is markedly different from the spectra of a bulk or thin film

samples and deserves a mention here. The atomic periodicity in such superlattices gets modulated by the mass periodicity along the growth direction, resulting in a folding of the Brillouin zone. This causes the phonon modes to fold back to the center of the zone, enabling some new modes to satisfy the $q = 0$ Raman selection rule, as was seen for $^{70}(\mathrm{Ge})_{\mathfrak{m}}{}^{74}(\mathrm{Ge})_{\mathfrak{m}}$ [39] and $^{28}(\mathrm{Si})_{\mathfrak{m}}{}^{30}(\mathrm{Si})_{\mathfrak{m}}$ [40] superlattices, $\mathfrak{m}$ being the number of monolayers. The appearance and the energies of these additional localized modes in the Raman spectra of an isotopic superlattice depend on $\mathfrak{m}$.

2.1.2.2 Electronic Gaps:

The isotopic mass dependence of the fundamental energy gaps in a semiconductor stems in through the following effects [41] : i) electron-two phonon interaction : simultaneous interaction of two phonons having wave vector q at the j^{th} branch of phonon dispersion relation with two different polarization, with an electron with wave vector k at the n^{th} branch of electron dispersion relation. This is also called the Debye-Waller term and originate from the 2nd order electron-phonon interaction Hamiltonian in 1st order perturbation theory; ii) the self-energy terms (also called Fan-terms) of a single electron which absorb or emit a phonon and originate from the 1st order electron-phonon interaction Hamiltonian in 2nd order perturbation theory; and iii) change in lattice constant (a) or crystal volume with isotopic mass. The $\langle m \rangle$ dependence of band gap energy (E_g^i, i denoting the indirect gap) can be expressed as [42] :

$$\left(\partial E_g^i \Big/ \partial\langle m\rangle\right)_T = \left(\partial E_g^i \Big/ \partial\langle m\rangle\right)_{E-P} + \left(\partial E_g^i \Big/ \partial\langle m\rangle\right)_{vol} \qquad (2.1.4)$$

where *E-P* denotes the electron-phonon interaction terms (Debye-Waller and the Fan terms taken together) and vol denotes volume term. Both $\left(\partial E_g^i/\partial\langle m\rangle\right)_{E-P}$ and $\left(\partial E_g^i/\partial\langle m\rangle\right)_{vol}$ are proportional to the mean squared vibrational amplitude of atoms, $\langle u^2\rangle$ [43]. $\langle u^2\rangle$ is related to $\langle m\rangle$ by the Bose-Einstein factor n_B through the relation

$$\langle u_{q,j}^2\rangle = \frac{\hbar}{\langle m\rangle\omega_{q,j}}\left\{n_B(q,j) + \frac{1}{2}\right\} \qquad (2.1.5)$$

As $n_B(q,j) \to 0$ at low temperatures, it is easy to see that $\langle u_{q,j}^2\rangle$ is proportional to $\langle m\rangle^{-1/2}$ under the quasi-harmonic approximation. At high temperatures, as $n_B(q,j) \to k_B T/\hbar\omega_{q,j}$, $\langle u_{q,j}^2\rangle$

becomes independent of $\langle m \rangle$ but linear in temperature. Thus, the $\langle m \rangle$ dependence of E_g^i becomes progressively less important at high temperatures.

The low temperature photoluminescence (PL) spectra from copper donors and phosphorous acceptors bound excitons was used to investigate the band gap difference between several isotopically enriched Ge crystals [6]. The PL spectra is marked by the no-phonon (NP) lines (the bound excitons that decay without any phonon assistance), the transverse optic (TO), longitudinal acoustic (LA), transverse acoustic (TA) replicas, and the free excitonic (FE) decay lines. The NP lines are located at the bandgap energy minus the free exciton binding energy minus the bound exciton localization energy. Consequently, the difference between the energy of the Cu-NP (or P-NP) lines in the two samples reflect the difference in their band gap at the measured temperature. This is based on the assumption that the excitonic binding and the localization energies are same in all the isotopically engineered Ge samples. The $\langle m \rangle$ dependence of the indirect gap $\left(\partial E_g^i / \partial \langle m \rangle\right)_T = \left(\partial E_{NP} / \partial \langle m \rangle\right)_T$ was found to be 0.35 ± 0.02 meV/amu. for the set of isotopically enriched Ge samples under investigation [6]. Although both the terms in the right hand side of equation (2.1.4) has a $\langle m \rangle^{-1/2}$ dependence at low temperature, for a small difference in $\langle m \rangle$ between the different enriched samples, an approximate linear fit is often considered where $\left(\partial E_g^i / \partial \langle m \rangle\right)_T$ comes out to be a constant. Later, the data from low temperature PL measurements on $^{\mathrm{Nat}}$Ge and isotopically mixed $^{70/76}$Ge were combined with the previously obtained data from isotopically enriched Ge samples and compared [44]. The energy of the Cu-NP line in the $^{70/76}$Ge and $^{\mathrm{Nat}}$Ge was found to lie above the value predicted by the quasi-harmonic approximation, the deviation being more for the disordered $^{70/76}$Ge sample. The deviation was related to the dependence of phonon self-energy on isotopic disorder, affecting the electron-phonon interaction term.

Optical absorption method was employed to investigate isotope dependence of the direct gap in Ge using isotopically engineered (both enriched and disordered) Ge samples [45]. The measurements revealed $\left(\partial E_0 / \partial \langle m \rangle\right)_T = 0.49 \pm 0.03$ meV/amu. ('0' denoting the direct gap). Modulation spectroscopy on isotopically engineered Ge samples was also used to investigate the isotope dependence of the energy at other critical transition points [46]. The measurements revealed $\left(\partial E_g^i / \partial \langle m \rangle\right)_T$ and $\left(\partial E_0 / \partial \langle m \rangle\right)_T$ to be 0.36 meV/amu. and 0.49 meV/amu., respectively. The isotope dependence of the $E_0 + \Delta_0$ direct transitions was determined to be

$\{(\partial(E_0 + \Delta_0)/\partial\langle m\rangle)\}_T = 0.74$ meV/amu., giving the $\langle m\rangle$ dependence of the spin-orbit splitting alone to be $(\partial\Delta_0/\partial\langle m\rangle)_T = 0.25$ meV/amu. Later, the isotope dependence of the E_1 and $E_1 + \Delta_1$ transition points in Ge was investigated by employing ellipsometric measurements on isotopically engineered Ge samples [47]. PL spectroscopy was used to study the isotope dependence of the indirect gap in ^{Nat}Si, enriched Si, and disordered $^{28/30}$Si at low temperatures [48]. The shift in E_g^i with respect to ^{28}Si was found to be 114 μeV, 1.04 meV, 2.09 meV, and 1.48 meV for ^{Nat}Si, ^{29}Si, ^{30}Si, and $^{28/30}$Si, respectively. Cathodoluminesence (CL) measurements were performed at liquid nitrogen temperature on microwave plasma-assisted CVD grown $^{12}C_{1-x}{}^{13}C_x$ diamond ($x = 0.001, 0.24, 0.49, 0.74,$ and 0.98) films [49]. The FE spectra, rather than the bound excitons spectra was used for the analysis. The FE spectra from the $^{12}C_{1-x}{}^{13}C_x$ samples is shown in Figure 2.2(a). The band gap dependence on x was estimated to be of the form $E_g^i(x) = 5497.66 + 14.37x + 0.99x^2$ meV. The difference in E_g^i between ^{12}C and ^{13}C was calculated to be 15.4 meV, an order of magnitude larger than the reported difference in E_g^i for Si and Ge. This difference in E_g^i was later used in an isotopic $^{12}C/^{13}C$ homojunction superlattice, to confine charge carriers in the lower gap ^{12}C nanoscale layers [8].

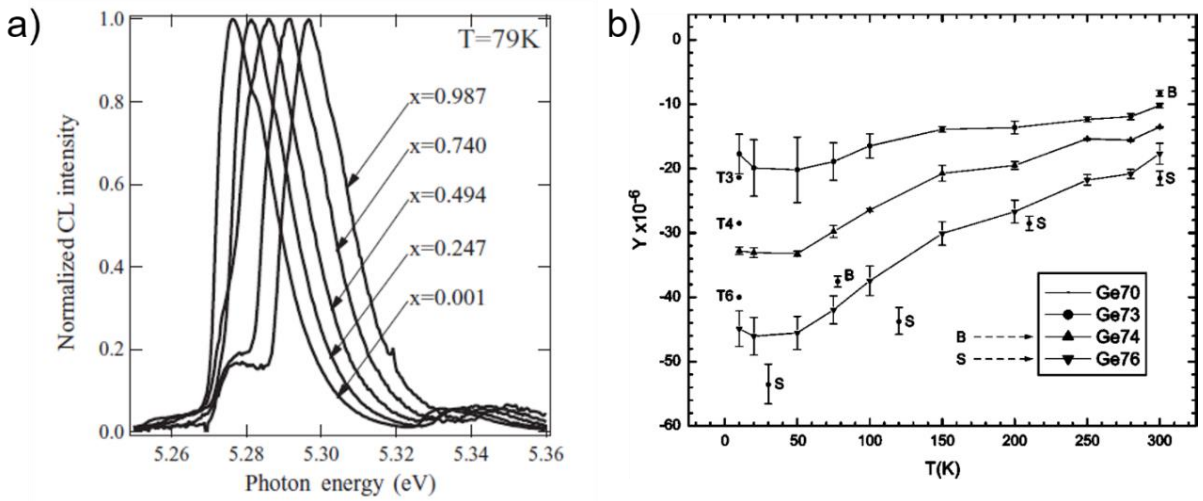

Figure 2.2: *(a) Free excitonic CL spectra collected at $T = 79\,K$ from different isotopically engineered C diamond films. (Reproduced with permission from Watanabe et al. [49]). (b) x-ray back scattering measurement results on the fractional change in relaxed lattice constant $(\Delta a/a)$ of ^{73}Ge, ^{74}Ge, and ^{76}Ge with respect to ^{70}Ge as a function of temperature. The abscissa represents*

$Y = (a_{\langle m \rangle} - a_{70})/a_{70}$ *in ppm. The points labelled* $T3, T4$, *and* $T6$ *are theoretical calculated values of* Y *at* $T = 0K$, *for* ^{73}Ge, ^{74}Ge, *and* ^{76}Ge *respectively. (Reproduced with permission from Hu et al. [5]).*

2.1.2.3 Lattice Constant

With $U_0(V)$ as the crystal binding energy and F_{ph} as the phonon free energy (considering N atoms producing 3N independent phonon modes having wave vector q in the j^{th} branch), the total Helmholtz free energy of the crystal at a temperature T can be written as

$$F_t = U_0(V) + F_{ph} = U_0(V) + \sum_{q,j}\left[\frac{1}{2}\hbar\omega_{q,j} + k_B T ln\left\{1 - exp\left(-\frac{\hbar\omega_{q,j}}{k_B T}\right)\right\}\right] \quad (2.1.6)$$

The zero-pressure volume of the crystal at equilibrium can be evaluated by setting $(\partial F_t/\partial V)_T$ to zero. The relative change in lattice constant $(\Delta a/a)$ can be calculated from the relative change in crystal volume $(\Delta V/V)$ as a function of $\omega_{q,j}$, and can be shown to be [50]

$$\frac{\Delta a}{a} = \frac{\hbar}{3\mathcal{B}V}\sum_{q,j}\gamma_{q,j}\omega_{q,j}\left[n_B(\omega_{q,j}) + \frac{1}{2}\right] \quad (2.1.7)$$

where $\mathcal{B}$ is the isothermal bulk modulus and $\gamma_{q,j}$ is the Grüneisen parameter of the mode. The isotope dependence of $\Delta a/a$ comes through the relation $\omega_{q,j} \propto \langle m \rangle^{-1/2}$ and is best observable at low temperatures. Theoretically, difference can be shown to exists even at $\mathrm{T} = 0$ K, due to the zero-point motion of atoms and the dependence of the zero-point energy on $\langle m \rangle$. At high temperatures, the lattice vibrational amplitude becomes progressively independent of $\langle m \rangle$ and the isotope dependence of the lattice constant disappears. Figure 2.2(b) shows the evolution of $\Delta a/a$ of ^{j}Ge bulk samples {with j =70(96.3%), 73(96.0%), 74(96.8%), and 76(85.1%)} relative to ^{70}Ge as a function of temperature [5]. In the low temperature regime, $\Delta a/a$ for ^{73}Ge, ^{74}Ge, and ^{76}Ge was found to be -17.7 ppm, -32.7 ppm, and -44.9 ppm, respectively relative to ^{70}Ge, in close agreement with the values calculated theoretically using a thermodynamic model (equation 2.1.7). Similar measurements carried out on isotopically engineered Si revealed the $\Delta a/a$ of ^{30}Si to be -30 ppm and -18 ppm with respect to $^{\mathrm{Nat}}$Si at $\mathrm{T} = 30$ K and $\mathrm{T} = 300$ K respectively [51]. $\Delta a/a$ was measured at $\mathrm{T} = 298$ K using the x-ray diffraction technique on $^{\mathrm{Nat}}$C as well as other isotopically engineered diamond like $^{12}\mathrm{C}_{0.99}{}^{13}\mathrm{C}_{0.01}$, $^{12}\mathrm{C}_{0.62}{}^{13}\mathrm{C}_{0.38}$, $^{12}\mathrm{C}_{0.38}{}^{13}\mathrm{C}_{0.62}$,

and $^{12}C_{0.01}{}^{13}C_{0.99}$ [52]. The lattice constant of diamond as a function of ^{13}C concentration (x) in $^{12}C_{1-x}{}^{13}C_x$ was found by fitting the experimental data with the equation $a(25℃, x) = 3.56715 - 0.00053x$ Å. $\Delta a/a$ between the two extreme samples (99% ^{12}C and 99% ^{13}C) was found to be -150 ppm at $T = 298$ K.

2.1.3 Impact of Isotope Engineering on Semiconductor Physics

2.1.3.1 Lattice Thermal Conductivity

In a semiconductor or a dielectric, the heat energy is transported by the phonons, primarily by the low frequency acoustic phonons. The flatness of the optical phonon dispersion curve results in their extremely small group velocity, rendering them ineffective in carrying the thermal energy. The phononic thermal conductivity (κ) can be expressed as

$$\kappa(T) = \frac{1}{3} C(T) \langle v_{ph} \rangle \lambda_{ph}(T) \quad (2.1.8)$$

where $C(T)$ is specific heat of the material at a temperature T, $\lambda_{ph}(T)$ is the phonon mean free path in the material at T, $\langle v_{ph} \rangle$ is the average phonon group velocity in the material. $\lambda_{ph}(T)$ can be further expanded as $\langle v_{ph} \rangle . \tau_{ph}(T)$ where $\tau_{ph}(T)$ is the relaxation time of phonons in the material at T. The isotope dependence of κ comes from the fact that the phonon decay rate and hence the phonon mean free path are affected by the average isotopic mass and/or the isotopic disorder. In as early as 1942, Pomeranchuk's commented that isotopes can disturb the periodicity of a lattice and contribute to thermal resistance [53]. Later as enriched precursors became accessible, experimental studies on κ of isotopically engineered bulk semiconductors became more feasible, Ge being the most investigated semiconductor [54], [55]. According to the Casimir's theory, the inverse thermal resistivity (thermal conductivity) originating from diffuse scattering of phonons from crystal boundary should have a $\sim T^3$ dependence at low temperature [56]. This is due to the fact that boundary scattering rate of phonons is actually temperature independent, and κ (in low temperature regime) should essentially mimic the $\sim T^3$ dependent of specific heat. Peierl's predicted that in the high temperature regime, κ of a crystal should increase exponentially with decreasing T primarily due to the $\sim e^{-\theta_D/\mathscr{b}T}$ ($\mathscr{b}$ is a constant and θ_D the Debye temperature) dependence of the anharmonic Umklapp scattering rate of phonons on temperature [57]. In between the two regimes at a

temperature T_{max}, the maximum of the thermal conductivity (κ_{max}) occurs. The isotope effect on the thermal conductivity is most prominent around T_{max}.

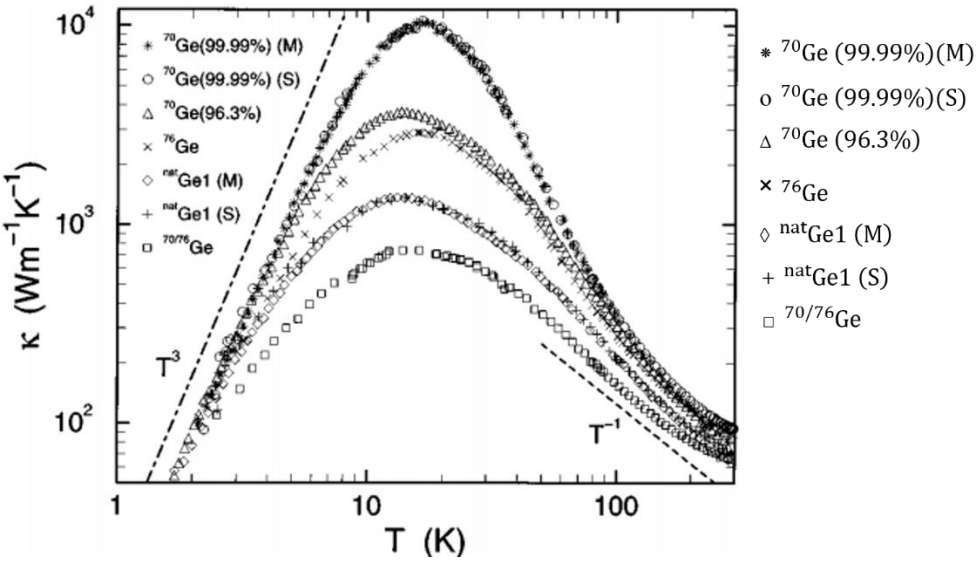

Figure 2.3: *Evolution of the lattice thermal conductivity of different isotopically engineered Ge samples: ^{70}Ge(99.99%), ^{70}Ge(96.3%), ^{76}Ge(86.3%), ^{Nat}Ge, and $^{70/76}$Ge as a function of temperature. The $^{70/76}$Ge sample had 43.0% of ^{70}Ge and 48.0% of ^{76}Ge and residual ^{72}Ge and ^{74}Ge. M and S represents the measurements done at labs in Moscow and Stuttgart respectively. The black dotted lines represent the T^3 and T^{-1} dependence of κ at low and high temperatures respectively. (Reproduced with permission from Asen-Palmer et al. [55]). For clarity, the figure legends are highlighted alongside.*

Figure 2.3 shows the measured evolution of κ of different isotopically engineered Ge samples with T (between 2 K and 200 K) [55]. The samples analyzed consisted of isotopically enriched ^{70}Ge (samples from Stuttgart (S) and Moscow (M) which were purified to 99.99%. The other ^{70}Ge sample used in their work was purified to 96.3%), isotopically disordered $^{70/76}$Ge and ^{Nat}Ge sample. A modified Callaway-Holland model was implemented to fit the experimental data. The fit revealed that κ_{max} (at $T_{max} = 16.5$ K) for the ^{70}Ge (99.99%), is enhanced by a factor of 8 compared to that of the ^{Nat}Ge sample, while that for the $^{70/76}$Ge sample is reduced by a factor of 1.8 as compared to ^{Nat}Ge. At $T = 300$ K, a 30% increment in κ for the ^{70}Ge (99.99%) sample as

compared to ^{Nat}Ge was also reported. Similar measurements on Si showed a $\sim 60\%$ enhancement in κ of the ^{28}Si(99.85%) as compared to the ^{Nat}Si sample at $T = 300$ K [58], although theoretical calculations predicted only a $\sim 12\%$ increment at room temperatures [59]. At $T_{max} \sim 20$ K, an enhancement of κ_{max} by a factor of 6 was shown for ^{28}Si compared to ^{Nat}Si. Later, κ of four different isotopically enriched ^{28}Si samples (between 99.92% and 99.98% purity) were measured using high precision steady-state heat flow technique in three different laboratories [4]. An erratum, correcting the earlier claims was published [4], which showed the enhancement of κ at $T = 300$ K for the ^{28}Si sample is indeed $10 \pm 2\%$ compared to ^{Nat}Si, as predicted theoretically. The measurements also showed the enhancement of κ_{max} by a factor of 8 at $T_{max} \sim 26$ K for ^{28}Si with respect to ^{Nat}Si.

For C diamond, a $\sim 50\%$ enhancement in $\kappa(T = 300\ K)$ for enriched ^{12}C ($^{13}C < 0.05\%$) with respect to ^{Nat}C was shown [60], [61]. The increment is significantly higher than Si and Ge. The physical reason for this is the combination of extremely strong atomic bonds and light atomic weight producing extremely high phonon frequencies and phonon group velocities in diamond. Also the Debye temperature of diamond being very high, the anharmonic scattering rates (both normal and Umklapp) are smaller at room temperature compared to that in Si and Ge, thereby producing extremely high values of κ. The empirical model that was used to fit the measured κ of ^{12}C (0.1% ^{13}C) also predicted that if the ^{13}C concentration in enriched ^{12}C can be made two orders of magnitude lower, that is 0.001% of ^{13}C, κ_{max} can reach and even exceed a record value of 2000 W(cm-K)$^{-1}$ [62]. Time-resolved x-ray scattering technique was used to compared the κ of molecular beam epitaxy (MBE) grown ^{28}Si thin film, twenty undoped bilayers structures of $(^{29}Si/^{30}Si)_{20}$ and $(^{28}Si/^{30}Si)_{20}$ superlattices, and ^{Nat}Si [63], [64]. The results highlighted some key facts: the room temperature κ of ^{28}Si film is enhanced by $\sim 30 \pm 13\%$ compared to ^{Nat}Si. κ for the superlattice structures were shown to be decreased by a factor of $2 - 3$ compared to ^{Nat}Si. The reason for the drop in κ for the superlattices was stated to be the decrease in phonon group velocity due to folding of the Brillouin zone and the increase in interfacial thermal resistance (or Kapitza resistance) between the isotopically modulated layers. Single layer graphene with patches of different isotopic compositions (0.01%, 1.1%, 50%, and 99.2% of ^{13}C content) was grown over a Cu foil in a CVD chamber and then on a suspended monolayer of graphene, the κ of the different isotopic regions was measured by optothermal Raman technique [65]. It was found that κ values

for 1.1% and 99.2% ^{13}C graphene are almost the same, since the mass-variance and hence the disorder induced scattering rate of phonons in both are comparable. Also at $T = 300\ K$, the isotopically enriched (0.01% ^{13}C) graphene has κ above 4000 W(m-K)$^{-1}$ which is about more than double the value for the isotopically mixed graphene (50% ^{13}C).

2.1.3.2 Spectroscopy and Mass Transport

Local Vibrational Mode Spectroscopy: Impurities of any form when introduced in a crystal lattice, break its symmetry. Typically, with lighter impurities within a host of heavier atoms (like H and O in Si and Ge, Si in GaAs, etc), when the mass difference and/or the difference in bond strength between an impurity and host atoms becomes large, the vibrational frequency (energy) becomes too high to propagate through the lattice. As a result, the vibrational energy remains trapped (localized) over the bond until it can decay into the lower frequency modes (other localized modes or phonon modes) [66]. This causes new modes to appear in the vibrational spectrum and are called the local vibrational modes (LVM).

The energy and the lifetime of the LVMs can provide a wealth of information regarding the vibrational dynamics of impurities in semiconductors. The LVM of interstitial oxygen (O_i) is the most studied among other impurities, since oxygen is the most common impurity in Czochralski-grown group-IV semiconductors. $X - O_i - X$ or X_2O_i (X being the host Si or Ge) quasimolecule has three fundamental modes of vibration [44]: the symmetric stretch mode (υ_1), the antisymmetric stretch mode (υ_3), and the transverse mode (υ_2). Each of the different isotopic combination of $^{i}X - {}^{16}O - {}^{j}X$ ($i\,j$ being the mass number of the isotopes of X) quasimolecule gives rise to a line in the local vibrational spectra (LVS). The strength (intensity) of the line is proportional to the abundance of the isotopes in question which gives rise to a fine structure, especially in an element like ^{Nat}Ge which has five stable isotopes. Additional lines in the LVS appear due to the coupling between LVMs, which occur due to the anharmonic interaction between the υ_2 and υ_3 vibrational modes [67], [68]. Consequently, the LVS of $^{Nat}Ge_2$: ^{16}O was found to have a fine structure consisting of 22 lines between $860\ cm^{-1}$ and $864.2\ cm^{-1}$ at $T = 2.03\ K$ which increased to 38 at $T = 6\ K$ [69]. The number of lines increases with temperature since the excited υ_2 levels at the ground state of υ_3, wherefrom the coupled $\upsilon_3 + \upsilon_2$ coupled transitions originate, starts becoming thermally populated. Isotopically enriched samples clean up the LVS.

For example, if we have a 100% enriched ^{j}Ge sample, the possible isotopic combinations reduce to 1 compared 11 in $^{\mathrm{Nat}}$Ge. Figure 2.4(a) shows the comparison between the LVS of $^{\mathrm{Nat}}\mathrm{Ge}_2$: ^{16}O (left) and the superimposed spectra of enriched $^{j}\mathrm{Ge}_2$: ^{16}O ($j = 70, 73, 74, 76$) (right) recorded at $\mathrm{T} = 2.03$ K [69]. Apart from the additional $^{71}\mathrm{Ge}_2$: ^{16}O and $^{75}\mathrm{Ge}_2$: ^{16}O lines, which originate from traces of ^{72}Ge in ^{70}Ge and ^{74}Ge in ^{76}Ge, the fine structure is significantly reduced in the enriched samples which makes analyzing the spectra much easier. A similar effect, namely the simplification of the LVS of $\mathrm{O_i}$ was found with the use of enriched ^{j}Si ($j = 28, 29, 30$) [70]. The spectral cleanup and small degree of mass disorder in the enriched ^{j}Si samples also made possible observing new coupled $\upsilon_2 + \upsilon_3$ modes, never before observed in $^{\mathrm{Nat}}$Si.

Optical Spectroscopy: Luminescence spectroscopy from excitons bound to the shallow and deep centers, both neutral and ionized, can provide a wealth of information not only regarding the nature of the defect center but also about the host semiconductor material as well.

Figure 2.4(b) shows the low temperature PL spectra of excitons bound to neutral P and B atoms in $^{\mathrm{Nat}}$Si and enriched ^{28}Si (but of less chemical purity compared to the $^{\mathrm{Nat}}$Si sample) [71]. The bound excitons are devoid of any kinetic energy due to the localization, resulting in extremely sharp line in the PL spectra, revealing finely resolved structures and details, not commonly observable in the FE spectra. Clearly evident is the fact that the no-phonon (NP) lines of the bound excitons are much narrower in shape in ^{28}Si than the $^{\mathrm{Nat}}$Si, in spite of the poor chemical purity of ^{28}Si [71]. In fact, the linewidth of the P bound exciton line in ^{28}Si was recorded to be equal to the best available instrumental linewidth of $0.014\ \mathrm{cm}^{-1}$. The inhomogenous broadening of the PL lines in $^{\mathrm{Nat}}$Si was explained to be originating due to the statistical fluctuation of the isotopic distribution in $^{\mathrm{Nat}}$Si within an effective bound exciton volume. This immediately showed the need of isotopic enrichment to exploit the full potential of luminescence spectroscopy in investigating the optical properties of semiconductors. In other measurements, the NP spectral lines of excitons bound to neutral acceptors (A^0X) in $^{\mathrm{Nat}}$Si was found to show a small doublet splitting [72]. The A^0X initial state in Si has three populated levels corresponding to the three valley-orbit electron states. Each of these states shows a doublet splitting because the neutral acceptor ground state in $^{\mathrm{Nat}}$Si itself has a doublet splitting.

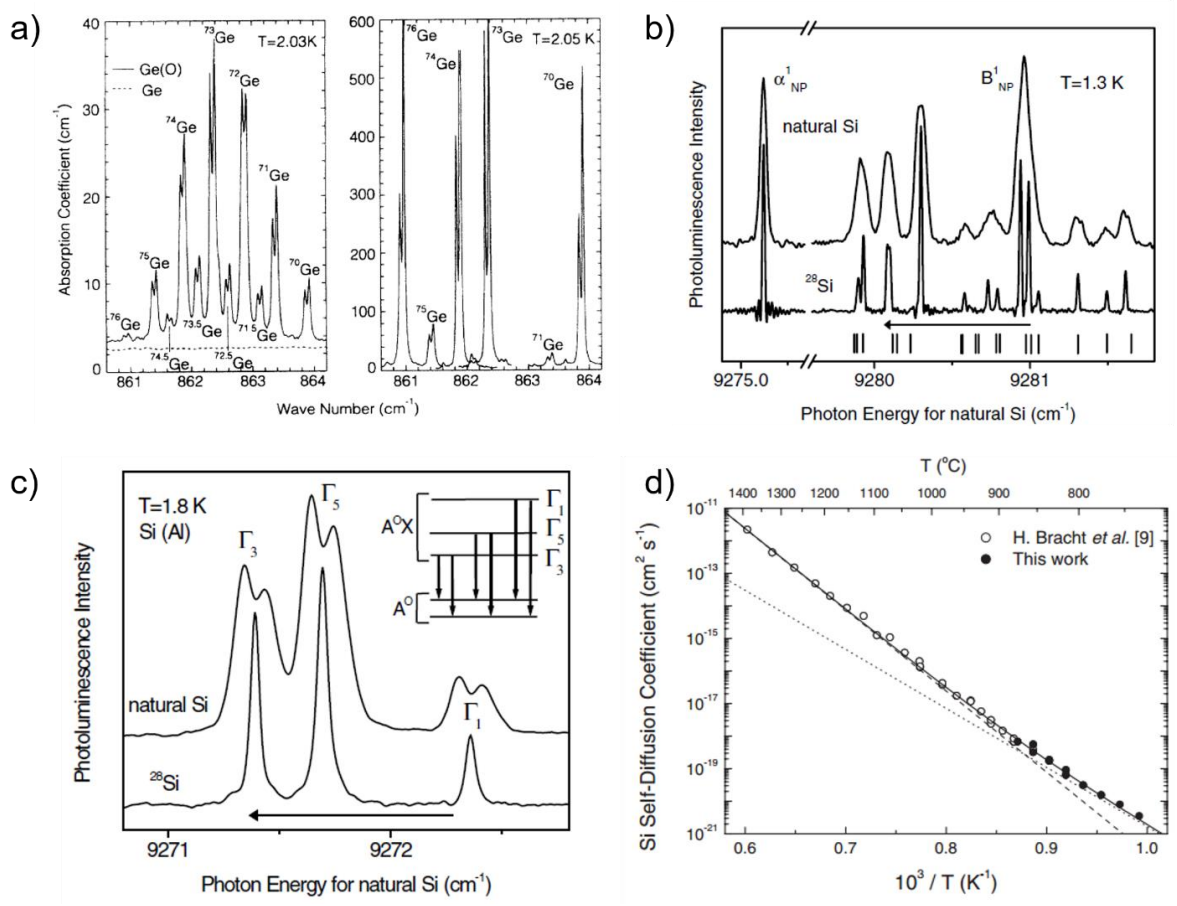

Figure 2.4: *(a) LVS of* $^{Nat}Ge_2$*:*^{16}O *(left) and the superimposed spectra of enriched* $^{j}Ge_2$*:* ^{16}O $(j = 70, 73, 74, 76)$ *(right). (Reproduced with permission from Mayur et al. [69]). (b) High resolution NP PL lines of excitons bound to neutral B (*B^1_{NP}*) and P (*α^1_{NP}*) impurities in* ^{Nat}Si *(top) and enriched* ^{28}Si*(bottom). (c) High-resolution NP lines of excitons bound to neutral Al acceptor in* ^{Nat}Si *(top) and enriched* ^{28}Si *(bottom). Inset: Energy level diagram showing the doublet splitting of the* A^0 *ground state in* ^{Nat}Si *(absent in enriched* ^{28}Si*) as well as the triplet* A^0X *excited state. The spectrum in both (b) and (c) obtained from* ^{28}Si *is red-shifted by 0.92 cm*$^{-1}$*. (the length of the arrow) to account for the band gap difference between the two. (Both (b) and (c) reproduced with permission from Karaiskaj et al. [72]). (d) Evolution of* D_{SD} *for Si as a function of annealing temperature. The solid circles represent the* D_{SD} *values obtain from Raman spectroscopic investigation [73], while the open circles represent the* D_{SD} *values obtained from the SIMS measurements. The dashed and the dotted lines represent the contribution of self-interstitial and self-vacancy to* D_{SD}*. (Reproduced with permission from Bracht et al. [74]).*

On the contrary, in the Al^0X PL spectrum in ^{28}Si, the lines apart from being much narrower had no sign of any doublet splitting. The conclusion drawn from these observations were that the statistical fluctuation in the random isotopic distribution surrounding a given neutral acceptor atom in ^{Nat}Si helps lifting the degeneracy in the A^0 ground state, resulting in a doublet splitting of the PL lines. Surprisingly, ^{Nat}Si which is close to being entirely ^{28}Si, the isotopic randomness is an extremely subtle phenomenon and yet resulted in such large splitting of the A^0X lines. Figure 2.4(c) also shows the effect of the isotopic composition on absorption spectrum [75]. A larger binding energy is observed for ^{30}Si as compared to ^{28}Si, with the difference being $0.73\ \mathrm{cm}^{-1}$ for B and $0.32\ \mathrm{cm}^{-1}$ for P impurities. The reason for this was explained in the realm of the virtual crystal approximation, where the difference in average isotopic mass affects the electron and hole effective masses at the respective band edges, leading to a change in their impurity binding energies. The broadening of the transition lines in ^{Nat}Si is again related to the broadening of the impurity ground state due to random isotopic fluctuation around an impurity site. The phenomenon being absent in enriched ^{28}Si is the cause of the incredible sharpness of the lines. The sharpness of optical transition lines in enriched Si helped unravel such details regarding the deep luminescence centers in Si, never before possible with ^{Nat}Si. Isotopic fingerprint study of the impurity atoms (enriched ^{28}Si prepared with controlled isotopic composition of the impurity) enabled identifying not only the number but also the type of atoms involved with deep centers in Si. Some important ones include the singly ionized (S^+) and neutral (S^0) substitutional sulphur donor center [76], Cu-related centers [77], Ag and Au centers [78], and even complex four and five atomic centers involving Cu, Li, Au, and Pt [79], [80].

Mass Transport: Diffusion is a fundamental process of mass-transport in a homogenous solid and plays an important role in material fabrication and device engineering in modern semiconductor technology. As a result, considerable efforts were made to understand the mass-transport of self and impurity atoms as well as dynamics of point defects in semiconductors. Even then, the exact diffusion mechanism in Ge and more so in Si are not clearly understood. Self-diffusion, a basic diffusion for example, a key process in impurity diffusion in elemental semiconductors and annealing of implantation damage, has significant difference in the reported values of self-diffusion coefficient (D_{SD}). Tracing the radio isotopes, though formed an integral part of diffusion related studies, the method was rather limited by the half-lives of the radio isotope. Stable isotope tracing

has been an alternate route to study the dynamics of self-diffusion in semiconductors. Isotope tracing using SIMS on $^{74}Ge/^{70}Ge$ heterostructure, both in the as-grown and the annealed samples, enabled calculating the self-diffusion enthalpy (H_{SD}) and entropy (S_{SD}) in Ge [81]. The reported values of H_{SD} and S_{SD} in Ge were ~3.0 eV and $\sim 9k_B$ respectively. A more precise value of H_{SD} in Ge of 3.13 eV was obtained using neutron reflectivity measurement on a multilayer stack (containing 10 bilayers) of $^{Nat}Ge/^{70}Ge$ [82].

Although it is more or less accepted that the self-diffusion in Ge is mainly mediated through vacancies, the picture remained unclear for Si. SIMS based measurements on $^{28}Si/^{Nat}Si$ heterostructures, annealed at $855 - 1388$ ℃ yielded a single activation enthalpy of self-diffusion, H_{SD} [74]. Splitting D_{SD} into contributions from self-interstitial (I) and self-vacancy (V) as $D_{SD} = f_I C_I^{eq} D_I + f_V C_V^{eq} D_V + D_{ex}$ ($f_{I,V}$ are the correlation factors, $C_{I,V}^{eq}$ are corresponding equilibrium atomic fractions, $D_{I,V}$ are the corresponding diffusion coefficients, and D_{ex} is an exchange term), the I-mediated and V-mediated self-diffusion enthalpies in Si were respectively found to be 4.95 eV and 4.10 eV, showing that self-interstitial dominate the process of self-diffusion in Si within the investigated temperature range. The entropy of I-mediated and V-mediated self-diffusion was calculated to be $14.3k_B$ and $5.5k_B$ respectively. Raman spectroscopic measurement was conducted on $^{28}Si/^{30}Si$ superlattices annealed at $735 - 875$℃ [73]. The confined phonon modes in an as-grown superlattice undergo a shift in position as atoms interdiffuse across the homo-interface when a superlattice is annealed. From the shift, the isotopic concentration at a given depth was calculated. Figure 2.4(d) displays the combined data from the SIMS and Raman measurements showing evolution of D_{SD} as a function of temperature [73]. Clearly, D_{SD} cannot be described by a single activation enthalpy. Rather, the best fit to the entire experimental data can be obtained by using two enthalpies of the form $D_{SD} = 2175.4exp(-4.95\ eV/k_BT) + 0.0023exp(-3.60eV/k_BT)\ cm^2s^{-1}$. The enthalpy of the second term matches closely the value reported for self-vacancy diffusion while that of the first term matches exactly with the self-interstitial diffusion, leading to the conclusion that the self-diffusion in Si is interstitial mediated at high temperatures and vacancy mediated at lower temperatures with the crossover occurring at about 900 ℃. Isotope tracing also enabled elucidating the transport of atoms in self-assembled growth of Ge quantum dots [83]. ^{70}Ge quantum-dots were grown using enriched solid precursors in a MBE, by impingement of ^{70}Ge atoms on top of a metastable 2D

^{76}Ge thin film. Subsequent Raman analysis indicated that the dots are not entirely made up of ^{70}Ge atoms. Rather, a major fraction of them ($\sim$90%) consisted of ^{76}Ge atoms from the metastable film while only $\sim$10% of them were ^{70}Ge atoms from direct impingement.

2.1.3.3 Spin Physics and Quantum Information Processing

Quantum computing and quantum information processing (QIP) are fast-emerging concepts that can soon surpass the computing power currently achievable using classical technologies. The added advantage of Si based QIP is its compatibility with the well-established solid state platform and the integrability with modern classical devices. The first idea of Si based QIP was envisioned by Kane [84] where the nuclear spin (NS) of ^{31}P donor in Si was proposed as a qubit. Also put forward was the idea to isotopically enrich the host Si, since the ^{29}Si NSs are a source of magnetic noise and can disrupt the performance of the ^{31}P NS qubit. A different class of Si based QIP device was also proposed, that used the NS of ^{29}Si as qubit rather than the NS of dopant ^{31}P [85]. Figure 2.5(a) shows the schematics of this proposed device with an array of ^{29}Si NSs on a NS-free ^{28}Si platform. The magnetic field gradient (7 Tesla on one side and 9 Tesla on the other, a gradient of 2 Tesla over the length of the chain) would be used to select a particular qubit for quantum operation. By a swapping mechanism, the NS states would be transferred to the adjacent qubit and finally the electron spin of the ^{31}P at the end of the chain would read out the NS state of the last qubit [85].

Initialization of qubits is an important step in QIP operations. It involves preparing an ensemble of identical qubits in a state of superposition which allows manipulating the qubits together and finally reading them out all at once. An essential parameter, the coherence time (T_2) of a qubit is the time for which the quantum superposition state survives, should be longer than the time required for a quantum computation or else the information will be lost in the middle of a calculation. Isotope engineering has played a great role, not only in initialization of NSs but also in improvement of T_2. Using enriched ^{28}Si, it was possible to remove the inhomogeneous line broadening (otherwise present in $^{\mathrm{Nat}}$Si) in the PL spectrum of ^{31}P bound excitons. The sharpness of the transition lines revealed a clear hyperfine splitting due to coupling of the electron spins bound to the ^{31}P atom with the ^{31}P NS [86]. Introducing a second laser pulse, at one of the two PL energies, corresponding to the ^{31}P NS up or down configuration led to fast initialization, not only of $\sim$90% of the electron spin but also $\sim$75% of the ^{31}P NS into the desired state [87]. Initialization of the ^{29}Si NSs is even more challenging, since unlike the ^{31}P donors, they do not have any electron

spin that can couple to the NS. Si samples, enriched with ^{31}P were prepared with controlled concentration of ^{29}Si such that the ^{31}P electron are proximally located to the ^{29}Si nucleus [88]. Although this process was supposed to attain the required initialization via coupling the electron spins of ^{31}P with the NSs of ^{29}Si, it turned out to be rather slow ($>$ 1hr). Later, a Si sample was prepared that had vacancy-oxygen complexes as nearest neighbors to ^{29}Si [89]. On exciting the defect into a metastable spin triplet state, electron spin with large spin polarization was achieved which was subsequently coupled to the neighboring ^{29}Si NS, leading to fast initialization of $\sim$90% of NSs into the desired state.

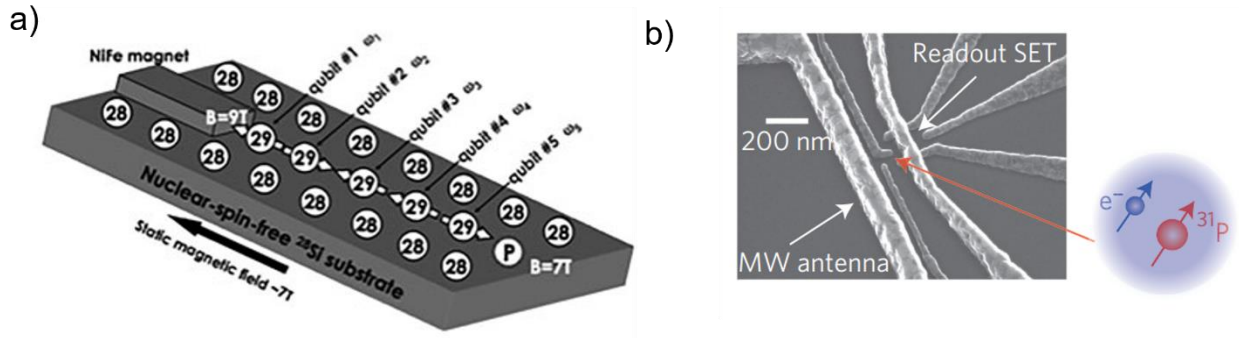

Figure 2.5: *(a) Schematics of a proposed five ^{29}Si qubit QIP device with a field gradient applied in the direction of the qubit chain for qubit selectivity. The ^{31}P at the end of the chain is for qubit readout. (Reproduced with permission from Itoh et al. [85]). (b) SEM image of a QIP device showing the location of the ^{31}P electron spin and NS qubit in a top gated nanostructure on a NS-free ^{28}Si platform. (Reproduced with permission from Muhonen et al. [90]).*

As mentioned above, isotope engineering also played a significant role in the improvement of T_2. Since the electron spin of ^{31}P couple to the ^{31}P NS, the presence of ^{29}Si atoms in the vicinity of the ^{31}P atom can lead to hyperfine interaction between the ^{29}Si NS and the ^{31}P electron spin, leading to a decoherence of the ^{31}P NS. The measured T_2 of the ^{31}P NS in enriched ^{28}Si exceeded 180s at cryo-temperatures, long enough to complete a quantum calculation [91]. The long T_2 in enriched ^{28}Si also provided enough time to complete two-qubit (^{31}P electron spin and the ^{31}P NS) quantum operations [7]. Figure 2.5(b) shows the scanning electron microscope (SEM) image of a Si based QIP device [90]. The device not only allowed quantum operations (initializations,

manipulation and readout) of the ^{31}P electron spin qubit and the ^{31}P NS qubit but also a coherent transfer between the two spin qubits. Additionally, every aspect (including T_2) of the electron spin qubit was found to be significantly better when ^{28}Si was used as the host material as compared to when ^{Nat}Si was used. Similar improvements were reported for single electron spin quantum dot qubit in ^{28}Si host [92]. In diamond too, isotope engineering enabled some significant breakthroughs in the qubit operation of the nitrogen vacancy centers [93], [94].

2.2 Atom Probe Tomography on Nanoscale Materials

In addition to isotope engineering, APT also constitutes an important part of this thesis. In this section, the literature survey on APT is provided. The section begins with the roadmap of modern day atom probes from its earliest predecessor, the field ion microscope. Immediately follows is the literature review of some well-known techniques to fabricate atom probe tips from nanoscale materials. The section ends with a literature search on the atomistic mapping performed by the atom probe on metals and semiconductors.

2.2.1 Roadmap to Modern Day Atom Probes

APT is based on the field evaporation and removal of atoms as ions from the surface of a pointed specimen (tip). With precise control over this evaporation sequence and a knowledge of the local position and identity of the atoms that are evaporated from the specimen, the technique offers extensive capabilities for both 3D imaging and compositional analysis on a near-atomic scale (See section 3.1 for details of APT instrumentation and working principle). The modern day atom probes owes its existence to the field ion microscope (FIM), as developed by Müller and Bahadur in 1951 [95], [96], which had seen significant advancements in instrumentation and design ever since. The atom probe field ion microscope (APFIM) developed in 1968 consisted of a FIM with a time-of-flight mass spectrometer (TOF-MS) enabling the detection of the mass-to-charge ratio (m/q) of single cations, pulsed-field evaporated from the specimen surface [97]. The early predecessor of the 3D atom probe was the 1D or the imaging atom probe (IAP), developed by Panitz in 1973 [98]. It was a short flight path instrument with a large field of view and a spherical microchannel plate (MCP) amplifier centered at the specimen apex. It could detect the hit position of a single pulsed-field evaporated cation at any time, along with its chemical identity. The position sensitive atom probe (PoSAP) developed by Cerezo, Godfrey, and Smith in 1988 was in a way the first 3D atom

probe [99]. The 2D detector added to the earlier 1D atom probe revealed for the first time 3D atomistic images of internal structures of specimen. The scanning atom probe (SAP) developed by Nishikawa and Kimoto in 1993, employed a funnel shaped electrode in close proximity to the specimen [100]. The idea of microtip array was also developed during the same time. As the electrode is scanned, ions would start evaporating from the apex of a microtip whenever it is located within the aperture of the electrode. This strategy of scanning an electrode from microtip to microtip, maximized the amount of data that could be collected in a given amount of time. With further developments came the local electrode atom probe (LEAP) in 2001 [101], wherein a pulsed voltage was applied to a local electrode kept proximally ($\sim 30\ \mu m$) to the apex of a pointed specimen. The design led to tremendous field enhancements (generating the same field at the surface of a specimen at lower applied voltages). This made possible attaining a higher data collection rate with a minimal spread in the cation energy, leading to improved mass resolving power. In addition to the local electrode, the state-of-the-art commercial atom probes from Cameca like the laser assisted LEAP 3000, LEAP 4000 series and the latest LEAP 5000 APT, have the provision to employ an ultra-fast pulsed laser beam at the apex of a needle shaped specimen. Modern day atom probes can achieve a spatial depth resolution of < 0.1 nm along the $[hkl]$ direction being analyzed while the lateral resolution within a $\{hkl\}$ plane is between 0.3 to 0.5 nm.

2.2.2 Tip Fabrication for Atom Probe Analysis

There are a few criteria to be met by an APT tip in order to achieve sufficient field enhancement in order to assist the evaporation of atoms from the surface of the tip. This includes [102] i) the radius of curvature at the apex to be between 50 nm and 150 nm. A larger radius would require very high voltage for the field to reach the evaporation field and a smaller radius would lead to very small field of view. ii) a smooth surface free from sharp protrusions and cracks. Any sharp protrusions on the tip may act as a secondary tip and if the field enhancement at the protrusion is sufficient, atoms may start evaporating from it rather than the apex of the actual tip. Also since the data reconstruction is done on the assumption that the cap of the tip is hemispherical, any departure in shape in form of grooves and cracks may lead to artifacts in the reconstruction. iii) the region of interest within few 100 nm from the tip apex. This is to ensure that the region of interest is included within the data set. To capture a region of interest which is located at larger distance, the size of the data set increases, slowing down the data processing. Like the APT itself, the tip fabrication

process too has undergone several improvements over the years from earlier electropolishing [103] and chemical polishing [104] techniques to the more recent ion-beam milling based processes. The ion-beam milling is conducted in a focused ion beam microscope (or simply FIB) by the energetic Ga^+ions. Nowadays, an additional SEM column is added to a FIB column in a dual channel FIB (or simply Dual-FIB). It enables recording images of the ion-milling process. For bulk samples, thin films, and even the thin film superlattices, the well-established lift-out technique is mostly followed [105]. In brief, a wedge-shaped piece of the sample is milled and lifted out using a micromanipulator needle and transferred on to a micro-post. A micro-post array is a prefabricated heavily doped Si wafer with 100 μm tall post, with an end diameter of about 2 μm. The attachment of the section to the micro-post is done by cold Pt deposition. The micro-needle is cut off from the specimen by the Ga^+ ions. The wedge-shaped specimen then undergoes annular-milling using the high energy $(\sim 30\ \text{kV})$ Ga^+ ions. Milling patterns of various diameters are normally integrated with the FIB software, using which the desired tip shape can be obtained. Finally, the tip is sharpened and rough patches are polished off using the low energy $(\sim 2-5\ \text{kV})$ Ga^+ ions.

Although the lift-out technique may still be applicable, fabricating tips of a nanoscale sample like a NW or a nanoparticles is more challenging and often calls for innovative measures. The SEM images in Figure 2.6(a) shows the sequential steps (from top to bottom) of how an atom probe tip was fabricated from a $LiMnO_2$ nanoparticle [106]. First, a micro-needle is attached to a $LiMnO_2$ nanoparticle, by means of electrostatic attraction. No cold Pt paste is used for the attachment. After the transfer, a protective Pt layer was deposited over it in a Dual-FIB microscope. Finally, a needle shaped tip was carved out of it, by annular ion-milling. The SEM images in Figures 2.6(b)-(f) show different ways by which the atom probe tips were fabricated of NWs. In Figure 2.6(b), a micro-needle was attached to the middle of a GaN NW using cold Pt welding, plucked from the growth substrate, placed in a FIB-bored hole on the top of a micro-post and welded, and finally the micro-needle was detached from the NW [107]. In Figure 2.6(c), Si NWs were VLS-grown using Au catalysts directly on top of Si micro-posts [108]. The micro-posts were fabricated by dicing and subsequent etching a Si (111) wafer. Figure 2.6(d) shows a GaN NW that was plucked from a TEM grid using a micro-needle. The whole micro-needle (with the NW attached on its top) was then inserted into the APT chamber for analysis [109]. Figure 2.6(e) shows a dummy NW that was first picked up and attached to a micro-needle. Then the dummy NW was used to pick up a target NW which was subsequently transferred on to a micro-post [110]. Figure

2.6(f) shows a different approach that was adopted for short Si NWs where the *pluck-and-place* technique cannot be applied. The NWs were first given a protective Ni/Pt coating, then circular markers were laid in order to identify the position of the NW during milling, and the lamella was lifted out and milled into needle like shape [111].

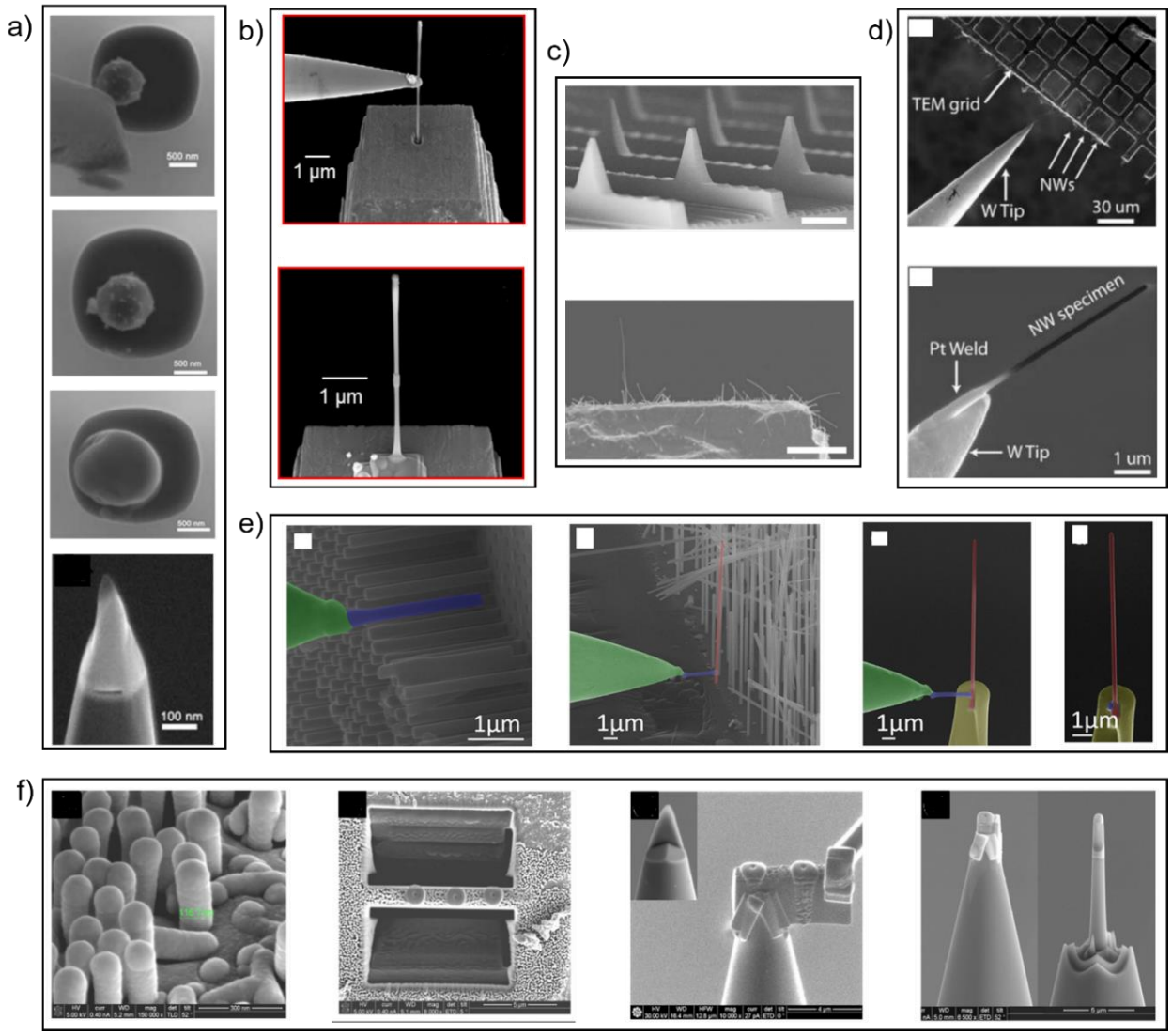

Figure 2.6: *(a) From the top: A $LiMnO_2$ nanoparticle, electrostatically attached to a micro-needle is being transferred to a micro-post. The micro-needle detached from the nanoparticle. A protective Pt layer deposited over the nanoparticle. Needle shaped tip prepared by annular ion-milling. (Reproduced with permission from Devraj et al. [106]). (b) Top: A single NW, picked up using a W micro-needle and is being placed into a FIB-bored hole on the top of the APT micro-tip post. Bottom: The micro-needle detached from the NW. (Reproduced with permission from Sanford et*

al. [107]). (c) Top: APT micro-posts on Si (111) produced by dicing the wafer and subsequent etching of the particulates left by the grinding. Bottom: Si NWs directly grown on a micro-post. The scale bar in the top and the bottom figures represent 5 μm and 100 nm respectively. (Reproduced with permission from Perea et al. [108]). (d) Top: A W micro-needle is being used to pick up a NW from a TEM grid. Bottom: The NW welded to the micro-needle inside a Dual-FIB. (Reproduced with permission from Agarwal et al. [109]). (e) From left: a W micro-needle (green) is being used to pick up a dummy NW (blue). The dummy NW is being used to pick up the target NW (red). The target NW is being welded to an APT micro-post (yellow). The dummy NW is detached from the target NW without dislodging the latter from its position. (Reproduced with permission from Koelling et al. [110]). (f) From left: The short Si NWs coated with Ni/Pt in FIB. Circular markers are laid, each centered on a single NW and a thin lamella, containing 3 NWs, is milled out. The lamella is lifted out using a micro-needle and welded to an APT micro-post with the marker right at the center of the post. FIB milling the structure into the desired shape of an APT tip with the NW in its center. (Reproduced with permission from Blumtritt et al. [111]).

2.2.3 3D Tomographic Imaging

APT has been inducted as a mainstream characterization tool, not only by the material scientists but also by a variety of other scientific fields, as evident from the sharp yearly rise in the number of peer-reviewed publications related to APT in the past few years [112]. A big chunk of these publications is related to APT investigations in metals and metallic alloys. This thesis is not related by any means to APT investigation of metals, which is why we shall keep the literature survey on the same down to a bare minimum. The investigations on metals and metallic alloys varied from characterization of their compositional, in some cases structural properties to studying buried interfaces [113]. However, the major impact of APT on metallic samples probably lies in the studying the solid-solid phase transformation in alloys [114]–[116]. Precipitate formation and their evolution has been studied widely using APT in Al based alloys, Ti alloys, Ni superalloys, steels, Mg alloys to name a few. Parallel developments took place to the algorithms that were being used to identify and analyze the precipitates or clusters. Out of them, the iso-concentration surface method is a popular one, used not only to identify clusters but also to define the buried homo and hetero-interfaces. In this method, the user defines a concentration threshold c_{th} for a particular atomic/ionic species on the basis that the concentration of that atom within a cluster is higher than

that in the rest of the matrix. An algorithm then divides the entire data set into sections where the concentration of the chosen atom is higher (or lower, as determined by the user) than c_{th} from the rest of the matrix. The threshold c_{th} therefore needs to be chosen judiciously to obtain morphologically stable results. An example of cluster determination, by the use of iso-concentration surface method (defined by $c_{th} = 9.0$ at. % of Al) in Ni-Al-Cr alloy, is shown in Figure 2.7(a) [117].

The incorporation of the pulsed laser to an APT, led to a tremendous expansion of its scope from the world of metals and metallic alloys into semiconductors and even wide band gap insulators based materials and devices. The closest to this thesis is the UV laser-assisted APT investigation of the interfacial properties and the distribution of different isotopes in a $^{28}Si/^{30}Si$ [118] and $^{70}Ge/^{Nat}Ge$ [119] superlattice structure. Figure 2.7(b) shows the 3D atom-by-atom mapping of a $^{28}Si/^{30}Si$ superlattice. In this case, the iso-concentration surface method (defined by $c_{th} = 50.0$ at. % of ^{28}Si) was used to determine the location of the interfaces between the ^{28}Si and ^{30}Si layers. For years, APT has been heavily used to determine dopant levels, carrier and other impurity concentrations in semiconductors. Such parameters being the key to understand and improve device performances. APT helped determine the implantation profile of As atoms in Si as well as the distribution of dopant B atoms in a multi-layer stack of Si/SiGe/Si [120]. Group III-V compound semiconductors were also analyzed to fulfill a variety of objectives. For example, initial TEM characterization of $(In_xGa_{1-x})N/GaN$ multi-quantum well structures proved to be complicated and the artifacts in the diffraction contrast were misinterpreted as In clusters. Later APT came to the rescue providing 3D distribution of In atoms. Subsequent In iso-concentration surface analysis confirmed the absence of any form of In clustering [121]. Similarly, when both TEM and SIMS failed, APT was able to shed some light as to why the observed quantum efficiency of In doped multi-quantum well photovoltaic device was lower than the theoretical limit [122]. It was shown that the interface at the doped-to-undoped transition was abrupt (0.6 nm per decade of In composition) while the reverse, that is undoped-to-doped transition was diffused. This variation in interface abruptness indicated the possibility of a loss of carrier confinement in the wells and hence the lowering of efficiency.

Additionally, APT also led to some important revelations related to the critical components of a metal-oxide-semiconductor (MOS) transistor. The high-k gate dielectric, such as the HfO_2, is

one such critical component, with promises to replace SiO_2 as the conventional gate material. It was shown that when deposited on bare Si surface whose native oxide was removed by HF etching, the HfO_2 film was non-uniform and infused with Si from the substrate underneath. Conversely, when deposited on Si surface that had the native oxide, the HfO_2 film was uniform with a proper stoichiometry of Hf and O and no Si infusion [123]. Poly-Si, a promising gate electrode material, is often doped with B to increase the conductivity and to tune the work function of the electrode. APT investigation on B doped Poly-Si film, deposited on SiO_2/Si showed the B atoms to be segregated along the grain-boundaries of poly-Si [124]. This was in contradiction to the conventional belief that B atoms are distributed randomly in Poly-Si. The low contact resistance and the low temperature of formation has made the transition-metal silicides a popular material for laying the transistor contacts. The phase stability of Ni-Pt silicide, undergoing rapid thermal annealing, was studied using APT [125]. The study suggested the NiSi phase to nucleate uniformly and spread laterally, while the Ni_2Si phase to nucleate and grow only along the silicide/Si interface boundary. A similar observation was made for Pt. In another study, dopants were seen to aggregate at the silicide/Si interface, as the silicide formation was initiated on As and Ge doped Si substrates [126]. Other noteworthy mentions of APT investigation on semiconductor devices include those conducted on the Fin-FETs [127], [128], the static random access memory transistor [129], and Si based photovoltaic devices [130].

Just like the bulk and the thin film counterparts, the advances in NW applications depend on a continuous feedback from the knowledge of a NW's composition and morphology. The 3D reconstruction and the proximity histogram in Figure 2.7(c), show that APT was able to obtain an atomistic level compositional map of the constituent atoms within a single InAs NW [131]. An atom-by-atom mapping of Ge, InSb, GaP, InP, and Ge-Si core-shell NWs [110] and a Ge-GeSn core-shell NW [132] were also obatined using APT. The knowledge of the distribution of dopants within a semiconductor NW is critical for their application in next-generation nanophotonic and nanoelectronic devices. APT was successfully used to map the distribution of dopants in several semiconductor NWs like the Mg dopants within a GaN NW [109], N dopants in ZnO NW [133], B dopants within a Si NW [134], P dopants in Ge NW [135], and Si dopant in GaAs NW [136] with near atomic scale spatial resolution. The dopant distribution in the aformentioned NWs was found to be uniform except the P distribution within a Ge NW. The P atoms were found to be located preferentially near the surface of the NW. The effect was later explained to be arising due

to the presence of stepped truncated facets, in addition to the close-packed planar main facet, at the catalyst(Au)-NW interface, during the VLS growth. It is a well-known fact that metal atoms from a catalyst droplet get incorporated within a semiconductor NW during the VLS growth. While some catalyst like Ga, In, Al can act as dopants to group IV NWs, others like Au and Ag can prove to be detrimental to the semiconductor properties affecting the minority carrier lifetime. The sensitivity of atom probe in detecting extreme low concentrations down to ppm. level, enabeled mapping the distribution of Au impurity atoms within an InAs [131] and Si [137] NW and Al [138] impurity atoms within a single Si NW. Figure 2.7(d) shows the 3D distribution and the 1D concentration profile of the Al impurity atoms along the growth axis of a Si NW, recorded within a cylinder of diameter 10 nm (inset) [138]. The recorded Al concentration was found to be orders of magnitude higher than the equilibrium solid solubility of Al in Si and yet their distribution was relatively uniform with no signs of precipitate or clustering. The phenomenon was explained by the kinetics driven solute trapping effect taking place at the catalyst-NW interface during the VLS growth [138]. Interfaces between homo and heterojunctions play a crutial role in device performances and play a big role in semiconductor physics today. A big challenge in modern-day material characterization is probing the properties of burried interfaces, especially at the nanoscale. Iso-concentration surfaces drawn within the atomistic maps of GaN/InGaN axial [107] and radial [139] heterostructure NWs enabled not only locating the burried interfaces but also the intermixing of atoms and therefore the abruptness of the interface.

APT is also used to characterize a wide range of battery materials, catalyst materials, terrestrial as well as extraterrestrial geological materials, and even biomineralized materials like the chiton tooth and the elephant tusk. The recent focus of atom probe groups all-round the globe is to extend the scope of this technique to fully organic materials. We end this section by mentioning a recent trend associated with APT, the correlative-APT. In this method, the APT is combined with some other microscopic technique, mainly STEM (even SEM and electron backscattered diffraction (EBSD) are starting to be implemented). This requires careful sample preparation which not only meet the requirement of APT but is also compatible with the STEM sample holder. Correlative APT can provide complementary information (like high-resolution compositional information from APT and high-resolution structural information from STEM) for a comprehensive understanding of material properties [140]. Additionally, such information can

improve the reconstruction algorithms with inputs like the shape evolution of the tip during evaporation and provide a window into the physics of field evaporation, laser-tip interaction, etc.

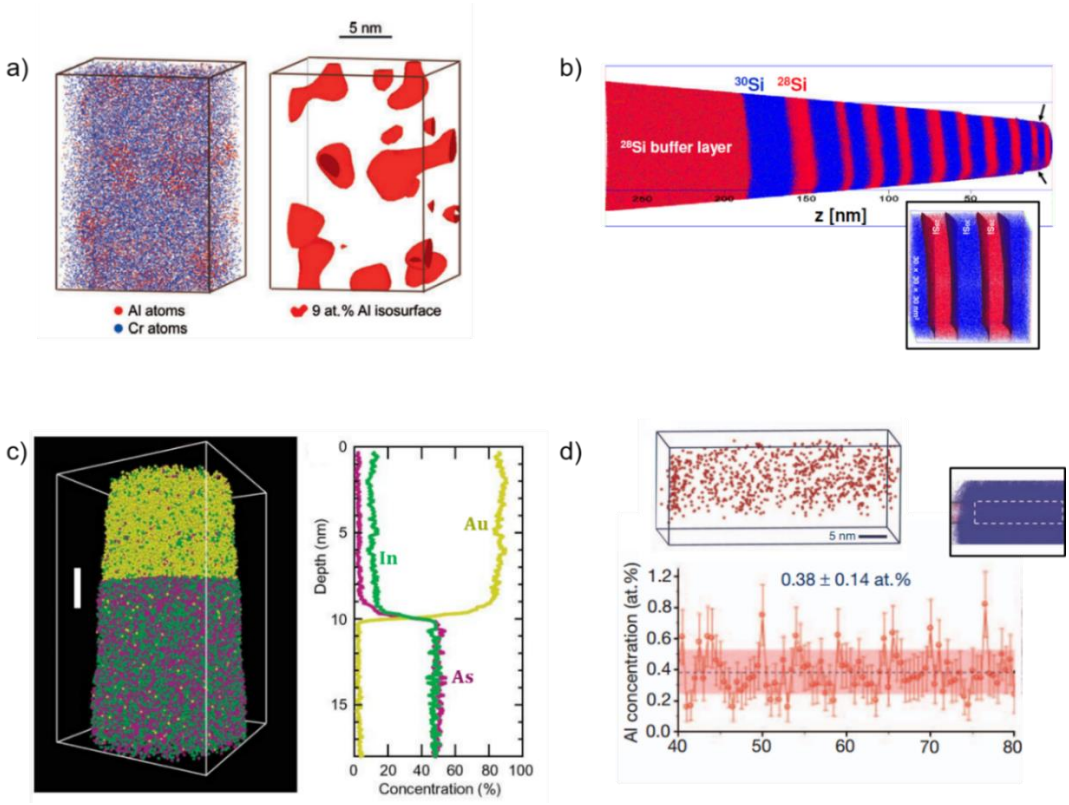

Figure 2.7: *(a) 3D distribution showing the Al and Cr atoms within a Ni-Al-Cr alloy (left) and the location of a fraction (30%) of the γ′ precipitate, denoted by 9.0 at.% Al iso-concentration surfaces (right). (Reproduced with permission from Yoon et al. [117]). (b) 3D atom-by-atom mapping of the ^{28}Si and ^{30}Si isotopes within a $^{28}Si/^{30}Si$ superlattice. (Reproduced with permission from Moutanabbir et al. [118]). Inset: The homointerfaces drawn at 50.0 at.% of ^{28}Si isoconcentration surface. (c) 3D distribution of atoms within a InAs NW. Alongside, the proximity histogram, depicts the 1D concentration profile of the In (green), As (purple), and Au (yellow) atoms across the catalyst-NW interface. (Reproduced with permission from Perea et al. [131]). (d) The 3D distribution of Al impurity atoms along the growth axis of a Si NW (top). The axial concentration of Al atoms along the growth axis of a Si NW (bottom). The concentration was averaged over a cylinder of diameter 10nm (inset). The black dotted line depicts the average axial concentration within the cylinder and the shaded region depicts the uncertainty of the measured average concentration (which is about 0.14 at.%). (Reproduced with permission from Moutanabbir et al. [138]).*

CHAPTER 3 EXPERIMENTAL TECHNIQUES: INSTRUMENTATION AND UNDERLYING MECHANISMS

APT, Raman scattering spectroscopy, and TEM are the three main analytical techniques that has been used in this thesis. APT was used to generate 3D atomistic images of the various specimen studied in this thesis, Raman spectroscopy was used to investigate the phonon behavior in the isotopically engineered Si NWs, and TEM was used to investigate the crystallinity of the samples under investigation. In this chapter, we provide a brief description of the instrumentation associated with these techniques. Additionally, the theoretical concepts that lead to a proper understanding of the working principle of APT and Raman spectroscopy are also discussed.

3.1 Atom Probe Tomography

APT provides 3D images with a near atomic scale spatial resolution of the internal structures of a specimen. The UV-laser assisted LEAP4000XSi was used for the APT analysis in this thesis. Section 3.1.1 provides a summary of the main components of an APT setup while in section 3.1.2 the physics of field evaporation has been discussed.

3.1.1 Instrumentation

A schematic diagram of laser-assisted local electrode atom probe (LEAP) is given in Figure 3.1(a). It involves the field induced evaporation or removal of atoms as cations, from the surface of needle shaped specimen (tip). In order to generate the required electrostatic field, a high dc voltage (V_{dc} ~10 kV) is connected to the micro-tip coupon, to which the tip is attached. There are two modes of operation, the high-voltage (HV) pulsing mode and the laser pulsing mode. A funnel shaped local electrode (LE) with an apex diameter aperture of $\sim 40 \pm 10$ μm is proximally (~30 μm) located to specimen. In HV pulsing mode, negative voltage pulses (V_p, having a pulse duration of a few tens of ns and rise and decay times $0.5 - 5$ ns) of amplitude $\sim 15 - 20\%$ of V_{dc} are applied to the LE [102], [141]. In the laser pulsing mode, the LE is kept grounded and high intensity ($> \mathrm{G\,Watt/m^2}$), ultrashort laser pulses ($100\ \mathrm{fs} - 10\ \mathrm{ps}$) with frequency in the order of a few hundred KHz are focused on to the tip [141]. Nonetheless, the grounded LE in laser pulsing mode helps in aligning the tip with the center of the position sensitive detector. To keep potential scattering agents (like gas molecules, dust particles, etc) away from the

flight path of the cations, the LEAP system is kept inside an ultrahigh vacuum chamber ($< 10^{-10}$ Torr). Also, to minimize the thermal energy spread of the cations, the LEAP chamber is maintained at sub liquid-nitrogen temperatures (< 77 K) during operation.

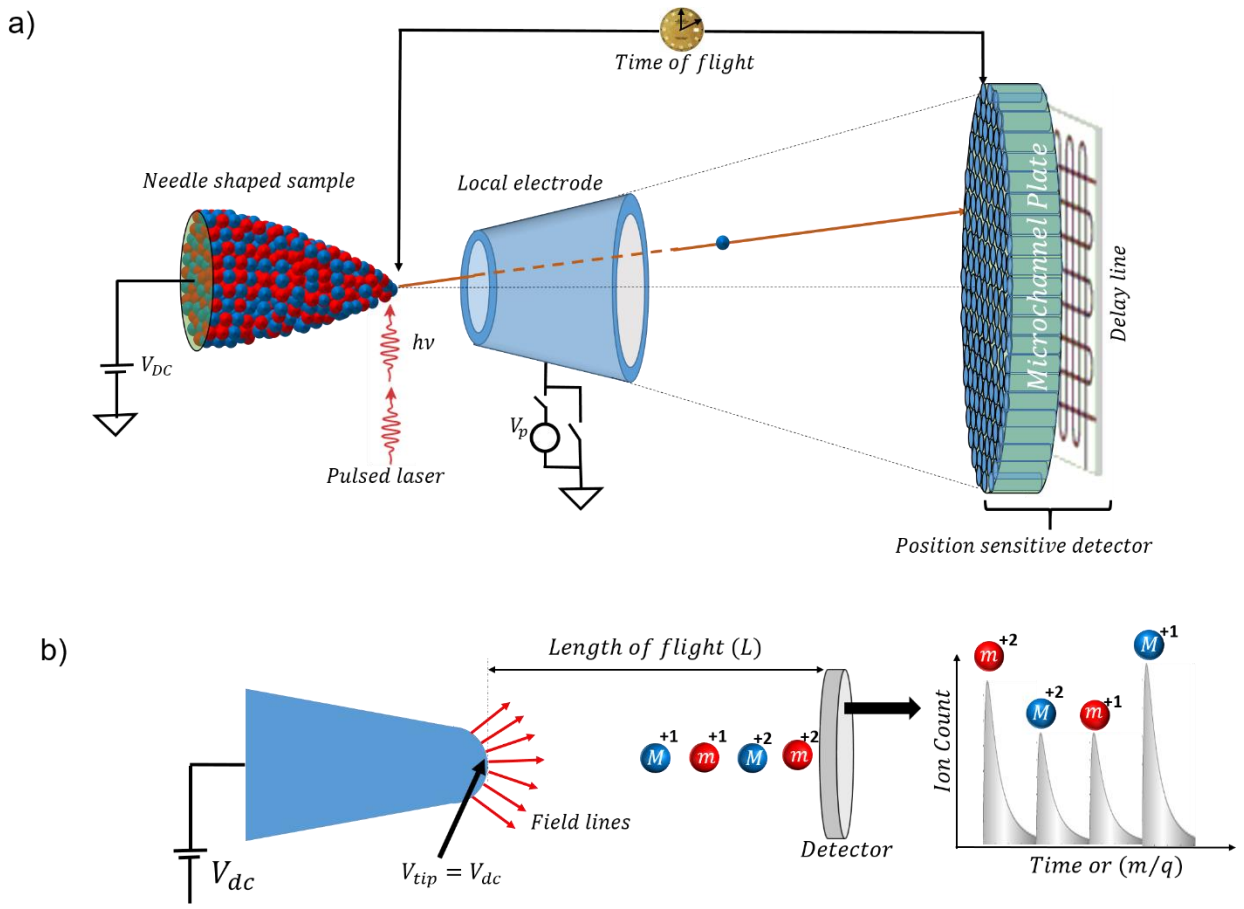

Figure 3.1: *(a) Schematic illustration of an APT setup showing the needle shaped tip, the local electrode, the position sensitive detector (MCP and the delay line) and a pulsed laser being applied to the tip. (b) Schematic illustration of a time-of-flight mass spectrometer.*

The detection system of an APT consists of a position-sensitive detector along with a time of flight mass spectrometer (TOF-MS). The position sensitive detector consists of a micro-channel plate (MCP) primary detector, behind which is a delay-line detector. As a cation hits the MCP, the TOF-MS records its time of flight. The time of flight of a cation stores the information regarding

its mass-to-charge state ratio (m/n) and therefore its chemical identity. The position sensitive detector records x and y coordinates of the hit position of the cation, the accumulation of which enables forming an image of the surface of the tip apex. Since the detector is a projection of the surface of the tip apex, the hit position of a cation on the detector contains information regarding its original X and Y coordinates on the tip surface wherefrom it was evaporated. While the tip apex is $\sim$100 nm across, the diameter of the detector is $\sim$100 mm, giving the projected image of the tip surface a magnification of about 10^6 [141]. At this magnification, the interatomic distances of 0.2 nm gets projected on the detector as $\sim$2.0 mm, which can easily be resolved by the delay lines that are used in the modern day LEAPs. Since atoms are removed layer by layer starting from the surface of the tip, the sequence of evaporation events (N) is used to construct the 3rd coordinate (Z) of a cation (depth inside the specimen). In the laser (voltage) pulsing mode, the evaporation sequences are marked by the precisely timed laser (voltage) pulses. The four essential information m/n value of a cation, it's evaporation sequence (N), and its hit position (x and y coordinates) on the detector are send to a computer. A reconstruction algorithm then converts this information into the cations coordinates inside the specimen and its chemical identity: $x, y, N, (m/n) \rightarrow X, Y, Z, Atom\ type$. Finally, with basic inputs to the reconstruction software, like the initial shape (shank angle, apex radius) of the tip, a description of the tip shaped as it evolved during field evaporation, a map or image of the specimen's constituent atoms is created in 3D.

Figure 3.1(b) shows the schematics of a TOF-MS. The HV pulsing or laser pulsing provides control over the instant in the time of departure of an ion from the tip surface. The time of flight (t_{flight}) is the measure of the time interval between the application of the triggering pulse and the moment the ion hits the detector. The energy of an ion of mass m, ionized to its n^{th} ionization state, as it accelerates through the electrostatic field is neV_{dc}. In metallic samples, the voltage at the apex of the tip is the same as the dc bias voltage V_{dc}. In a non-metallic (semiconductor and insulator) tip, the initial carrier (electrons or holes) density within the tip is very low, especially at the low temperatures at which an APT operates. As we shall see in section 3.1.2, there could be various ways by which excess carriers could be generated inside a non-metallic tip. After the excess carrier generation, the internal dc-field pushes the free holes towards the surface of the tip, eventually leading to complete screening of the field to within few nm of the tip surface. The surface of the non-metallic tip thus attains a high concentration of free carriers, imparting it a semi-

metallic or sometimes even metallic character. Hence the $V_{tip} \approx V_{dc}$ approximation is valid for non-metallic tips as well. If the apex of the tip has a radius r_{apex}, then the electric field at the surface of the tip apex is $F = V_{dc}/k\, r_{apex}$, where k is a constant depending on the shape of a tip. The field drops off within few r_{apex} from the surface of the tip. Departing the surface with no initial velocity, the ions are accelerated to their final velocity v_{ion} within this distance of few r_{apex} of its flight towards the detector, after which they drift the field-free region with the velocity v_{ion}. The final kinetic energy of the ion is therefore $mv_{ion}^2/2$, v_{ion} being equal to the L/t_{flight} where L is the ion flight path length. Neglecting the first few r_{apex}, which the ion traversed with a non-uniform velocity, L is approximately equal to the known separation between the tip and the detector. The energy balance equation leads to

$$\frac{m}{n} = 2eV_{dc}\left(\frac{t_{flight}}{L}\right)^2 \quad (3.1.1)$$

The ions thus arrive at the detector temporally separated according to their mass-to-charge state ratio. Lighter the mass and higher the charge state, the faster it arrives to the detector. An example is shown in Figure 3.1(b) of two isotopes of an element, a heavier atomic mass M and a lighter atomic mass m in two different charge states +1 and +2, all evaporated at the same time. The m^{+2} ion reaches the detector first and a line marking its arrival appears on the mass spectra. It would be followed by the M^{+2} ion and then the m^{+1} ion (for isotopes where the atomic masses are separated by a few amu., the M^{+2} would generally have a smaller m/n compared to m^{+1}). The last to arrive would be M^{+1}. The mass spectra thus have a line for each of the four ion types, separated from each other by their t_{flight} values. For convenience of display and to enable fast identification of the elemental nature of the ions, the mass-spectra is calibrated into m/n according to equation (3.1.1). The width of a line in the mass spectra appear due to uncertainties in measuring t_{flight} accurately. During HV pulsing, depending on the instant at which the ion is created (during the rise edge of V_p or the falling edge), it will be accelerated by different stages of the varying fields. For HV pulsing, equation (3.1.1) is modified to include the effect of the pulse as

$$\frac{m}{n} \approx 2e\left(\frac{t_{flight}}{L}\right)^2 \left(V_{dc} + \beta V_p\right) \quad (3.1.2)$$

where β is a constant less than 1. The ions created during the falling edge of V_p will not necessarily acquire the full energy of the pulse and thus appear heavier. This effect is referred to as energy deficit and results in a spread in the energy of an ion. This gets reflected in the shape of the lines in the mass spectra, a sharp rising edge and a long tail [142]. During laser pulsing, the duration of the thermal pulses (rise and fall in tip temperature) are not the same as the laser pulse widths. If the temperature of a cylindrical metallic tip increases from its base value T_{base} to the maximum value T'_{max} at time $t = 0$, then the time evolution of temperature for $t > 0$ can be shown to follow the equation [143]

$$T(t > 0) = T_{base} + \frac{T_{rise}}{\sqrt{1 + \frac{2t}{\tau_{cooling}}}} \qquad (3.1.3)$$

where $T_{rise} = T'_{max} - T_{base}$ and $\tau_{cooling}$ is some characteristics cooling time of the tip. The evaporation of ions from the tip surface can take place at any time within a span of τ_{ev} where

$$\tau_{ev} = \frac{k_B T'_{max}}{Q_n(F)} \tau_{cooling} \qquad (3.1.4)$$

Longer the value of τ_{ev}, greater is the uncertainty in determining t_{flight} of an ion. The ions which evaporate during the collapse of the thermal pulse cannot acquire the full energy of the pulse, leading to an energy deficit and creating tails in the mass spectra. Consequently, in the laser pulsing mode, the shape of the lines in the mass spectra can vary significantly from one analysis to another since the $\tau_{cooling}$ of the tip apex strongly depends on the specimen geometry as well as the thermal transport properties of the material. The broadening of the lines in the mass spectra can affect the mass resolving power of the TOF-MS. Closely spaced lines may overlap or one or more peak may even hide under the tail of another stronger peak, affecting the accuracy of compositional analysis. Ideally, to be able to separate ions of similar t_{flight}, the lines in the mass spectra should be narrow not only at mid-height but also at lower heights. The mass resolution $m/\Delta m$ is a measure of the mass sensitivity of a TOF-MS, where Δm is the width of a line at different heights, like the width at 50% height (FWHM), at 10% height (FW0.1M), and even at 1% height (FW0.01M). Energy compensation devises such as reflectrons and dual counter-electrodes are used to correct the energy deficit causing significant improvements to $m/\Delta m$ value at lower height regions of a spectral line.

$m/\Delta m$ >1000 at FWHM and ~400 at FW0.1M are a routine phenomenon in a modern day long flight path LEAP.

Figures 3.2(a)-(b) show the schematic illustration of the two key components of a position sensitive detector, the MCP and the delay line detector, respectively. In an electronic circuit, all signals must eventually be converted to currents and a MCP plays the role of a current amplifier. The current that can be generated by a single cation is too weak to perform any signal processing with it. A MCP has a large number of independent channels and each channel works as an independent electron multiplier. The channels are hollow glass capillaries with the inner walls coated with an electron emissive layer. A single incident cation (although MCP could work for single incident electron and photon as well) enters a channel and emits a secondary electron after striking the channel wall. This secondary electron is accelerated by an electric field developed by a voltage applied across the both ends of a MCP. The secondary electron strikes the channel surface and generates more secondary electrons. This process is repeated several times along the channel length yielding a cloud of several thousand electrons which emerge from the rear end of the plate, thereby producing an amplification of several orders of magnitude to the original signal. The detection efficiency of a LEAP is practically constant over a wide range of masses and energy of the impacting cation. Rather it is mainly determined by the open area of a MCP (area of the detector covered by the channels) and the incident angle of ion impact [102], [141]. Ion impact between the channels leads to detection losses and reduce the detection efficiency. Also for an ion that enter the channel nearly parallel to the angle of channel opening, can start a cascade only at larger depths inside the channel. In such an event, the signal amplification can fall short of the threshold detection level of the delay-line and are not used for processing. The LEAP 4000XSi used in this thesis has a detection efficiency between $50-60\%$. The state-of-the-art LEAP 5000XSi series has a detection efficiency close to 80%.

The cascade of electrons at the rear end of a MCP channel is focused on to a one, two or three serpentine of wires. For example, let us say that the blue wires in Figure 3.2(b) are being used to detect the x coordinate of the hit position. The passage of the electron pulse induces two electrical signals which meanders through the wires towards each end of the conductive lines. If one pulse is detected at a time t_{x1} and the other pulse at time t_{x2}, then the delay between the arrival time of the two pulses is $t_{x2}-t_{x1}$. If l be the total length of the blue line and if a pulse take a total time t_x to traverse this length l, then x-coordinate of the impact can be calculated from [102], [141]

$$x = l\frac{t_{x2} - t_{x1}}{2t_x} \quad (3.1.5)$$

The y coordinate is detected by wrapping a second set of wires (red) in a meandering pattern, rotated at right angles with respect to the first. The blue wires would allow about half the electron cloud to pass through it to impact the red wires. The y coordinate of the impact position can be estimated by an equation similar to (3.1.5). The crossed serpentine of wires provide approximately 1000×1000 pixels across the detector face [141]. This, combined with the accuracy of time measurements that are currently possible using the ATDC (amplifier time-to-digital conversion) systems, allows a high precision in detecting the hit position of a cation [144].

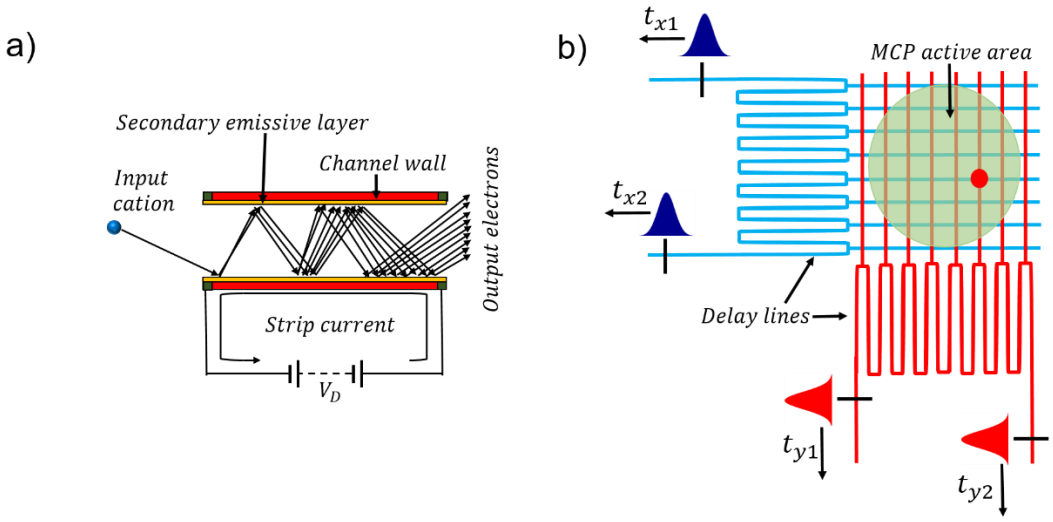

Figure 3.2: *(a)-(b) Schematic illustration of the two key components of an APT detector: (a) a microchannel plate, and (b) a delay line detector.*

In spite of all the excellent characteristics, an APT has several limitations. A delay-line detector is limited by its ability to resolve multi-hit events when cations arrive too closely together in space or time. If two pulses arrive on two different locations on the delay-line (spatially separated) but at the same time, the signals corresponding to the individual impact can overlap and thus get detected as a single event. Similar limitation arises when the hits are separated temporally and not spatially and can lead to loss of signal. To avoid multi-hit events, the rate of evaporation is maintained at a very low value during an atom probe run. The evaporation rate can be set to as low

as 0.01, meaning 100 laser (voltage) pulses would be required to evaporate a single cation. Additionally, advanced signal processing techniques are implemented nowadays to deconvolute any signal that might have overlapped due to multi-hit event. Second major limitation is the low detection efficiency of the detector. Modern day detectors can convert about 99.9% of the hits into electrical signal, independent of the mass and the energy of the cation. So, although the low detection efficiency does not affect the composition analysis (the stoichiometry remains the same) some applications like crystallography which require 100% detection efficiency cannot be performed with an atom probe. This is not a major concern since other analytical techniques like the TEM can be used to obtain crystallographic information. But the two limitations, poor detection efficiency and the need to keep the evaporation rate low severely limit the ion yield of an atom probe. It can take several hours to obtain a data set consisting of about 10 million atoms. The fact that an atom probe cannot analyze materials in their as-grown state is a limitation in itself. The tip fabrication requires additional resources (like the focused ion beam) and is a time-consuming process. Additionally, the high static fields used in an atom probe generate tremendous electrostatic pressure, often leading to tip fracture in the middle of a run.

3.1.2 The Physics of Field Evaporation

Field evaporation refers to the electric field induced removal of an atom as ion from its lattice. When the electric field is intense, an atom can be pulled away from the surface while one or more of its electrons are drained back into the surface. The exact mechanism of charge draining is a subject of debate. While the image-force model [145] assumes that an atom gets fully ionized at some critical distance before it can leave the surface, the Gomer's model assumes that charge is progressively drained away from an atom as it escapes the surface [146]. The image-force model being more simple is often used to establish a theoretical background of field evaporation from metallic samples. For desorption from a surface, an atom needs to be supplied with sufficient energy to surmount the binding energy (Λ) required to break free from the lattice bonds. The energy required to ionize the atom into its n^{th} ionization state is $\sum_{i=1}^{n} I_i$, where I_i is the ionization energy of the i^{th} ionization state. The n electrons that are removed from the atom are drained back to the surface, leading to an energy gain of $n\phi_e$ by the surface (ϕ_e being the work function of the specimen). Hence under the no-field condition, the energy barrier (Q_0) that an atom must overcome in order to be removed from the surface and get ionized to its n^{th} ionization state is given by [147]

$$Q_0 = \Lambda + \sum_{i=1}^{n} I_i - n\phi_e \quad (3.1.6)$$

According to the classic ionic model for field-evaporation which assumes a Schottky-like effect of the reduction in barrier height in presence of a field, the potential barrier height $Q_n(F)$ in presence of an electric field F is lowered from Q_0 and is given by

$$Q_n(F) = Q_0 - \sqrt{\frac{n^3 e^3}{4\pi\varepsilon_0} F} \quad (3.1.7)$$

where e is the charge of an electron and ε_0 is the free space permittivity. The probability of field evaporation (P_{ev}) of an atom is given by the Maxwell-Boltzmann (MB) equation [148]:

$$P_{ev} \propto exp\left(-\frac{Q_n(F)}{k_B T}\right) \quad (3.1.8)$$

where k_B is the Boltzmann constant and T is the absolute temperature. Atoms on the surface undergo thermal vibrations and during each vibration normal to the surface the atom tries to overcome the Schottky hump $Q_n(F)$. If the normal component of vibration has a frequency ν, then the rate of field evaporation (Γ_{ev}) from a specific $\{hkl\}$ plane can be written in form of an Arrhenius-type equation with $Q_n(F)$ as the activation energy [149]:

$$\Gamma_{ev} = \nu exp\left(-\frac{Q_n(F)}{k_B T}\right) \quad (3.1.9)$$

In a metallic tip when V_{dc} is applied, the free electrons are pushed inwards to create an electric dipole layer at the surface, screening the field to within 0.1 nm from the surface. Additionally, the needle-like shape of the tip helps in generating tremendous field enhancement at its apex. The combination of these two factors, the field screening at the surface and the field enhancement at the apex of a tip, is the reason that $Q_n(F)$ is minimum at the surface of the tip apex. Hence, according to equation (3.1.8) the probability to surmount the Schottky hump is the greatest for an atom located at the surface of the tip apex and not anywhere else on the tip. Hence the need to fabricate a needle-shaped tip for atom probe analysis.

During an atom probe analysis, V_{dc} is maintained in a way that $Q_n(F)$ does not vanish completely. The field at which the Schottky hump reduces to zero is called the evaporation field and is given by :

$$F_{ev} = \frac{4\pi\varepsilon_0}{n^3 e^3}\left(\Lambda + \sum_{i=1}^{n} I_i - n\phi_e\right)^2 \qquad (3.1.10)$$

When the evaporation field is reached, atoms at the surface of the tip apex will start to evaporate randomly without there being any control over their evaporation sequence. To control the evaporation, two different approaches are taken. In the first approach V_{dc} is maintained at a value just below the evaporation voltage and negative HV pulses (V_p) are applied to the LE. The HV pulses create an additional field enhancement at the tip apex lowering the Schottky hump periodically. However, for the HV pulses to induce field evaporation, the specimen needs to be a good electrical conductor (metals or heavily doped semiconductors). The whole electrical environment surrounding a tip in a LEAP chamber acts as a low-pass filter [150]. With poorly conducting specimen like intrinsic semiconductors and insulators, the HV pulses are not fully transmitted on to the tip. This drastically lowers the evaporation rate and degrades the precision with which an evaporation sequence can be measured. The second approach is laser pulsing. Just like the HV pulsing, in the laser pulsing mode V_{dc} is maintained at a value just below the evaporation voltage of the specimen. The tip is illuminated with an intense ultrafast pulsed laser. The LE is kept grounded. The exact function of the pulsed laser is again a subject of debate. The most widely accepted theory is that the laser absorption increases the temperature of the tip thereby providing the atoms with additional thermal energy to overcome $Q_n(F)$. In a material of conductivity σ_e and permeability μ_e, light of frequency ω_1 is absorbed within the skin-depth from the surface of the material. However, at low T when the skin-depth becomes smaller than the electron mean free path ℓ_e, an anomalous skin-depth is often considered, which can be shown to be [151] :

$$\delta_a \approx \sqrt[3]{\frac{2\ell_e}{\sigma_e \mu_e \omega_1}} \qquad (3.1.11)$$

The electrons located within a depth δ_a from the surface absorbs the photons within the first few fs of its illumination. During this time, the lattice remains frozen. After the characteristic electron–lattice coupling time ($100\ \text{fs} - 10\ \text{ps}$ in metals) the thermal energy from the electron cloud is transferred to the lattice, raising the lattice temperature [102]. For laser pulses of longer duration

(ps-laser), the electron cloud gets coupled to the lattice within the laser pulse duration and the lattice starts acquiring thermal energy directly from the photons.

The alternative theory describing the role of the pulsed laser in field evaporation involves the non-linear optical processes [152]. The intrinsic electric field (E_1) associated with a pulsed laser of pulse duration τ_p and energy E_{Pulse} and spot diameter σ_{spot} is given by

$$E_1 = \sqrt{\frac{32E_{Pulse}}{4\pi\varepsilon_0 c\tau_p\sigma_{spot}^2}} \quad (3.1.12)$$

where ε_0 and c has their usual meaning. The duration of E_1 is same as τ_p. Furthermore, at the apex of a metallic tip this field can be enhanced by several folds due to the plasmonic effect. Therefore, in a fs-laser ($\tau_p \sim 100$ fs) with energetic laser pulses ($\sim$nJ), E_1 at the apex of a metallic tip can reach orders of $\mathrm{V/nm}$. This field together with electrostatic field generated by V_{dc} is sufficient to induce field evaporation of atoms from its surface. The non-linear optical rectification process induced by the ultrashort laser pulses was also proposed [153]. In this process, a second order polarization $\left(P_i^{(2)}\right)$ is generated at the tip apex by the electric field of the laser light. The magnitude of $P_i^{(2)}$ is directly related to the intensity of the incident laser and hence is maximum for a fs-laser. According to the dipolar radiation theory, $P_i^{(2)}$ re-radiates its own electric field (F_{OR}), a process known as optical rectification. The duration of F_{OR} is of the same order as the laser pulse duration. It was argued that F_{OR} in conjunction with the static field generated by V_{dc} induces field evaporation of atoms from metallic tips. These theories based on the non-linear optical processes suffered from criticisms as experimental evidences suggested that atoms evaporate from the surface of metallic tips over a duration longer than the laser pulse duration [143], [154]. The duration of both E_1 and F_{OR} being same as the duration of the laser pulse can therefore not be responsible for field evaporation of atoms. The thermal pulsing mechanism is currently the most widely accepted theory.

At liquid nitrogen temperatures and lower, the density of mobile carriers in intrinsic semiconductors and dielectrics are too small to screen off the electric field at the surface of the tip and to absorb the laser effectively to create a rise in temperature of the lattice. The classical theories of field evaporation by laser pulsing, originally developed for metallic tips, therefore had to be adapted to first explain the carrier generation mechanisms in semiconducting and insulating tips.

Several mechanisms of excess carrier generation have been proposed. It was shown that the dc-field inside a semiconducting tip causes band-bending at the surface. A pulsed laser illuminated on such a tip, photo-excites carriers across the gap from the valence band to the conduction band [155]. Calculations showed the photo-excited free hole density at the surface in Si and Ge tips, illuminated by a fs-pulsed laser can reach values of semi-metallic electron densities. These free-holes in turn absorb the laser just like the free-electrons does in a metal. Subsequently, they transfer the energy to the lattice leading to a rise in lattice temperature. The dc-field inside a semiconducting tip can reach the order of $\sim \mathrm{V/nm}$. Such high field induces tunneling states above the valence band maxima, increasing the optical absorption coefficient, a phenomenon known as the Franz–Keldysh effect. For Si tips the optical absorption coefficient of 1030 nm light was shown to increase from $\sim 10\ \mathrm{cm^{-1}}$ under no-field to $\sim 200\ \mathrm{cm^{-1}}$ at a dc-field of $1\ \mathrm{V/nm}$ [156]. The increased optical absorption triggered photo-excitation of carriers, leading to a free-hole concentration of $\sim 10^{21}\ \mathrm{cm^{-3}}$ at the surface of a Si tip. For an MgO tip the surface/defect states were shown to play an important role in the initial excess carrier generation [157]. Since the surface states lie mainly within the band gap, the laser photo-excites carriers into these surface states, creating free-holes in the valence band. Another interesting mechanism that was suggested for wide band gap insulators is the free carrier generation by means of impact ionization [158]. If the dc-field penetrating into the tip is greater than the breakdown field of the material, the breakdown mechanism may trigger an avalanche of free electrons and holes. The exact mechanism of excess carrier generation is still a subject of open debate. A combination of different mechanism may even be responsible for excess carrier generation in semiconducting and insulating tips. No matter what the exact mechanism is, the order of magnitude of the free carrier concentration is very important for the purpose of field screening. The free carriers screen off the dc field and the screening length typically has an inverse square root dependence on the free carrier density. In metals, the free electron concentration of the order of $10^{22}\ \mathrm{cm^{-3}}$ helps to screen the field to within 0.1 nm from the surface, a distance smaller than even the interplaner distance. The reduced potential barrier is therefore felt only by the atoms at the surface. In semiconductors and insulators, if the generation mechanism cannot create free carriers of the same order of magnitude, the field might penetrate up to several atomic planes beneath the surface. This can affect the depth resolution that can be achieved and also lead to evaporation of cationic complexes rather than as single cations.

3.2 Raman Scattering Spectroscopy

Raman spectroscopy is a non-destructive technique that relies on the inelastic scattering of light from a material. It involves the interaction between light and the vibrational/rotational motion of atoms in a molecule or in a lattice. In this thesis, Raman measurements were performed using the commercial Renishaw Invia spectrometer. Section 3.2.1 describes the basic components of a Raman spectrometer. A theoretical discussion on the inelastic light scattering is given in section 3.2.2. Since only the 1st order Raman spectrum has been used for analysis in this thesis, the theoretical discussion of light scattering has been done in realm of a 1st order Raman effect.

3.2.1 Instrumentation

Any Raman setup requires the following basic components: (1) a coherent and monochromatic light source; (2) an efficient optical system to deliver the light on to the sample and collect the scattered light and direct it towards the detectors; (3) A spectrometer to filter out any unwanted radiation and analyze energy (wavelength) distribution of the scattered light; and (4) a photon counter to count the number of photons at a particular wavelength. The Renishaw Invia spectrometer is a fully automated system, equipped with four different laser lines: the green (514 nm), the blue (488 nm), the red (632 nm) and the infrared (785 nm) lines. A simple schematic illustration of the Raman setup is shown in Figure 3.3. As a laser enters the spectrometer, it passes through a laser line filter. The laser line filter has a narrow pass-band, centered at the incident laser wavelength. It allows the light from the tuned laser source to pass through it while blocks all other light. The beam of light then passes through a beam expander, which generates a collimated beam but expands the beam width at its output compared to that at its input. After passing through a set of beam splitters, mirrors, and lenses the light finally enters the microscope where it is focused on to a sample, resting on a piezo-controlled stage.

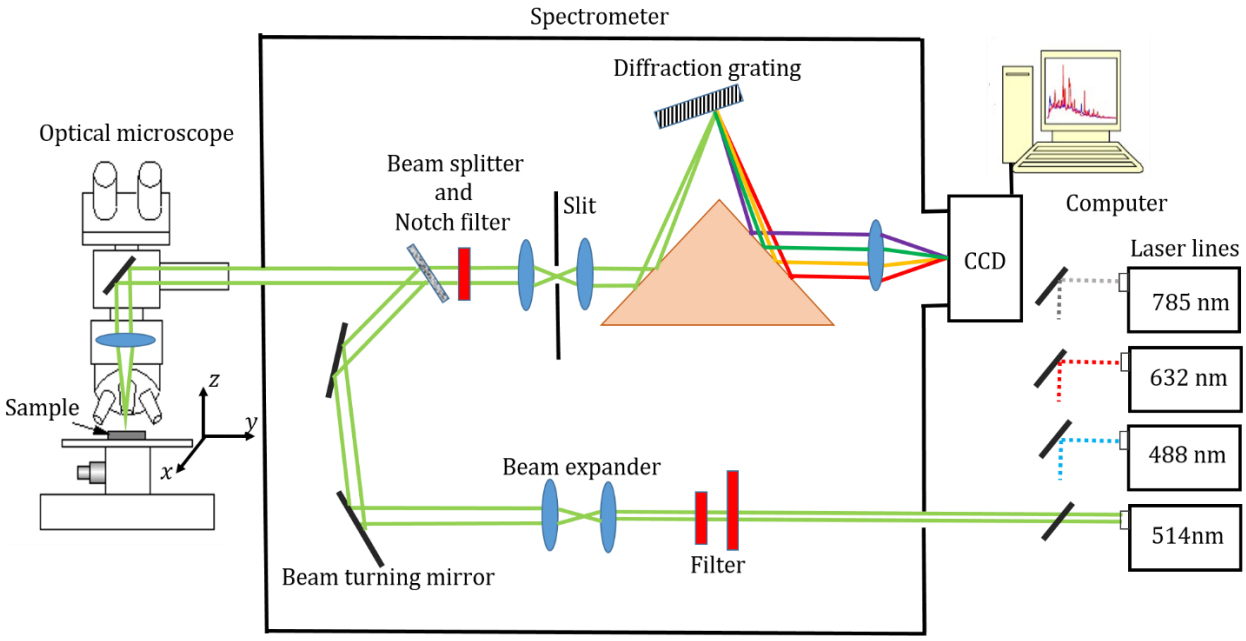

Figure 3.3: *Schematic illustration, showing the different components of a Raman spectrometer.*

The light from the sample is scattered randomly in all direction, over a total solid angle of 4π sr. Depending on its numerical aperture, the microscope objective is able to capture only a small fraction of this scattered light which gets scattered back into the objective. This backscattered light then passes through a notch filter. A notch filter has a stop band of $\pm 50 - 60\ \mathrm{cm}^{-1}$ centered at the incident laser light wavelength. This filter stops the Rayleigh scattered light which has the same wavelength as that of the incident light, while the Raman Stokes and Anti-Stokes light can pass through it (as long as they are not located within its stop band). Some modern-day spectrometers use a three-stage grating in place of the notch filter, in which the first two diffraction gratings are used to reject the Rayleigh scattered light. A diffraction grating (or the third grating in the three-stage grating spectrometer) then disperses the different spectral components of the light at slightly different angles, which are then focused on to a charge-coupled device (CCD) detector. At the CCD detector, the photons are converted into electrons which are digitized and read-out to a computer. The software then interpolates the digital signal based on the number of pixels in the detector and the linear dispersion of the diffraction grating to create a calibration that enables the intensity of the scattered light to be plotted as a function of wavelength over a given spectral range. Additional components are required to perform polarized Raman measurements: a polarizer set in the path of the incident laser, a half-wave plate to rotate the polarization of the incident and the scattered light,

and also a sample rotator which is required to align a sample (say a NW) at a particular angle with respect to the incident laser polarization.

The spatial resolution achievable in any diffraction-limited optical system is primarily determined by the laser wavelength, the numerical aperture of the microscope objective, and the refractive index of the surrounding medium. The highest resolution achievable at a wavelength λ_1 and an objective (in air) of numerical aperture NA equals $0.61\lambda_1/NA$. However, aberrations in the optical components often lower the spatial resolution from the theoretical value. The depth resolution achievable in confocal mode is more complex, depending mainly on the confocal design of the Raman spectrometer. In a truly confocal design which incorporates a fully adjustable confocal pinhole aperture, a depth resolution in the order of $1-2$ μm is achievable. The spectral resolution in a dispersive Raman spectrometer depends on many factors: (1) The spectrometer focal length which is the distance between the dispersion grating and the detector. The longer the spectrometer focal length, the higher the spectral resolution. Commercial Raman spectrometers have focal lengths ranging from 200 mm (for low/medium resolution) to 800 mm and higher (for high resolution). (2) The groove density of the diffraction grating, typically measured as number of lines per mm. Higher groove density of the grating leads to higher spectral resolution. The dispersive power of a grating is defined as $d\theta/d\lambda_1 = \mathfrak{n}N'/cos\theta$, where $\mathfrak{n}$ is the order of the spectrum, N' is the grove density and θ is the angle of dispersion of the $\mathfrak{n}^{th}$ order principle maxima of wavelength λ_1. Hence, with the use of a high groove density and higher order spectrum, a high angular separation of any two spectral components is achievable, leading to higher spectral resolution. Typical gratings used for Raman vary from 300 lines/mm (low-resolution) to 1800 lines/mm (high-resolution). Although special grating with extremely high groove density (like 2400 lines/mm and even 3600 lines/mm) are available, the physical constraints linked with a spectrometer itself (focal length, detector capacity) limits the spectral resolution. (3) The detector capacity also influences the spectral resolution. Typically, smaller the size of each pixel on a detector, the higher is the spectral resolution achievable with it.

3.2.2 Inelastic Scattering of Light

Raman spectroscopy is based on the principle of inelastic scattering of light from a material. When an incident light interacts with an atom, it distorts (polarizes) the electron cloud around the nucleus of an atom, thereby setting up oscillating electric and magnetic multipoles. These oscillating

multipoles re-radiates light at their characteristic frequencies, in any random direction and with any random state of polarization with respect to the incident light, hence called scattered light. However, due to the extremely small mass of the electron cloud, only a negligible fraction of the incident energy is used up in polarizing it, which causes the scattered light to have the same energy as the excitation (or incident) light. This is called the elastic or Rayleigh scattering and is the dominant scattering process. In addition to the electron cloud distortion, any vibrational spectroscopy like the Raman spectroscopy, requires the incident light to alter the nuclear coordinates (in form of vibrations or rotations) of an atom as well. This causes a non-negligible exchange of energy between the incident light and an atom. Consequently, the re-radiation occurs at an energy which is different from the energy of the incident light. This is called inelastic scattering of light. In Raman spectroscopy, we measure the energy of this inelastically scattered light relative to the energy of the incident light.

The classical theory of Raman scattering is based on the principle of induced dipole (in reality both electric and magnetic multipoles are induced, but the electric dipolar term is usually orders of magnitude stronger than the other terms) during the interaction of the incident electromagnetic wave with the material. The ρ^{th} component of the total time-dependent induced electric dipole moment vector of an atom can be expressed as a sum of moments as [159] :

$$p_\rho = p_\rho^{(1)} + p_\rho^{(2)} + p_\rho^{(3)} + \cdots \text{ with } p_\rho^{(1)} \gg p_\rho^{(2)} \gg p_\rho^{(3)} \qquad (3.2.1)$$

$p_\rho^{(1)}$ is linearly dependent on the electric field of the incident light as $p_\rho^{(1)} = \alpha_{\rho\sigma} E_1^\sigma$. The dependence of $p_\rho^{(2)}$ and $p_\rho^{(3)}$ on the electric field are quadratic and cubic respectively as $p_\rho^{(2)} = {}^1/_2\, \beta_{\rho\sigma\tau} E_1^\sigma E_1^\tau$ and $p_\rho^{(3)} = {}^1/_6\, \gamma_{\rho\sigma\tau\chi} E_1^\sigma E_1^\tau E_1^\chi$ and so on. α is a 2nd rank polarizability tensor, β is a 3rd rank hyperpolarizability tensor, γ is a 4th rank second hyperpolarizability tensor and so on. When dealing in the Cartesian system ρ, σ, τ, χ can be $x, y,$ or z and a summation over the dummy Greek indices are considered, for example $p_x^{(1)} = \alpha_{xx} E_x + \alpha_{xy} E_y + \alpha_{xz} E_z$ and so on. The theoretical development of 1st order Raman scattering is often done considering only the $p^{(1)}$ moment while the higher order moments are neglected. If ω_1 and k_1 be the frequency and wave vector of the incident light respectively, then the electric field can be expressed as $E_1(r,t) = E_1^0(k_1, \omega_1)\, cos(k_1.r - \omega_1 t)$, E_1^0 being the amplitude of oscillation. The induced dipole moment can be written as :

$$p^{(1)}(r,t) = \alpha(k_1,\omega_1)E_1(r,t) = \alpha(k_1,\omega_1)\,E_1^0(k_1,\omega_1)\,cos(k_1.r - \omega_1 t) \qquad (3.2.2)$$

The ability of the electric field of light to distort the local electron cloud of an atom in a molecule or in a lattice depends on its nuclear coordinate, which is why the polarizability is a function of the instantaneous position of an atom. If atoms in a molecule (lattice) are vibrating with a frequency ω_{vib} and wave vector q then the displacement of the k^{th} atom from its equilibrium position is given by $Q_k(r,t) = Q_k^0(q,\omega_{vib})\,cos(q.r - \omega_{vib}t)$, Q_k^0 being the amplitude of vibration. For small displacements about the equilibrium position, the polarizability as a function of the atomic position can be expanded in a Taylor series around the polarizability value (α_0) at the atom's equilibrium position. Under Taylor approximation equation (3.2.2) can be shown to take the form :

$$p^{(1)}(r,t,q) = \alpha_0(k_1,\omega_1)E_1^0\,(k_1,\omega_1)\,cos(k_1.r - \omega_1 t)$$

$$+\frac{1}{2}\sum_k \left(\frac{\partial\alpha}{\partial Q_k}\right)_{Q_k=0} Q_k^0(q,\omega_{vib})E_1^0(k_1,\omega_1)\,[cos\{(k_1-q)r - (\omega_1-\omega_{vib})t\} +$$

$$cos\{(k_1+q)r - (\omega_1+\omega_{vib})t\}] \qquad (3.2.3)$$

Equation (3.2.3) reveals that the induced dipole moments oscillate at three distinct frequencies $\omega_1, \omega_1 - \omega_{vib}$, and $\omega_1 + \omega_{vib}$ which results in scattered radiation at these same three frequencies. The scattered light at frequency ω_1 corresponds to the Rayleigh scattering while the two other components which are shifted to lower or higher frequencies correspond to the Raman scattering process. This phenomena of a change in wavelength of light on scattering was first observed by Sir Chandrasekhar Venkata Raman [160] who was awarded the Nobel prize in 1930 and the effect thus rightly bears his name. The light scattered with the down-shifted frequency of $\omega_s = \omega_1 - \omega_{vib}$ and wave vector $k_s = k_1 - q$ is referred to as Stokes scattering while the light with an up-shifted frequency of $\omega_s = \omega_1 + \omega_{vib}$ and wave vector $k_s = k_1 + q$ is referred to as Anti-Stokes scattering. The fact that $(\partial\alpha/\partial Q_k)_{Q_k=0}$ must be non-zero is a necessary condition for Raman scattering. This means, that in order to be Raman active, the vibrational displacement of an atom in a molecule (lattice), corresponding to the particular vibrational mode must result in a non-zero change in the atomic polarizability at its equilibrium position. The intensity of the scattered light at a frequency ω_s collected at an angle θ with respect to the axis of the induced dipole is given by $I_s = k_{\bar{v}}\bar{v}_s^4 p_o^2 sin^2\theta$ where p_o is the amplitude of the induced dipole moment, $\bar{v}_s$ is the

wavenumber of the scattered light given by $\omega_s = 2\pi c\bar{\nu}_s$ and $k_{\bar{\nu}}$ is a constant given by $k_{\bar{\nu}} = \pi^2 c/2\varepsilon_0$, where c and ε_0 has their usual meaning.

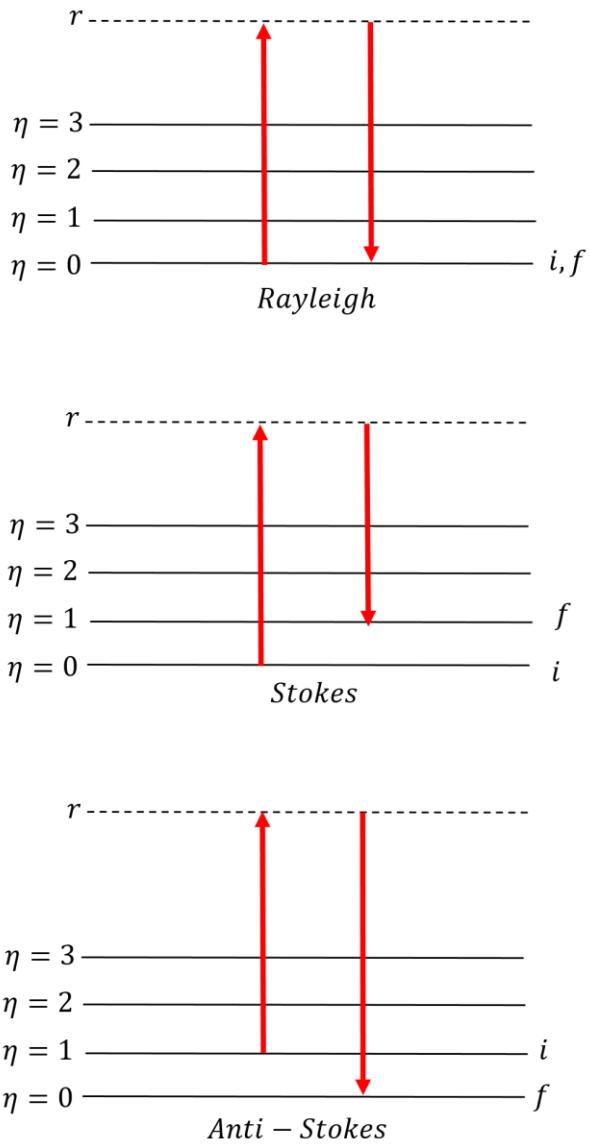

Figure 3.4: *Energy level diagram related to the Rayleigh, Raman Stokes, and Raman Anti-Stokes scattering of light.*

Conventionally, a Raman spectrum is plotted with the Rayleigh peak at the center of the wavenumber (energy) axis. The Stokes and the Anti-Stokes lines thus appear symmetrically at $\mp\omega_{vib}$ relative to the Rayleigh peak. The Stokes line is always found to have a much stronger

intensity as compared to the Anti-Stokes line which is in contradiction with the classical electromagnetic theory. The intensities being proportional to the fourth power of the frequency (wavenumber), the Anti-Stokes (at $\omega_{Anti-Stokes} = \omega_1 + \omega_{vib}$) line should have a higher intensity than the Stokes (at $\omega_{Stokes} = \omega_1 - \omega_{vib}$) line. This is resolved using a semi-classical approach to Raman scattering. According to the harmonic oscillator model, the vibrational energy of an atom, confined to specific vibrational modes, is quantized in nature and is given by $\mathcal{E}_\eta = (\eta + 1/2)\hbar\omega_{vib}$ where η is the vibrational quantum number and ω_{vib} is the vibrational frequency of the mode. An energy level diagram depicting the Rayleigh, Stokes, and Anti-Stokes scattering is shown in Figure 3.4. If there are n' photons in the incident light each of energy $\hbar\omega_1$, then the interaction of the incident light with an atom leads to annihilation of a photon of energy $\hbar\omega_1$ and wave vector k_1 and creation of a new photon with energy $\hbar\omega_s$ and wave vector k_s. As a result, the radiation now consists of $n' - 1$ photons of energy $\hbar\omega_1$ and one photon of energy $\hbar\omega_s$. This annihilated photon from the incident light is not truly absorbed by the atom in the strict spectroscopic sense, since there is no energy conservation in the process yet. Rather it is virtually absorbed where the photon perturbs the atom from an initial state i to a virtual state r, located at an energy $\hbar\omega_1$ above i. The atom relaxes from this unstable virtual state to a final state f, after the characteristic lifetime of the state r and a photon of energy $\hbar\omega_s$ is released in the process.

The atom may relax back to the same state from where it was initially excited ($= i$ and $\hbar\omega_s = \hbar\omega_1$) which means the scattered photon has the same energy as the incident photon. This is Rayleigh scattering. Otherwise, the atom may return back to a state different from where it was initially excited. This is Raman scattering for which $f \neq i$ and $\hbar\omega_s$ is $\hbar\omega_1$ minus the energy difference between the final and the initial states $(\hbar\omega_{fi})$. Since at the end of the light matter interaction, energy must be strictly conserved, there is a net exchange of the energy $\hbar\omega_{fi}$ between the incident light and the atom. When the final state is located higher than the initial state $(f > i)$, the scattered light has an energy $\hbar\omega_s = \hbar\omega_1 - \hbar\omega_{fi}$. As can be seen in Figure 3.4, $\hbar\omega_{fi}$ can be equal to integral multiples of the quantized vibrational energy, that is $\hbar\omega_{fi} = \pm\Delta\eta\hbar\omega_{vib}$, where $\Delta\eta = \pm 1$ for 1st order Raman scattering (involving one quanta of vibration or one phonon) and $\Delta\eta = \pm 2, \pm 3, \ldots\ldots$ for higher order scattering processes. With $\Delta\eta = +1$ we have $\hbar\omega_{fi} = \hbar\omega_{vib}$ and $\hbar\omega_s = \hbar\omega_1 - \hbar\omega_{vib}$, signifying that at the end of the scattering process a phonon of energy $\hbar\omega_{vib}$ has been created. This is the 1st order Stokes scattering. On the other hand, when the final

state is located lower than the initial state $(f < i)$, $\Delta\eta = -1$ giving $\hbar\omega_{fi} = -\hbar\omega_{vib}$ for the 1st order process. The scattered light has an energy $\hbar\omega_s = \hbar\omega_1 + \hbar\omega_{vib}$ signifying that a phonon of energy $\hbar\omega_{vib}$ has been annihilated. This is the 1st order Anti-Stokes scattering. Due to this exchange of energy between the light and matter, Raman scattering is often called an active process. Raman scattering is also inherently incoherent which results in the scattering intensity from N non-interacting atoms to be simply N times that of one atom and is independent of the structure or shape of the material system. The Stokes and Anti-Stokes intensities at a temperature T are proportional to the population of atoms in the respective initial states:

$$\frac{I_{Stokes}}{I_{Anti-Stokes}} \propto \left(\frac{\omega_1 - \omega_{fi}}{\omega_1 + \omega_{fi}}\right)^4 \frac{N_{Stokes}}{N_{Anti-Stokes}} \qquad (3.2.4)$$

The populations, N_{Stokes} and $N_{Anti-Stokes}$ are determined by the MB distribution. For the 1st order process, the MB distribution gives

$$\frac{N_{Stokes}}{N_{Anti-Stokes}} = exp\left(\frac{\hbar\omega_{vib}}{k_B T}\right) \qquad (3.2.5)$$

This results in a more intense Stokes line compared to the Anti-Stokes line. In a full quantum treatment, the probability of each of these transitions are evaluated using the Fermi's golden rule [161]. Although we provided here the basic theoretical description of the first order Raman scattering, it is worth mentioning that there are many variations in the Raman spectroscopy technique, mostly aimed at improving this inherently weak Raman signal intensity by different ways of sample preparation, sample illumination, and detection of scattered light. Few noteworthy mentions include the tip enhanced Raman spectroscopy, the resonance Raman spectroscopy, the stimulated Raman spectroscopy, coherent Anti-Stokes Raman spectroscopy, and the surface enhanced resonance Raman spectroscopy. Each technique may require additional components and modifications to the basic instrumental design shown in Figure 3.3.

3.3 Transmission Electron Microscopy

A TEM maps the distribution (both spatial and angular) of the electrons scattered by a specimen. The distribution is then used to generate high-resolution images and/or obtain crystallographic properties of a specimen. In this thesis, the TEM was used to obtain crystallographic information about the samples under investigation. But unlike the APT or the Raman spectrometer, the TEM

do not constitute an integral part of this thesis. Hence we shall not go on to describe the underlying physics and mechanism associated with the TEM. Rather, in the next section we give a brief description of the key components of a TEM.

A TEM can achieve a spatial resolution which is orders of magnitude higher than that in an optical microscope. This is due to the fact that the wavelength (λ_{el}) of an electron wave can be made as small as a tiny fraction of the interatomic distance in crystalline solids. The wave-particle duality ensures that the de-Broglie wavelength of an electron to be h/p, where p is its momentum. With an acceleration voltage of the order of few 100 kVs that are used in modern TEMs, an electron can attain a velocity (v_{el}) which can be a significant fraction of light's velocity c. The relativistic wavelength of an electron can be shown to be:

$$\lambda_{el} = \frac{h}{\sqrt{2m_0 eV\left(1 + \frac{eV}{2m_0 c^2}\right)}} \qquad (3.3.1)$$

where m_0 is the electron rest mass. For example, at $\mathrm{V} = 100$ kV, $v_{el} \sim 0.55\mathrm{c}$ and $\lambda_{el} \sim 3.7$ pm which decreases to ~ 2.0 pm at $\mathrm{V} = 300$ kV. In practical systems, aberrations and other imperfections in the magnetic lenses lower the resolution of a TEM from this theoretical limit. Nonetheless, a proper focusing of an electron beam into a nm scale spot size and the use of aberration correcting components allow a TEM to resolve even the individual atoms of a specimen.

Like any instrument that involves energetic particles, a TEM operates under high vacuum. The first component in a TEM column is the electron gun which generates a beam of electrons, with energy high enough to enable them to pass through a TEM specimen. The electron emission from the cathode could be by several means [162]: (1) Thermionic emission occurs from the tip of a V-shaped metallic wire with high melting temperatures and chemically stable at high temperatures (such as tungsten). Electron are emitted from the wire when provided with enough thermal energy to surmount the work function of the metal. This is done by sending a high dc current through the wire, raising its temperature to about $2500 - 3000$ K. (2) In Schottky emission an additional static field at the tip lowers the work function and increases the rate of thermionic emission from the cathode (Schottky effect). (3) Cold field emission occurs when the strength of the field at the tip is extremely high. At high field, the width of the barrier decreases thus increasing the chances of an electron to tunnel through the barrier. It can be shown that the tunneling

probability is maximum when the barrier width gets close to λ_{el} [162]. For that, the required field at the tip could be of the order of $1\ \mathrm{V/Å}$. The gun or the cathode is applied with a strong negative potential. After emission, the electrons attain their final kinetic energy as they are accelerated through a potential difference between the cathode and the anode (a round metallic plate with a central hole). For acceleration, it is necessary that the anode is at a positive potential with respect to the cathode. The most convenient situation therefore is to electrically ground the anode and maintain the cathode at a strong negative potential.

The typical diameter of an electron beam that exits the accelerating anode is $\sim 40\ \mu\mathrm{m}$. It then passes through a series of two (sometimes three) condenser lenses [162], [163]. The first condenser lens is a strong lens with a small focal length (f_m) and a magnification factor ($\mathcal{M}$) of $\sim 1/100$. It focusses the beam onto its back-focal plane into a diameter about $0.4\ \mu\mathrm{m}$. The second condenser lens is a weak lens with long f_m and with little or no magnification. Adjusting its strength allows the diameter of the electron beam at the specimen to be varied continuously over a wide range of values, from the smallest possible spot size under fully focused condition to larger spot sizes for under-focused and over-focused conditions. The condenser aperture controls the fraction of the beam that is allowed to hit the specimen and therefore helps in controlling the intensity of illumination. The lens closest to the specimen is the objective lens. It is a strong lens with a short focal length $f_m \sim 1 - 2\ \mathrm{mm}$. At such small focal lengths, the specimen is normally immersed within the pre-field (the part of the magnetic field that acts on the electron even before it reaches the center of the lens) of the objective, analogous to the immersion type lenses in optical microscope. The coefficients of spherical and chromatic aberrations are known to scale up with f_m. For the objective lens with small f_m, the coefficients of aberration are small, a criterion essential in improving the spatial resolution of the final image. The combined action of second condenser lens and the objective pre-field controls the convergence angle of the electron beam on the sample. When the second condenser lens produces a nearly parallel beam of electrons, the objective pre-field focusses them into a nanoprobe of diameter ranging from $1 - 10\ \mathrm{nm}$. On the other hand, when second condenser lens causes the beams to cross-over at the front focal plane of the objective, the pre-field creates a nearly parallel beam of electrons, a condition essential for imaging and diffraction.

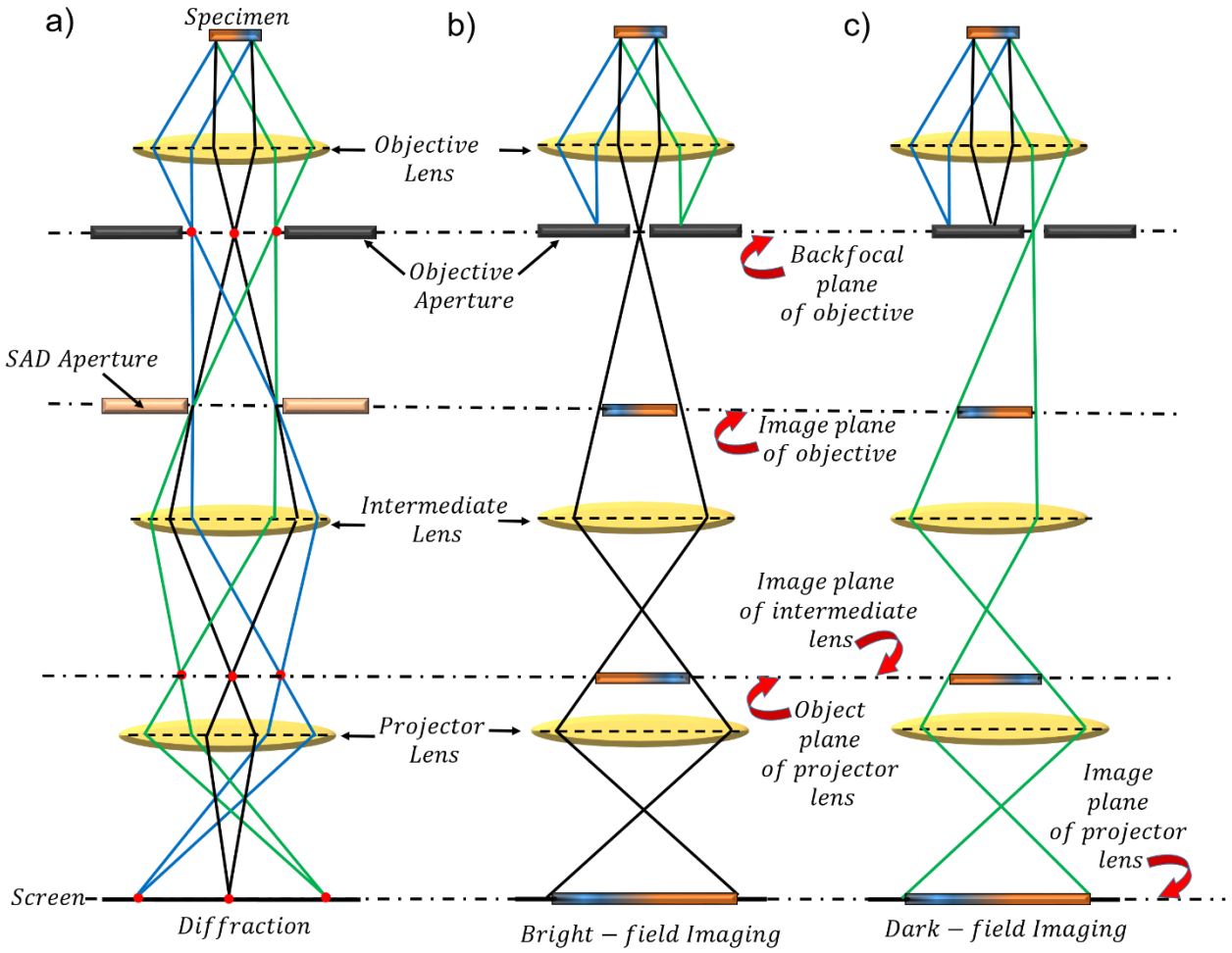

Figure 3.5: *Ray diagram depicting the position of each lens and aperture, located between the specimen and the screen in a TEM column during operations in (a) the diffraction mode (b) the bright field imaging mode and (c) the dark field imaging mode.*

The objective lens produces real images of the specimen with $\mathcal{M} \approx 50 - 100$ at a distance of about 10 cm below the lens. The diffraction pattern of a specimen is first generated at the back-focal plane of the objective lens, where the objective aperture is inserted. The location of each lens and aperture in a TEM column is depicted in the ray diagram in Figure 3.5. The behavior of the objective lens, to a good approximation, can be considered equivalent to that of a thick optical lens [162]. The electrons that passes the specimen parallel to the axis gets deflected from the principle plane and meets the axis at the back-focal plane, at a distance f_m from the principle plane. The electrons which arrive at the sample along the axis but gets deflected (scattered) by an angle α as

it passes the specimen, arrives at the principle plane at distance $\sim f_m tan\alpha$ from the axis. When an aperture of diameter $\mathfrak{D}$ is inserted at the back-focal plane of the objective, it can be shown that only those electrons which suffered a scattering from the specimen by an angle smaller than $tan^{-1}(\mathfrak{D}/2f_m)$ will pass through the aperture while those scattered at higher angles will get absorbed by the aperture diaphragm [163].

In between the objective aperture and the final projector lens lies the intermediate lenses (collectively called as intermediate lens). Changing the magnification of the intermediate lenses in small steps, the magnification of the final image can be varied over a large range, typically from $10^3 - 10^6$. By varying the strength of the intermediate lens, either a diffraction pattern or the image of the specimen can be obtained at its back-focal plane (the object plane of the projector lens). This gives rise to the two well-known modes of operation of a TEM, the diffraction mode (Figure 3.5(a)) and the imaging mode (Figures 3.5(b)-(c)). In the imaging mode, the objective aperture could be placed at the center of the axis such that it allows only the undeflected (not scattered by the specimen) electrons to pass through it (Figure 3.5(b)). This is bright-field imaging where the parts of the specimen which scatter electrons strongly appear dark relative to the surrounding parts. Or else, the aperture could be slightly shifted to an off-axis position such that it blocks the undeflected electrons (Figure 3.5(c)). This is dark-field imaging in which the parts of the specimen that do not scatter the electrons appear dark relative to the surrounding parts.

In the diffraction mode, an additional aperture called the selected area diffraction (SAD) aperture is inserted in the image plane of the objective lens. The first real magnified image of the specimen is formed in this plane. Electrons which fall within the SAD aperture dimeter $\mathfrak{D}_{\mathrm{SAD}}$ will be able to cross it. This correspond to a diameter of $\mathfrak{D}_{\mathrm{SAD}}/\mathcal{M}$ at the specimen where $\mathcal{M}$ is the magnification of the objective lens. The SAD aperture therefore allows collecting the diffraction pattern from a small selected region of a sample. The final lens component in the TEM column is the projector lens. Its job is to produce an image or diffraction pattern across the entire TEM screen whose dimension is of the order of few cm. The projector lens is a strong lens with a short f_m (few mm). The image plane of the intermediate lens acts as the object plane of the projector lens. The screen in a modern day TEM is a CCD detector. However, the impingement of the energetic electrons can easily damage a CCD detector. Thus, the CCD is preceded by a phosphor screen which first converts the electron hits to visible light, which in turn are detected by the CCD and converted to electrical signals for processing. Just like the optical counterparts, the electron lenses

too suffer from aberrations like the spherical aberration, chromatic aberration, and axial astigmatism. Although the first two can be minimized by using strong lenses of short focal length, special stigmators are required to correct astigmatism. Stigmators are a combination of 4-8 magnetic lenses which corrects the azimuthal variation of the focusing power of the main condenser lens and the objective lens.

CHAPTER 4 ARTICLE 1: LASER-ASSISTED FIELD EVAPORATION AND THREE-DIMENSIONAL ATOM-BY-ATOM MAPPING OF DIAMOND ISOTOPIC HOMOJUNCTIONS

This article has been published in Nano Letters (Nano Lett., 2016, 16 (2), pp 1335–1344; DOI: 10.1021/acs.nanolett.5b04728; Publication Date (Web): January 7, 2016). The article demonstrates the 3D atomistic imaging in an isotopic diamond superlattice. It also highlights the underlying physical mechanism that lead to the controlled field evaporation of atoms from the diamond tip. The supporting information of this article is given in Appendix A of the thesis.

4.1 Authors

Samik Mukherjee[†], Hideyuki Watanabe,[§] Dieter Isheim[¥], David N. Seidman[¥], and Oussama Moutanabbir[*,†]

[†]*Department of Engineering Physics, École Polytechnique de Montréal, Montréal, C. P. 6079, Succ. Centre-Ville, Montréal, Québec, H3C 3A7 Canada*

[§] *Correlated Electronics Group, Electronics and Photonics Research Institute, National Institute of Advanced Industrial Science and Technology (AIST), Tsukuba Central 4, 1-1-1, Higashi, Tsukuba, Ibaraki 305-8562, Japan*

[¥]*Department of Materials Science and Engineering and Northwestern University Center for Atom Probe Tomography (NUCAPT), Northwestern University, Evanston, IL 60208-3108, USA*

4.2 Abstract

It addition to its high evaporation field, diamond is also known for its limited photoabsorption, strong covalent bonding, and wide bandgap. These characteristics have been thought for long to complicate the field evaporation of diamond and make its control hardly achievable on the atomistic-level. Herein, we demonstrate that the unique behavior of nanoscale diamond and its interaction with pulsed laser lead to a controlled field evaporation thus enabling three-dimensional atom-by-atom mapping of diamond $^{12}C/^{13}C$ homojunctions. We also show that one key element in this process is to operate the pulsed laser at high energy without letting the dc bias increase out of bounds for diamond nanotip to withstand. Herein, the role of the dc bias in evaporation of diamond is essentially to generate free charge carriers within the nanotip via impact ionization. The mobile free charges screen the internal electric field eventually creating a hole rich surface where

the pulsed laser is effectively absorbed leading to an increase in the nanotip surface temperature. The effect of this temperature on the uncertainty in the time of flight of an ion, the diffusion of atoms on the surface of the nanotip is also discussed. In addition to paving the way towards a precise manipulation of isotopes in diamond-based nanoscale and quantum structures, this result also elucidates some of the basic properties of dielectric nanostructures under high electric field.

Keywords: Diamond; stable isotopes; chemical vapor deposition; dielectric nanostructure; atom probe tomography; field evaporation.

4.3 Introduction

Diamond has some unique properties like high breakdown voltage and high thermal conductivity which make it a suitable material for next-generation power electronics [164] and thermal management applications [165]. Another major and fast emerging branch of current diamond research is founded on the ability to control defects and isotopes in diamond structures with potential applications in spin physics [166], quantum information processing [167], [168], magnetometry [169], [170], and band gap engineering for optoelectronics [8] to name a few. To a large extent, establishing these emerging nanoscale and quantum device structures depends on the availability of isotopically engineered nanoscale structures [8] or a control over the density and distribution of defects [168] or both [166]. Having a precise knowledge of the local concentration and spatial distribution of one or more atomic species involved is often imperative for understanding and elucidating the observed results and device performances. This calls for a characterization techniques sensitive enough not only to distinguish between two isotopes but also capable of resolving different atomic species spatially on a near atomic scale. Atom probe tomography (APT) is a state-of-the-art characterization technique that provides sub-nanometer scale spatial resolution with a high mass resolving power and a sensitivity that is below 10 atomic ppm. Although secondary ion mass spectrometry (SIMS) is successful in providing both dopant and isotopic characterization of diamond [171], the spatial resolution is rather limited and the need for analyzing a large area hinders its ability to probe nanoscale or smaller structures [118].

Though initially restricted to only small geometries and few nanometers thick layers of dielectrics, the advent of ultraviolet (UV) laser-assisted APT has created new possibilities of probing dielectrics and oxides on a much larger length scale [172]. For instance, recent works have demonstrated APT mapping of MgO and ZnO materials [173]. Earlier attempts to field evaporate

diamond date back to 1990s in preliminary studies by Nishikawa et *al.* [11] using a scanning atom probe in a voltage-pulsing mode. However, these investigations have only led to cluster disintegration with a maximum cluster size as large as 16 carbon atoms with a total number of evaporated atoms too small to be statistically meaningful. One reason why APT analysis of diamond has always been a major challenge is because this material has the highest known evaporation field of all the elements in the periodic table, 155 V/nm [174]. The process of field evaporation of diamond becomes even more complex if one considers that the lasers that are typically used in laser assisted APT (UV or visible) have energies lower than the band gap energy of diamond. In principle, this suggests a limited photoabsorption of the laser light at the diamond nanotip surface. In spite of these anticipated limitations, we demonstrate below that diamond can be effectively field evaporated thus allowing a detailed three-dimensional (3D) atom-by-atom mapping of isotopically modulated diamond nanoscale layers. The underlying physical phenomena leading to the evaporation of diamond atoms as ions, which involves the interaction of the UV laser light with the diamond nanotip, are discussed.

4.4 Experiment

The samples investigated in this research work are ^{12}C /^{13}C diamond homojunctions schematically illustrated in Figure 4.1(a). The growth was carried out using a 1.5 kW ASTeX 2.45 GHz microwave plasma assisted chemical vapor deposition. The growth details are provided in the supplementary information (Appendix A). Figure 4.1(b) displays a cross-sectional transmission electron microscopy (TEM) image of an as-grown sample. The insets in Figure 4.1(b) exhibit high-resolution TEM images of regions near the surface and interface with the HPHT substrate. The HRTEM data demonstrate that the as-grown diamond samples are of high crystalline quality. It is also noteworthy that TEM images does not distinguish between ^{12}C and ^{13}C layers as the two isotopes have the same atomic number. The 3D atomistic imaging of the as-grown sample was performed utilizing a UV laser-assisted Local Electrode Atom Probe (LEAP). First, a needle shaped nanotip was fabricated using a Helios dual beam focused ion beam (Dual FIB) microscope. The sequential steps involved in the fabrication of the nanotip are shown in Figure 4.2. The details of nanotip fabrication and LEAP experiment are given in supplementary information (Appendix A).

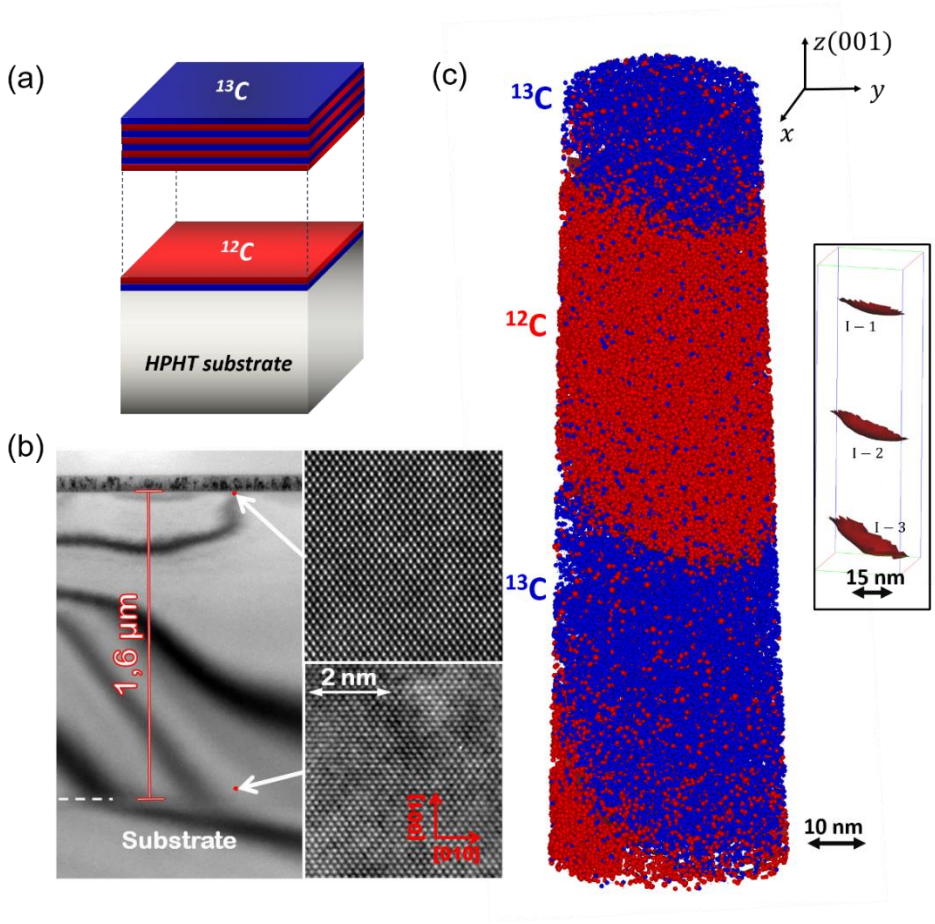

Figure 4.1: *(a) Schematics of the CVD-grown isotopically modulated $^{12}C/^{13}C$ nanoscale layers investigated in this work. (b) Cross-sectional transmission electron microscopy image of the as-grown diamond superlattice. Insets: High-resolution TEM images of regions near the surface (top) and interface with HPHT substrate (bottom) demonstrating the high crystalline quality of the sample. The growth direction of the sample is (001). The scale bar is the same for the top and bottom image. (c) 3-D atom-by-atom reconstruction of the isotopically modulated diamond superlattice sample. The analysis direction of the sample is also (001). The ^{12}C atoms are shown in red bubbles and the ^{13}C atoms are shown in blue bubbles. For the sake of clarity, only 10% of the collected atoms are displayed. Inset: The interface between ^{12}C and ^{13}C, defined as isoconcentration surfaces drawn at 50 at.% concentration of ^{12}C.*

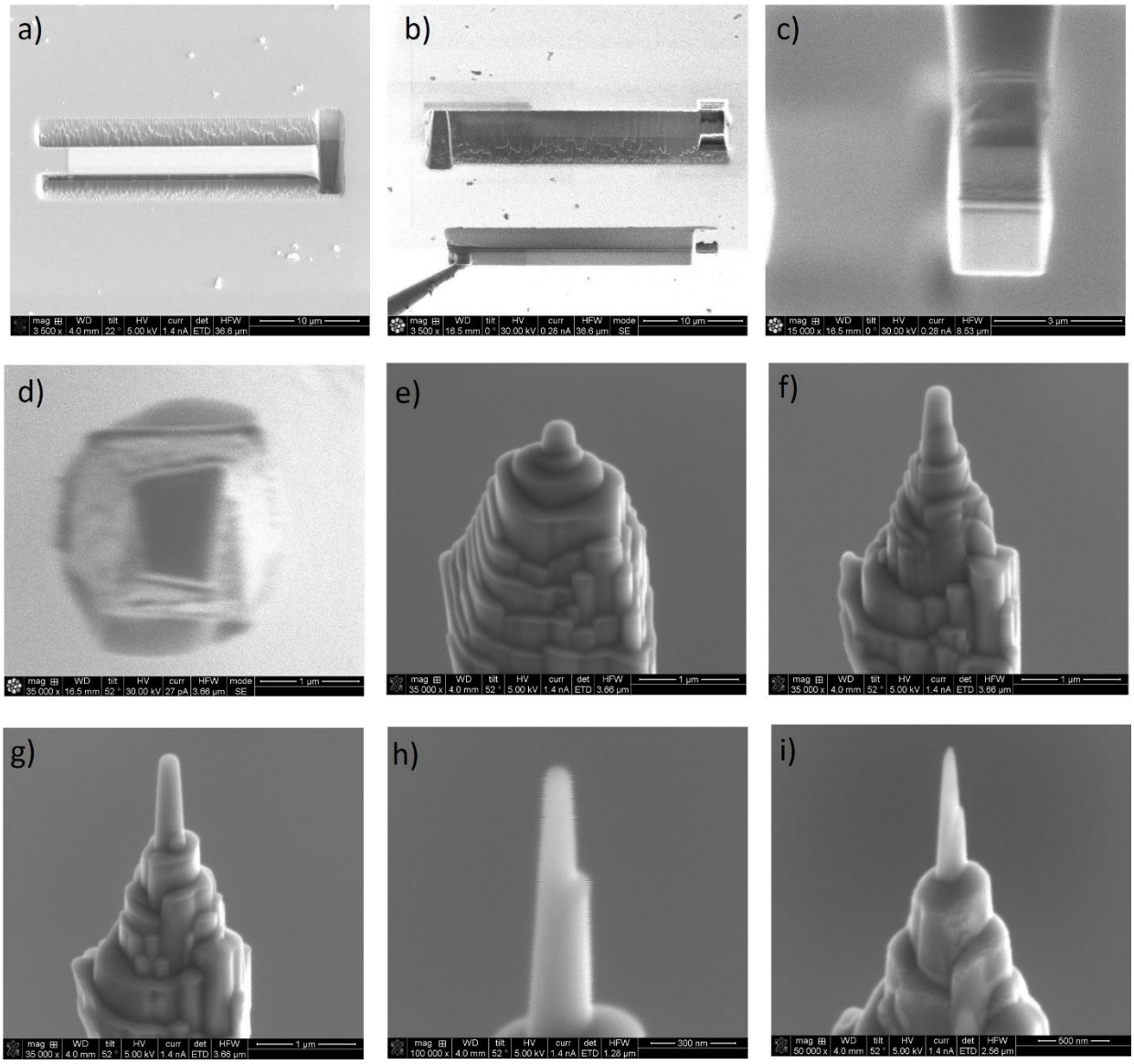

Figure 4.2: *Sequential steps of FIB fabrication of a diamond nanotip. (a) A small piece of the as grown sample was first coated with Ni (70 nm) and then Pt (0.15 µm). Trenches were milled on 3 sides of a chosen section on the sample by Ga^+ ion (30 kV) FIB milling. (b) After milling off the 4^{th} side, the section was lifted out using a micromanipulator. (c) The section was then attached to an APT micro-post using cold Pt welding. (d) To initiate the nanotip sharpening process, first a pyramidal shape was given to the attached sample using rectangular milling patterns. (e), (f), and (g) Circular milling patterns of varying diameter were used to give a needle-like shape to the nanotip. (h) Final polishing of the nanotip was done using low energy Ga^+ ions (5 kV) (i) Final shape of the nanotip before inserting into the APT chamber.*

The laser pulse energy for the LEAP experiment was set at 1000 pJ, which is significantly higher than typical values used in APT analysis. Attempts were made to evaporate the diamond atoms using lower laser pulse energy. For values of E_{Pulse} of 100 pJ and lower, no evaporation of atoms from diamond tip was recorded. For $E_{Pulse} = 500$ pJ, only partial 3-D reconstructions were obtained and the evaporation was unstable leading to the fracture of almost every nanotip. A possible explanation for this may be that for $E_{Pulse} \leq 500$ pJ, the increase of a nanotip temperature was insufficient to meet the set-point detection rate value which was 0.03 ions.pulse^{-1} for our experiments. This may have caused the steady-state dc voltage on the nanotip to rise sharply in order to meet the set point detection rate leading ultimately to the nanotip fracture. For $E_{Pulse} = 500$ pJ, we obtained a partial reconstruction (See Figure S-A2 of the supplementary information in Appendix A) but the evaporation was not stable. Using $E_{Pulse} = 1000$ pJ however, we observed the onset of a stable field evaporation for a dc voltage of ~5 kV, which APT nanotips can withstand. Figure 4.1(c) displays a representative 3-D APT reconstructed image of the sample with ^{13}C atoms displayed in blue and ^{12}C atoms in red. Only 10% of the total collected ^{12}C and ^{13}C atoms are shown for clarity. The inset in Figure 4.1(c) displays the interfaces between ^{12}C and ^{13}C, which are defined by iso-concentration surfaces (shown in brown) corresponding to 50 at.% concentration of ^{12}C. This result is a clear demonstration that a material with a high dielectric constant and strong covalent bonding such as diamond can be field evaporated and mapped using APT.

4.5 Results and Discussion

The mass spectrum (up to m/n = 40 Da) for $E_{Pulse} = 1000$ pJ is shown in Figure 4.3(a). We did observe a few molecular ion clusters but no greater than three C atoms, as can be verified from the full mass spectra displayed in the inset of Figure 4.3(a). The presence of triply-charged ions is indicative of a very high electric field at the nanotip surface. In addition to ^{12}C and ^{13}C peaks, we also detected peaks which correspond to complex ions of the two C isotopes. The mass spectra in Figure 4.3(a) also reveals a clear peak at m/n value of 7 Da and a small peak at 14 Da corresponding to nitrogen ($^{14}N^{2+}$ and $^{14}N^{+}$ respectively). The average nitrogen concentration within the diamond superlattice structure was calculated to be ~0.05 at.%. The proximity histogram displaying the atomic concentration profiles of both ^{12}C and ^{13}C taken along the length of the tip (z-axis in Figure 4.1(c)) is shown in Figure 4.3(b). The $^{13}C/^{12}C$ interfaces are denoted as I-1, I-2, and I-3 and are indicated by the vertical black dotted lines. The $^{13}C/^{12}C$ interfaces exhibit

interfacial broadening of the concentration profiles. The physical origin of this behavior will be discussed later in the text. The proximity histogram also tells us that the individual layers are not 100% isotopically pure, but they are rather rich in one of the two carbon isotopes. For example at the middle of the 2nd layer (between I-1 and I-2) the ^{12}C concentration is ~87 at.% and the remainder is ^{13}C. This effect could have occurred from two sources: i) During the growth itself due to the reservoir effect. When a precursor was switched from $^{i}CH_4$ to $^{j}CH_4$ to grow a new layer, some of the previous unexhausted $^{i}CH_4$ precursor may have been present in the growth chamber and hence a certain fraction of ^{i}C became incorporated in a ^{j}C layer and *vice versa*; and ii) Growth of a microwave plasma CVD diamond is controlled by a balance of etching by atomic hydrogen and growth of carbon. Therefore, there may occur a mechanism or process that facilitates re-growth of C etched by hydrogen.

In the following, we elucidate the fundamental phenomena underlying the field evaporation of diamond. First, we examine the classic ionic model for field-evaporation, which works reasonably well for metallic elements and alloys [147]. In the absence of an electric field, the energy Q_0 required to remove an atom from the surface of a material and ionize it to the n^{th} ionization state is estimated utilizing a Born-Haber cycle given by $Q_0 = \Lambda + \sum_{i=1}^{n} I_i - n\phi_e$ where Λ is the sublimation energy, I_i is the i^{th} ionization energy, n is the charge state of the field-evaporated ion, and ϕ_e is the local work-function for a specific $\{hkl\}$ plane from which an atom is field-evaporated in the n^{th} charge state. In presence of an electric field, the activation energy $Q_n(F)$ for forming an ion in the n^{th} charge states is given by $Q_n(F) = Q_0 - (ne)^{3/2}F^{1/2}$, where e is the charge of an electron and F is the electric field from the site on which the atom is sitting on a specific $\{hkl\}$ plane [147]. Therefore, evaporation field F_{ev}, for an ion in the n^{th} charge state is given by:

$$F_{ev} \approx \left(\Lambda + \sum_{i} I_1^n - n\phi_e\right)^2 \frac{1}{n^3 e^3} \qquad (4.1)$$

which is a minimum for a specific integer n.

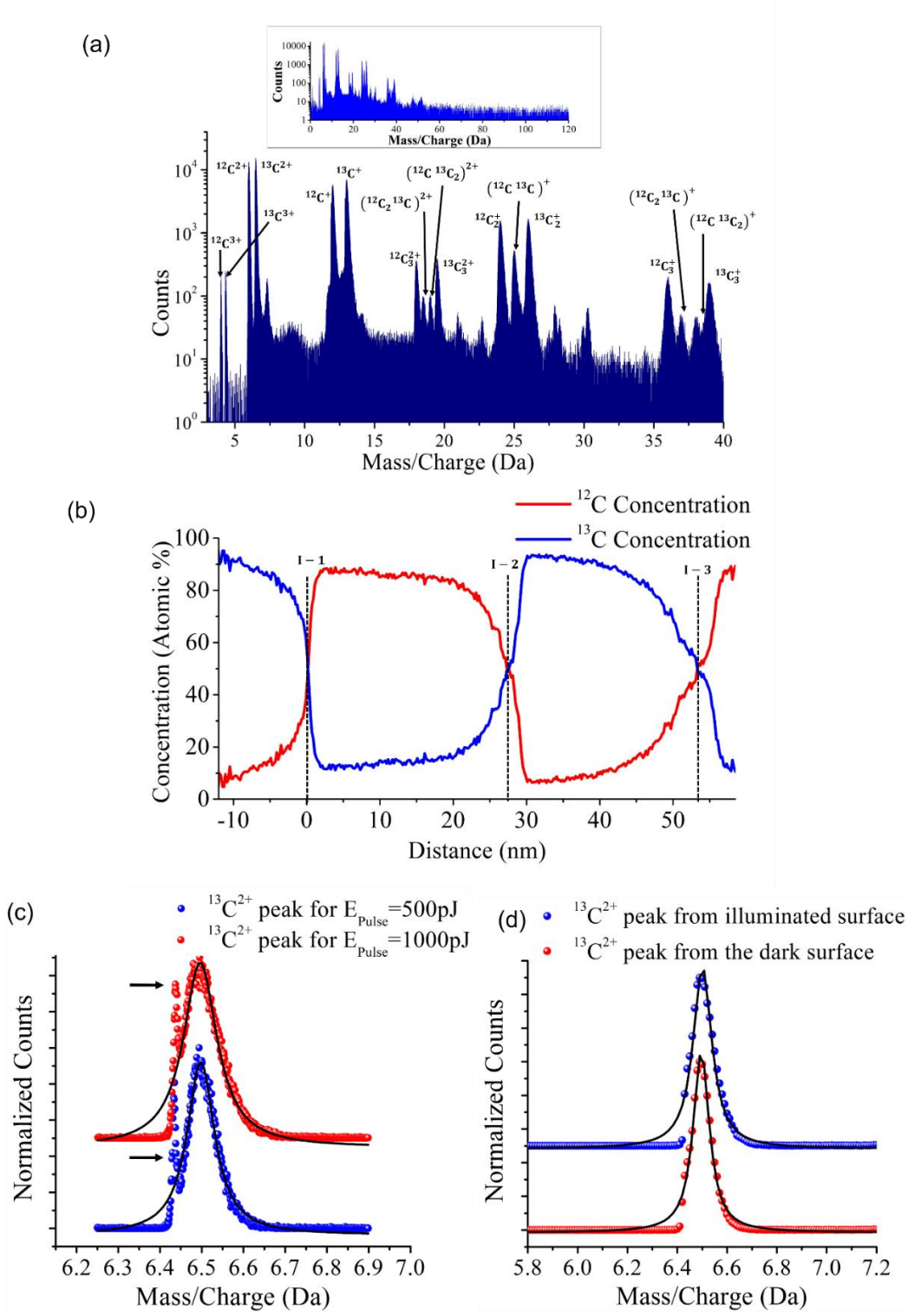

Figure 4.3: *(a) Mass spectra recorded at E_{Pulse} =1000 pJ, showing singly, doubly, and triply charged states of both ^{12}C and ^{13}C (in blue). The spectra reveal clusters with a maximum size up to 3 carbon atoms. The inset showing the mass spectra up to m/n = 120 Da confirming the absence*

of clusters higher than three carbon atoms. We also see some additional weak peaks in the mass spectra that are not labelled. For example, the peaks at 22 Da and 22.5 Da can be attributed to $^{12}CO_2^{2+}$ *and* $^{13}CO_2^{2+}$ *respectively. The peaks at 28 Da and 30 Da most likely originate from* N_2^+ *and* NO^+. *(b) The proximity histogram showing the atomic concentration of both* ^{12}C *(in red) and* ^{13}C *(in blue) along the long axis of the tip (z axis in Figure 4.1(c)). (c) The comparison between the normalized mass spectra of* $^{13}C^{2+}$ *recorded at* E_{Pulse} *of 500 pJ (blue spheres) and 1000pJ (red spheres). The width of the mass spectra was calculated by fitting the raw data with Lorentzian line shapes (continuous black lines). There is an additional (cannot be identified at the moment) peak present (marked by black arrows) just before the* $^{13}C^{2+}$ *peak. This was not taken into account during the fitting (d) The comparison between the normalized mass spectra at* E_{Pulse} *1000 pJ for of* $^{13}C^{2+}$ *atoms located at the surface on the dark side (red spheres) and the illuminated side (blue spheres) of the nanotip. The width of the mass spectra was calculated by fitting the raw data with Lorentzian line shapes (continuous black lines). Note that the unidentified additional peak disappears in the mass spectra for the surface atoms.*

For many metals n is equal to two, while for refractory metals n can be 3 or 4. The field-evaporation rate Γ_{ev}, of an ion from a specific $\{hkl\}$ plane is given by an Arrhenius-type equation, where the activation energy $Q_n(F)$, is a function of F [147] :

$$\Gamma_{ev} = \nu exp\left(-\frac{Q_n(F)}{k_B T}\right) \qquad (4.2)$$

where ν is the frequency factor, k_B is the Boltzmann constant and T is the absolute temperature. For metallic element and metallic alloys, the physical picture is very clear. When a dc voltage is applied to a metallic nanotip, the free electrons are pushed inwards to create an electric dipole layer at the surface. The Debye screening length of the electric field at the surface is of the order of 0.1 nm and by Gauss's law the electric field inside a metal is zero. Hence, it is only the atoms at the surface of a metal that feel the decreased barrier height. The electric field is inversely proportional to the local radius of curvature and therefore the $\{hkl\}$ planes with the smallest radius of curvature have the highest local electric fields. Thus, the smaller is the local radius of curvature the smaller is $Q_n(F)$. There are two possible explanations for the role played by a pulsed laser in laser-assisted APT. First, the laser enhances the temperature of the nanotip from the base temperature T_{Base} to

a maximum surface temperature $T'_{max} = T_{Base} + \delta_T J$, where J is the laser intensity and δ_T is a constant coupling the laser intensity to temperature. Second, the electric field of an ultrafast laser lowers the potential barrier $Q_n(F)$ by non-linear optical rectification processes [153], [175]. Both the processes enhance the evaporation rate of a surface atom according to equation (4.2).

For non-linear optical effects to occur, the laser intensity needs to be extremely high or else the second-order effects get masked by the linear optical effects. This is why a femtosecond pulsed laser with high energy pulses has the best chance to generate non-linear optical effects if its intensity, $J = \textit{Energy per pulse}/(\textit{Pulse duration} \times \textit{Spot area})$ is extremely high. We can eliminate the possibility of any non-linear effect in our APT experiments because the UV laser utilized is a picosecond laser. This leaves us with two major questions to answer. In diamond, which is a dielectric, where the charge carrier density below 100 K is as small as 100 cm^{-3}, how is the electric field being screened and how the UV laser with photon energy (E_{Photon}) of 3.49 eV is being absorbed by diamond, which has a band gap (E_{Gap}) of 5.45 eV. As mentioned above, prior attempts to field-evaporate diamond utilizing a scanning atom probe were performed using the voltage pulsing mode and yielded a small number of clusters of carbon atoms, 3, 5, 8, and even 16 and mainly in form of hydrides [11]. If F is unscreened, as is the situation for a dielectric, and therefore it penetrates deep into the bulk from the surface, it is practically impossible to remove atoms layer-by-layer from the surface of a nanotip. This leads to evaporation of atoms in cluster because the decreased barrier height $Q_n(F)$ is not just felt by the surface atoms but also by the atoms located several atomic layers beneath the surface. As evident from the mass spectrum in Figure 4.3(a), we observed a few molecular ions, but only with a maximum cluster size of three carbon atoms and the majority of the evaporated species are monoatomic. This provides clear evidence on the field-screening in diamond nanotips.

For APT analyses of intrinsic semiconductors and dielectrics, the density of mobile carriers at temperatures < 100 K is too small to screen effectively an electric field. To explain screening of an electric field in intrinsic semiconductors and bulk insulators several mechanisms for the generation of excess charge carriers have been proposed, like the photo-generation of excess free carriers through electronic excitations from the valence band to the conduction band [155] and increased optical absorption subjected to a strong electric field, ~1 V nm^{-1}, known as the Franz–Keldysh effect [156]. However, both effects require E_{Photon} to be greater than or at least close to

E_{Gap}. Excess free carriers may also be generated in a dielectric by impact ionization under the high internal electric fields [176]. Dielectric breakdown due to impact ionization was demonstrated to be the source of excess carriers for field evaporation of MgO in APT [158]. This phenomenon does not pose any restriction on the laser energy to be used. The computed free hole density at the surface of a MgO nanotip, as a result of impact ionization, is $\sim 10^{21}$ cm^{-3} and the field is screened within 1-2 nm from the surface. The average carrier density in the core is orders of magnitude lower.

Analogously, the phenomenon of impact ionization seems to be the dominant mechanism for excess carrier generation in the diamond nanotip. The critical breakdown field of diamond is very high, between 1.1 and 21.5 $MV.cm^{-1}$ with the upper limit for undoped diamond [177]. For our undoped diamond samples, the initial free charge density at 85K (before impact ionization) is so small that the entire applied dc voltage ($\sim$5 kV) drops across the length of the nanotip ($\sim$few μm) and the initial voltage at the apex of the diamond nanotip is zero. This gives an initial internal electric field ($\Delta V/\mathfrak{L}$) which is greater than critical breakdown field. Once the free carriers are generated, the free holes drift to the surface in order to screen the internal electric field. The exact value of the surface hole concentration can be computed numerically by solving the coupled drift-diffusion and Poisson's equation. In general, it is reasonable to assume that, for the field evaporation to take place, the free hole concentration at the surface of the diamond nanotip (n_h) can reach any value between semi-metallic and metallic free carrier concentrations ($n_h \sim 10^{19} cm^{-3} - 10^{22} cm^{-3}$). In the core of the nanotip, the carrier concentration is several orders of magnitude smaller. Typically, the field screening length depends on the surface hole concentration. For close to metallic concentrations it can be a fraction of a nm whereas for semi-metallic and lower concentrations it can reach several nm. We will consider the screening length to be $\sim$2 nm based on grounds explained later in the text. Impact ionization thus creates a hole rich shell at the surface of the nanotip as shown schematically in Figure S-A1 of supplementary information (Appendix A). The electric field within this shell is strong (strongest at the curved surface) and keeps the impact ionization going whereas the field in core of the nanotip (after the screening is complete) is zero.

A steady state is attained as the concentration of holes that are generated by the impact ionization is balanced by the concentration of holes that are diffusing away (towards the core) and

recombining with electrons that diffuse from the bulk to the surface and the electrons donated to the surface by the evaporating cations. The steady state carrier concentration at the core is reached by means of diffusion (holes from the surface towards the core and electrons from the core towards the surface). Impact ionization also explains why earlier attempts to field evaporate diamond in pulsed voltage mode $(V_{dc} = 3.24\ \text{kV and}\ V_p = 1.30\ \text{kV})$ resulted in evaporation of carbon atoms in large clusters [11]. The generation rate of electrons $(\mathrm{G_e})$ and holes $(\mathrm{G_h})$ by impact ionization in diamond in presence of an electric field F can be represented by the empirical expression [177] : $\mathrm{G_e} = \mathrm{G_h} = 1.935 \times 10^8 \exp(-7.74 \times 10^6/F)\ \mathrm{cm^{-3}s^{-1}}$. With lower value of $\mathrm{V_{dc}}$ and hence F, it is possible that either the dielectric breakdown was never achieved or may be breakdown was achieved but the smaller rate of carrier generation meant lower steady state carrier density at the surface and a much longer screening length. The pulsed voltage V_p, possibly did not have any effect on the impact ionization. As pointed out by Gilbert et *al*., the whole electrical environment surrounding the nanotip in an APT chamber acts as a RC low-pass filter [150]. In pulsed voltage mode where the voltage pulses have a rise time in the nanosecond range, the material which is being evaporated should have a resistivity below $\sim 10 - 10^2\ \Omega - \mathrm{cm}$, or else the voltage pulses cannot be fully transmitted to the material.

The absorption of the laser comes from two different contributions. The HOMO-LUMO gap of Si and MgO cluster of atoms were shown to decrease at high fields [172]. The HOMO-LUMO gap of a cluster of atoms translates into the band gap in bulk material. With the partial or complete closure of the band gap at the surface of the diamond nanotip, we can expect some absorption of the UV laser due to electronic excitation from conduction band to valence band as the band gap becomes smaller than the photon energy. The other and the major contribution comes from the free carrier absorption. The temperature rise of the surface can be visualized as follows: unlike a metal where electrons absorb the laser energy and make interband transitions, the free holes at the surface of the diamond nanotip absorb the UV laser light and make intraband transitions (between different subbands) and finally relax by colliding with the lattice vibrations, thereby raising the temperature of the lattice. A rough estimate of the surface temperature can be made using the conservation law:

$$\int_{T_{Base}}^{T'_{max}} C(T)dT = \alpha_{free-hole}(1-R)J\tau_p \quad (4.3)$$

where $C(T)$ is the temperature dependent heat capacity, T_{Base} and T'_{max} are the base temperature of the APT chamber and the maximum temperature of the surface respectively, R is the reflectivity, J is the intensity of the laser light and τ_p is the duration of a UV laser pulse. We deduce that the maximum surface temperature (T'_{max}) on the illuminated side can vary from ~152 K to ~306 K whereas on the dark side (right side in Figure 4.1(c)) it can vary from ~147 to ~274 K in the hole concentration range considered ($10^{19} - 10^{22}\text{cm}^{-3}$) (details in supplementary information, Appendix A). For a surface with 'N' kink sites and a vibrational frequency of the surface atoms ν, the rate of evaporation of atoms from the surface during a single pulse is given by [143] :

$$\phi_{ev} \approx \nu N\left[\frac{k_B T'_{max}}{Q_n(F)} \times \tau_{cooling}\right] exp\left\{-Q_n(F)\Big/k_B T'_{max}\right\}$$
$$= \nu N[\tau_{Ev}] exp\left\{-Q_n(F)\Big/k_B T'_{max}\right\} \quad (4.4)$$

where $\tau_{cooling}$ is an effective cooling time of the surface. This equation suggests that the atoms at the illuminated side are evaporated at a slightly higher rate than on the dark side. Such non-uniform temperature and evaporation rate leading to an asymmetry in the nanotip shape was also observed for UV laser assisted APT on Si [178]. This phenomenon could be at the origin of the slanted shape of the isoconcentration surfaces between the ^{12}C and ^{13}C layers observed in the inset of Figure 4.1(c). For example, at the first interface, when at the illuminated side (the left side in Figure 4.1(c)) the ^{12}C atoms (from the 2nd layer) has started evaporating, the dark side (the right side in Figure 4.1(c)) is still evaporating atoms from the first ^{13}C layer. The 3-D IVAS reconstruction which is performed layer-by-layer, gives the illusion that at one side of the sample, at every interface, atoms from the layer beneath the interface has diffused into the layer on top. This explains the broadening of the concentration profiles at every $^{13}C/^{12}C$ interfaces in Figure 4.3(b). During reconstruction of the data, we slice up the reconstructed volume to thin cylinders each of fixed bin widths. The concentration data points appearing in the proximity histogram is an average inside each such slice. Since we have a non-uniform evaporation rate from the illuminated to the dark side of the nanotip inducing an asymmetry in the reconstructed data, the average concentration gives the impression that there is a lot of intermixing of isotopes at the interfaces. Hence in Figure 4.3(b), estimating the

interface width ($\mathcal{L}$), normally done by calculating the separation between 10% and 90% concentration points at each interface would give a faulty value of $\mathcal{L}$.

In context of the discussion above, we can narrow down the range of surface free hole concentration we considered earlier. With $n_h = 10^{19}\text{cm}^{-3}$ the rise in temperature ($T_{Rise} = T'_{max} - T_{Base}$) is only about 65 K which cannot be enough to evaporate diamond. In fact, a T_{Rise} of ~100 K was calculated for evaporation of Si [156] which has an evaporation field about one fifth that of diamond. Also with only 2% loss in intensity for $n_h = 10^{19}\text{cm}^{-3}$, leads to almost no difference in T'_{max} from the illuminated to the dark side of the nanotip and hence cannot explain the slanted isoconcentration surfaces. On the other hand, if the surface hole concentration would be equal to that of metallic free carrier concentrations, the field should have been well screened within ~one-tenth of a nm from the surface and we should not have observed the few clusters of three C atoms in the mass spectra. All of this suggests that the free surface hole concentration must lie above the lower limit of the range considered initially but below the metallic free carrier concentrations. This also justifies our approximation of considering an intermediate value of the field screening length of ~2 nm. The surface temperature can impact the uncertainty in the time-of-flight (TOF) of atoms. Indeed, the finite width of peaks in a mass spectra appear due to the uncertainty in the TOF, which in turn is related to the evaporation time of an atom, τ_{Ev} given by the terms in square bracket in equation (4.4). Hence the width of the mass spectra gives an estimate of the surface temperature of the nanotip from which a cation was evaporated. In Figure 4.3(a) we clearly see that the peaks in the mass spectra which are separated even by less than 1 Da are clearly resolved demonstrating the fact that the high surface temperature and the broadening of the mass spectra is not enough to spoil the mass resolving power of atom probe. The temporal evolution of tip temperature is often obtained by solving 1D diffusion equations and $\tau_{cooling}$ is estimated from the size of the heated zone and the thermal diffusivity [179]. This model gives a good estimate of the temperature of a metallic nanotip. With a metallic nanotip with an apex radius much smaller than the laser wavelength, the absorption of photons occurs within the anomalous skin depth from the surface (rather than the actual skin depth) which is ~50 nm for most metals at low temperature. Hence for metals, with negligible radial variation in nanotip temperature, the entire heated zone (typically much smaller than spot size) [179] is assumed to have the same temperature. The heat diffuses away from this zone along the long axis of the tip.

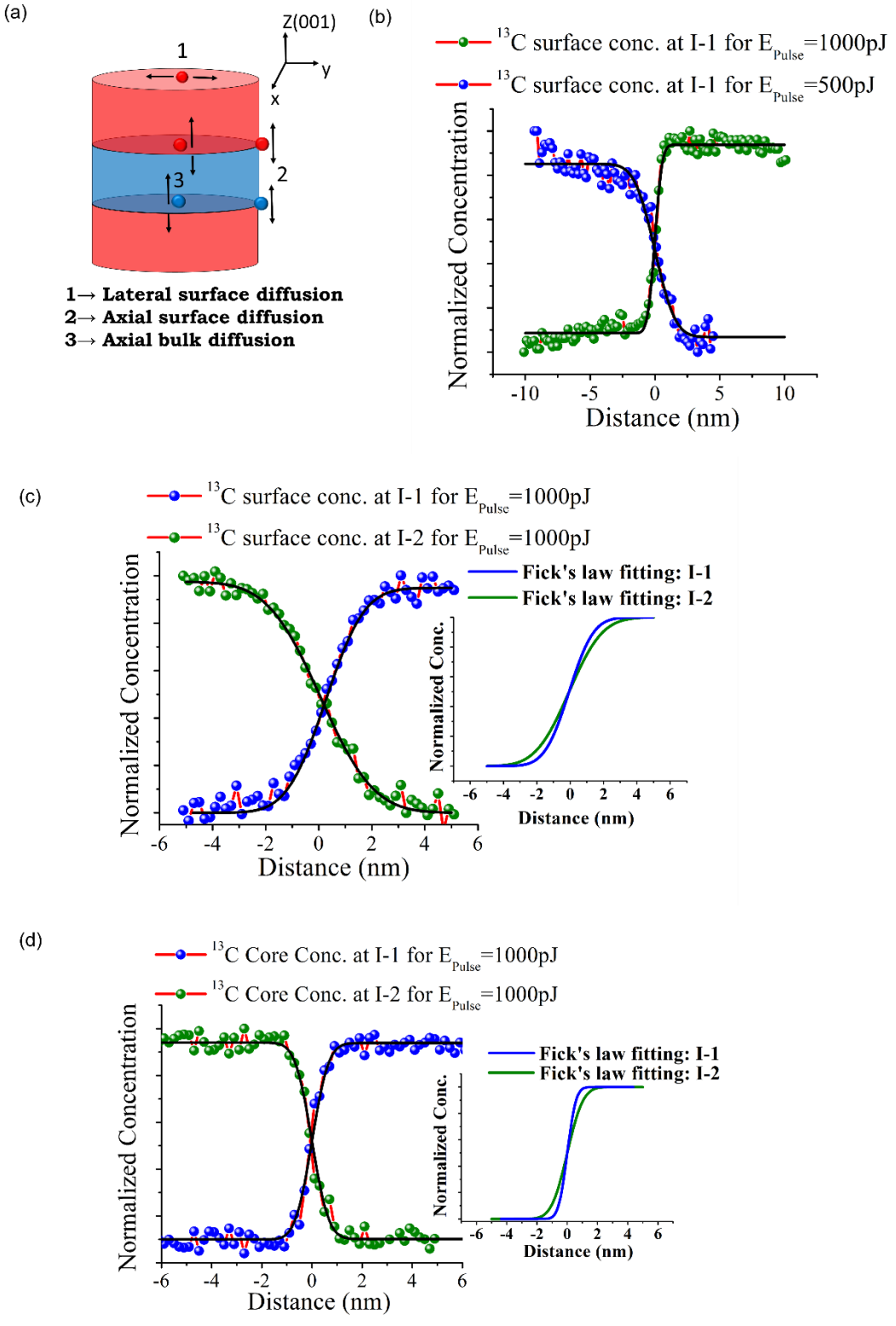

Figure 4.4: *(a) Schematics depicting various diffusion processes (details in text). (b) Normalized concentration profile for ^{13}C atoms at the surface (dark side) of the nanotip at I-1 for E_{Pulse} =*

1000 pJ and 500 pJ. The data points are displayed with sphere (green and blue spheres for 1000pJ and 500pJ respectively). In (b), (c), and (d) the red dashed lines are the cubic spline interpolation of the raw data and continuous black line is the fit using Fick's second law. (c) Normalized concentration profile for ^{13}C atoms at the surface (dark side) of the nanotip at I-1 and I-2 for $E_{Pulse} = 1000$ pJ. The data points are displayed with sphere (blue and green spheres for I-1 and I-2 respectively). Inset: Displaying only the Fick's law fitting of the raw data. It is clear, that the diffusion length of the ^{13}C atoms at the surface (dark side) of the nanotip is more at I-2 than at I-1. (d) Normalized concentration profile for ^{13}C atoms at the core of the nanotip at I-1 and I-2 for $E_{Pulse} = 1000$ pJ. The data points are displayed with sphere (blue and green spheres for I-1 and I-2 respectively). Inset: Displaying only the Fick's law fitting of the raw data. It is evident that the diffusion length of the ^{13}C atoms at the core of the nanotip is more at I-2 than at I-1. Also, the diffusion length of the ^{13}C atoms at the core of the nanotip at I-1 or I-2 is much less that that at the surface for the same pulse energy.

In our experiment, since the concentration of free carriers varies radially, the laser absorption and hence the radial temperature variations are quite significant as discussed above. The picture described above for cooling of metallic nanotips should be slightly modified in order to adapt it to our diamond nanotip. We think that there might be a 2-step heat diffusion process: a fast process and a slow one. During the laser pulse, the surface of the nanotip (within the heated zone) reaches a high temperature whereas the core remains at 85K. First, the heat which is only localized in the thin layer at the surface, dissipates away towards the core. Both the core as well as the surface then reaches an average equilibrium temperature. This temperature must be much lower than the surface temperature because the entire core is at the base temperature. As a result, the evaporation of atoms from the surface of the nanotip can be assumed to stop once this average temperature is reached. This is the fast process where the high surface temperature *rapidly* cools down to an average temperature. This rapid cooling is due to the extremely high thermal conductivity of diamond and due to the fact that the heat has to diffuse only a small distance (of the order of the radius of the nanotip) rather than its entire length. Once this average temperature is reached, the heat can be assumed to diffuse slowly along the length of the tip as predicted by the solution of 1D heat diffusion equation. A precise estimate of $\tau_{cooling}$ under the given scenario can be extremely

complicated where we have the tip whose surface is non-uniformly heated, the core at a base temperature, a material with high thermal conductivity value, isotopically enriched layers, presence of isotopic interfaces, surface scattering of phonons which can all affect the lattice thermal conductivity.

The other factor affecting τ_{Ev} is the maximum surface temperature T'_{max}. As shown in Figure 4.3(c), we have overlapped the $^{13}C^{2+}$ peak of the mass spectra recorded for $E_{Pulse} = 1000$ pJ and 500 pJ. The full width at half maxima (FWHM) of the mass spectra was extracted by fitting the data with a Lorentzian lineshape. The FWHM is 16% larger for the spectra recorded at $E_{Pulse} = 1000$ pJ than at 500 pJ. It is to be noted that the mass spectra in Figure 4.3(c) was collected from the entire reconstruction region (both dark side as well as the illuminated side). If we assign an average maximum surface temperature (simple average of T'_{max} from the dark side and the illuminated side) then the ratios of the FWHM suggest an average T'_{max} of the nanotip for $E_{Pulse} = 1000$ pJ is $\sim 16\%$ higher as compared to 500 pJ. This value is slightly lower than the value we calculated from our model which suggests the average T'_{max} of the nanotip for $E_{Pulse} = 1000$ pJ should be $18 - 25\%$ higher as compared to $E_{Pulse} = 500$ pJ. Next, we have carefully extracted the surface atoms on the dark side and the illuminated side of the nanotip. The method to extract the core and surface atoms has been shown in the supplementary information section, Figure S-A3(a) and the corresponding atom-by-atom reconstructions in Figure S-A3(b) and (c) in Appendix A. In Figure 4.3(d) we have overlapped the mass spectra of $^{13}C^{2+}$ cations extracted from the dark side and the illuminated surface of the nanotip for $E_{Pulse} = 1000$ pJ. The FWHM extracted from the Lorentzain fitting of the data suggests that T'_{max} is $\sim 13\%$ higher on the illuminated side as compared to the dark side. This is a direct evidence of the non-uniform temperature distribution on the surface of the nanotip. The value also falls within the range that our model predicts.

The high surface temperature also induces a certain amount of surface diffusion of atoms. Surface diffusion of atoms is considered to be a parasitic effect in APT, affecting the spatial resolution of the instrument. We have carefully scrutinized the effect of the energetic laser pulses on surface diffusion, the details of which are provided in the supplementary information section (Appendix A). The main results have been summarized below. As shown in Figure 4.4(a), we consider three diffusion processes: Process (1), the lateral surface diffusion of atoms on a layer

which is on the verge of evaporation; process (2): the axial surface diffusion of atom leading to interfacial broadening; and process (3): the bulk interdiffusion of atoms (self-diffusion) which also contributes to interfacial broadening. We assume process (1) to be the same for every layer. Detailed quantitative analysis of these processes is provided in the supplementary information (Appendix A). From Figure 4.4(b) we calculated the diffusion length, ℓ of ^{13}C atoms extracted from the surface (dark sides) at the respective I-1's of the nanotips evaporated at $E_{Pulse} = 1000$ pJ and 500 pJ (See the corresponding reconstructions in Figure S-A3 b(2) and c(2) of the supplementary information section in Appendix A). ℓ of process (2) at I-1 for $E_{Pulse} = 1000$ pJ and 500 pJ was found to be 1.63 ± 0.01 nm and 1.46 ± 0.01 nm respectively. The $\sim$11.5% increase in ℓ of process (2) for $E_{Pulse} = 1000$ pJ can be attributed to the increase in surface temperature induced by doubling the pulse energy. In Figure 4.4(c) we have plotted the concentration profile at I-1 and I-2 of ^{13}C atoms extracted from the surface (dark side) of the nanotip evaporated at $E_{Pulse} = 1000$ pJ. The value of ℓ for process (2), that is the axial surface diffusion length at I-1 and I-2 was calculated to be 1.63 ± 0.01 nm and 1.94 ± 0.01 nm respectively ($\sim$19% increase at I-2). In Figure 4.4(d), we have plotted the concentration profile at I-1 and I-2 of ^{13}C atoms extracted from the core of the nanotip evaporated at $E_{Pulse} = 1000$ pJ. Also from Figure 4.4(c) and (d) the interface width ($\mathcal{L}$) at I-1 at the core and the surface (dark side) of the nanotip was calculated to be $\sim 0.58 \pm 0.01$ nm and $\sim 2.03 \pm 0.01$ nm, respectively (a decrease of $\mathcal{L}$ by a factor of $\sim$3.5 at the core of the nanotip than at the surface). The value of $\mathcal{L}$ at the core is even lower than the value reported for isotopically modulated Si layers which was evaporated using a much lower pulse energy of 40 pJ [118]. These comparisons reveal that the data recorded from the core of the tips provide the true information of interfacial widths as diffusion affects the atoms at the core of the nanotip to a much lesser extent than those at the surface. This indicates that by extracting the 3-D maps from the core and omitting the atoms from the surface of the nanotip is an effective way to circumvent the effects of surface diffusion induced-mixing.

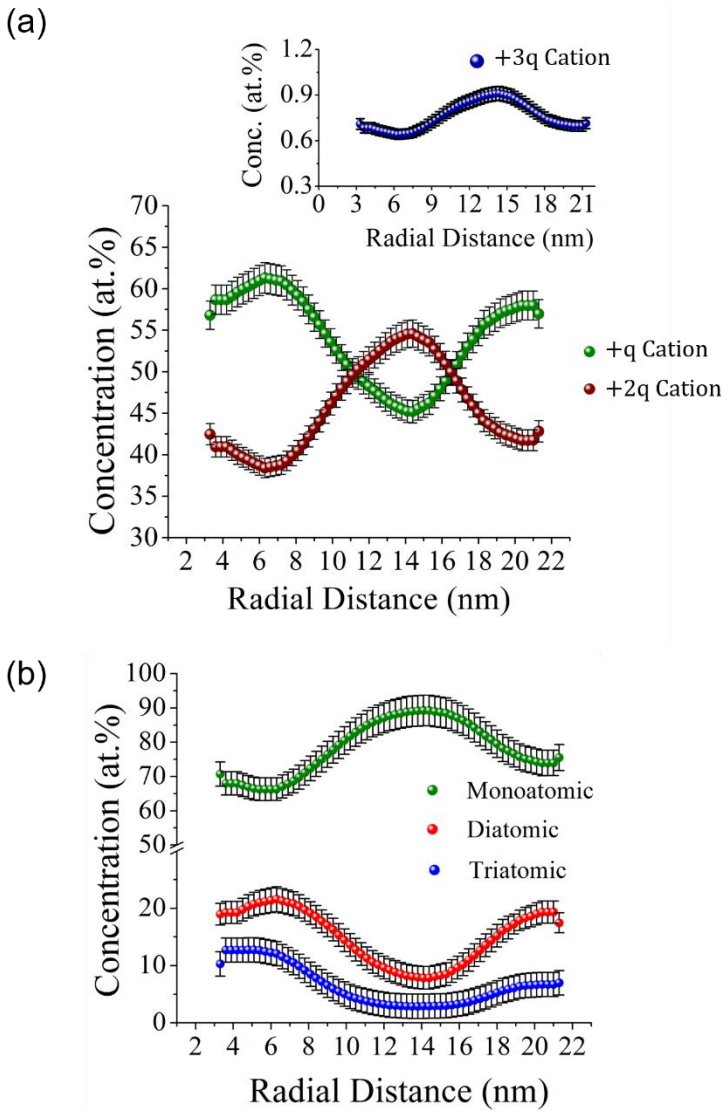

Figure 4.5: (a) *Plot of normalized concentration of +q, +2q and +3q (inset) cations with radial distance for* $E_{Pulse} = 1000$ *pJ. The +2q and +3q (inset) cations have the highest concentration roughly at the center which corresponds to the center of the nanotip (reason explained in the text). (b) Plot of normalized concentration of mono, di, and tri atomic species with radial distance for* $E_{Pulse} = 1000$ *pJ. The minima in the concentrations of di and tri atomic specis occur roughly at the center of the nanotip(reason explained in the text). Also noteworthy is that the location of the extremum values occurs slightly to the right in both the figures rather than being exactly at the center. This might be due to the fact that the nanotip had an inherent asymmetry from the FIB fabrication process or the non-uniform temperature distribution has shifted the field extrema from the center to one side of the nanotip.*

As the mass spectra in Figure 4.3(a) reveals that the evaporated cations consist not only of monoatomic species but also a few clusters of two or three atoms as well as with different charge states varying from +1 to +3. A map of these different atomic species, would help highlighting some fundamental aspects about the nanotip geometry, the distribution of temperature and field within the nanotip. We extracted from APT map a thin slice (3-4 nm) of atoms from the top ^{13}C rich layer and plotted the radial variation of normalized concentration profiles of +q, +2q, and +3q cations in Figure 4.5(a) and mono, di, and tri atomic species in Figure 4.5(b) (The technique for extracting the slice has been shown in Figure S-A2 and S-A4(a) of the supplementary information section in Appendix A). In Figure 4.5(a) we see that the +2q and +3q (inset) cations have the highest concentration roughly at the center. Note that the center of the slice corresponds to the center of the nanotip. The reason for this is not too far to conceive: the actual shape of the nanotip is parabolic or needle shaped (See Figure 4.2(i), the final shape of the nanotip). The free holes after being generated by impact ionization drift towards the surface to screen the electric field and concentrate maximum at the apex of the parabolic nanotip due to the lightning rod effect, which is why the field strength is maximum and the field screening length is minimum at the nanotip apex. As a result, the +2q and +3q charge states are evaporated from the region of the highest field strength. The distribution of the di and tri atomic species as shown in Figure 4.5(b), is in a way complementary (lowest concentration roughly at the center) to the distribution of +2q and +3q cations. Clusters of two or three atoms evaporate from regions where the field instead of being screened at the surface, extends deep up to a few atomic layers beneath the surface. As discussed earlier, the distribution of free holes ensures that the screening length is minimum at the apex and hence the observed minima in concentration of di and tri atomic species. The concentration of di and tri atomic species though rises up slightly as we move towards the periphery of the nanotip, but it never surpasses the concentration of the monoatomic species. This shows that the field screening was extremely good for our experiment and the screening length is small throughout the nanotip cross section, though it is slightly larger at the periphery as compared to the apex of the nanotip, which is expected. Similar plots for the nanotip evaporated at $E_{Pulse} = 500$ pJ is shown in Figure S-A4(b) of the supplementary information section in Appendix A. We also found the fraction of +2q and +3q cations is more and the fraction of di and tri atomic species is less at $E_{Pulse} = 500$ pJ compared to 1000 pJ (See Figure S-A4(c) of the supplementary information section in Appendix A). The reason for this is that in an APT instrument the user defined laser

pulse energy is synchronized with the automatic bias voltage. With the same set-point detection rate, lower the value of E_{pulse}, higher the bias voltage applied to the base of the nanotip. This is consistent with our observation that with $E_{Pulse} = 500$ pJ the applied bias to the base of the nanotip, though having large fluctuations leading to unstable evaporation, was consistently greater than the 5 kV value reported for the evaporation done at $E_{Pulse} = 1000$ pJ. The bias voltage and hence the internal field affects the rate of electron and hole generation by impact ionization according to the equations [177] $G_e = G_h = 1.935 \times 10^8 \exp(-7.74 \times 10^6/F)$ $cm^{-3}s^{-1}$. This leads to a stronger internal field at $E_{pulse} = 500$ pJ and hence higher values of G_e and G_h compared to $E_{Pulse} = 1000$ pJ. Greater the rate of generation of free carriers greater the steady state concentration of free hole at the surface of the nanotip. This leads us to believe that the magnitude of the steady state electric field at the surface of the nanotip must have been higher and the field screening length smaller at $E_{Pulse} = 500$ pJ as compared to that with $E_{Pulse} = 1000$ pJ explaining the observation.

4.6 Summary

In conclusion, achieving a successful 3-D atom–by-atom imaging of diamond isotopes using APT is based on a controlled field evaporation resulting from the unique behavior of nanoscale diamond under high electric field and its interaction with a pulsed laser. We propose the following scenario for this laser-assisted field evaporation: (i) The initial applied dc voltage creates a strong electric field inside the diamond tip to induce dielectric breakdown and an avalanche of free electrons and holes are generated by impact ionization; (ii) The free holes move to the surface to screen the electric field and the steady state free hole concentration at the surface becomes close to metallic free carrier densities; (iii) The incident laser is absorbed by the free holes at the surface and as they relax by colliding with the lattice vibrations the temperature of tip surface is elevated. Due to strong absorption of the UV-laser light by the surface free holes at the illuminated side of the tip, the laser intensity reaching the dark side of the tip is reduced. This leads to difference in maximum surface temperature on the illuminated side and dark side which is confirmed by the relative increase in the width of the mass spectra of $^{13}C^{2+}$ cation at the illuminated surface of the nanotip from the non-illuminated surface. The difference in maximum temperature leads to a slight difference in evaporation rate of atoms from the two sides of the tip which manifests itself in form of slanted iso-concentration surfaces in the reconstructed data. The radial distribution of the various

cations and clusters sizes helped provide a qualitative picture of the field distribution and strength within the nanotip. Last but not the least, we quantified various diffusion processes that take place at the core and the surface of the nanotips during the field-evaporation. We also demonstrated that clear 3-D maps can be obtained by omitting from the analysis, the atoms located at regions near the surface of the nanotip. This ability to achieve a 3-D atom-by-atom mapping of diamond isotopes paves the way for an atomistic-level control of isotopes in diamond-based nanoscale and quantum structures. Additionally, our result also contributes to elucidating the basic properties of dielectric nanostructure under high electric field.

4.7 Acknowledgement

O.M. acknowledges funding from NSERC-Canada (Discovery Grants), Canada Research Chair, Fondation de l'École Polytechnique de Montréal, and MRIF Quebec. The local electrode atom-probe tomograph at the Northwestern University Center for Atom-Probe Tomography (NUCAPT) was acquired and upgraded with equipment grants from the MRI program of the National Science Foundation (grant number DMR-0420532) and the DURIP program of the Office of Naval Research (grant numbers N00014-0400798, N00014-0610539, N00014-0910781). NUCAPT is a Research Facility at the Materials Research Center of Northwestern University, supported by the National Science Foundation's MRSEC program (grant number DMR-1121262). Additional instrumentation at NUCAPT was supported by the Initiative for Sustainability and Energy at Northwestern (ISEN). The authors thank A. Hähnel for TEM analysis.

CHAPTER 5 ARTICLE 2: SHORT-RANGE ATOMIC ORDERING IN NON-EQUILIBRIUM SILICON-GERMANIUM-TIN SEMICONDUCTORS

This article has been published in Physical Review B Rapid Communication (PRB 95, 161402 (R), (2017); DOI: https://doi.org/10.1103/PhysRevB.95.161402; Publication Date (Web): April 2017). The article describes the atom probe investigation on the randomness of atomic distribution in non-equilibrium SiGeSn ternary alloys. The supplementary material of this article is given in Appendix B of the thesis.

5.1 Authors

S. Mukherjee[1], N. Kodali[1], D. Isheim[2], S. Wirths[3], J. M. Hartmann[4], D. Buca[3], D. N. Seidman[2], and O. Moutanabbir[1,*]

[1] *Department of Engineering Physics, École Polytechnique de Montréal, Montréal, C. P. 6079, Succ. Centre-Ville, Montréal, Québec H3C 3A7, Canada.*

[2] *Department of Materials Science and Engineering and Northwestern University Center for Atom Probe Tomography, Northwestern University, Evanston, IL 60208-3108, USA.*

[3] *Peter Grünberg Institute 9 and JARA - FIT, Forschungszentrum Juelich, Juelich 52425, Germany.*

[4] *CEA, LETI, Minatec Campus, 17 rue des Martyrs, Grenoble 38054, France*.

5.2 Abstract

The precise knowledge of the atomic order in monocrystalline alloys is fundamental to understand and predict their physical properties. With this perspective, we utilized laser-assisted atom probe tomography to investigate the three-dimensional distribution of atoms in non-equilibrium epitaxial Sn-rich group IV SiGeSn ternary semiconductors. Different atom probe statistical analysis tools including frequency distribution analysis, partial radial distribution functions, and nearest neighbor analysis were employed in order to evaluate and compare the behavior of the three elements to their spatial distributions in an ideal solid solution. This atomistic-level analysis provided clear evidence of an unexpected repulsive interaction between Sn and Si leading to the deviation of Si atoms from the theoretical random distribution. This departure from an ideal solid solution is

supported by first-principles calculations and attributed to the tendency of the system to reduce its mixing enthalpy throughout the layer-by-layer growth process.

5.3 Introduction

The assumption that the arrangement of atoms within the crystal lattice is perfectly random is a broadly used approximation to establish the physical properties of semiconductor alloys. This approximation allows one to estimate rather accurately certain thermodynamic as well as material parameters like the excess enthalpy of formation, Vegard-like lattice parameters, and band gaps that are smaller than the composition weighted average (optical bowing). However, it has been proposed that some ternary semiconductors can deviate from this assumed perfect solid solution. Indeed, both calculations and experiments suggested the presence of local atomic order in certain III-V alloys [16]–[18], [180]–[184]. This phenomenon manifests itself when at least one of the elements forming the alloy preferentially occupies or avoids specific lattice sites. This induces short-range order in the lattice with an impact on the basic properties of the alloyed semiconductors [16]–[18], [182], [183].

The recent progress in developing Sn-rich group IV (SiGeSn) ternary semiconductors and their integration in a variety of low dimensional systems and devices have revived the interest in elucidating the atomistic-level properties of monocrystalline alloys [185]–[196]. Interestingly, unlike III-V semiconductors, achieving a direct bandgap in $Si_xGe_{1-x-y}Sn_y$ requires a sizable incorporation of Sn (> 10 at. %), which is significantly higher than the equilibrium solubility (<1 at.%). Understanding the atomic structure of these metastable alloys is therefore imperative for implementing predictive models to describe their basic properties. With this perspective, we present a first study of the atomic order in $Si_xGe_{1-x-y}Sn_y$ alloys (x and y in $0.04 - 0.19$ and $0.02 - 0.12$ range, respectively). We employed Atom Probe Tomography (APT) which allows atomistic level investigations [158], [197]–[199] and statistical tools to analyze the three-dimensional (3-D) distributions of the three elements. This analysis unraveled an unexpected repulsive interaction between Sn and Si leading to a deviation of Si atoms from the theoretical random distribution.

5.4 Experiment

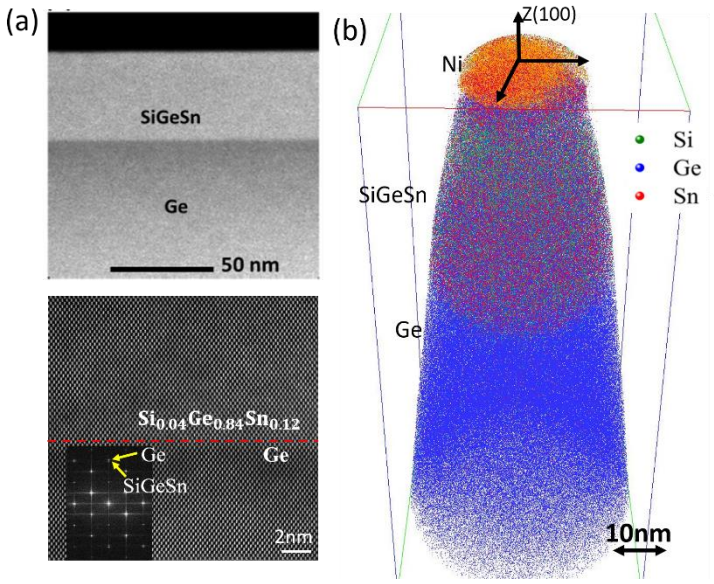

Figure 5.1: *(a) High angle annular dark field STEM (top) and high resolution STEM (bottom) images of the $Si_{0.04}Ge_{0.84}Sn_{0.12}$/Ge interface. Inset: A diffraction pattern taken from a selected region at the interface (b) 3-D reconstruction of the ternary alloy ($Si_{0.04}Ge_{0.84}Sn_{0.12}$), showing the Ni capping layer, the SiGeSn thin film and a portion of the Ge buffer layer. For the sake of clarity, only 10% of Ge atoms and 50% of Sn atoms are displayed.*

The samples investigated in this work were grown using a metal cold-wall reduced pressure chemical vapor deposition (CVD)[186], [200], [201] using Si_2H_6, Ge_2H_6, and $SnCl_4$ as precursors and a relatively low growth temperature of 350 - 475°C resulting in a normal growth rate of $\sim 1 nm/s$. Further details of epitaxial growth of $Si_xGe_{1-x-y}Sn_y$ are described in the supplemental material (Appendix B). Figure 5.1(a) shows the scanning transmission electron microscope (STEM) images of the layer with highest Sn content ($Si_{0.04}Ge_{0.84}Sn_{0.12}$), confirming the pseudomorphic growth of the ternary layers without dislocations or extended defects. Figure 5.1(b) shows the corresponding 3-D APT reconstructed map. The details of APT analysis are given in supplemental material (Appendix B) along with data sets recorded from different layers (Figure S-B1). For cluster analysis, iso-concentration surfaces were first defined at varying Sn and Si concentrations within the reconstructed maps. No evidence of any aggregates was found regardless of the content. The mass spectra of Si, Ge, and Sn, displaying all the isotopes and the evaporated charge states are shown in Figure S-B2 in the supplemental material (Appendix B). In order to

investigate the short-range atomic distribution, we performed a series of statistical analyses, namely the frequency distribution (FD) analysis, the partial radial distribution function (p-RDF) analysis, and the nearest neighbor (NN) analysis within pre-defined regions in 3-D maps. The theoretical formalism of each method is outlined in the supplemental material (Appendix B).

5.5 Results and Discussion

Figure 5.2(a) displays the FD of Si, Ge, and Sn in $Si_{0.04}Ge_{0.84}Sn_{0.12}$. The coefficient of determination ($\mathcal{R}^2$) between the observed value (y_i) and the binomial distribution (f_i) was calculated from the residual sum of squares, $S_{res} = \sum_i (y_i - f_i)^2$ and total sum of squares, $S_{tot} = \sum_i (y_i - \bar{y})^2$ and the relation $\mathcal{R}^2 = 1 - S_{res}/S_{tot}$ with $\bar{y} = {}^1\!/_n \sum_{i=1}^{n} y_i$. The figure shows that the mean values of the experimental FD for Si, Ge, and Sn correspond to 4.0, 84.0 and 12.0 at.%, respectively. This agrees with the concentrations found in the proximity histogram in Figure S-B1(a) in the supplemental material (Appendix B). Additionally, it reveals that while Ge and Sn closely follows the binomial distribution (calculated $\mathcal{R}^2$ for Ge and Sn are 0.9999 and 0.9978 respectively), Si shows a small disagreement with the binomial distribution (calculated $\mathcal{R}^2$ for Si is 0.9679). We eliminate statistical fluctuations as a possible reason for this observed deviation because the probed volume is large enough to have a significant number of Si atoms. In Figure 5.2(b), we show the p-RDF of Sn and Si in $Si_{0.04}Ge_{0.84}Sn_{0.12}$ with respect to (wrt.) Sn, Ge, and Si. It is worthwhile to state that in all analyses carried out for different layers, Ge is always found to be random. Henceforth, we shall restrict our discussion mainly to the behavior of Si and Sn. Also noteworthy is the fact that p-RDF is meaningful only for $r \geq 0.5\ nm$. For $r < 0.5nm$, APT data analysis program does not find any atom and generates random values for p-RDF. The p-RDF's in all the plots for $r < 0.5nm$ has therefore been shaded. The following facts are evident from Figure 5.2(b): Si shows a negative correlation wrt. Sn and a positive correlation wrt. Ge as well as itself; Sn has its p-RDF at unity wrt. Ge and Si while it shows signs of a positive correlation wrt. itself. The p-RDF of Sn and Si wrt. Sn in the top panel in Figure 5.2(b) show a puzzling behavior. First, Sn is seen to have a positive correlation with itself. However, the FD and the NN distribution (later in Figure 5.4) do not give any indication that Sn deviates from a perfect random distribution. Second, the p-RDF's do not converge to unity at large values of r, unlike that in the lower two panels in Figure 5.2(b). We think that this unexpected behavior might be due to minute long-range compositional variations of Sn across the reconstructed APT maps.

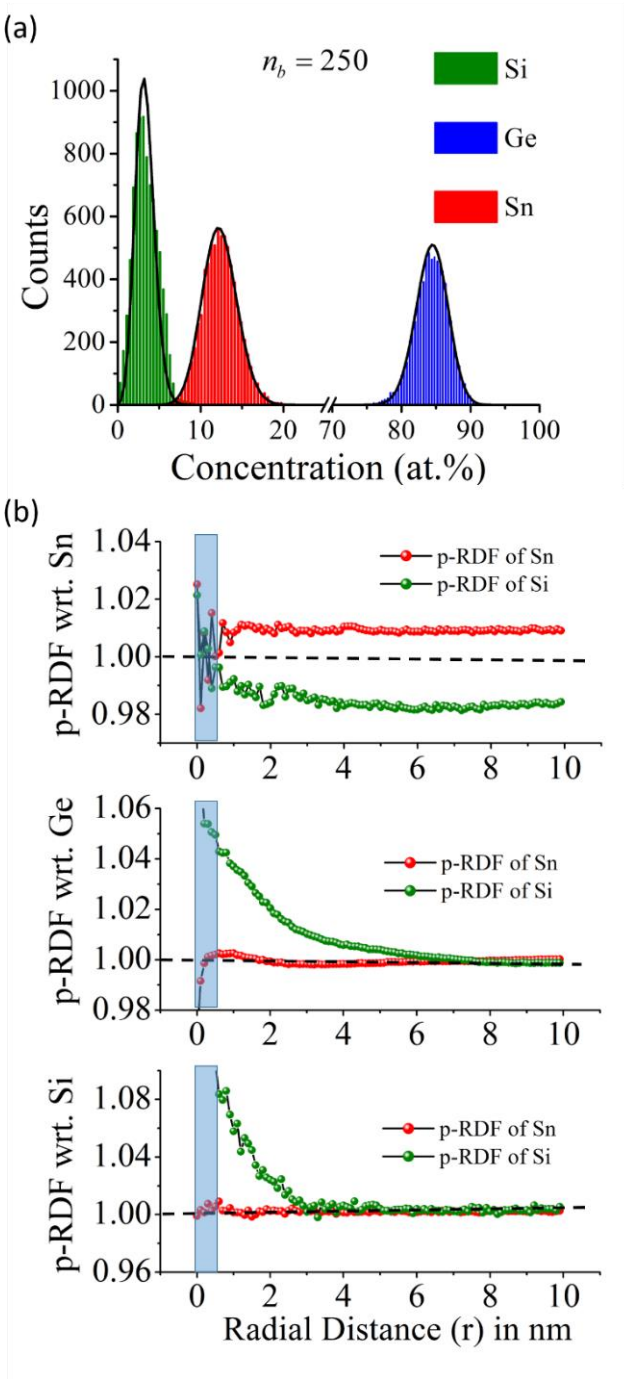

Figure 5.2: *(a) Frequency distribution of Si (green), Ge (blue), and Sn (red) in* $Si_{0.04}Ge_{0.84}Sn_{0.12}$ *as determined from APT reconstruction (in histograms). The corresponding binomial distribution of these atoms are shown in black continuous lines (b) The partial radial distribution function of Sn and Si atoms with respect to Sn (top), Ge (middle), and Si (bottom) in the same sample as in (a) for* $r = 10$ *nm. The Integrated Visualization and Analysis Software (IVAS) computed error bars are smaller than the data symbols. The black dotted line represents* $p - RDF = 1$.

The observations in Figure 5.2 provide clear evidence that Si atoms are disrupted from a perfect random distribution. The negative correlation shown by Si wrt. Sn hints at the presence of a repulsive interaction between the two species. This phenomenon provides new insights into the growth kinetics of metastable alloys by CVD [25], where the growth conditions prevent Sn atoms from forming equilibrium aggregated phase, despite the fact that the growth of a complete monolayer takes place in $\sim 0.1\text{s}$ which is a very slow process compared to the time scale of surface diffusion events. The data presented in Figure 5.2 suggest that the repulsive interaction between Si and Sn is resulting from these elements diffusing away from each other during the growth, justifying the negative correlation of Si wrt. Sn. Note, that the p-RDF's are plotted relative to each other and normalized to the bulk concentration of an element. The repulsive interaction should have a subtle effect on the distribution of Sn and Ge as well, but the p-RDF's of Sn and Ge when plotted wrt. Si do not reflect this behavior due to their higher concentrations wrt. Si. The Si atoms diffusing away from Sn can either hop to other Ge atoms or make a large number of hops to other Si atoms (which are scarce). Hence, we see a positive correlation of Si wrt. Ge and also wrt. itself. Since bulk diffusion is energetically less favorable than surface diffusion, it is reasonable to conclude that the observed departure for an ideal solid solution occurs during the layer-by-layer growth. It is important to note that this phenomenon is peculiar to Sn-rich ternary alloys since extended x-ray absorption fine structure (EXAFS) investigations indicated the atomic distribution in Sn-rich strained and relaxed GeSn binary alloys to be random [202], also asserting the fact that epitaxial strain is not responsible for the observation we made in Figure 5.2.

Interestingly, the analysis of ternary layers with lower Sn contents ($\leq$ 4 at. %) indicates that the aforementioned departure from a perfectly random alloy is either absent or too small to be detected. For instance, Figure 5.3(a) exhibits the FD for each element in $\text{Si}_{0.10}\text{Ge}_{0.875}\text{Sn}_{0.025}$. Noteworthy is the overlap between the observed distribution and the binomial distribution (black lines) assuming a complete random alloy ($\mathcal{R}^2$ was calculated for Si, Ge, and Sn to be 0.9989, 0.9999, and 0.9959, respectively). Figure 5.3(b) shows the measured Sn and Si p-RDF within a sphere of radius 10 nm. Here, the p-RDF of Sn wrt. Sn shows the telltale signature of statistical fluctuations owing to its small concentration of only 2.5 at. %. The p-RDF fluctuates around the mean value of unity with the magnitude of these fluctuations decreasing with increasing *r*. Note that the volume of the shell considered during p-RDF analysis and consequently the number of atoms which lies inside the shell increases as a function of r^2. Finally, the p-RDF of Sn steadies

down to the value of unity. The p-RDF of Si wrt. Si and Sn are qualitatively similar, none showing any noticeable deviation from 1. The p-RDF of Sn wrt. Si, Ge and Si wrt. Ge (Figure S-B3 in the supplemental material in Appendix B) confirm that at low Sn content, all atoms are randomly distributed within the alloy, reinforcing the results of the FD analysis.

Figure 5.4 displays the analysis of NN distribution $NN_{A-A} - k$, where 'A' is Si or Sn; k is 2 (2nd NN), 3 (3rd NN), and 5 (5th NN) for $Si_{0.04}Ge_{0.84}Sn_{0.12}$. Figure 5.4(b) shows the departure of the observed NN distribution from the theoretical value, $P_k(r, C)$. The $NN - 1, 4, 10$ distribution for Si and Sn and their corresponding departure from $P_k(r, C)$ in $Si_{0.04}Ge_{0.84}Sn_{0.12}$ is shown in Figure S-B4 in the supplemental material (Appendix B). Figure 5.4 and Figure S-B4 show that while NN_{Sn-Sn} follow the probability distribution closely, NN_{Si-Si} does not. A shoulder starts to develop at a lower value of r than the maxima of $P_k(r, C)$ in the observed NN_{Si-Si} distribution, which gets more prominent with increasing k. The rest of the measured NN_{Si-Si} distribution shows a minute right shift relative to $P_k(r, C)$. These observed departures are clear indications of a disruption in Si distribution creating local pockets where there are more Si wrt. a given Si atom. In these pockets, the Si concentration is slightly higher than the average bulk concentration making the average distance between the NN's slightly smaller than what is expected theoretically. The minute right shift also indicates that the rest of the matrix is slightly depleted of Si making the NN distances slightly larger than that in a perfect random distribution. The shoulder is obviously absent in $NN_{Si-Si} - 1$ (Figure S-B4(a) in the supplemental material in Appendix B) due to the fact that no atom can be located at a distance smaller than the first nearest neighbor distance. Also noteworthy is the fact that such features are absent in the NN distributions within the alloy with low Sn content of 2.5 at.% (Figure S-B5 in the supplemental material in Appendix B). The deviation shown NN_{Sn-Sn} in Figure S-B5(b) is purely random in nature owing to its small concentration, in contrast to the deviation shown by NN_{Si-Si} in Figure 5.4(b) (a +ve deviation below the maxima of $P_k(r, C)$, a −ve deviation at the maxima of $P_k(r, C)$, followed by a small +ve deviation above the maxima of $P_k(r, C)$). It must however be remembered that the observed deviation of Si in Sn-rich alloys from a perfect random atomic distribution must not be confused with the formation of aggregates [203], [204].

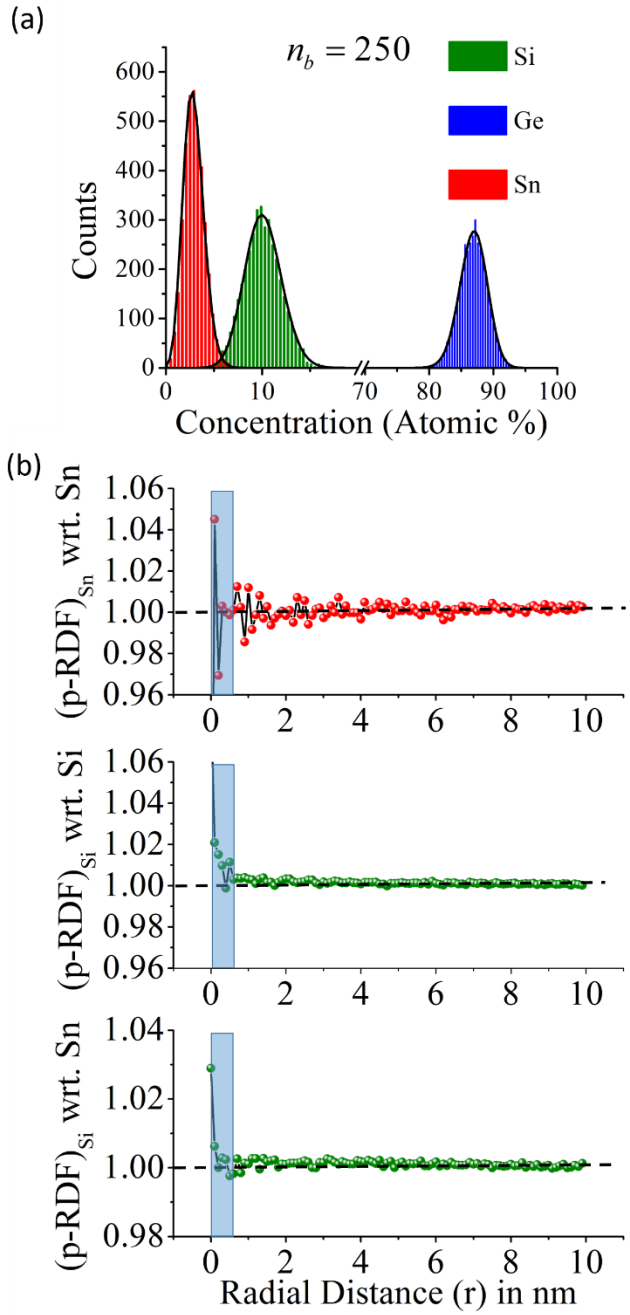

Figure 5.3: *(a) Frequency distribution of Si (green), Ge (blue), and Sn (red) in* $Si_{0.10}Ge_{0.875}Sn_{0.025}$ *as determined from APT reconstruction (in histograms). The corresponding binomial distribution of these atoms are shown in black continuous lines. (b) The partial radial distribution function in the same sample as in (a) for* $r = 10$ *nm of Sn atoms wrt. Sn (top), Si wrt. Si (middle), and Si wrt. Sn (bottom). The IVAS computed error bars are smaller than the data symbols. The black dotted line represents* $p - RDF = 1$.

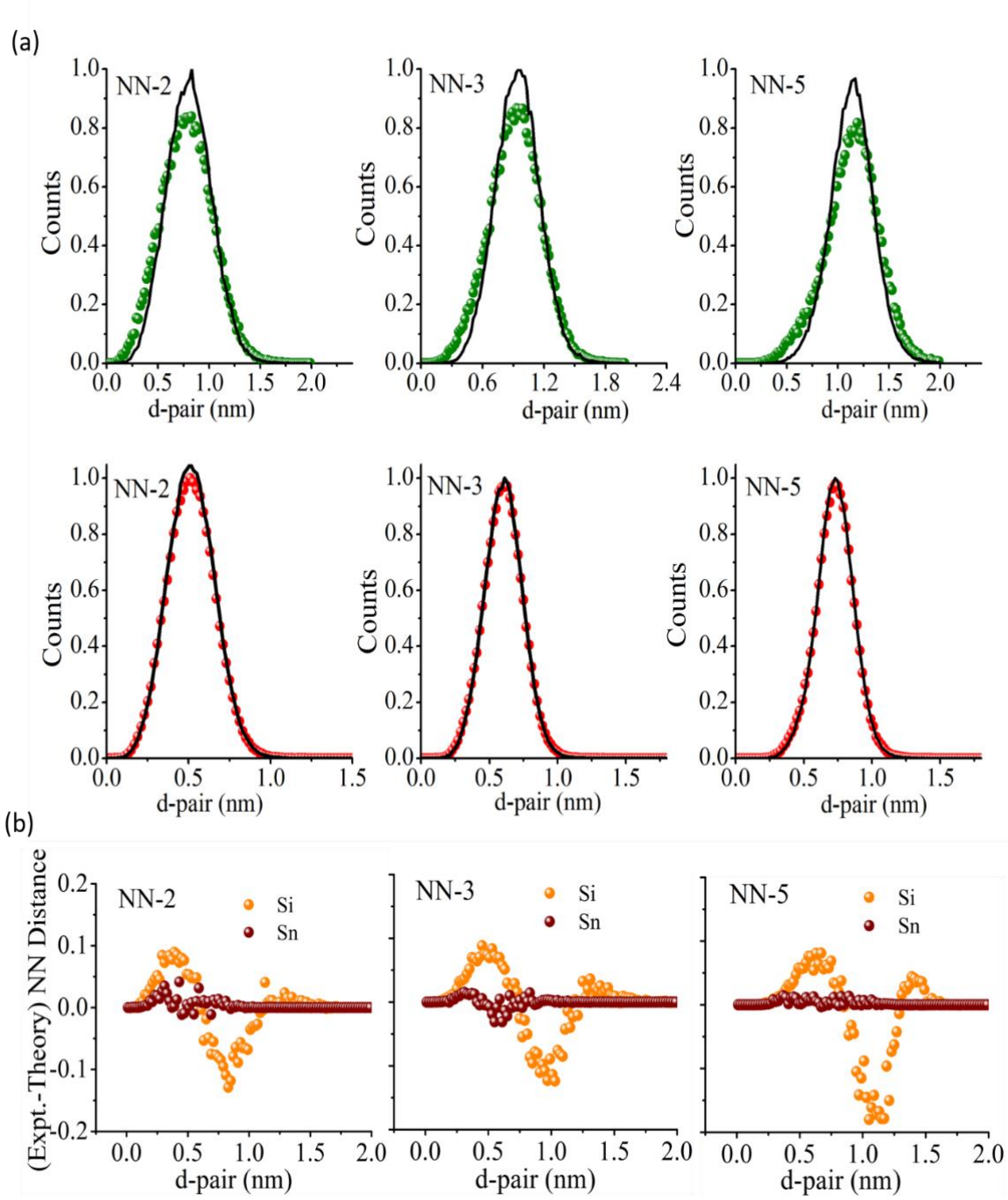

Figure 5.4: *(a) Si-Si and Sn-Sn NN 2, 3, and 5 distribution in the alloy containing 12.0 at.% Sn. The distribution as determined from APT reconstruction are shown in solid spheres: Si (green) and Sn (red). The corresponding binomial distribution are shown in black continuous lines. All the data sets are normalized with respect to the theoretical probability distribution, $P_k(r, C)$. (b) Departure of the observed Si-Si and Sn-Sn NN 2, 3, and 5 distributions from the binomial distribution. The y-axis in all the three figures are the same.*

The revelation that Si atoms in monocrystalline Sn-rich ternary alloys deviate from the behavior in an ideal solid solution is indeed surprising. We attributed this disruption in Si distribution to a repulsive interaction between the Sn and Si atoms. In order to elucidate the energetics of this phenomenon, we performed detailed density functional theory (DFT) calculations using the Quantum Espresso code (details in the supplemental material in Appendix B) on a 32 atom supercell. As shown in Figure S-B7 in the supplemental material in Appendix B, we found that a Si-Sn bond is indeed energetically not favorable requiring an additional energy of $\sim +50-250$ meV/unit cell as compared to the most stable configurations (NN $-$ 3 and NN $-$ 4). A similar observation was made during a recent EXAFS study on SiGeSn ternary alloys [205]. These calculations support qualitatively the hypothesized repulsive interaction between Si and Sn atoms. Here, it is important to notice that the incorporation of a large radius Sn atom in Ge lattice would create a local distortion leading to more compressive Ge regions around Sn. This seems to affect the incorporation of Si, which has a smaller radius, and perhaps prefers to incorporate in available sites far from these compressive regions. What we must remember, however, is that the growth of a metastable alloy is a kinetically controlled non-equilibrium process. Owing to limited mobility, atoms after deposition on the surface are inhibited to reach the equilibrium state within the growth time-scale. The problem therefore reduces to a surface process where one needs to evaluate how atoms behave at the surface before they become buried underneath the next growing layer. Herein, one can reasonably neglect bulk diffusion as it implies energy barriers that are significantly higher than those for surface diffusion. One can also intuitively assume that, once atoms are deposited on a surface, the system will begin to evolve to minimize the mixing enthalpy ΔH_{mix} in an effort to reduce its Gibbs free energy. This evolution is abruptly brought to an end after the next growing layer sweeps across the entire surface. Since Ge is the solvent and Si and Sn are solutes, the mixing enthalpy ΔH_{mix} is given by: $\Delta H_{mix} = H_{alloy} - xH_{Si} - (1-x-y)H_{Ge} - yH_{Sn}$. With the mole fractions and the enthalpies of the pure elements (H_{Si}, H_{Ge}, H_{Sn}) predetermined, H_{alloy} becomes a determining parameter. H_{alloy} is affected by factors like epitaxial strain, micro-strain, and chemical interaction. Micro-strain arises when the lattice has to accommodate two atoms of dissimilar size yet maintaining a uniform lattice constant throughout the crystal. For example, with $\mathcal{N}$ the total number of atoms and Ω_{Si-Sn} the Si-Sn interaction parameter, the micro-strain contribution coming from Si-Sn bonds in a regular solution is given by $\mathcal{N}\Omega_{Si-Sn}(xy)$. Unlike the epitaxial strain and the micro-strain whose contribution to H_{alloy} is always positive, the chemical interaction

contribution (ΔH_{Ch}) to H_{alloy} can be positive or negative. This depends on the nature of charge transfer between two atoms forming a bond. For example, calculations showed that in ordered $GaInP_2$, the difference in electronegativity between the atoms causes charge to flow from the less ionic $Ga-P$ bond to the more ionic $In-P$, giving a small positive value of ΔH_{Ch} [180]. The process of charge transfer takes place not only for bonding atoms which belong to different groups (hence different electronegativity) but also for isovalent heteropolar atoms like the group IV elements. Indeed, first-principles calculations found a small positive and a small negative value of ΔH_{Ch} for SiGe and SiC respectively [206].

5.6 Summary

In summary, we performed atomic scale studies on Sn-rich metastable SiGeSn ternary alloys using APT. To investigate the randomness in the distribution of different atoms within the alloys, we implemented different statistical techniques, namely the FD, p-RDF, and the NN distribution. Our study shows that the Si atoms deviate from a perfectly random solid solution within the alloy with large Sn content. The phenomenon is attributed to a repulsive interaction between Sn and Si, thereby inducing local disruptions in an otherwise random distribution of Si. The DFT calculations also demonstrated that having Si and Sn atoms as nearest neighbors is indeed energetically unfavorable. These departures from an ideal solid solution shown by Si is either absent or too weak to be detected in alloys with low Sn content (< 4 at. %). The observed short range ordering must be taken into account for a more accurate evaluation of lattice parameter, lattice relaxation, thermodynamic parameters, band structure, and opto-electronic properties of group IV ternary semiconductors.

5.7 Acknowledgement

The work was supported by NSERC-Canada, Canada Research Chair, Calcul Québec, and Compute Canada. The LEAP at the Northwestern University Center for Atom-Probe Tomography (NUCAPT) was acquired and upgraded with equipment grants from the MRI program of the National Science Foundation (grant number DMR-0420532) and the DURIP program of the Office of Naval Research (grant numbers N00014-0400798, N00014-0610539, N00014-0910781). NUCAPT is supported by the NSF's MRSEC program (grant number DMR-1121262).

CHAPTER 6 ARTICLE 3: PHONON ENGINEERING IN ISOTOPICALLY DISORDERED SILICON NANOWIRES

This article has been published in Nano Letters (Nano Lett., 2015, 15 (6), pp 3885–3893; DOI: 10.1021/acs.nanolett.5b00708; Publication Date (Web): May 20, 2015). The article discusses the effect of isotopic disorder on the phonon properties of Si NWs. The supporting information of this article is given in Appendix C of the thesis.

6.1 Authors

S. Mukherjee,[†] U. Givan,[‡] S. Senz,[‡] A. Bergeron,[†] S. Francoeur,[†] M. de la Mata,[§,Δ] J. Arbiol,[§,#,Δ] T. Sekiguchi,[‖] K. M. Itoh,[‖] D. Isheim,[¥] D. N. Seidman,[¥] and O. Moutanabbir[,†]

[†] *Department of Engineering Physics, Polytechnique Montréal, C. P. 6079, Succ. Centre-Ville, Montréal, Québec H3C 3A7, Canada*

[‡] *Max Planck Institute of Microstructure Physics, Weinberg 2, D 06120 Halle (Saale), Germany*

[§] *Institut de Ciencia de Materials de Barcelona, ICMAB-CSIC, Campus de la UAB, 08193 Bellaterra, Catalonia, Spain*

[#] *Institució Catalana de Recerca i Estudis Avançats (ICREA), 08010 Barcelona, Catalonia, Spain*

[‖] *Department of Applied Physics and Physico-Informatics, Keio University, Hiyoshi, Yokohama, Japan*

[¥] *Department of Materials Science and Engineering, Northwestern University Center for Atom Probe Tomography, Northwestern University, Evanston, IL 60208-3108, USA*

[Δ] *Institut Català de Nanociència i Nanotecnologia, ICN2, Campus UAB, 08193 Bellaterra, Catalonia, Spain*

6.2 Abstract

The introduction of stable isotopes in the fabrication of semiconductor nanowires provides an additional degree of freedom to manipulate their basic properties, design an entirely new class of devices, and highlight subtle but important nanoscale and quantum phenomena. With this perspective, we report on phonon engineering in metal catalyzed silicon nanowires with tailor-made isotopic compositions grown using isotopically enriched silane precursors $^{28}SiH_4$, $^{29}SiH_4$,

and $^{30}SiH_4$ with purity better than 99.9%. More specifically, isotopically mixed nanowires $^{28}Si_x{}^{30}Si_{1-x}$ with a composition close to the highest mass disorder (x ~ 0.5) were investigated. The effect of mass disorder on the phonon behavior was elucidated and compared to that in isotopically pure ^{29}Si nanowires having a similar reduced mass. We found that the disorder-induced enhancement in phonon scattering in isotopically mixed nanowires is unexpectedly much more significant than in bulk crystals of close isotopic compositions. This effect is explained by a non-uniform distribution of ^{28}Si and ^{30}Si isotopes in the grown isotopically mixed nanowires with local compositions ranging from $x \sim 0.25$ to 0.70. Moreover, we also observed that upon heating phonons in $^{28}Si_x{}^{30}Si_{1-x}$ nanowires behave remarkably differently from those in ^{29}Si nanowires suggesting a reduced thermal conductivity induced by mass disorder. Using Raman nanothermometry, we found that the thermal conductivity of isotopically mixed $^{28}Si_x{}^{30}Si_{1-x}$ nanowires is ~30% lower than that of isotopically pure ^{29}Si nanowires in agreement with theoretical predictions.

Keywords: Nanowires; stable isotopes; phonons; thermal conductivity; Raman spectroscopy; atom probe tomography.

6.3 Introduction

Isotope engineering in semiconductors, which refers to controlling the content of each stable isotope within a lattice, has been a powerful paradigm to investigate and manipulate some of the important physical properties of semiconductors and exploit them in innovative device structures [5], [7], [54], [64], [207]–[215]. Isotopes of an element differ in the number of neutrons in the nucleus. This creates differences between the isotopes in their lattice dynamics and nuclear properties. For instance, the slight difference in zero-point motion leads to a difference in atomic volume between the isotope atoms, which influences the lattice constant [5]. Also, the difference in electron-phonon coupling between crystals of different isotopic composition was found to affect the electronic band gap [209]. The nuclear spin is another significant difference between stable isotopes. For instance, natural silicon (Si) has three stable isotopes: ^{28}Si , ^{29}Si , and ^{30}Si , with isotopic abundances of 92.23, 4.67, and 3.10 at.%, respectively. Among these three isotopes, only ^{29}Si has a nuclear spin of $1/2$, whereas ^{28}Si and ^{30}Si are nuclear spin-free. This property has been crucial in the realization of Si-based quantum information devices [7], [210]–[212]. One of the most drastic isotope related effect in semiconductors is found in phonon properties [54], [64], [213]–[215]. Mass fluctuation induced by isotope disorder acts as a substitutional defect in a crystal

thus affecting the phonon mean free path and consequently the phononic thermal conductivity. Measurements on isotopically pure Ge [54] and Si [213] crystals showed an enhanced thermal conductivity as compared to their natural counterparts. Also, lower thermal conductivity was recently demonstrated in Si isotope superlattices [64].

All the aforementioned properties of semiconductor stable isotopes have been investigated and exploited in bulk materials or thin films. Indeed, conspicuously missing are experimental investigations of the influence of stable isotope *impurities* on the basic characteristics of nanoscale materials despite the crucial information they could provide concerning their physical properties. Interestingly, there have been only a few theoretical studies on the influence of the isotopic content on basic phonon-related properties of Si nanowires (NWs) [9], [10]. For instance, molecular dynamics (MD) simulations suggested that the thermal conductivity of Si NWs is reduced exponentially by isotopic impurities at room temperature [9], [10]. In the MD research, the simulated thermal conductivity of a $^{28}Si_{0.5}{}^{30}Si_{0.5}$ NW yields ~80% of that of a isotopically pure ^{28}Si NW. Also for a $^{28}Si/^{29}Si$ multilayer NW with a 1.09 nm period, the calculated thermal conductivity was found to be ~70% of that of isotopically pure ^{28}Si NW [9]. Other calculations demonstrate an improvement of more than 25% in thermoelectric figure of merit of $^{28}Si_{0.5}{}^{29}Si_{0.5}$ NWs as compared to ^{28}Si NWs [10]. No experiments have, however, been conducted to elucidate these effects. With this perspective, we report in this work the first experimental investigation of the influence of isotope disorder on the phonon behavior in isotopically engineered Si NWs.

6.4 Experiments

The growth of NWs was carried out using the classical gold (Au) catalyzed vapor phase epitaxy using monoisotopic silane $^{28}SiH_4$, $^{29}SiH_4$, and $^{30}SiH_4$ with isotopic purity higher than 99.9%. These precursors were synthesized through the hydrogenation of isotopically enriched SiF_4 [216]. The growth conditions are provided in the supplementary information (Appendix C). Figure 6.1(a) illustrates the schematics of the two sets of nanowires investigated in this work. The samples consist of isotopically pure ^{29}Si NWs and isotopically mixed $^{28}Si_x{}^{30}Si_{1-x}$ NWs. The former were grown by injecting the monoisotopic $^{29}SiH_4$ precursor, whereas for the latter $^{28}SiH_4$ and $^{30}SiH_4$ were simultaneously introduced in the growth chamber. The control of the content of each isotope in the growing isotopically mixed NWs was achieved through the control of the partial pressures of the two precursors. The low magnification SEM images (taken at a tilt of 60º) of the

$^{28}Si_x{}^{30}Si_{1-x}$ NWs and ^{29}Si NWs are displayed in the inset of Figure 6.1(a). The grown NWs are typically 5 μm-long with a diameter in the $30 - 100$ nm range. Figure 6.1(b) shows the scanning transmission electron microscope (STEM) image of a ^{29}Si NW. The NW has grown in the [121] direction and the image is taken from $[1\bar{1}1]$ Si zone axis. The SEM analysis indicates that, while the majority of ^{29}Si NWs have grown along the [111] direction, a few have actually grown at an angle of ~19.5º with respect to the [111] direction, corresponding to the $[121]$ crystallographic direction. It is noticeable that the NW surface is decorated with Au clusters mainly near the tip of the NW. This is attributed to Au diffusion from the catalyst droplet along the NW sidewalls during the quenching to room temperature after growth interruption [217], [218]. The high magnification STEM image of the NW included in Figure 6.1(b) and the power spectrum (fast Fourier transform (FFT)) in the inset show that the grown NWs are of the highest crystalline quality. The STEM analysis of the $^{28}Si_x{}^{30}Si_{1-x}$ NWs (not shown here) confirms that the two sets of NWs have identical structural and morphological properties.

Raman spectroscopy was employed to investigate the vibrational properties of these NWs. To enable the analysis of individual NWs, the as-grown NWs were first transferred onto Au-capped Si to suppress the background signal from the underlying substrate during subsequent Raman analysis. Backscattering micro-Raman experiments were carried using two laser lines, the 488 nm (low power measurements) and 514 nm (high power measurements) lines at incident power densities in the range of $0.08 – 11.76$ mW/μm^2 (see supplementary information in Appendix C for more details). The average length of the NWs after dispersion on Au was found to be on the order of 2 to 3 μm. All Raman measurements were performed on single NW that are in an excellent thermal contact with Au layer (Figure 6.1(c)). Clustered and suspended NWs were avoided in this analysis as they heat up faster when exposed to laser beam, which influences their Raman modes [219]. Figure 6.2 shows the Si-Si LO phonon spectra of a single $^{28}Si_x{}^{30}Si_{1-x}$ NW and a ^{29}Si NW at different incident laser power densities. A detailed comparison of Raman spectra of $^{28}Si_x{}^{30}Si_{1-x}$ and ^{29}Si single NWs at low power regime is provided in Figure S-C1 (supplementary information in Appendix C). Note that all effects related to phonon confinement are excluded here as the diameter of the investigated NWs is larger than the phonon mean free path in Si around room temperature. Recorded spectra were fitted with Voigt line profiles to extract peak positions and full width at half maximum (FWHM).

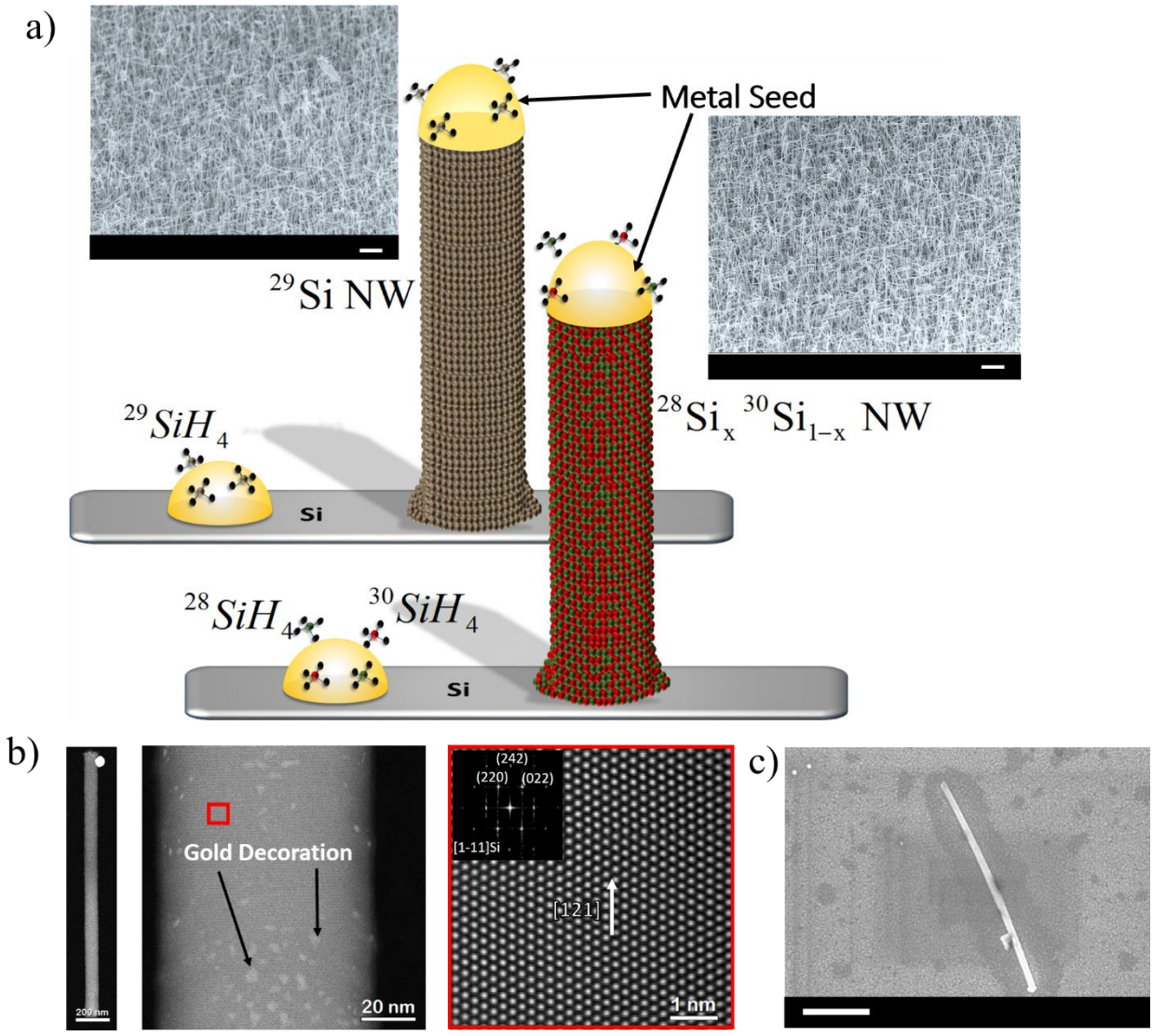

Figure 6.1: *(a) A schematic illustration of the VLS growth of the isotopically engineered Si NWs. Vapor phase precursors are supplied to Au-Si eutectic droplet. For the isotopically pure NWs the precursor is $^{29}SiH_4$ (purity 99.9%) and for the isotopically mixed NWs, a mixture of $^{28}SiH_4$ (purity 99.99%) and $^{30}SiH_4$ (purity 99.9%) was injected. Crystallization of Si atoms from the supersaturated droplet takes place at the droplet-nanowire interface which becomes the growth front. Inset: Low magnification SEM images of as grown isotopically mixed $^{28}Si_x{}^{30}Si_{1-x}$ NWs and isotopically pure ^{29}Si NWs, both recorded at a tilt angle of 60º. The scale bars in both the figures denote 1μm. (b) STEM images of the isotopically pure ^{29}Si NWs. Left: A single ^{29}Si NW. The NW has grown along the [121] direction and the image taken from the [1-11] Si zone axis. The scale bar in the figure is 200nm. Middle: STEM image of the NW sidewalls showing gold decoration on*

the facets. The scale bar in the figure is 20nm. Right: High magnification STEM image (taken from the region marked by the red box in the middle image) and the power spectrum (fast Fourier transform (FFT)) in the inset shows the high crystalline quality of the NW. The scale bar in the figure corresponds to 1nm. (c) SEM image of a single ^{29}Si NW after sonication and dispersion atop Au capped Si substrate. The scale bar denotes 1μm.

6.5 Results and Discussion

A first analysis of the data is based on the quasi-harmonic approximation, which is a valid approximation for semiconductors at room temperature [83]. Herein, it is important to minimize the excess local heating of the NWs, which would occur when the incident laser power is sufficiently high. Hence, all calculations involving the quasi-harmonic approximation were carried out on data sets recorded at the lowest incident power density of $0.08\ \mathrm{mW/\mu m^2}$, at which the local temperature of the NWs is confirmed to be equal to the ambient temperature of 300K (see the supplementary information in Appendix C). A close inspection of the spectra exhibited in Figure 6.2 shows two separate phonon related effects. First, at all incident laser powers, the Raman spectrum for $^{28}Si_x{}^{30}Si_{1-x}$ NWs is always broader and red shifted as compared to the spectrum of ^{29}Si NWs. Second, regardless of the type of the NW, as the incident power increases, all peaks broaden and gets red-shifted. This effect is due to laser-induced heating of the NWs. Figure 6.3 depicts the evolution of the average peak position and the evolution of the average FWHM with incident power density for both $^{28}Si_x{}^{30}Si_{1-x}$ and ^{29}Si NWs. Figures 6.3(a) and (b) displays the data recorded at low laser power densities averaged over a large number (> 10 of single NWs). High power measurements are given in Figures 6.3(d) and (e). The peak position and FWHM of 4-5 individual $^{28}Si_x{}^{30}Si_{1-x}$ and ^{29}Si NWs, as extracted from the Voigt fit of the raw data, at both low and high power levels are displayed in Figure S-C2 and C3 (supplementary information in Appendix C). Interestingly, both the broadening and the red shift are found to be more pronounced for $^{28}Si_x{}^{30}Si_{1-x}$ NWs. For instance, the average peak position within the laser power range investigated varies by about 4 cm^{-1} for $^{28}Si_x{}^{30}Si_{1-x}$ NWs as compared to ~1 cm^{-1} for ^{29}Si NWs. This indicates that the two types of NWs react differently to local heating induced by laser.

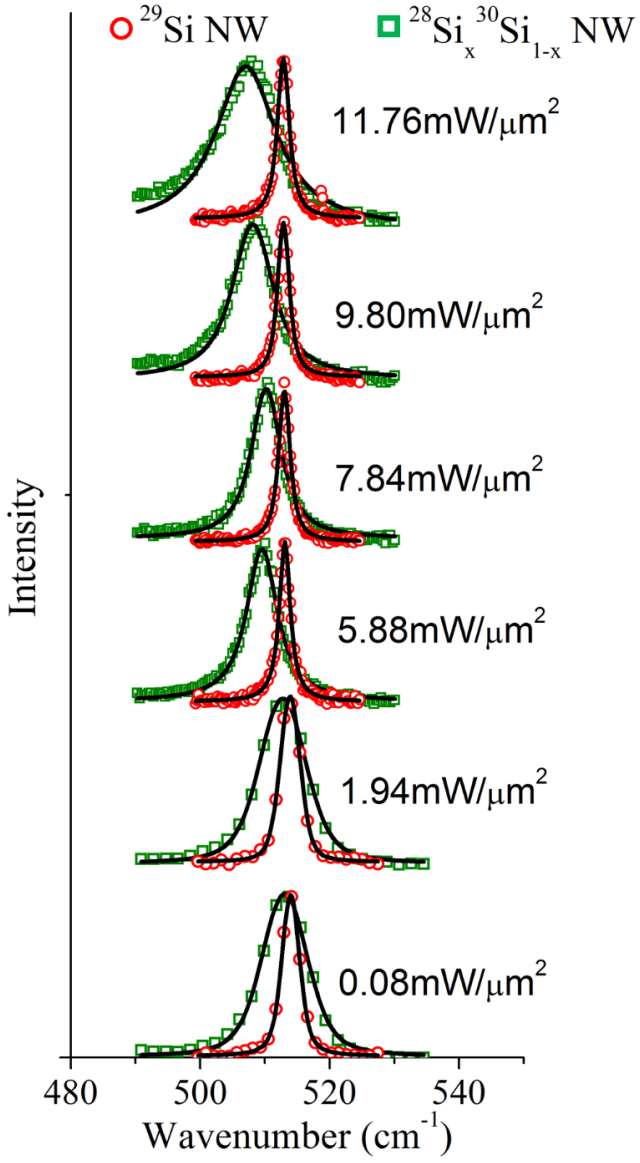

Figure 6.2: *Si-Si LO normalized phonon spectra of a $^{28}Si_x{}^{30}Si_{1-x}$ NW and a ^{29}Si NW at different incident laser power densities. The spectra at 1.94 mw/μm^2 and 0.08 mw/μm^2 were recorded using the 488nm laser and the remaining spectra using the 532nm laser. The spectra shown here are representative of a single $^{28}Si_x{}^{30}Si_{1-x}$ NW and a single ^{29}Si NW. The data points for the $^{28}Si_x{}^{30}Si_{1-x}$ NW are shown as empty green squares and that of the ^{29}Si NW correspond to empty red circles. The black continuous curve corresponds to the Voigt fit.*

In the following, we elucidate the origin of the remarkable changes in Raman spectra as a function of the NW isotopic content. According to the Virtual Crystal Approximation (VCA), a simple harmonic analysis predicts that the energy of a phonon mode is inversely proportional to the square root of the average isotopic mass [207] $-\ \omega_{Phonon} \propto \sqrt{1/\langle m \rangle}$. Here $\langle m \rangle$ is the average isotopic mass given by $\langle m \rangle = \sum_i c_i m_i$, with c_i being the fractional composition of an isotope of mass m_i. Using the ratio of the average peak position at the lowest incident power density of $0.08\ \mathrm{mW/\mu m^2}$ (Figure 6.3(a)) and the known value of $\langle m \rangle_{29-\mathrm{Si}}$, we computed $\langle m \rangle_{\mathrm{Iso-Mix}} = 29.05\ \mathrm{amu}$. Thus, the corresponding fractional composition of ^{28}Si in the isotopically mixed NWs is $x = 0.47 \pm 0.07$ calculated from the known values of $\langle m \rangle_{28-\mathrm{Si}}$ and $\langle m \rangle_{30-\mathrm{Si}}$ in the identity: $\langle m \rangle_{\mathrm{Iso-Mix}} = x.\langle m \rangle_{28-\mathrm{Si}} + (1-x).\langle m \rangle_{30-\mathrm{Si}}$. Note that composition calculated employing the quasi-harmonic approximation is always an average estimate. In Figure 6.3(a), the shift rate of the average peak position with power density up to 5-6 $\mathrm{mW/\mu m^2}$ is only slightly higher for $^{28}\mathrm{Si_x}^{30}\mathrm{Si_{1-x}}$ NWs as compared to ^{29}Si NWs (the corresponding slopes of the dotted lines are 0.38 and 0.30 $\mathrm{cm^{-1}\mu m^2/mW}$, respectively). At higher power densities, the behavior of $^{28}\mathrm{Si_x}^{30}\mathrm{Si_{1-x}}$ NWs is markedly different from ^{29}Si NWs with the average phonon frequency of the former undergoing a drastic red shift as compared to the latter (Figure 6.3(d)). The evolution of FWHM follows the same trend as the shift in phonon frequency. Below $\sim 6\ \mathrm{mW/\mu m^2}$, the average FWHM of $^{28}\mathrm{Si_x}^{30}\mathrm{Si_{1-x}}$ NWs and ^{29}Si NWs evolve qualitatively similarly with incident power density. At all incident power densities, the spectra of $^{28}\mathrm{Si_x}^{30}\mathrm{Si_{1-x}}$ NWs are always broader than that of ^{29}Si NWs. This can be also verified from the respective spectra displayed in Figure 6.2. At low and mid power ranges, the average FWHM of the former is about $3 - 3.5\ \mathrm{cm^{-1}}$ broader than the latter. A detailed discussion on the origin of this effect will be presented later in the text. As it can be seen in Figure 6.3(e), at high power regime the spectra of $^{28}\mathrm{Si_x}^{30}\mathrm{Si_{1-x}}$ NWs start to broaden much *rapidly* as compared to ^{29}Si NWs. The difference in absolute values of the average FWHM between Figures 6.3(b) and (e) comes simply from the difference in spectral resolution between the two setups (supplementary information in Appendix C).

The red shift in peak position and broadening of Raman spectra with increasing power densities are indicative of how the NWs are reacting to laser-induced heating. From Figure 6.3, it can be seen that the behavior of the two types of NWs only show slight differences at low power, but at high power $^{28}\mathrm{Si_x}^{30}\mathrm{Si_{1-x}}$ NWs are much more affected than ^{29}Si NWs. A convenient way

to quantify this heating effect is to extract the NWs local temperature. Herein, an estimate of the effective local temperature is made from the shift in average peak position with the incident laser power. The peak position of a NW, $\Omega(T)$, at a temperature T, is given by [38] $\Omega(T) = \omega_0 + \Pi'(T)$, where ω_0 is the peak position at 0K and $\Pi'(T)$ is the shift of peak position at T, given by:

$$\Pi'(T) = \mathcal{C}\left[1 + \frac{2}{e^{\hbar\omega_0/2k_BT} - 1}\right] + D\left[1 + \frac{3}{e^{\hbar\omega_0/3k_BT} - 1} + \frac{3}{\left(e^{\hbar\omega_0/3k_BT} - 1\right)^2}\right] \quad (6.1)$$

where $\mathcal{C}$ and D are constants. The first term is related to three-phonon anharmonic interaction and the second term represents the four phonon interaction. The probability of the latter being small, we can reasonably neglect it to be left with the first term in the right hand side of equation (6.1). Balkanski et *al*. calculated the phonon frequency for ^{Nat}Si at 0 K [38], $\omega_0^{\mathrm{Nat-Si}} = 529\ \mathrm{cm}^{-1}$ (using only the three phonon process). By taking into account the change in the reduced mass, we calculate $\omega_0^{\mathrm{Iso-Mix}}$ (for the $^{28}\mathrm{Si_x}^{30}\mathrm{Si}_{1-x}$ NWs) and $\omega_0^{29-\mathrm{Si}}$ (for the ^{29}Si NWs) to be 519.80 cm^{-1} and 520.81 cm^{-1}, respectively. $\mathcal{C}$ was estimated from the data recorded at the lowest laser power density ($0.08\ \mathrm{mW/\mu m^2}$) corresponding to a temperature of 300 K. Next, $\Pi'(T)$ was calculated from Figures 6.3(a) and (b) for different incident power densities and the NWs local temperature was then estimated as displayed in Figures 6.3(c) and (f). The plots reveal that $^{28}\mathrm{Si_x}^{30}\mathrm{Si}_{1-x}$ NWs are getting slightly more heated up as compared to ^{29}Si NWs in the low power density regime ($< 6\ \mathrm{mW/\mu m^2}$), the temperature of the former is higher by $\sim 10 - 15$K at 1.94 $\mathrm{mW/\mu m^2}$ and $\sim 25 - 30$K at 5.88 $\mathrm{mW/\mu m^2}$ as compared to the latter. However, at the highest power of 11.76 $\mathrm{mW/\mu m^2}$ the difference in temperatures is quite significant. Indeed, the temperature of $^{28}\mathrm{Si_x}^{30}\mathrm{Si}_{1-x}$ NWs is almost 120K higher than that of ^{29}Si NWs. At low power regime, the rate of increase of temperature with increasing laser power, $\Delta T/\Delta P$ for $^{28}\mathrm{Si_x}^{30}\mathrm{Si}_{1-x}$ NWs is ~ 1.30 times that of ^{29}Si NWs and becomes ~ 6 times in the high power regime ($6 - 12\ \mathrm{mW/\mu m^2}$).

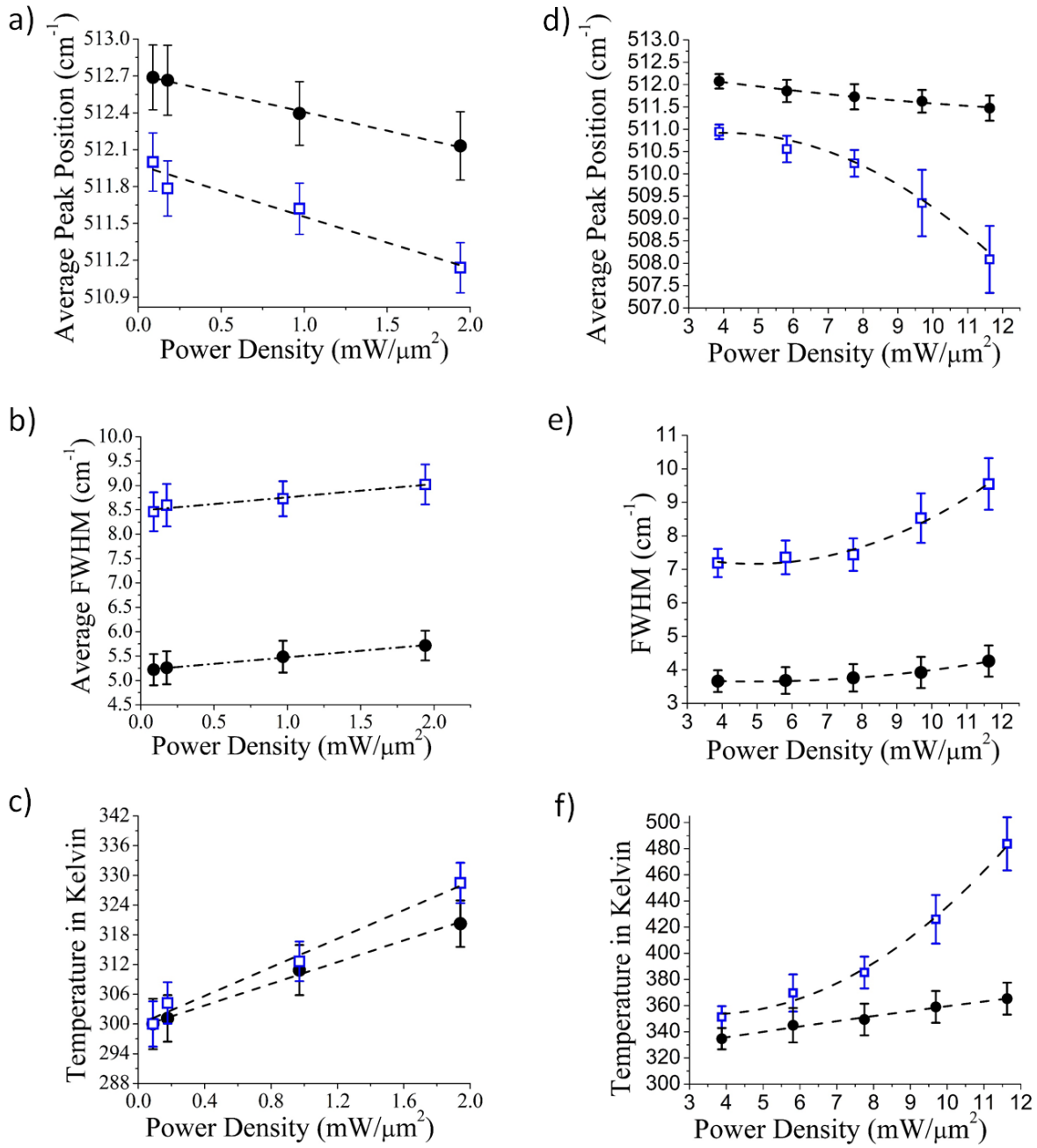

Figure 6.3: *(a) and (b) represent measurements using 488nm laser at low incident power density whereas (d) and (e) represent measurements using 532nm laser at high incident power density. In all figures, the empty blue squares correspond to the isotopically mixed $^{28}Si_x{}^{30}Si_{1-x}$ NWs and the filled black circles represent the isotopically pure ^{29}Si NWs. (a) and (d): Evolution of average peak position with incident laser power density for both $^{28}Si_x{}^{30}Si_{1-x}$ NWs and ^{29}Si NWs. (b) and (e): Evolution of the average FWHM with incident laser power density for both $^{28}Si_x{}^{30}Si_{1-x}$ NWs and*

^{29}Si NWs. In (a) and (b) the averaging was done over measurements on more than 10 single NWs and in (d) and (e) the averaging was done over measurements on 7 single NWs. The error bars in (a), (b), (d), and (e) are double the standard deviation of the peak position and FWHM from respective average values. (c) and (f): Plots of the effective local temperature of the NWs extracted from the shift in average peak position in (a) and (d) respectively. The error bars represent the uncertainty in the calculated temperature due to the standard deviation of the measured peak position. The dotted lines in (a) - (f) are guides to the eye.

To evaluate the change in thermal conductivity between the two sets of NWs, which led to the result described above, we used Raman nanothermometry [220], [221] in conjunction with a heat transport model. This model draws its basis from the assumptions that the region of a NW exposed to laser acts as the heat source and that the major portion of the generated heat is dissipated by conduction along the NW growth axis and at the NW-Au interface (Figure S-C4 and its associated discussion in the supplementary information in Appendix C). Around 300K, based on the rate of increase of temperature, we estimated the ratio of thermal conductivities of ^{29}Si NWs to $^{28}Si_x{}^{30}Si_{1-x}$ NWs ($\kappa_{Si-29}/\kappa_{Iso-Mix}$) to be ~1.30. This means there is a ~30% decrease in $\kappa_{Iso-Mix}$ as compared to κ_{Si-29}. Interestingly, this value is close to the theoretical prediction of 30% reduction in case of $^{28}Si_{0.5}{}^{30}Si_{0.5}$ bulk alloys as compared to ^{Nat}Si at room temperature [222], but it is slightly higher than ~20% reduction predicted for $^{28}Si_{0.5}{}^{29}Si_{0.5}$ NW as compared to ^{28}Si NW at 300K [9]. It is also noteworthy that the observed mass disorder-induced change in Si NW thermal conductivity is lower than the 50% reduction demonstrated for $^{12}C_{0.5}{}^{13}C_{0.5}$ graphene as compared to purified ^{13}C graphene [65]. For Si NWs, Yang and co-workers predicted that at room temperature a much significant reduction in thermal conductivity up to ~70% can be achieved when a ^{28}Si NW is mixed at 50% with ^{42}Si atoms [9]. However, ^{42}Si being radioactive with a half-life of ~13 ms cannot obviously be implemented for any practical purpose. Note that the ratio of thermal conductivity was specifically calculated in the low power regime because the fluctuations in the measured peak position of different $^{28}Si_x{}^{30}Si_{1-x}$ NWs at high power regime are very large (Figure S-C2 I(b), in in the supplementary information in Appendix C) thus making the estimation of the temperature of $^{28}Si_x{}^{30}Si_{1-x}$ NWs fraught with large uncertainties.

Although our experimental data are consistent with early theoretical predictions, isotope mixing alone cannot explain all the observed differences in phonon properties between isotopically disordered and pure NWs. In Figure 6.3(b), the FWHM of $^{28}Si_x{}^{30}Si_{1-x}$ NWs is consistently larger by almost $3-3.5\ \mathrm{cm}^{-1}$ at all incident power compared to the ^{29}Si NWs. As phonon confinement is excluded here, broadening of a Raman spectrum occurs due to scattering of phonons. In general, greater the broadening of a Raman line, greater is the rate of phonon scattering in the material. At a first glance, it appears that excess broadening is due to the sole effect of scattering of phonons from the mass disorder, but our analysis suggests that this contribution alone is not sufficient. Herein, in order to quantify the effect of mass disorder, we first compare our data with the results of Raman measurements on isotopically engineered bulk samples [30]. In those studies, Cardona and co-workers measured bulk Si samples of different isotopic composition. The Raman spectra of a material has a slight dependence on the excitation wavelength [223], but at low incidence power this dependence can be neglected. We focus mainly on bulk $^{28}Si_{0.5}{}^{30}Si_{0.5}$ sample as it has almost the same average isotopic composition as our isotopically mixed NWs and hence nearly the same mass variance, g_2, which is given by:

$$g_2 = \frac{\sum_i c_i m_i^2 - (\sum_i c_i m_i)^2}{(\sum_i c_i m_i)^2} = \frac{\langle m^2 \rangle - \langle m \rangle^2}{\langle m \rangle^2} \qquad (6.2)$$

There are various scattering mechanisms for phonons in a material. The first is the anharmonic scattering of a zone-center phonon into two or three phonons with larger wave vector and smaller energy. Anharmonic scattering increases with temperature and at a given temperature the rate of anharmonic scattering of phonons is inversely proportional to the average isotopic mass [30]. The second is the isotope scattering of phonons which is proportional to g_2 [31]. The third is the Umklapp scattering of two phonons, which produces a third phonon outside the 1st Brillouin zone. Umklapp scattering becomes important for temperatures above the Debye temperature, which is 645K for Si [224]. Thus, this scattering is irrelevant in our case as the temperature of the analyzed NWs remains significantly below this temperature (Figure 6.3). The fourth is the surface scattering of phonons, which is also temperature independent but depends inversely on the size of the material under consideration [225]. Surface scattering can be neglected for bulk materials but not for NWs. The fifth is the Fano scattering, which is the scattering of phonons from thermally generated electron hole pairs [226]. Since Fano scattering is significant only at high levels of

carrier injection, it can be neglected for intrinsic Si NWs investigated in this work. This leaves us with just two scattering mechanisms in bulk samples, the anharmonic scattering and scattering from isotope disorder. We extracted from Ref [30] that for the bulk $^{28}Si_{0.5}{}^{30}Si_{0.5}$ sample, $\Delta_{Anhrm}^{Iso-Mix\ Bulk}$, the contribution of anharmonic scattering of phonons and $\Delta_{Isotope}^{Iso-Mix\ Bulk}$, the contribution of isotope scattering of phonons to the total line broadening at $T = 6K$ are about 1.16 $cm^{-1}$and 0.065 cm^{-1}, respectively. We extrapolated $\Delta_{Anhrm}^{Iso-Mix\ Bulk}$ to $T = 300K$, using the following equation [38]:

$$\Delta_{Anhrm}(T) = A\left[1 + \frac{2}{e^{\hbar\omega_0/2k_BT} - 1}\right] \qquad (6.3)$$

Similar to equation (6.1), we have neglected the four phonon interaction and normalized the data for $\Delta_{Anhrm}^{Iso-Mix\ Bulk}$ at $T = 6K$ to find the constant A. ω_0 for the bulk $^{28}Si_{0.5}{}^{30}Si_{0.5}$ sample was calculated by the same approach used to calculate $\omega_0^{\mathrm{Iso-Mix}}$ and $\omega_0^{29-\mathrm{Si}}$. We found $\Delta_{Anhrm}^{Iso-Mix\ Bulk}(T = 300K) = 1.36\ \mathrm{cm}^{-1}$. The difference in spectral resolution between our setup and the setup used in Ref. [30] is accounted for in this analysis [227]. Summing up the discussion in form of equations, the FWHM of bulk $^{28}Si_{0.5}{}^{30}Si_{0.5}$ sample consists of two contributions:

$$FWHM_{Bulk}(T = 300K) = \Delta_{Anhrm}^{Iso-Mix\ Bulk}(T = 300K) + \Delta_{Isotope}^{Iso-Mix\ Bulk} \qquad (6.4)$$

In comparison, the FWHM of isotopically mixed $^{28}Si_x{}^{30}Si_{1-x}$ NWs, after correcting for the spectral resolution, consists of three contributions:

$$FWHM_{Iso-Mix\ NW} = \Delta_{Anhrm}^{Iso-Mix\ NW}(T = 300K) + \Delta_{Isotope}^{Iso-Mix\ NW} + \Delta_{Surface}^{Iso-Mix\ NW} \qquad (6.5)$$

$\Delta_{Surface}^{Iso-Mix\ NW}$ is the broadening due to surface scattering of phonons. This contribution is peculiar to NWs, but absent for bulk materials. Similarly, for the FWHM of the isotopically pure ^{29}Si NWs:

$$FWHM_{Si-29\ NW} = \Delta_{Anhrm}^{Si-29\ NW}(T = 300K) + \Delta_{Surface}^{Si-29\ NW} \qquad (6.6)$$

Next, we take $\Delta_{Anhrm}^{Iso-Mix\ Bulk}\big|_T = \Delta_{Anhrm}^{Iso-Mix\ NW}\big|_T$ and $\Delta_{Isotope}^{Iso-Mix\ Bulk} = \Delta_{Isotope}^{Iso-Mix\ NW}$, because the anharmonic scattering and isotope scattering of phonons depend on the temperature and isotopic composition, but not on the size of the material as long as confinement effects are unimportant. Thus, $\Delta_{Isotope}^{Iso-Mix\ NW} = 0.065\ \text{cm}^{-1}$ and at the lowest incident laser power density, corresponding to a temperature of about $300\ \text{K}$, $\Delta_{Anhrm}^{Iso-Mix\ NW}$ is 1.36cm^{-1}. We can now relate $\Delta_{Anhrm}^{Si-29\ NW}$ to $\Delta_{Anhrm}^{Iso-Mix\ NW}$ through the inverse mass relation at a fixed temperature $\Delta_{Anhrm}\big|_T \propto 1/\langle m\rangle$, giving $\Delta_{Anhrm}^{Si-29\ NW}\big|_{300K} = \Delta_{Anhrm}^{Iso-Mix\ NW}\big|_{300K} \times (\langle m\rangle_{Iso-Mix}/\langle m\rangle_{Si-29}) \approx 1.36\ \text{cm}^{-1}$. Putting the value of the FWHM of ^{29}Si NWs at the lowest incident power and $\Delta_{Anhrm}^{Si-29\ NW}$ in equation (6.6) we deduce the contribution of surface scattering to the NWs $^{29}\text{Si} - {}^{29}\text{Si}$ Raman peak broadening: $\Delta_{Surface}^{Si-29\ NW} \approx 0.88\ \text{cm}^{-1}$. Note that the contribution of surface scattering of phonons, which is diameter dependent, is the same for both types of NWs investigated in this work as they have comparable diameters. It is therefore reasonable to conclude that the surface induced broadening of Raman spectra is the same for both types of NWs, that is $\Delta_{Surface}^{Iso-Mix\ NW} \approx \Delta_{Surface}^{Si-29\ NW} = 0.88\ \text{cm}^{-1}$. Now, the left hand side (LHS) of equation (6.5) at the lowest incident laser power density is $5.5\ \text{cm}^{-1}$, whereas the right hand side (RHS) after summing up $\Delta_{Anhrm}^{Iso-Mix\ NW}$, $\Delta_{Isotope}^{Iso-Mix\ NW}$, and $\Delta_{Surface}^{Iso-Mix\ NW}$ equates to $2.3\ \text{cm}^{-1}$. The fact that the equality of LHS and RHS in equation (6.5) does not hold suggests that there must be some other source of spectral broadening that has not been considered in equation (6.5). We rule out the possibilities of phonons scattering at crystallographic defects because the two sets of NWs are of high crystalline quality. This suggests that the excess broadening is induced by effects other than those listed above.

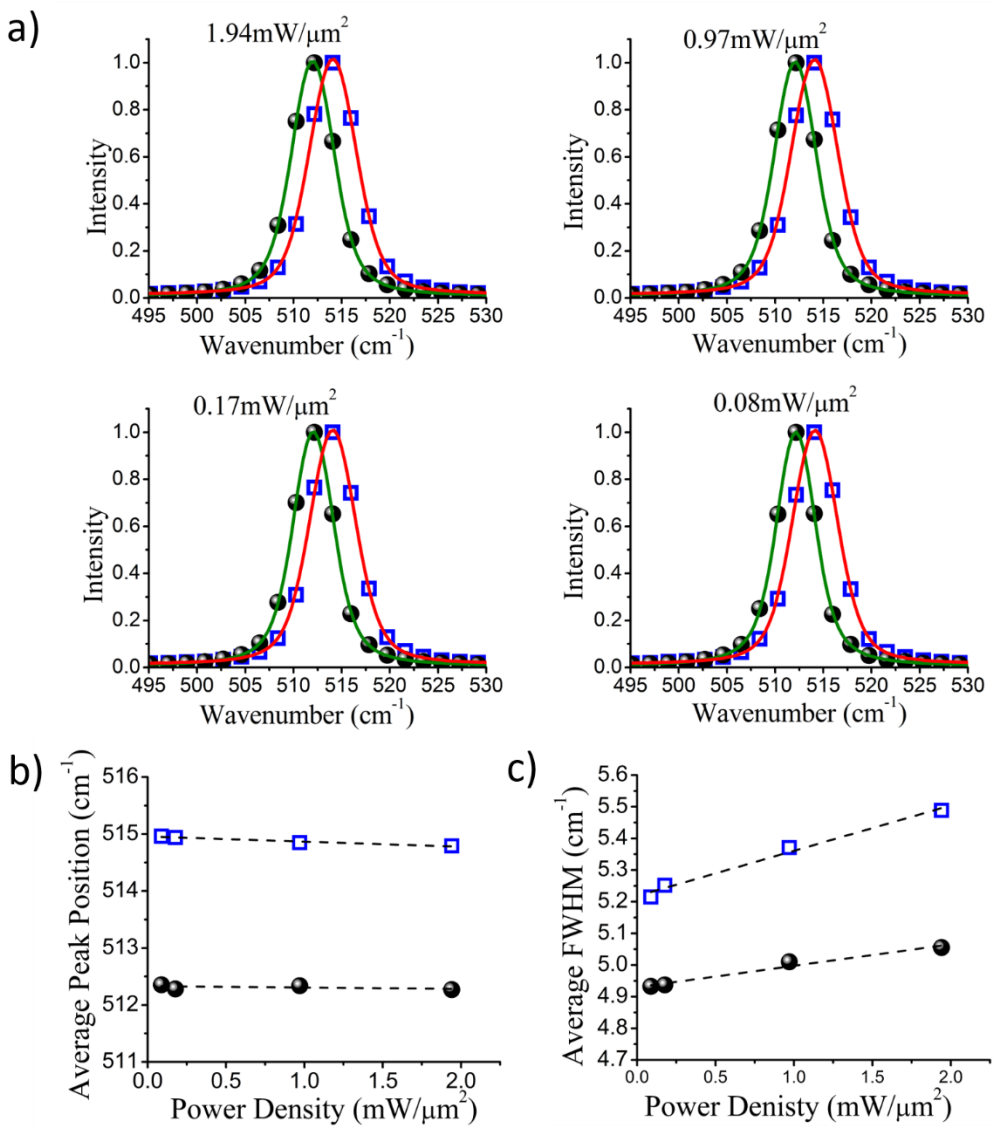

Figure 6.4: *(a) Si-Si LO normalized phonon spectra of $^{28}Si_{0.6}{}^{30}Si_{0.4}$ and ^{29}Si bulk crystals at different incident laser (488nm) power densities: 1.94mW/μm², 0.97 mW/μm², 0.17 mW/μm², and 0.08 mW/μm². (b) Evolution of average peak position and (c) evolution of average FWHM with incident laser power density for both $^{28}Si_{0.6}{}^{30}Si_{0.4}$ and ^{29}Si bulk samples extracted from the corresponding Voigt fits. In all the three figures the data points for the $^{28}Si_{0.6}{}^{30}Si_{0.4}$ bulk sample are shown in empty blue squares and that of ^{29}Si bulk sample are shown in filled black circles. The averaging was done over measurements on four different spots on each sample. In (a) the red and the green curves correspond to the Voigt fit of the respective raw data. In (b) and (c) the error bars in both the figures are smaller than the data symbols used. The dotted lines in both the figures are guide to the eye.*

To verify the calculations above, we performed a series of control experiments on isotopically mixed and isotopically pure bulk samples. These isotopically engineered bulk crystals were grown by Floating Zone technique. The Secondary Ion Mass Spectrometer analysis (not shown here) estimated that the isotopically mixed bulk sample is composed of about 60% of ^{28}Si and 40% of ^{30}Si . The spectra of both ^{29}Si and $^{28}Si_{0.6}{}^{30}Si_{0.4}$ bulk samples at 4 different laser power densities are shown in Figure 6.4(a). For these crystals, the average mass of the $^{28}Si_{0.6}{}^{30}Si_{0.4}$ sample is slightly smaller than that of ^{29}Si bulk sample. Consequently, the spectra of the former are blue shifted at all incident power as compared to the latter. The evolution of the average peak position and the average FWHM with incident laser power densities for both bulk samples are shown in Figure 6.4(b) and (c), respectively. The data displayed in Figure 6.4(b) and (c) were averaged over measurements on four different spots on each sample. The $^{28}Si_{0.6}{}^{30}Si_{0.4}$ and ^{29}Si bulk sample have peaks at 514.9 cm^{-1} and 512.3 cm^{-1}, respectively. Unlike the case of Si NWs, these phonon frequencies do not change significantly with increasing laser power density. This is an expected behavior because the effect of laser heating is ineffective in bulk samples, which have higher thermal conductivities as compared to the NWs. The average FWHM, nearly 3 cm^{-1} smaller than those measured for NWs, also shows a very limited increase with laser power density that is almost identical for both bulk samples. It is worth noting that the Si-Si mode of the $^{28}Si_{0.6}{}^{30}Si_{0.4}$ bulk sample is broader only by 0.4 cm^{-1} at the lowest incident laser power than the Si-Si mode of ^{29}Si bulk sample, which is significantly less than the 3.2 cm^{-1} difference found between the modes of the two sets of NWs. Even the difference of 0.4 cm^{-1} between the average FWHM of the two bulk samples at the lowest laser power density is not entirely coming from isotope scattering effect. Indeed, the average mass of $^{28}Si_{0.6}{}^{30}Si_{0.4}$ being smaller than the average mass of ^{29}Si, the anharmonic scattering of phonons, which scales inversely with average mass, is larger in the $^{28}Si_{0.6}{}^{30}Si_{0.4}$ bulk sample as compared to that of the ^{29}Si bulk sample at a fixed temperature. The contribution of this excess anharmonic phonon scattering to the Raman linewidth is hidden within the difference of 0.4 cm^{-1} between the average FWHM of the two bulk samples.

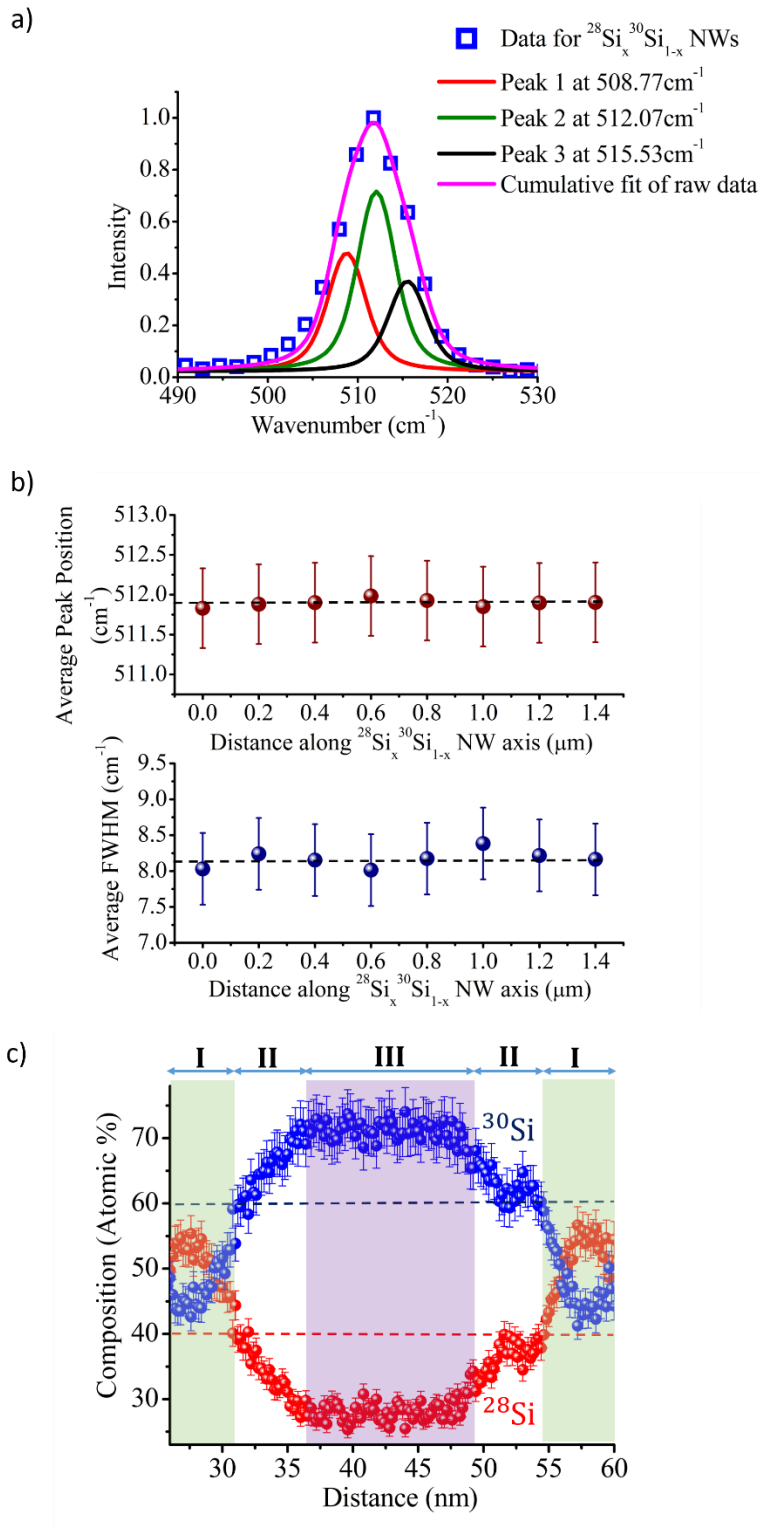

Figure 6.5: (*a*) *The spectrum of a single $^{28}Si_x{}^{30}Si_{1-x}$ NW at an incident power density of 0.08mW/μm^2 – data points shown in empty blue squares and the cumulative Voigt Fit (pink) has*

been simulated using the convolution of three different spectrum (red, green, and black) each representing different isotopic composition (details in text) within the NW; (b) Peak position and FWHM profiles measured along the growth axis of individual $^{28}Si_x{}^{30}Si_{1-x}$ nanowires. Each data point is an average over a few measurements on different nanowires. The horizontal dashed lines indicate the average values; (c) APT radial profile of ^{28}Si (red) and ^{30}Si (blue) isotopes across the diameter of an isotopically mixed nanowire. The offset in x-axis reflects the thickness of the Ni protective layer deposited around the nanowire to prevent any damage that may occur during FIB processing.

A plausible explanation of the observed broadening is the non-uniform mixing of ^{28}Si and ^{30}Si isotopes during the VLS growth of $^{28}Si_x{}^{30}Si_{1-x}$ NWs. Indeed, the excess broadening of the Raman spectra for the $^{28}Si_x{}^{30}Si_{1-x}$ NWs probably originate from the overlap of several narrower peaks corresponding to different regions within a NW with different isotopic content. For instance, in Figure 6.5(a), the Raman spectrum of a single $^{28}Si_x{}^{30}Si_{1-x}$ NW recorded at the lowest laser power is deconvoluted in three different peaks corresponding to a ^{28}Si-rich area, a ^{30}Si-rich area, and a transition zone. Since the broadening due to isotopic scattering of phonons at 300 K is only $0.065\ \mathrm{cm}^{-1}$, the FWHM of each of the three peaks has been kept the same as that of an isotopically pure ^{29}Si NW. Peak 1 (Red) is at 508.77 cm^{-1}, peak 2 (Green) is at 512.07 cm^{-1}, and peak 3 (Black) is at 515.33 cm^{-1}. The local compositions of ^{28}Si corresponding to these 3 peaks are 26.9%, 45.8%, and 65.3%, respectively. The estimated uncertainty from the spectral resolution of our Raman setup is about 7%.

Interestingly, Raman spectra recorded along the growth axis of individual $^{28}Si_x{}^{30}Si_{1-x}$ NWs show that neither the peak position nor the FWHM of Si-Si mode vary along the nanowire growth axis (Figure 6.5(b)). This suggests that the isotopic content is uniform along the growth axis and thus the inferred non-uniformity of the isotopic content seems to be associated with the radial distribution of the two isotopes. To verify this intriguing observation, the nanowires investigated by Raman were also analyzed using atom probe tomography (APT) which is the only technique capable of providing the three-dimensional (3-D) distribution of different isotopes in a nanoscale structure with a near atomic resolution. Details of the APT analysis will be reported

elsewhere. Figure 6.5(c) displays the radial profiles of ^{28}Si and ^{30}Si isotopes across the diameter of an isotopically mixed nanowire. The average isotopic composition as estimated from APT $^{28}Si_{0.40}{}^{30}Si_{0.60}$ which is close to the average composition obtained from Raman analysis ($^{28}Si_{0.47}{}^{30}Si_{0.53}$). Importantly, we note that, as predicted from Raman spectra, APT analysis also confirms that the radial distribution of the two isotopes is not uniform, whereas their profiles along the growth axis (not shown here) remain unchanged also in agreement with Raman data (Figure 6.5(b)). Moreover, APT profiles demonstrate that the two isotopes are distributed in three different regions (Figure 6.5(c)): (1) Near the surface where ^{28}Si (^{30}Si) content is higher (lower) than its average content in the entire nanowire (region I). The width of this region is about 26.3 % of the nanowire diameter; (2) At the core of the nanowire where ^{30}Si (^{28}Si) content is higher (lower) than its average content in the entire nanowire (region III). The width of this region is about 34.3% of the nanowire diameter; (3) A transition region between the two regions I and III where the content of ^{30}Si (^{28}Si) increases (decreases) monotonically inward from nanowire surface to its core. The width of this region is about 39.4% of the nanowire diameter. The average isotopic composition of each region is: x (I) = 0.54$\pm$0.01 ($^{28}Si_{0.54}{}^{30}Si_{0.46}$); x (II) = 0.35$\pm$0.01 ($^{28}Si_{0.35}{}^{30}Si_{0.65}$); and x (III) = 0.75$\pm$0.01 ($^{28}Si_{0.25}{}^{30}Si_{0.75}$). Clearly, APT analysis confirms Raman-based observations reported above. At the same time, the 3-D atom-by-atom distribution of each isotope within a single nanowire also raises fundamental questions about the basic mechanisms and dynamics of the VLS growth. Addressing these very important questions extends beyond the main focus of this Letter.

6.6 Summary

In summary, we have demonstrated the growth of isotopically mixed Si NWs via the VLS process using isotopically enriched silane precursors $^{28}SiH_4$, $^{29}SiH_4$, and $^{30}SiH_4$. Using Raman spectroscopy, the vibrational properties of these NWs were investigated and compared to that of isotopically pure ^{29}Si NWs having a similar reduced mass. The outcome of the comparative study indicates that there is an enhanced phonon scattering in isotopically mixed NWs, which manifests itself at two interrelated levels. First, the measured Raman spectra of the $^{28}Si_x{}^{30}Si_{1-x}$ NWs were found to react to laser power quite differently from those of ^{29}Si NWs. The red shift in peak position and the broadening of Raman spectra are more significant for the former as compared to the latter with the local temperature of the $^{28}Si_x{}^{30}Si_{1-x}$ NWs at the highest power density being

almost 120 K above that of the ^{29}Si NWs. Based on Raman nanothermometry, we estimated ~30% reduction in the thermal conductivity of the $^{28}Si_x{}^{30}Si_{1-x}$ NWs as compared to that of the ^{29}Si NWs around 300 K. Second, the FWHM of the $^{28}Si_x{}^{30}Si_{1-x}$ NWs was found to be significantly larger than that of ^{29}Si NWs regardless of the laser power. We showed that this cannot come entirely from the isotope effect and that the origin of this excess broadening might lie in non-uniformity in mixing of the two isotope atoms within a $^{28}Si_x{}^{30}Si_{1-x}$ NW. This non-uniform mixing of ^{28}Si and ^{30}Si may unravel new insights into the dynamics of the VLS growth, which extends beyond the scope of the current work. The work presented here provides an essential body of information for devices looking to exploit the thermal properties of NWs. The results clearly show that the isotopically disordered and the isotopically pure NWs respond to laser heating almost similarly at low power ranges but their behavior differ drastically at high power range. For NW-based devices, the isotopically mixed NWs can be exploited for applications requiring lower thermal conductivity, whereas the isotopically pure NWs are ideal for a more efficient dissipation of heat.

6.7 Acknowledgement

OM acknowledges funding from NSERC-Canada (Discovery Grants) and Canada Research Chair, Fondation de l'École Polytechnique de Montréal. The work at Keio was supported in part by the Grant-in-Aid for Scientific Research by MEXT, in part by NanoQuine, in part by FIRST, and in part by JSPS Core-to-Core Program. J.A. acknowledges the funding from the Generalitat de Catalunya 2014 SGR 1638. M.d.l.M. thanks the CSIC Jae-Predoc program. J.A. and M.d.l.M. thank funding from Spanish MINECO MAT2014-51480-ERC. The microscopy works have been conducted in the "Laboratorio de Microscopias Avanzadas" at "Instituto de Nanociencia de Aragon - Universidad de Zaragoza". Authors acknowledge the LMA-INA for offering access to their instruments and expertise, especially to Dr. Cesar Magen.

CHAPTER 7 ROLE OF ISOTOPE DISORDER AND DEFECT IN HEAT TRANSPORT IN SILICON NANOWIRES

In this chapter, we discuss a set of investigations aiming at elucidating the combined effect of isotope disorder and crystal phase on nanoscale heat transport. The detailed report of the results shown here are in the process of being organized in two different manuscripts to be submitted soon to *Nano Letters*. In section 7.1 of this chapter, we start by describing and discussing atom probe measurements of the three-dimensional distributions of isotopes in individual isotopically mixed NWs. In section 7.2, we discuss the influence of both mass disorder and defect engineering on heat transport based on Raman measurements on suspended NWs.

7.1 Elucidating the Isotope Distribution within a $^{28}Si_x{}^{30}Si_{1-x}$ NWs

The study of the phonon behavior and the nanothermometric measurements of lattice disorder effects on phonon transport would be left incomplete without knowing the exact concentration and distribution of the two isotopes within $^{28}Si_x{}^{30}Si_{1-x}$ NWs. With this perspective, we report in this section the 3D atomistic imaging of a $^{28}Si_x{}^{30}Si_{1-x}$ NW. Although in chapter 6 we presented the 1D concentration profile of ^{28}Si and ^{30}Si isotopes across a NW, here we provide additional details related to the APT analysis along with the 3D atomistic images as we attempt to shed some new light on the phenomenon of non-uniform isotopic distribution reported in chapter 6.

The atom probe tip fabrication is described in Appendix D. The APT analysis was performed utilizing a UV laser-assisted Local Electrode Atom Probe (LEAP). Evaporation of individual atoms was assisted by focusing a UV laser (355 nm), with a spot diameter of ~5 μm and a pulse duration of ~15 ps. The evaporation rate (ion pulse^{-1}), the laser pulse repetition-rate, and energy per pulse were 0.02, 250 kHz, and 30 pJ, respectively. The base temperature and base pressure within the APT chamber were maintained at 50 K and 3.2×10^{-11} Torr, respectively. The 3D reconstructions were performed using Cameca's IVAS program. Figure 7.1(a) shows the 3D atom-by-atom reconstruction of a 80nm long segment of a $^{28}Si_x{}^{30}Si_{1-x}$ NW, with the ^{30}Si atoms displayed in blue bubbles and ^{28}Si atoms in red bubbles. Of the total collected atoms, only 30% of each of the two Si isotopes are shown here for clarity. Figure 7.1(b) shows the recorded mass spectra with both singly and doubly charged state of the three Si isotopes. The appearance of

^{29}Si within a NW is possibly from traces of $^{29}SiH_4$ in purified $^{30}SiH_4$ and $^{28}SiH_4$ precursors. The intensity of the ^{29}Si peaks (both singly and doubly charged) are weaker by about two orders of magnitude as compared to the two primary peaks belonging to ^{28}Si and ^{30}Si. The inset shows the mass spectra of Au (from the entire reconstructed data set). The strength of the Au peak, reflecting the Au concentration, is about 3 orders of magnitude smaller than the strength of the main Si peaks. The inset also shows the iso-concentration surface defined at $c_{th} = 93.0$ % of ($^{28}Si^{2+} + {}^{30}Si^{2+}$) ions and the location of the Au atoms (marked by black arrow) can be clearly seen to be mostly on the NW surface (possibly due to surface diffusion of Au from the catalyst droplet). Metal atoms are also known to get incorporated within a NW during the VLS growth [138]. However, the strength of the Au peak in the mass-spectra recorded inside the NW is as low as the background noise level, indicating extremely low concentration of impurity Au within the $^{28}Si_x{}^{30}Si_{1-x}$ NW.

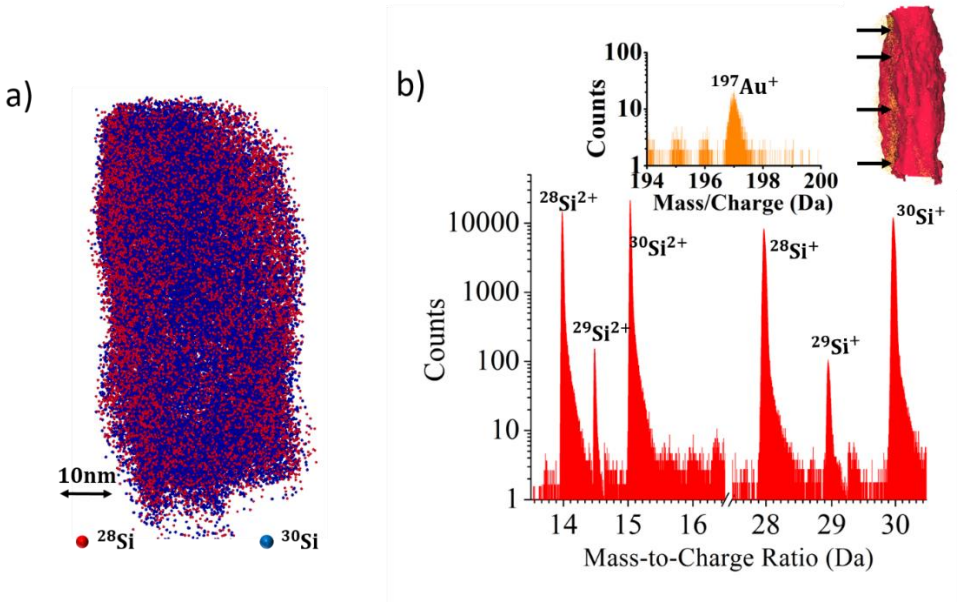

Figure 7.1: *(a) 3D atom-by-atom reconstruction of a $^{28}Si_x{}^{30}Si_{1-x}$ NW, with the ^{28}Si atoms shown in red and the ^{30}Si atoms shown in blue. (b) The mass spectra collected from the reconstruction in (a), showing the single and doubly charge states of the three Si isotopes. Inset: The mass spectra of Au and the iso-concentration surface (red) used to extract the NW out of the Ni layer. The gold atoms (marked by black arrows) can be seen to reside mostly at the surface of the NW.*

Even before drawing any concentration histograms, immediately evident from Figure 7.1(a) is the fact that the two Si isotopes are not randomly distributed within a $^{28}Si_x{}^{30}Si_{1-x}$ NW as one

would expect based on the current understanding of the VLS growth. The ^{30}Si isotopes look more concentrated towards the center while the ^{28}Si isotopes are concentrated towards the periphery of the NW. For quantification, we took the axial and radial concentration profiles of the two Si isotopes, as shown in Figure 7.2. Figures 7.2(a) and (b) show the average radial concentration of the ^{28}Si and ^{30}Si isotopes respectively, within the region of interests (ROIs). The ROIs are three cuboids, each of thickness 5 nm, placed equidistance from each other along the growth axis of the NW and are labelled as ROI1, ROI2, and ROI3 in the inset in Figure 7.2(a). It is evident that there is a region of width ~ 15 nm at the center of the NW where the concentration ratio of the ^{28}Si to ^{30}Si is $\sim 3:7$. From the surface of the NW down to a thickness of $\sim 3-4$ nm, the ratio of the two isotopes alters to $\sim 5.5:4.5$. In between the two, there is a transition region where the ^{30}Si concentration gradually decreases and the ^{28}Si concentration gradually increases as we move from the core towards the surface of the NW. The width of this transition region encircling the core is about $\sim 5-6$ nm. The average concentration of the two Si isotopes in the whole NW is ~ 40 at. % of ^{28}Si and ~ 60 at. % of ^{30}Si. This is surprising at first, since the NWs were grown using identical (2 sccm.) co-flow of the enriched precursors, in order to obtain equal concentration of the two isotopes, which creates the highest mass disorder. This 4:6 overall concentration of ^{28}Si and ^{30}Si, could have occurred due to small fluctuations in the actual flow of the precursors from what the mass flow controller reflected. In Figures 7.2(c)-(f) the axial concentration of the two isotopes is shown. The ROIs are cuboids of width 2.0 nm as shown in the inset of each axial profile. In Figure 7.2(c), the ROI is placed right at the center of the NW which is progressively moved towards the surface of the NW in Figures 7.2(d) to (f). In Figure 7.2(f), the ROI captures the atoms located within $2-3$ nm from the NW surface. The axial concentration profiles served two main purposes: first, it shows the non-uniform distribution of the two isotopes is repeated at every layer of the growing NW. Except for small fluctuations, the axial concentration remains fairly constant all along the long axis of the NW. Second, it reinforces the observation we made in Figure 7.2(a)-(b). The mean axial concentrations are shown by the dotted lines. At the center of the NW, the concentration of the two isotopes are about ~ 30 at. % of ^{28}Si and ~ 70 at. % of ^{30}Si. The ^{28}Si concentrations progressively increases and the ^{30}Si concentration progressively decreases as we move towards the surface. Finally, Figure 7.2(f) shows that the concentration close to the surface is ~ 55 at. % and ~ 45 at. % of ^{28}Si and ^{30}Si, respectively. The average axial concentration of the two Si isotopes on the other half of the NW showed a similar trend and is not shown here.

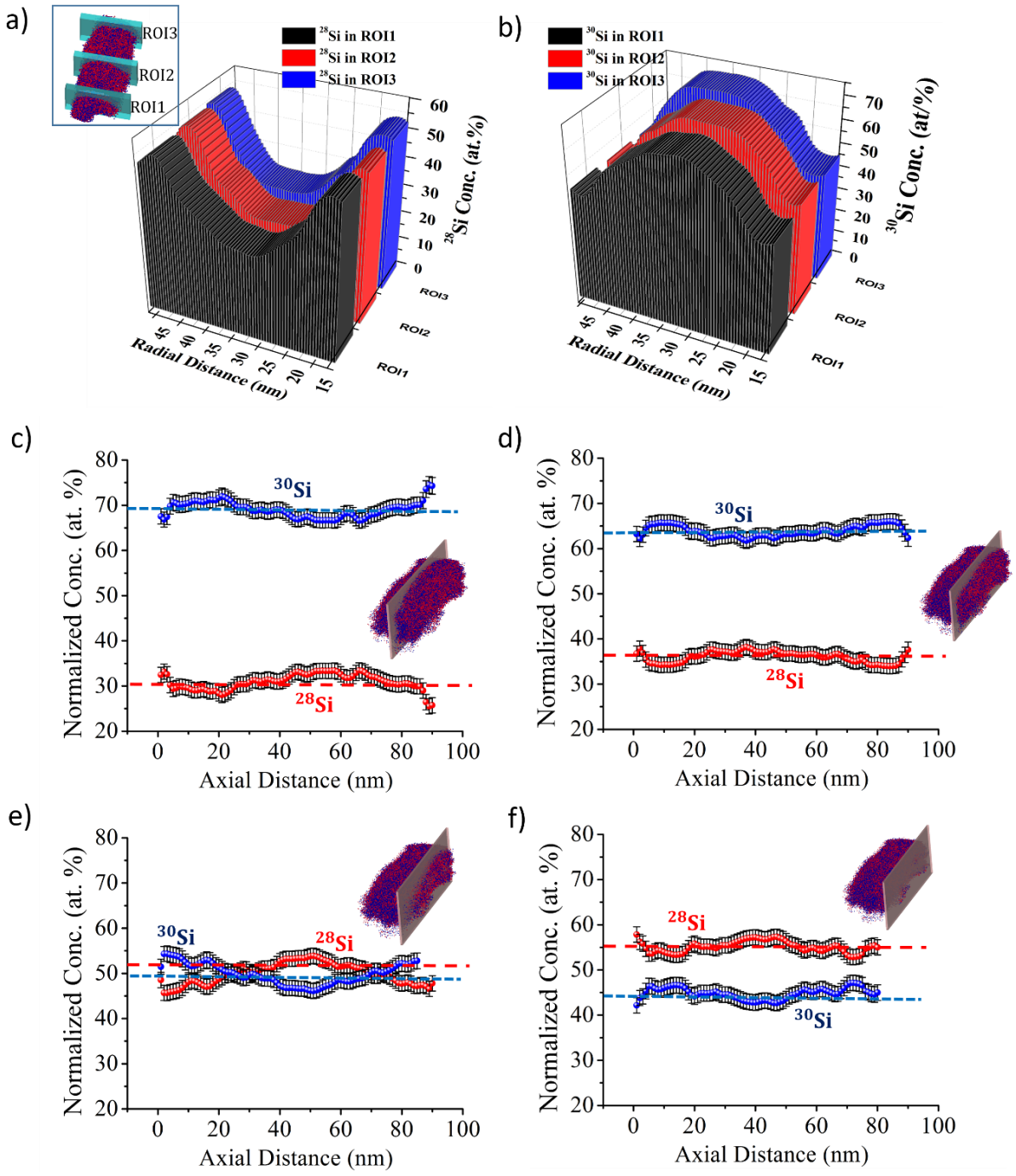

Figure 7.2: *Radial concentration of (a) ^{28}Si and (b) ^{30}Si respectively within the ROIs. (c)-(f) Axial concentration of the two Si isotopes within cuboids of width 2 nm placed along the growth axis of the NW. The ^{28}Si and ^{30}Si concentrations are shown using red and blue spheres, respectively. The mean axial concentrations in (c)-(f) are shown by the red and blue dotted lines respectively. The IVAS generated error bars are shown in black. The placement of the ROIs are shown in the inset of each plot.*

The exact reason for this non-uniform distribution of the two Si isotopes within a NW is not well understood at the moment. The best we have at this point is to hypothesize that this distribution might be related to the atomistic processes taking place at the catalyst-NW interface. It has been long assumed that during the VLS growth, the catalyst-NW interface always remains planar and the NW growth take place by nucleation and step-flow at this planar interface. However, recent *in situ* TEM experiments demonstrated that for a wide variety of catalyst-semiconductor systems, the planar main facet truncates into oblique facets at the vapor-liquid-solid triple phase boundary (TPB) [228]–[230], as shown schematically in Figure 7.3(a). The existence of this truncated facets depends on the balance of the capillary forces [230]. For $\langle 111 \rangle$ oriented Si NWs, it has been confirmed by both *in situ* experiments and theoretical simulations that the $\{111\}$ main facet truncates into $\{113\}$ and/or $\{120\}$ inclined facets [229], [231], [232], with the nucleation kinetics of atoms on the main facet being markedly different from that on the truncated oblique facets. On the closely-packed $\{111\}$ main facet, growth takes place by first forming a critical nucleus followed by a 2D step propagation. Molecular dynamics show that a considerable amount of supersaturation (often called a critical supersaturation which depends on the growth conditions) is required to overcome the energy barrier for the formation of the critical nucleus [229]. On the other hand, the less densely packed oblique facets have a high density of terrace steps and kinks. This special morphology reduces nucleation barrier and with it the critical supersaturation required for nucleation on these oblique facets. In fact, it was argued that if these oblique facets can get an atomic scale roughness, then the nucleation on these facets can occur with any finite supersaturation, that is without any nucleation barrier [229]. The molecular dynamic simulations also showed that Si atoms from an Au catalyst droplet are first incorporated at these oblique facets, due to their proximity to the Si rich contact line. When growth take place on these oblique facets, several small nuclei form and dissolve on the main $\{111\}$ facet, in an attempt to overcome its large nucleation barrier. Even after the growth of a complete layer on the oblique facets, growth on the main facet remains virtually non-existent. It is only when all nucleation sites on the oblique facets are exhausted, that the crystallization is driven on to the main facet [231]. The same conclusion was reached during *in situ* TEM annealing experiments on VLS grown Au-catalyzed Ge NWs [233].

It seems from our APT measurement that the lighter $^{28}\mathrm{Si}$ isotope attaches preferentially to these oblique facets. The width of the $^{28}\mathrm{Si}$ rich area from the surface of a $^{28}\mathrm{Si_x}{}^{30}\mathrm{Si_{1-x}}$ NW is the

same as that of the typical width of $3-5$ nm of the oblique facets reported for Au-catalyzed Si NWs [210],[211]. Although nothing to do with isotopes, a similar behavior was observed in VLS-grown Ge and Si NWs, where APT investigations revealed a local enhancement in the dopant P and B concentration near surface of a NW [234]. The non-uniformity was explained in terms of facet mobility, defined as growth velocity per unit supersaturation. The high supersaturation of Ge (Si) on the low mobility planar (111) facet results in local depression in P (B) concentration. On the other hand, the comparatively lower supersaturation of Ge (Si) on the high mobility oblique facets lead to local enhancement of P (B) concentration. In our case, the isotopes are chemically indistinguishable and the critical supersaturation required to overcome the nucleation barrier on the main (or the oblique) facets are identical for both ^{28}Si and ^{30}Si. The other factor that can possibly be responsible for the observed phenomena is the difference in the diffusion coefficients (D_{28} and D_{30}) between the two isotopes, which is higher by about 4% for ^{28}Si with respect to ^{30}Si. In the following, we paint a picture of the chain of events that could have happened during the growth of a complete layer of atoms.

Owing to their proximity to the Si rich contact line, the Au catalyst deposits the atoms on to the oblique facets, as demonstrated in Ref [231]. These atoms need to make several diffusive jumps (random walk) before they can find a suitable site for nucleation on the terrace steps and kink sites on the oblique facets, as shown schematically in Figure 7.3(b-1). With every diffusive hop, the small difference between the D_{28} and D_{30} adds up. As an analogy, we can think of a race between two groups of people, one group wearing red shirts and the other wearing the blue shirt. The completion of the race requires say H (H is a large positive number) steps from the start line to the finish line. Let us assume that the red shirts are slightly more agile and therefore completes a single step slightly faster than those with the blue shirt. After the two groups start the race together, the small difference between the two groups of people will be hardly noticeable in the first few steps. But as the number of steps keep increasing, the difference will start becoming more prominent. In fact, if H is sufficiently large, the racers will arrive at the finish line in two separate group: all the red shirts will arrive together in the first group followed by all blue shirts in the second group.

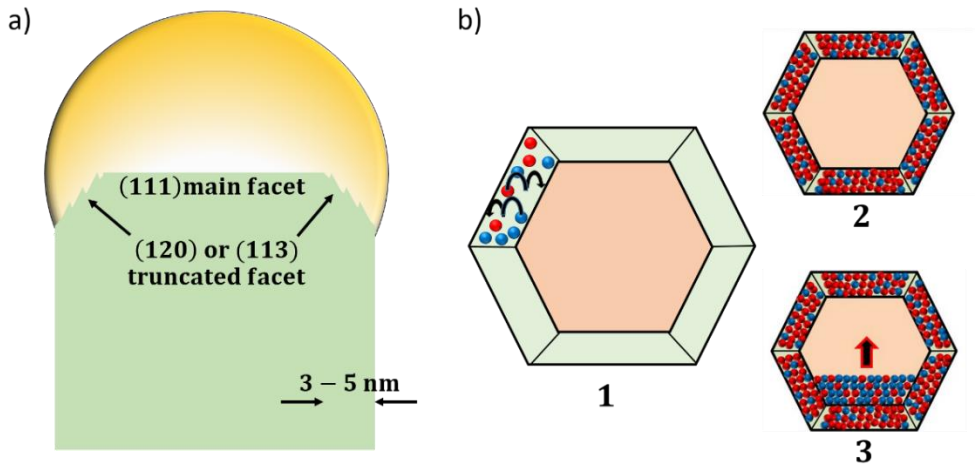

Figure 7.3: *(a) Schematic illustration of the Au catalyst-NW interface, showing the (111) main facet terminating into the stepped truncated facets. (b) Schematic illustration of the nucleation of atoms (^{28}Si atoms are depicted in red and the ^{30}Si atoms depicted in blue): (1) Atoms after being deposited on to the truncated facet make a large number of diffusive hops until they find a nucleation site. (2) While a complete layer has grown on the truncated facet, there is still no sign of any critical nucleus formation on the main facet. (3) Once all nucleation sites are exhausted on the truncated facet, the crystallization is driven on to the main facet. Growth on the main facet takes place by the formation of a critical nucleus and 2D step propagation.*

A similar thing should happen to the atoms but unlike the race, the nucleation phenomena is statistical in nature which is why we get to see a distribution rather that two distinct groups. Although an average of H random hops may be required to find a nucleation site, some ^{30}Si atoms may actually attach to a site in less than H hops while some ^{28}Si atoms may need more than H hops. Note, that the ratio of the average composition of the two isotopes within a NW is ^{28}Si: ^{30}Si = 4:6. The Au catalyst must have had the same ratio of the two isotopes which is deposited on the oblique facets. From the above description it would be fair to assume that on an average, a higher percentage of the ^{28}Si atoms (~15 at.% higher than the average according to APT data) complete the number of diffusive hops required to nucleate on the oblique facets than the ^{30}Si atoms (~15 at.% lower than the average), shown schematically in Figure 7.3(b-2). Once the oblique facets are exhausted, the nucleation is driven on the main facets, but now the supply of atoms to the main facet is depleted more of ^{28}Si atoms than that of ^{30}Si atoms. As a result, the

critical nucleus formation and subsequent 2D step propagation on the main facet occurs with more ^{30}Si atoms (~10 at.% higher than the average) and less ^{28}Si atoms (~10 at.% lower than the average), shown schematically in Figure 7.3(b-3). We also think that while diffusing from the oblique facet to the main facet, it is possible that some atoms nucleate at and around the junction as well (since the junction can be seen as a kink and therefore must have a lower nucleation barrier than that on the main facet). This gives rise to the transition region where the ^{30}Si concentration raises and the ^{28}Si concentration falls as we move inwards, from the surface of a NW toward its core. The ratio of the average isotopic composition in this region (Region II in Figure 6.5(c)) is ^{28}Si: ^{30}Si is 3.5:6.5, (~5 at.% lower and higher than the average respectively).

7.2 Raman Spectroscopy on Suspended Nanowires

7.2.1 Isotopically Pure and Isotopically Mixed Nanowires

In this section, we aim at expanding our understanding of the effect of isotope disorder on heat transport in NWs using Raman spectroscopic measurements on the suspended NWs. The NWs were dispersed by the same method described in Chapter 6 [235]. But, instead of dispersing them on a Au substrate we used a Au-grid (purchased from Quantafoil). When NWs are dispersed on Au substrate, a significant portion of the local heat generated by the laser, flows into the substrate. To minimize the effects of the contact with the substrate, the NWs are dispersed on Au-grids. The Au-grid structure possess circular holes with diameter 3 μm with a spacing of 3 μm between the holes. As the NWs get dispersed on the grid, some of them land on top of these holes, as shown in the SEM image in the inset of Figure 7.4(a). Next, the Raman measurements were carried out at ambient temperature using a Reinshaw Invia spectrometer (488nm, Objective: 100X/0.9NA, Dispersion grating: 1800 lines/mm, Detector: liquid nitrogen cooled CCD, Power density: Varied in steps from 0.01 mW/μm^2 to 1.50 mW/μm^2). Similar to chapter 6, the raw data collected from individual $^{28}Si_x{}^{30}Si_{1-x}$ and ^{29}Si NWs were first normalized and fitted with Voigt line profile to extract the peak position and the line width (FWHM). In Figure 7.4(a) we show the evolution of the peak position with incident laser power. The data in Figure 7.4(a) is an average over the measurements done on few individual NWs of each type. Although not shown here, the evolution of the average FWHM of the $^{28}Si_x{}^{30}Si_{1-x}$ NWs is qualitatively similar to what we found in Figures 6.3(b) and (d) in chapter 6. The average width of the Raman line for the $^{28}Si_x{}^{30}Si_{1-x}$ NWs is

broader by about 3.5 cm^{-1} at the lowest power density. The reason for which was explained in chapter 6, the non-uniform distribution of the two isotopes within a single NW. The Raman peak positions in Figure 7.4(a) and equation (6.1) were used to calculate the average temperature of the NWs.

The evolution of the average temperature of the NWs is shown in Figure 7.4(b). Although the rise in temperature is non-linear over the entire incident power range, for the low power regime (first three data points: 0.01 $mW/\mu m^2$, 0.40 $mW/\mu m^2$, and 0.75 $mW/\mu m^2$) the evolution of temperature can be considered to be fairly linear. The effect of suspending the NWs is prominent, especially around the last two data points (1.0 $mW/\mu m^2$ and 1.50 $mW/\mu m^2$). In Figure 6.3(f), we saw that the average temperature of the $^{28}Si_x{}^{30}Si_{1-x}$ NWs reached 390 K at an incident power density of about 8.0 $mW/\mu m^2$, the same that has been reached here with only 1.50 $mW/\mu m^2$ in Figure 7.4(b). This shows that when dispersed on Au substrate, a large fraction of the heat that is generated within a NW due to laser heating, flows into the substrate. The inset in Figure 7.4(b) shows the linear dependence of the NWs local temperature as a function of the power density for the first three data points. The ratio of the thermal conductivities (κ) at around the room temperature for the two sets of NWs was calculated from the slopes of the linear fit (dot-dash lines in the inset). Since the error bars in the inset of Figure 7.4(b) overlap, it is difficult to quantify the ratio of the thermal conductivities with the utmost precision. However, we estimated that $\kappa_{29-Si}/\kappa_{Iso-Mix}$ ratio can lie between 1.17 and 1.32 (including error bars) and the average value of the ratio to be 1.24. This indicates an average decrease in the room temperature thermal conductivity of ~24.0 % for the $^{28}Si_x{}^{30}Si_{1-x}$ NWs with respect to the ^{29}Si NW. The results here also show that the presence of the substrate underneath the NWs had only a minimal effect on the $\kappa_{29-Si}/\kappa_{Iso-Mix}$ ratio calculated in chapter 6. In fact, the ratio of 1.30 calculated in chapter 6, lie within the uncertainty range of the measurements on the suspended NWs shown here.

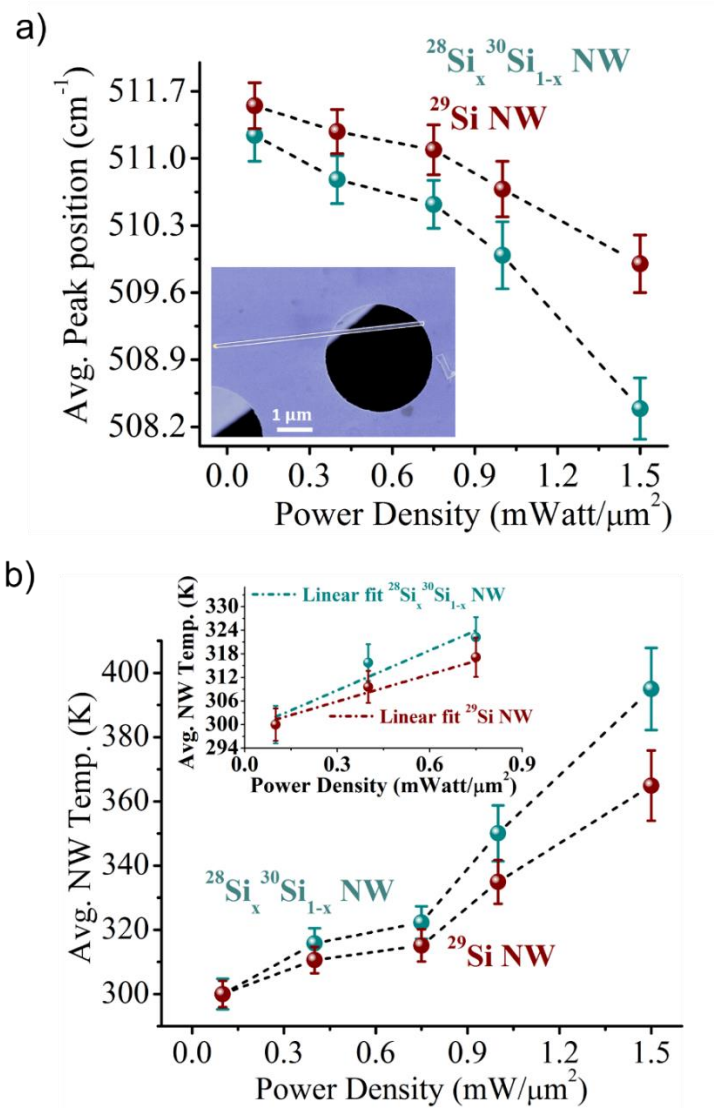

Figure 7.4: *(a) Evolution of average peak position with incident laser power density for both $^{28}Si_x\,^{30}Si_{1-x}$ NWs and ^{29}Si NWs. The error bars are double the standard deviation of the peak position from the average value. Inset: SEM image showing a NW suspended after being dispersed on a gold grid. The outline of the NW has been marked with false white color. (b) The evolution of the average temperature of the NWs as a function of incident power density. The error bars represent the uncertainty in the calculated temperature due to the standard deviation of the measured peak position. The black dotted lines in (a) and (b) are guides to the eye. Inset: The local temperature variation for the first three data points and the corresponding linear fits (dot-dash line).*

7.2.2 Isotopically Mixed Nanowires with Stacking Faults

Along with other NW parameters like the dimension, composition, and shape, studying the effect of polytypic crystal phase on the properties of a NW has emerged as an important research direction. For instance, the fact that crystal polytypes possess a different electronic band structure, widens up the scope for the electronic and optoelectronic applications of NWs [236], [237]. Additionally, the difference in the arrangement of atoms between the polytypes means that the phonons too would behave differently which makes studying the phonon transport in such polytypic NWs interesting. Herein, we report the Raman measurements done on a different set of isotopically mixed Si NWs having a polytypic crystalline structure. The fact that the polytypic NWs are also isotopically mixed, provides us with a unique platform to study and compare the combined effect of the mass-disorder the crystal phase on phonon transport.

The polytypic NWs that we are going to describe next, are also isotopically mixed $^{28}Si_x{}^{30}Si_{1-x}$ NWs. For convenience and to differentiate them from the $^{28}Si_x{}^{30}Si_{1-x}$ NWs described in chapter 6 and in the last section (which are also isotopically mixed but are purely diamond cubic) we would be calling them as p-$^{28}Si_x{}^{30}Si_{1-x}$ NWs ('p' standing for polytypic) from here on in the text. The substrate cleaning, Au deposition and annealing steps were identical to the ones reported in Chapter 6 (See Appendix C for the details). The growth initiation was done using a 22 sccm. flow of $^{Nat}SiH_4$ (diluted at 10% in H_2) at a 500 ºC, and a reactor pressure of 1.5 Torr. Then the $^{Nat}SiH_4$ flow was stopped and a co-flow of $^{30}SiH_4$ (99.9%) and $^{28}SiH_4$ (99.99%) (both at 2 sccm.) was introduced while always maintaining the pressure at 1.5 Torr. The reason for this is that the growth initiation is an important step which is well-documented in the literature for Si NWs grown using 10% $-{}^{Nat}SiH_4$. Therefore, the initiation step was done using the less expensive $^{Nat}SiH_4$ precursor rather than the highly expensive isotopically enriched precursors. Once the growth is initiated, the NWs would continue growing in a layer-by-layer fashion. These NWs are therefore expected to have a short ^{Nat}Si stem before the long isotopically mixed segments (a few microns). However, in some cases, this flow adjustments yields a non-uniform growth close to the base of the NWs. Indeed, SEM images (not shown here) showed that over 50% of the p-$^{28}Si_x{}^{30}Si_{1-x}$ NWs kinked along the $\langle 121 \rangle$ direction from the original $\langle 111 \rangle$ direction, close to their base. Additionally, we found from high resolution STEM and Raman investigations (discussed below) that the kinked NWs possess lamellar $\langle 111 \rangle$ twins all along the length of the NW after the

kink. A twin boundary is a single atomic plane that separates two neighboring crystal domains with very specific relative crystallographic orientations [238]. This requires very little energy to form and consequently is a very common feature in III-V NWs. A twinning on the {111} planes causes a rotation of the crystal by a 60° along the crystallographic axis, an orientation that generates a reflection of the stacking order of the {111} planes. For Si and Ge NWs, such lamellar twins are often found in NWs that kink along the ⟨121⟩ direction at some point during the growth from the ⟨111⟩ direction [238], [239]. Although rare, other orientations of the twin planes in Si NWs have been also reported in literature like the {111} twin planes perpendicular to the growth axis of a ⟨111⟩ oriented NW [237] and twin planes inclined to the growth axis of a NW that kinked along ⟨331⟩ direction [240]. Recently, the underlying mechanism leading to the planar defect generation and growth of kinked polytypic NWs was proposed based on the correlated TEM and Raman analyses on kinked Ge NWs [241].

Like the Au catalyzed Si NWs, the Au catalyzed Ge NW growth consist of a planar main facet which truncates into oblique corner facets. The model suggests that any instability to the catalyst droplet generates a faulty {111} stacking sequence as a result of a faulted nucleation on a corner facet. The faulty stacking sequence produces an atomic step on the main {111} facet which becomes the preferred nucleation site. This faulted {111} sequence then propagates towards the ⟨121⟩ direction without generating any additional planar defects. After the growth of a few monolayers the same sequence is repeated leading to another faulted {111} stacking sequence parallel to the previous one and adding another atomic step on the planar main facet at the catalyst-NW interface. As the atomic steps continue to build up due to successive faulted nucleation events on the corner facet and multiple stacking faults, a pseudofacet develops at the catalyst-NW interface. This pseudofacet is inclined to the {111} plane that formed the original growth front. At this stage the catalyst droplet lies degenerately on the original {111} facet and the newly developed pseudofacet. Once the catalyst starts wetting the pseudofacet to a degree that is sufficient to sustain a stable growth, the NW starts to kink along the ⟨121⟩ direction with the pseudofacet now becoming the growth front. The faulted stacking sequence that eventually led to the kink is then repeated with every growing layer in the new direction. Kinking in NWs and formation of planar defect are often associated with kinetic effects induced by altering the growth temperature or to the variation in supersaturation induced by the changes in pressure. In our experiment, neither the temperature nor the pressure was altered at any point during the growth of the p-$^{28}Si_x\,^{30}Si_{1-x}$ NWs.

This leads us to believe that it was possibly the flow adjustments which caused instability to the catalyst droplet, causing faulted nucleation on the corner facet, eventually leading to faulted stacking sequence and kinking.

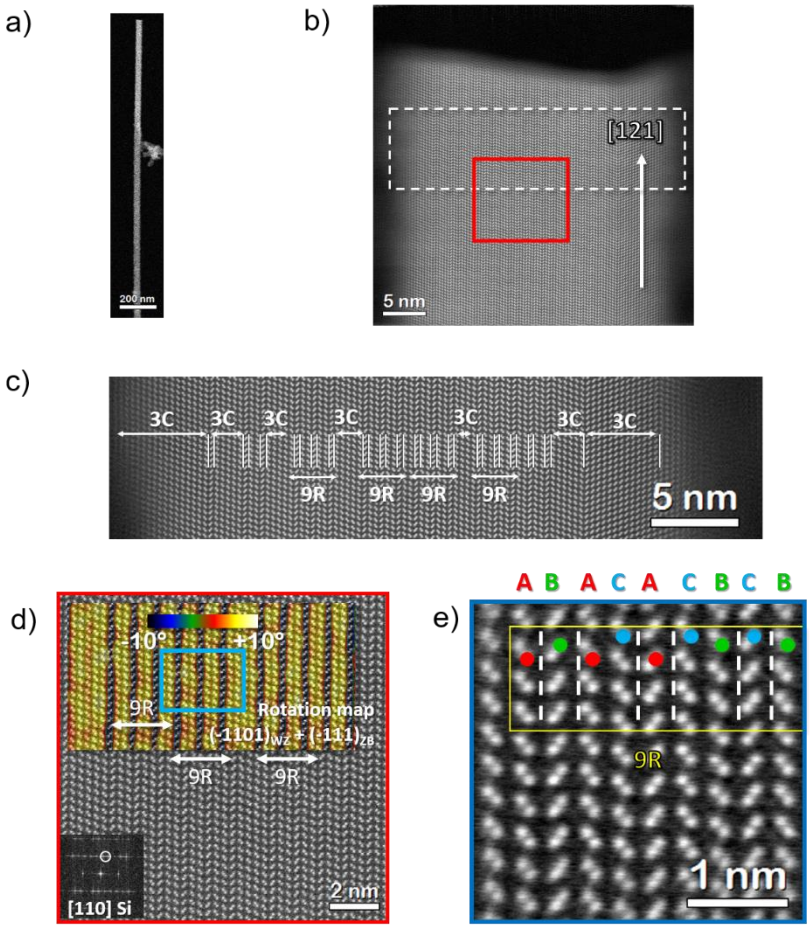

Figure 7.5: *(a)-(e) HAADF-STEM image of a p-$^{28}Si_x{}^{30}Si_{1-x}$ NW, recorded after the kink, at different levels of magnification (details in text). (c) is recorded from the white dotted rectangular box in (b). (d) is recorded from the red square box marked in (b). (e) is recorded from the blue square box marked in (d).*

Figures 7.5(a)-(e) show HAADF-STEM images of a p-$^{28}Si_x{}^{30}Si_{1-x}$ NW, recorded after the kink. The electron beam in the images were parallel to the [110] Si zone axis. Figure 7.5(a) exhibits the low magnification image of a NW after the kink. We do not see the gold catalyst atop

the NW. It could be that the catalyst got dislodged from its position, thereby ceasing any further axial elongation of the wire. Figures 7.5(b) and (c) are high magnification images of the NW. The NW has grown in [121] direction and has a diameter of $30 - 40$ nm. Figure 7.5(c) shows that the central part of this particular NW is polytypic in nature bounded by the diamond cubic (3C) Si domains. Every twin (marked by a white line) can be considered as a hexagonal Si monolayer. The twinned lattice has been clearly marked out in Figure 7.5(d) by the false yellow color. The selected area diffraction pattern viewed from the [110] direction is shown in the inset. The Bragg's spot marked by the circle was used to generate rotational map (marked by the false yellow color) in Figure 7.5(d). The rotation maps were generated using the geometric phase analysis software. We have chosen two reflection points separated by $+10°$, just to mark the twinned domains. The domains are actually mirror images of each other rotated by $180°$. Figure 7.5(e) shows the high-resolution image recorded at the highest magnification. The stacking sequence of ABACACBCB (each letter denotes a bilayer of atoms) is commonly known as the 9R polytype in Si.

The Raman spectra of individual suspended p-$^{28}Si_x{}^{30}Si_{1-x}$NWs (dispersed on Au-grids), recorded at the lowest incident power density of 0.01 mW/μm^2 are shown in Figures 7.6(a)-(c). A satellite peak at lower energy (compared to the 3C-Si peak) is clearly visible. Note that the position of the 3C-Si peak is located at 511.5 ± 0.5 cm^{-1}, similar to what we found for the diamond cubic 3C-$^{28}Si_x{}^{30}Si_{1-x}$ NWs reported in chapter 6 and section 7.2.1, indicating a similar isotopic ratio within the NWs. Interestingly, the width of the 3C-Si peak is also of the same order ($7.5 - 8.5$ wavenumbers), to what we found for the 3C-$^{28}Si_x{}^{30}Si_{1-x}$ NWs. The location of the satellite peak can be explained by the folding of the Brillouin zone, as depicted schematically in the phonon dispersion relation in Figure 7.6(d). As evident from Figure 7.5(f), the stacking faults distribution in the NW is periodic with a periodicity of $3a_{111}$, where a_{111} is the lattice spacing along the [111] direction. The lattice periodicity is thus modulated by the periodicity of the stacking faults. This leads to a folding of the Brillouin zone at $q = q_{max}/3$, where q is the phonon wave-vector, causing the phonon mode with $q = 2q_{max}/3$ (marked by a black dot) to fold back into the center of the zone, and therefore satisfy the $q = 0$ Raman selection rule. q_{max} is the wave vector at the edge of the zone at π/a_{111}. Similarly, if the periodicity of the stacking faults is $2a_{111}$, the folding will occur at the middle of the Brillouin zone and the phonon mode at the edge of the zone (at $q = q_{max}$) will be folded back and satisfy the Raman selection rule. This happens for the 2H polytype in Si.

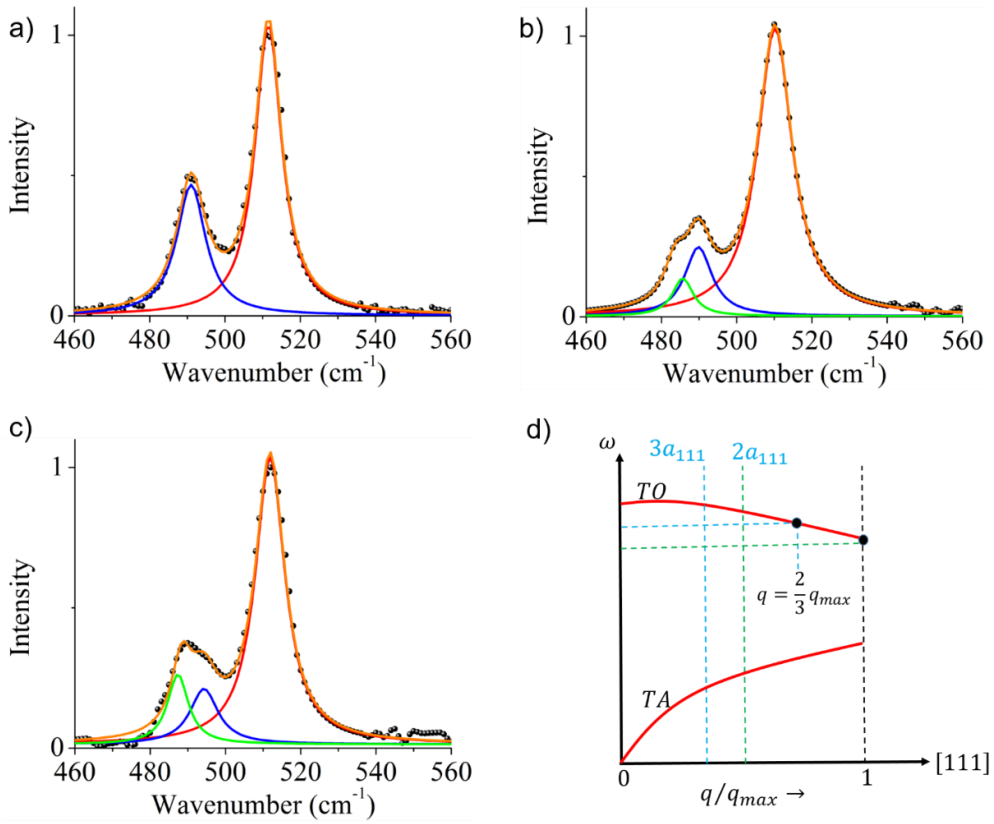

Figure 7.6: *(a)-(c) Raman spectra of a single suspended p-$^{28}Si_x{}^{30}Si_{1-x}$ NW, each having lamellar stacking faults along their <121> growth axis. The periodicities of the faults in the three NWs are possibly different (details in text) leading to different line shapes of the satellite peak. The spectra were recorded at the lowest incident laser power density of 0.01 mW/μm^2. The raw data (black spheres) was normalized and fitted with one, two, or three Voigt functions (red, blue and green lines), whichever gave the best R^2 value for the cumulative fit (orange lines). (d) Schematic illustration of the zone folding effect on the phonon dispersion relation in Si in presence of stacking disorder.*

For a ^{Nat}Si NW, the wavenumber of the folded mode for the 9R and 2H polytype were reported to be about 497 cm^{-1} and 495.5 cm^{-1}, respectively [239]. Assuming the ratio of the peak position to remain the same, that is $(\omega_{3C}/\omega_{9R})_{Nat-Si} = (\omega_{3C}/\omega_{9R})_{Iso-Mix}$, we can estimate the satellite peak for the 9R polytype to be located around 489 cm^{-1} for the p-$^{28}Si_x{}^{30}Si_{1-x}$ NWs

investigated here. This calculated value of the Raman peak for the 9R polytype in a p-$^{28}Si_x{}^{30}Si_{1-x}$ NW agrees with the experimental data presented in Figure 7.6(a). The satellite peak can be fitted accurately with a single Voigt function (blue line in Figure 7.6(a)) and can therefore be assigned to the presence of 9R polytypes in the p-$^{28}Si_x{}^{30}Si_{1-x}$ NWs. By a similar analysis, the 2H polytype peak in the p-$^{28}Si_x{}^{30}Si_{1-x}$ NWs can be shown to be around $487.5\ cm^{-1}$. In Figure 7.6(b), we see that the satellite peak cannot be fitted by a single Voigt function. The cumulative fit of the satellite peak is significantly improved by the use of two Voight functions. The peaks of the two Voigt functions are located at about $489.8 \pm 0.5\ cm^{-1}$ (blue) and $487.9 \pm 0.5\ cm^{-1}$ (green) in Figure 7.6(b), indicating at the possibility that the NW might have both 9R and 2H polytypes. In Figure 7.6(c) too, the satellite peak needs to be fitted using two Voight functions, but none of the peaks correspond to the value calculated for the 9R or 2H polytypes. The two Voigt peaks are located at about $495 \pm 0.5\ cm^{-1}$ (blue) and $484 \pm 0.5\ cm^{-1}$ (green). This might be due to the fact that the stacking faults in the particular NW is aperiodic. The presence of aperiodic stacking faults has been previously reported for VLS grown ^{Nat}Si NW [239]

The study indicates that the crystalline structure can vary from one NW to the other, depending upon the periodicity of the stacking faults. We also found many NWs that did not have the satellite peak suggesting the absence of stacking faults (probably the ones that did not kink). However, of all the p-$^{28}Si_x{}^{30}Si_{1-x}$ NWs that had the satellite peak, majority of them were found to possess the 9R polytype while only a few resembled the ones shown in Figures 7.6(b) and (c). Next, a nanothermometric measurement was undertaken but the Raman peak position of only those suspended p-$^{28}Si_x{}^{30}Si_{1-x}$ NWs which showed signatures of the 9R polytype were measured as function of the laser power density. For the other polytypes (9R+2H and aperiodic), we did not find enough NWs to present a statistically significant data-set. The measurement, displaying the average Raman peak position of the diamond cubic (3C) phase and the hexagonal (9R) phase within the p-$^{28}Si_x{}^{30}Si_{1-x}$NWs, is shown in Figure 7.7(a). The average local temperature of the cubic phase (3C) and the hexagonal (9R) phases within the p-$^{28}Si_x{}^{30}Si_{1-x}$NWs were calculated from the shift in Raman peak position and equation 6.1. Once again, the local temperature of both the phases is assumed to be $300\ K$ at the lowest incident laser power. Figure 7.7(b) shows the evolution of the local temperature of the 3C and the 9R phases. The overall temperature of the p-$^{28}Si_x{}^{30}Si_{1-x}$ NWs is determined by taking a simple average of the local temperatures of the 3C and the 9R phases.

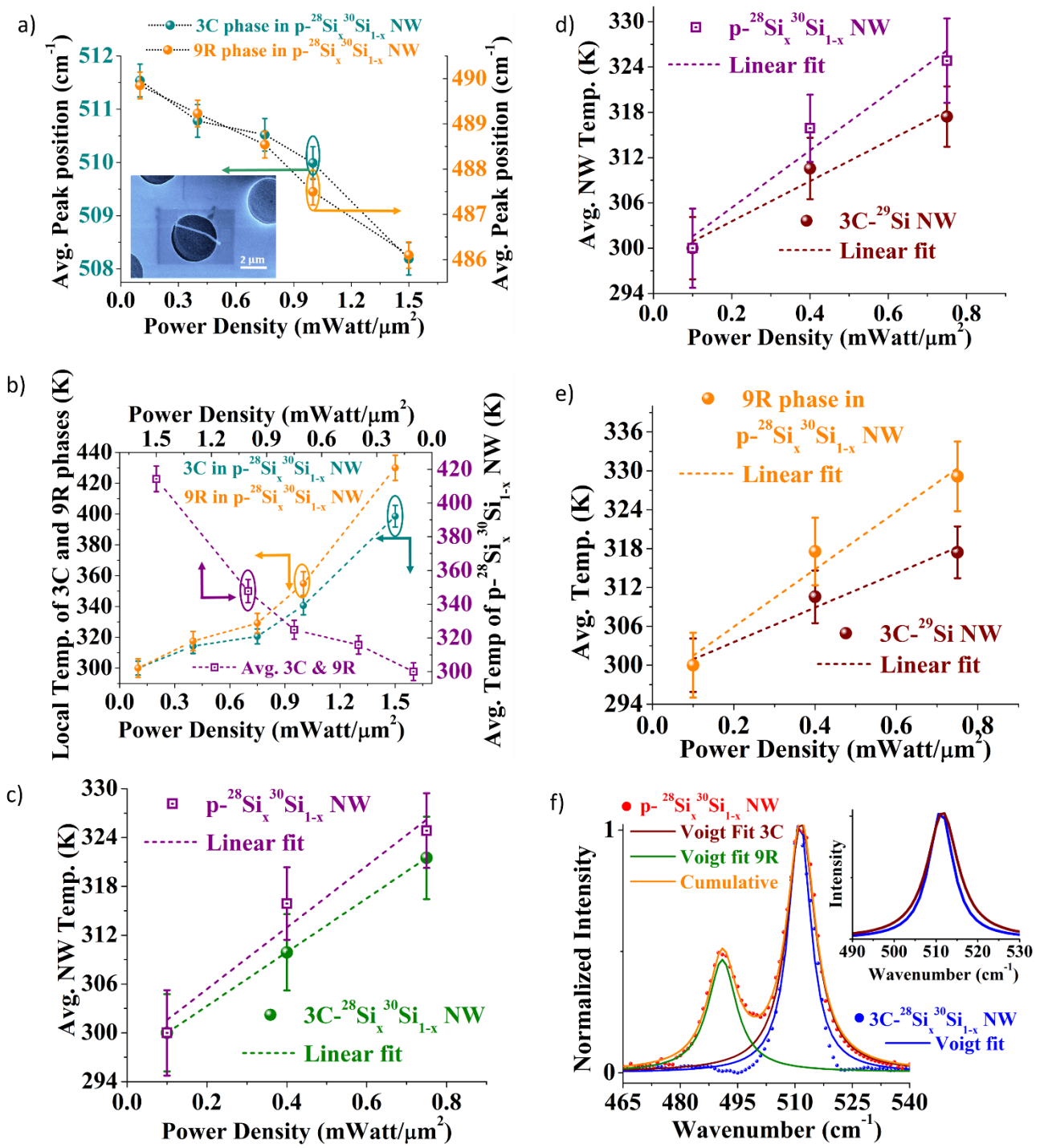

Figure 7.7: *(a) Evolution of average Raman peak position of the 3C (cyan) and the 9R (orange) phases within the p-$^{28}Si_x{}^{30}Si_{1-x}$ NWs, as a function of laser power density. The error bars are double the standard deviation of the measured peak position from the average value. Inset: SEM image of a kinked p-$^{28}Si_x{}^{30}Si_{1-x}$ NW. The portion of the NW after the kink is suspended on top of a hole in the Au-grid. (b) Evolution of the average local temperature of the 3C (cyan) and the 9R (orange)*

phases and of the p-$^{28}Si_x{}^{30}Si_{1-x}$ NWs (magenta) as a function of laser power density. (c)-(e) Comparison of the evolution of the average temperature as a function of laser power density and the corresponding linear fit for (c) the p-$^{28}Si_x{}^{30}Si_{1-x}$ NWs (magenta) and the 3C-$^{28}Si_x{}^{30}Si_{1-x}$ NWs (green). (d) the p-$^{28}Si_x{}^{30}Si_{1-x}$ NWs (magenta) and the 3C-^{29}Si NWs (brown). (e) the 9R phase within the p-$^{28}Si_x{}^{30}Si_{1-x}$ NWs (orange) and the 3C-^{29}Si NWs (brown). The comparisons in (c)-(e) are done only for the first three data points. The error bars in (b)-(e) represent the uncertainty in the calculated temperature due to the standard deviation of the measured peak position. (f) Raman spectra collected from a p-$^{28}Si_x{}^{30}Si_{1-x}$ NW and from a diamond cubic 3C-$^{28}Si_x{}^{30}Si_{1-x}$ NW. The raw data was normalized and fitted with Voigt line profile(s). Inset: The overlap of the Voigt line profiles originating from the 3C phase within the p-$^{28}Si_x{}^{30}Si_{1-x}$ NW (brown) and the 3C-$^{28}Si_x{}^{30}Si_{1-x}$ NW (blue).

Immediately evident from Figure 7.7(b) is that the 9R phase gets heated up more rapidly than the 3C phase within the p-$^{28}Si_x{}^{30}Si_{1-x}$ NWs. The ratio of the thermal conductivities was calculated from the slope of the first 3 data points (the linear regime of the temperature vs power density plots) which showed that the lattice thermal conductivity of the 9R phase is lower by ~18% compared to the 3C phase in p-$^{28}Si_x{}^{30}Si_{1-x}$ NWs. Next, we compared the temperature evolution of the p-$^{28}Si_x{}^{30}Si_{1-x}$NWs (the average of 3C and the 9R phases, the purple boxes in Figure 7.7(b)) and the pure diamond cubic (3C) $^{28}Si_x{}^{30}Si_{1-x}$NWs. Figure 7.7(c) shows that owing to the presence of the 9R polytypes, the temperature of the p-$^{28}Si_x{}^{30}Si_{1-x}$ NWs raises more rapidly compared to the 3C-$^{28}Si_x{}^{30}Si_{1-x}$ NWs. The average lattice thermal conductivity of p-$^{28}Si_x{}^{30}Si_{1-x}$ NWs is reduced by ~10% compared to 3C-$^{28}Si_x{}^{30}Si_{1-x}$ NWs, close to $T = 300K$. This value is somewhat lower than the value of 15% reduction at room temperature, predicted from theoretical calculations on 3C-^{Nat}Si NWs and p-^{Nat}Si NWs (having the 9R polytypes) [242]. The reduction in lattice thermal conductivity for the p-$^{28}Si_x{}^{30}Si_{1-x}$ NWs can depend on the degree of hexagonality, that is on the fraction of the total NW volume occupied by the hexagonal 9R phase.

Next, the temperature evolution of the p-$^{28}Si_x{}^{30}Si_{1-x}$ NWs is compared to the pure diamond cubic (3C) ^{29}Si NWs. From the slopes of the respective linear fit of the data, it emerges that the average lattice thermal conductivity of the p-$^{28}Si_x{}^{30}Si_{1-x}$ NWs is ~68% that of the 3C-^{29}Si NWs (~32% reduction), close to $T = 300K$. The reduction comes from two different factors:

first, the reduction due to mass-disorder and second, the reduction due to the polytypic nature of the p-$^{28}Si_x{}^{30}Si_{1-x}$ NWs. The highest reduction in lattice thermal conductivity relative to the 3C-^{29}Si NWs is experienced by the 9R phase within the p-$^{28}Si_x{}^{30}Si_{1-x}$ NWs. Figure 7.7(e) shows the temperature evolution of the two as a function of the laser power density. The ratio of the slopes of the respective linear fits suggests an average reduction of ~37% in the lattice thermal conductivity, close to $T = 300K$, for the 9R phase in p-$^{28}Si_x{}^{30}Si_{1-x}$NWs compared to the 3C-^{29}Si NWs. Finally, in Figure 7.7(f) we compare the Raman line-shape of a p-$^{28}Si_x{}^{30}Si_{1-x}$ NW (red spheres) and a 3C-$^{28}Si_x{}^{30}Si_{1-x}$ NW (blue spheres), both recorded at the lowest laser power density of 0.1 $mWatt/\mu m^2$. Both the data sets were first normalized relative to the strongest peak and fitted with Voigt line-profile(s). The inset in Figure 7.7(f) shows the comparison, where we have overlapped the Voigt profile originating from the 3C phase within the p-$^{28}Si_x{}^{30}Si_{1-x}$ NW (brown) with that of 3C-$^{28}Si_x{}^{30}Si_{1-x}$ NW (blue). The Raman line originating from the 3C phase within a p-$^{28}Si_x{}^{30}Si_{1-x}$ NW is wider by $1.2 \pm 0.5\ cm^{-1}$ compared to the width of the line originating from the pure diamond cubic 3C-$^{28}Si_x{}^{30}Si_{1-x}$ NW. Both have the same crystal phase (3C; diamond cubic), similar isotopic composition and hence the same rate of phonon scattering from the mass-disorder, same average atomic mass and hence the same rate of anharmonic phonon scattering, and even the p-$^{28}Si_x{}^{30}Si_{1-x}$ NWs and the 3C-$^{28}Si_x{}^{30}Si_{1-x}$ NWs have similar diameters and hence the same rate of boundary scattering of phonons. The excess width of the Raman line for the 3C phase within a p-$^{28}Si_x{}^{30}Si_{1-x}$ NW indicates towards the possibility of some extra phonon scattering mechanism present within these NWs but absent in the other. Therefore, the only likely explanation to the observed broadening is the scattering of phonons at the 3C/9R homo-interfaces within a p-$^{28}Si_x{}^{30}Si_{1-x}$ NW.

To summarize this chapter, we presented a qualitative mechanistic picture of the non-uniform distribution of the two Si isotopes within a $^{28}Si_x{}^{30}Si_{1-x}$ NW, as observed in the APT maps. The proposed mechanism is based on the amplification of the difference in the diffusion coefficient between the two Si isotopes, as they make a large number of diffusive hops to find a nucleation site on the oblique facets at the catalyst-NW interface. To verify the generality of this mechanism, the realm of experimental parameters need to be expanded to include different catalyst materials and growth conditions (partial pressure, temperature, rate, etc.) as outlined in chapter 9. The p-$^{28}Si_x{}^{30}Si_{1-x}$ NWs were grown at $500\ °C$ while the $^{28}Si_x{}^{30}Si_{1-x}$ NWs were grown at $480\ °C$, both using Au catalyst. The position and width of the Raman lines recorded on the p-$^{28}Si_x{}^{30}Si_{1-x}$

NWs after the kink (along the [121] direction) give us the primary indications that the two Si isotopes could also be non-uniformly distributed in these NWs, despite the different growth direction and growth temperature. This needs to be verified using APT. We also performed Raman investigations of isotopically engineered Si NWs, kept suspended to avoid the contact with the underlying substrate. The suspension was achieved by dispersion of the NWs on Au-grids. We found that we overestimated the ratio of the thermal conductivity of the two sets of NWs ($\kappa_{Si-29}/\kappa_{Iso-Mix}$) in chapter 6, but only slightly and the value lies within the uncertainty range of the measurements done on the suspended NWs. While the average reduction of $\kappa_{Iso-Mix}$ relative to κ_{Si-29} was found to be $\sim 30\%$ with the Au substrate underneath the NWs, it was $\sim 24\%$ with the NWs kept suspended, in close agreement with recent theoretical calculations [243].

Additionally, we investigated the phonon behavior in p-$^{28}Si_x{}^{30}Si_{1-x}$ NWs with lamellar stacking faults along the growth axis of the NWs. The correlation of Raman measurements with the HAADF-STEM measurements indicated the presence of 9R polytype within the NWs. In addition, the Raman data revealed that the periodicity of the stacking faults may vary from one NW to the other. We found evidence of a 9R+2H polytype as well as polytypes with no defined periodicity. The evolution of temperature as a function of laser power demonstrated that the lattice thermal conductivity of the 9R phase is reduced by $\sim 18\%$ relative to the 3C phase within the p-$^{28}Si_x{}^{30}Si_{1-x}$ NWs, close to $T = 300K$. The overall thermal conductivity of the p-$^{28}Si_x{}^{30}Si_{1-x}$ NWs is reduced by $\sim 10\%$ compared to the 3C-$^{28}Si_x{}^{30}Si_{1-x}$ NWs, close to $T = 300K$. The overall thermal conductivity of the p-$^{28}Si_x{}^{30}Si_{1-x}$ NWs is reduced by $\sim 32\%$ compared to isotopically pure and diamond cubic 3C-^{29}Si NWs, close to $T = 300K$. The largest reduction in thermal conductivity of $\sim 38\%$ is experienced by the 9R phase within the p-$^{28}Si_x{}^{30}Si_{1-x}$ NWs when compared to the 3C-^{29}Si NWs, close to $T = 300K$. The Raman line-shapes originating from the 3C-$^{28}Si_x{}^{30}Si_{1-x}$ and from the 3C phase within a p-$^{28}Si_x{}^{30}Si_{1-x}$ reveal a linewidth wider by $1.2\ cm^{-1}$ of the latter compared to the former. This is indicative of an additional phonon scattering mechanism presumably at the 3C/9R homo-interfaces within the p-$^{28}Si_x{}^{30}Si_{1-x}$ NWs.

CHAPTER 8 GENERAL DISCUSSION

In this chapter, we discuss the originality and the significance of this thesis. While the originality of the work lies in the novel ideas and the experiments we designed, the significance of the work lies in how the outcome of those experiments helped in answering the scientific questions, key to the core of this thesis.

We reported the first growth of isotopically engineered nanowires. All prior works on the isotope effects on the phonon transport in NWs being theoretical studies, ours was the first experimental demonstration. The theoretical investigations reported a $\sim 20\%$ and $\sim 30\%$ reduction in lattice thermal conductivities for $^{28}Si_{0.5}{}^{29}Si_{0.5}$ and $^{28}Si_{0.5}{}^{42}Si_{0.5}$ NWs respectively, compared to the isotopically pure NWs [9], [10]. Our experimental boundary conditions took into account only the effect of the isotope induced mass disorder, while all other parameters were kept the same between different sets of NWs. The degree of mass disorder and hence the reduction in thermal conductivity for the $^{28}Si_{0.4}{}^{30}Si_{0.6}$ NWs was found to lie in between the two extremum values, and is therefore in line with the theoretical studies. This managed to kindle some interest among the scientific community working on the phononic behavior and the thermoelectric properties in nanoscale materials [243]. Attempting to answer one question, we raised a new one, as the atomistic investigations of single isotopically mixed NW revealed a non-uniform distribution of the two isotopes. The peculiar distribution points towards a process never thought of before, namely the mass-sensitivity of the crystallization dynamics of atoms and the catalyst-NW interface. To ascertain the generality and to reach a definite conclusion about this mechanism, more experiments, as outlined in the following chapter, needs to be undertaken.

The persistent trial and error approach during the atom probe investigations of the isotopic diamond paid off. We demonstrated that indeed it is possible to field evaporate the atoms from a diamond tip in a well-controlled manner. The trick to achieve this control lied in the use of high laser energy and not letting the dc bias increase out of bounds for the atom probe tip to handle. Later, attempts were made by other groups to field evaporate diamond using lower laser energies (order of 100 pJ) which again led to evaporation in clusters of twenty or more atoms [244]. The isotopic modulation of our diamond sample, although did not play any role in controlling the field evaporation, proved to be a blessing in disguise. By using high laser energy to gain control, we compromised on the precision with which the atomic coordinates can be determined. Due to the

temperature rise of the tip surface, the atoms underwent diffusion, affecting the atom probe's spatial resolution adversely. The presence of the isotopically modulated layers enabled us to quantify the diffusion lengths. We showed that only the atoms at the surface of the tip undergo surface diffusion while the rest of the atoms are minimally affected by the temperature rise. This is a significant piece of information, which could be crucial for future tomographic investigations of diamond for quantum information processing applications, where both the control of field evaporation as well as the high spatial resolution and the accurate determination of the spatial coordinates of the defect centers and ^{13}C isotopes are deemed necessary.

The tomographic investigation of the randomness of atoms in the ternary semiconductor alloys was the first of its kind. Earlier studies on III-V alloys comprised either of the theoretical calculations or indirect experimental methods like observing line shapes in the PL spectra to detect the presence or absence of short-range ordering in the alloys. Alternatively, x-ray based techniques generates reciprocal space maps and require extensive curve fittings. Much straightforward relative to these indirect methods is *seeing* the atoms themselves, well-resolved from one another in real space and then using integrated statistical tools to find out the nature of the distribution of different atoms. Our results showed that indeed the atomic distribution can suffer small deviation from a perfect random state, which scales up with the Sn concentration. Although the observed deviation is small, the revelation is significant, which can have far reaching consequences. Different groups around the world are trying to incorporate even higher concentrations of Sn within Si and Ge lattices, in an attempt to tune the band gap and lattice constant independent of each other. It must therefore be remembered that at higher Sn concentrations, the atomic distribution can deviate even more from the perfectly random state, requiring a reassessment of the theoretical predictions of energy gaps. Our results also emphasize the need to undertake a tomographic investigation of any Sn based metastable alloys before any devices are engineered out of them.

In addition to the above-mentioned revelations that the APT measurements on isotopic diamond superlattice and the ternary SiGeSn alloys made, in more ways than one they helped us to achieve the core objective of this thesis. While the Raman analysis on the isotopically mixed $^{28}Si_x{}^{30}Si_{1-x}$ NWs gave an isotopic composition of ^{28}Si: ^{30}Si of 47 at.% and 53 at.%, it was APT which corrected this to an average composition of ^{28}Si: ^{30}Si to 40 at.% and 60 at.%, enabling an accurate quantification of the degree of the mass-disorder. Also, the source of the excess broadening of the Raman line of the $^{28}Si_x{}^{30}Si_{1-x}$ NWs relative to the pure ^{29}Si NWs could never

have been elucidated properly without the revelation of the non-uniform distribution of the two Si isotopes within a $^{28}Si_x{}^{30}Si_{1-x}$ NWs. The first significant contribution of the APT investigations on the diamond isotopic superlattice and the SiGeSn layers, is in laying the foundation of how to make tips for atom probe analysis and to properly analyze subtle effects in 3D data. The standard lift-out technique used in these studies was modified and adapted to make tips out of the $^{28}Si_x{}^{30}Si_{1-x}$ NWs. Surprisingly, despite being the easiest method, no previous APT investigations on NWs report a tip preparation done using this lift-out technique. Next, the art of drawing the iso-concentration surface with morphologically stable results requires an expert eye. The expertise was achieved while defining the $^{13}C/^{12}C$ homointerfaces using the iso-concentration surfaces. The prior knowledge of the width of each isotopically modulated diamond layers helped us in accurately defining the homointerfaces. This knowledge was used to extract the $^{28}Si_x{}^{30}Si_{1-x}$ NW from all the protective Ni coating layer surrounding the NW. Defining a faulty iso-concentration surface would have led to artifacts in the APT reconstructions. The diamond work also helped us with the knowledge of interpreting the mass spectra, looking for atomic clusters and overlaps of peaks in the mass spectra. For example, in the full mass spectra of the $^{28}Si_x{}^{30}Si_{1-x}$ NW along with the surrounding Ni layer, the $^{60}Ni^{+2}$ peak overlapped with the $^{30}Si^{+1}$ and the $^{28}Si^{+1}$ peak partially overlapped with the strong $^{58}Ni^{+2}$ peak. Identifying these overlaps was crucial for the proper definition of the iso-concentration surface to extract the NW out, which was done using only the $^{28}Si^{+2}$ and $^{30}Si^{+2}$ ions to avoid artifacts.

Making a successful APT run also depends to a large extent on the user controlled input parameters like the laser pulse energy, the evaporation rate, and the bias voltage. This was achieved, first with relatively straight forward APT run of the SiGeSn specimen. The parameters conventionally used for Si and/or Ge specimen were used as a starting point. For diamond, it was far more complicated with no prior knowledge of the starting parameters. It was only after several failed attempts and gaining a deep understanding of how the physics of field evaporation works for semiconductors and wide band gap insulators, that the idea to operate the laser at high pulse energy creeped in. Even then, during the APT run with the NWs, several tips fractured leading to only partial reconstruction of the NWs. Thanks to the expertise and knowledge gained from the prior APT experiments, an optimal choice of parameters eventually led to a successful APT investigation and a complete reconstruction of the $^{28}Si_x{}^{30}Si_{1-x}$ NW. The experience gained while analyzing the SiGeSn specimen gave us enough knowledge of how to properly handle an atom probe data set.

The knowledge came in handy during the revelation of the non-uniform distribution of the two Si isotopes within a $^{28}Si_x{}^{30}Si_{1-x}$ NW. The result was very surprising and suggested that isotopes within the NW could have segregated during the growth. We unleashed all the cluster analysis tools to verify for the same but found none. In fact, the actual distribution of the two Si isotopes at the core, the periphery and at the transition region was thoroughly investigated and matched with the expected distribution before coming to the conclusion that the observed effect is a real one and not some strange artifacts coming from the abnormalities in the field evaporation and/or data reconstruction.

As discussed earlier, the two pillars on which the success of isotopically engineered nanomaterials and devices stand are the ability to control the growth and the ability to characterize these materials. APT remains the only technique that can resolve and characterize the isotopes and will continue to be an indispensable part of future isotopically engineered nanomaterials and devices. However, the art of APT is far from being simple which is why such considerable efforts were made to master the technique. For example, an on-going experiment involve a correlative TEM-APT analysis of a p-$^{28}Si_x{}^{30}Si_{1-x}$ NW. The observed reduction in their thermal conductivity, relative to the diamond cubic $^{28}Si_x{}^{30}Si_{1-x}$ NWs and the diamond cubic ^{29}Si NW, needs a proper elucidation as to what fraction of the total reduction is coming from the isotope effect and what fraction from the crystal phase. With initial indications that the isotopes could well be non-uniformly distributed, a proper knowledge of the isotopic composition of each polytypes is necessary before any final conclusions are drawn, hence the need to correlate TEM data with the APT maps. The full arsenal of tip fabrication, APT run, reconstruction, and data handling techniques developed in this thesis will be called for in all similar analysis to follow.

CHAPTER 9 CONCLUSION AND RECOMMENDATIONS

In this chapter, we jot down the main conclusions in brief before moving on to the perspective future works. The main conclusion of this thesis are as follows:

1) Isotopically pure ^{29}Si and isotopically mixed $^{28}Si_x{}^{30}Si_{1-x}$ NWs were grown using Au-catalyzed VLS technique. The average fractional composition of the ^{28}Si and ^{30}Si isotopes within a $^{28}Si_x{}^{30}Si_{1-x}$ NW was determined by APT and was found to be 40.0 at.% and 60.0 at.%, respectively.

2) The phonons in the two sets of NWs were found to behave differently under laser induced heating. Raman nanothermometry on the suspended NWs revealed that the average reduction in the lattice thermal conductivity of the $^{28}Si_x{}^{30}Si_{1-x}$ NWs to be about 24% compared to the ^{29}Si NWs, around $T = 300K$. The same technique applied to NWs dispersed on Au-substrate revealed a reduction of about 30%. However, the value lies within the range of experimental uncertainties of the measurement done on the suspended NWs.

3) Atom probe tomography on a $^{28}Si_x{}^{30}Si_{1-x}$ NW revealed a non-uniform distribution of the two isotopes. Although the apparent reason for this is not conclusive at the moment, it could be related to the mass-sensitivity of the nucleation process during the VLS growth on the main and the truncated facets at the catalyst-NW interface.

4) Raman spectroscopic investigations were also carried out on p-$^{28}Si_x{}^{30}Si_{1-x}$ NWs, having lamellar stacking faults all along the length of a kinked NW. In conjunction with HRTEM images we ascertained the presence of 9R polytypic Si, bounded by regions with cubic Si. In some of the p-$^{28}Si_x{}^{30}Si_{1-x}$ NWs, we also found evidence of the presence of a 9R+2H polytype and aperiodic polytypes.

5) The lattice thermal conductivity of the 9R phase is reduced by about 18% relative to the 3C phase within the p-$^{28}Si_x{}^{30}Si_{1-x}$ NWs, around $T = 300K$. The overall thermal conductivity of the p-$^{28}Si_x{}^{30}Si_{1-x}$ NWs is reduced by about 10% when compared to the diamond cubic 3C-$^{28}Si_x{}^{30}Si_{1-x}$ NWs and by about 32% compared to isotopically pure and 3C-^{29}Si NWs, around $T = 300K$. The 9R phase within the p-$^{28}Si_x{}^{30}Si_{1-x}$ NWs experiences the largest reduction in thermal conductivity of about 37% around $T = 300K$, when compared to the 3C-^{29}Si NWs.

6) A controlled field-evaporation of diamond was achieved in atom probe tomography. We highlighted that the key to achieve control during the field evaporation of such materials with large evaporation fields is to operate the atom probe at high laser energies. We also discussed that an avalanche breakdown mechanism is responsible for the free carrier generation within the diamond tip.

7) Alongside other revelations like the presence of a non-uniform temperature distribution and how the different cations and atomic complexes are distributed within a diamond tip, a major highlight of the investigation was related to the diffusion of atoms during the laser assisted evaporation. Our results showed that the atoms at the surface, on the illuminated side of the tip undergoes the most diffusion, due to the temperature rise induced by the energetic laser pulses. Barring these atoms located to within 3-4 nm from the surface at the illuminated side, the remaining atoms are minimally affected by the laser pulses and do not undergo any significant diffusion to adversely affect the spatial resolution of the atom probe.

8) Atom probe investigations of the ternary SiGeSn alloys confirmed the absence of any form of Sn aggregates. However, it showed that the distribution of the atoms within such a metastable alloy might deviate from the expected random state, especially when the Sn concentration within an alloy is high. In our experiments, Si was found to deviate from the expected distribution, a phenomenon which was argued to be coming from a repulsive interaction between the largely dissimilar sized Si and Sn atoms.

With a lot more to be done, we have barely managed to scratch the surface of isotope engineering in nanoscale and quantum materials. The non-uniform distribution of the two isotopes within a $^{28}Si_x{}^{30}Si_{1-x}$ NW needs a deeper understanding before one can arrive at a definite conclusion regarding the root cause of this effect. The easiest way to ascertain if the presence of the truncated facets has any role to play, is to first determine (theoretically or by *in situ* TEM) two other (non-Au) metal catalysts, well-known for the VLS growth of Si NWs, one of which also give rise to these truncated facets while the other doesn't. The $^{28}Si_x{}^{30}Si_{1-x}$ NWs are then to be grown using these two metal catalysts and investigated subsequently in atom probe. Additionally, the molecular dynamics simulations which demonstrated the nucleation of Si atoms on the main and the truncated facets during the VLS growth of Au catalyzed Si NWs [231], should be tried out with two different masses of the ad-atoms, resembling the two isotopes used during our experiments.

This could be an alternate route to clearly elucidate the dynamics of VLS growth at the atomistic-level. The effect of polytypism and mass-disorder needs to be investigated in more detail. One way to do it would be to synthesize isotopically pure NWs with lamellar stacking faults. The combined effects of isotope and crystal phase can be investigated by studying the phonon transport in the p-^{29}Si NWs and the p-$^{28}Si_x{}^{30}Si_{1-x}$ NWs and compare them with the diamond cubic counterparts.

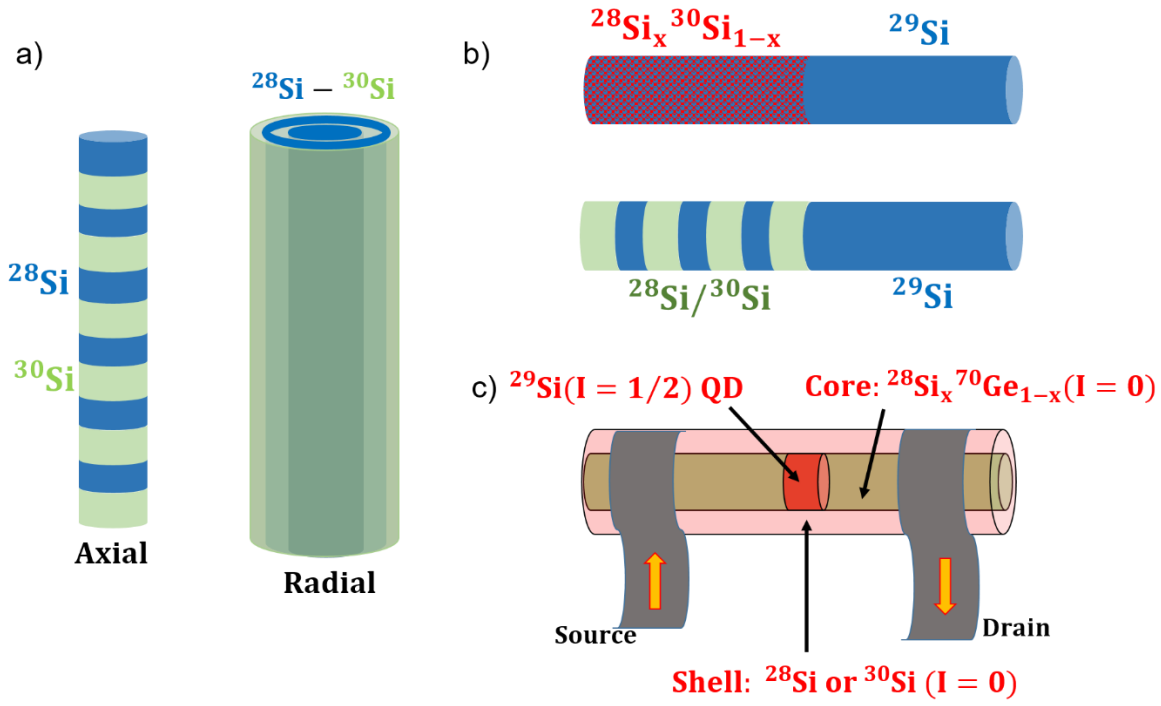

Figure 9.1: *(a) Schematic illustrations of a ^{28}Si-^{30}Si axial (left) and radial (right) superlattice NW. (b) Schematic illustration of axial homojunction NWs: a $^{28}Si_x{}^{30}Si_{1-x}$/^{28}Si NW (top) and a ^{28}Si-^{30}Si/^{28}Si NW (bottom). (c) Schematic illustration of a nuclear spin-engineered device with the antiparallelly magnetized ferromagnetic source/drain electrodes, tunnel-coupled to the ^{29}Si quantum dot.*

Theoretical calculations have shown that the lattice thermal conductivity in isotopic superlattice structures is significantly reduced from the natural or isotopically pure counterparts [64]. The experimental verification of the same could come from the synthesis of ^{28}Si/^{30}Si axial NWs such as the ones shown in the schematic illustration in Figure 9.1(a), subsequent APT analysis to know the interface sharpness and width of the isotopically modulated layers and finally

performing thermal conductivity measurements. The existing $^{28}Si_x{}^{30}Si_{1-x}$ NWs can be put under rapid thermal annealing (after etching the Au catalyst) which should evenly mix the non-uniformly distributed isotopes and can easily be verified using APT. Subsequent nanothermometric measurements could be undertaken to see if the non-uniformity affects the phonon transport to any significant extent. If found, the effect of this radial isotopic arrangement can be exploited by synthesizing isotopic core-shell and radial superlattices, like the one shown schematically in Figure 9.1(a). More exotic isotopically engineered Si NWs can be synthesized like those shown schematically in Figure 9.1(b), where one part of a NW is isotopically mixed or an isotopic axial superlattice and the other part is isotopically enriched. Such NWs can be used to realize a novel class of phononic devices such as phononic diodes and transistors. Rectification, which is the primary requirement of any two-terminal diode operation would require an asymmetry in the heat flow in one direction relative to the opposite direction. To achieve the same, a variety of concepts have been proposed involving the control of thermal conductivity through either chemical or morphological alteration of one side of the device structure [245]. This induces an increase in the interface thermal resistance which limits the rectification effect. To overcome this, the precise control of the isotopic content along the long axis of a NW can be implemented to achieve the necessary rectification without affecting the morphology or the chemical composition of the NWs. Such two-terminal phononic diodes can be used as a basic building block for the three-terminal phononic transistors, thereby opening up a viable opportunity to use the heat that gets rejected in modern day electronic circuit boards, as information carriers. The heat current flow from source to drain and can be manipulated by an independent phonon reservoir. By changing the temperature of the phonon bath, the I-V characteristics can be modified, in a similar fashion to the classical electronic transistors.

Isotope engineering can also be used to tailor the location and the composition of the nuclear spin-full ^{29}Si quantum dot embedded within a nuclear spin-free $^{28}Si_x{}^{70}Ge_{1-x}/^{28}Si$ core-shell NW, as schematically illustrated in Figure 9.1(c). Such devices hold the potential to form the nanoscale building block for quantum information processing, wherein the fast electron spins bound to the donor ^{31}P atoms can be used for quantum manipulation and read-out, while the long-lived slow nuclear-spin of the dot can be used for information storage. A structure such as the one shown in the schematic can not only exploit the collective quantum coherence in many nuclear magnetic moments to achieve ultra-fast switching of nuclear magnetization but also the usage of the spin

free core-shell structure will enable wave function engineering, thus allowing the quantum state of the electron to be optimized [246]. This thesis gives us the necessary confidence that not only can the isotopic composition and distribution be tailor made during the synthesis of nanoscale materials but also can be characterized with the utmost precision. The series of studies conducted in this thesis pave the way to dive deeper and explore the isotope effect in such novel and more exotic family of nano and quantum scale isotopically engineered semiconductors and exploit them in a variety of unique and innovative devices.

BIBLIOGRAPHY

[1] F. Soddy, “The Origins of the Conception of Isotopes - Nobel Lecture,” 1922.

[2] J. R. De Laeter, K. G. Heumann, and K. J. R. Rosman, “Isotopic Compositions of the Elements 1989,” *J. Phys. Chem. Ref. Data*, vol. 20, no. 6, pp. 1327–1337, Nov. 1991.

[3] E. E. Haller, “Isotopically engineered semiconductors,” *J. Appl. Phys.*, vol. 77, no. 7, p. 2857, Apr. 1995.

[4] R. K. Kremer, K. Graf, M. Cardona, G. G. Devyatykh, A. V. Gusev, A. M. Gibin, A. V. Inyushkin, A. N. Taldenkov, and H.-J. Pohl, “Thermal conductivity of isotopically enriched ^{28}Si: revisited,” *Solid State Commun.*, vol. 131, no. 8, pp. 499–503, Aug. 2004.

[5] M. Hu, H. Sinn, A. Alatas, W. Sturhahn, E. Alp, H. Wille, Y. Shvyd’ko, J. Sutter, J. Bandaru, E. Haller, V. Ozhogin, S. Rodriguez, R. Colella, E. Kartheuser, and M. Villeret, “Effect of isotopic composition on the lattice parameter of germanium measured by x-ray backscattering,” *Phys. Rev. B*, vol. 67, no. 11, 2003.

[6] G. Davies, E. C. Lightowlers, K. Itoh, W. L. Hansen, E. E. Haller, and V. Ozhogin, “Isotope dependence of the indirect energy gap of germanium,” *Semicond. Sci. Technol.*, vol. 7, no. 10, pp. 1271–1273, Oct. 1992.

[7] S. Simmons, R. M. Brown, H. Riemann, N. V Abrosimov, P. Becker, H.-J. Pohl, M. L. W. Thewalt, K. M. Itoh, and J. J. L. Morton, “Entanglement in a solid-state spin ensemble.,” *Nature*, vol. 470, no. 7332, pp. 69–72, Feb. 2011.

[8] H. Watanabe, C. E. Nebel, and S. Shikata, “Isotopic homojunction band engineering from diamond.,” *Science*, vol. 324, no. 5933, pp. 1425–8, Jun. 2009.

[9] N. Yang, G. Zhang, and B. Li, “Ultralow thermal conductivity of isotope-doped silicon nanowires.,” *Nano Lett.*, vol. 8, no. 1, pp. 276–80, Jan. 2008.

[10] J. Hattori and S. Uno, “Impact of Isotope Doping on Phonon Thermal Transport in Silicon Nanowires,” *Jpn. J. Appl. Phys.*, vol. 52, no. 4S, p. 04CN04, Apr. 2013.

[11] O. Nishikawa, T. Sekine, Y. Ohtani, K. Maeda, Y. Numada, M. Watanabe, M. Iwatsuki, S. Aoki, J. Itoh, and K. Yamanaka, “Development of a scanning atom probe and atom-by-atom mass analysis of diamonds,” *Appl. Phys. A Mater. Sci. Process.*, vol. 66, no. 7, pp. S11–S16,

Mar. 1998.

[12] J. B. Lewis, D. Isheim, C. Floss, T. Daulton, D. N. Seidman, P. R. Heck, A. M. Davis, M. J. Pellin, M. R. Savina, J. Hiller, A. Mane, J. Elam, O. Auciello, and T. Stephan, "Meteoritic Nanodiamond Analysis by Atom-Probe Tomography," *43rd Lunar Planet. Sci. Conf. held March 19-23, 2012 Woodlands, Texas. LPI Contrib. No. 1659, id.2192*, vol. 43, 2012.

[13] A. Cooper, E. Magesan, H. N. Yum, P. Cappellaro, and R. Walsworth, "Time-resolved magnetic sensing with electronic spins in diamond," *Nat. Commun.*, vol. 5, p. 20503, Jan. 2014.

[14] L. Childress, M. V. Gurudev Dutt, J. M. Taylor, A. S. Zibrov, F. Jelezko, J. Wrachtrup, P. R. Hemmer, and M. D. Lukin, "Coherent Dynamics of Coupled Electron and Nuclear Spin Qubits in Diamond," *Science*, vol. 314, no. 5797, pp. 281–285, Oct. 2006.

[15] F. Jelezko, T. Gaebel, I. Popa, M. Domhan, A. Gruber, and J. Wrachtrup, "Observation of Coherent Oscillation of a Single Nuclear Spin and Realization of a Two-Qubit Conditional Quantum Gate," *Phys. Rev. Lett.*, vol. 93, no. 13, p. 130501, Sep. 2004.

[16] A. Mascarenhas, S. Kurtz, A. Kibbler, and J. Olson, "Polarized band-edge photoluminescence and ordering in Ga0.52In0.48P.," *Phys. Rev. Lett.*, vol. 63, no. 19, pp. 2108–2111, Nov. 1989.

[17] T. Kanata, M. Nishimoto, H. Nakayama, and T. Nishino, "Valence-band splitting in ordered $Ga_{0.5}In_{0.5}P$ studied by temperature-dependent photoluminescence polarization," *Phys. Rev. B*, vol. 45, no. 12, pp. 6637–6642, Mar. 1992.

[18] D. C. Meyer, K. Richter, P. Paufler, and G. Wagner, "X-ray analysis of the short-range order in the ordered-alloy domains of epitaxial (Ga,In)P layers by diffraction anomalous fine structure of superlattice reflections," *Phys. Rev. B*, vol. 59, no. 23, pp. 15253–15260, Jun. 1999.

[19] R. C. Jones and W. H. Furry, "The Separation of Isotopes by Thermal Diffusion," *Rev. Mod. Phys.*, vol. 18, no. 2, pp. 151–224, Apr. 1946.

[20] W. H. Furry, R. C. Jones, and L. Onsager, "On the Theory of Isotope Separation by Thermal Diffusion," *Phys. Rev.*, vol. 55, no. 11, pp. 1083–1095, Jun. 1939.

[21] I. Chavet and R. Bernas, “Experimental study of an ion source for electromagnetic isotope separation with a view to high efficiency operation,” *Nucl. Instruments Methods*, vol. 51, no. 1, pp. 77–86, May 1967.

[22] J. H. Freeman, “A new ion source for electromagnetic isotope separators,” *Nucl. Instruments Methods*, vol. 22, pp. 306–316, Mar. 1963.

[23] F. M. Richter, E. B. Watson, R. A. Mendybaev, F.-Z. Teng, and P. E. Janney, “Magnesium isotope fractionation in silicate melts by chemical and thermal diffusion,” *Geochim. Cosmochim. Acta*, vol. 72, no. 1, pp. 206–220, Jan. 2008.

[24] F. Huang, P. Chakraborty, C. C. Lundstrom, C. Holmden, J. J. G. Glessner, S. W. Kieffer, and C. E. Lesher, “Isotope fractionation in silicate melts by thermal diffusion.,” *Nature*, vol. 464, no. 7287, pp. 396–400, Mar. 2010.

[25] V. S. Letokhov, “Laser isotope separation,” *Nature*, vol. 277, no. 5698, pp. 605–610, Feb. 1979.

[26] G. Meyer-Kretschmer and H. Jetter, “Laser isotope separation of uranium,” Naturwissenschaften, vol. 70, no. 7, p. 7-14, 1983.

[27] M. Saleem, S. Hussain, M. Rafiq, and M. A. Baig, “Laser isotope separation of lithium by two-step photoionization,” *J. Appl. Phys.*, vol. 100, no. 5, p. 53111, Sep. 2006.

[28] I. E. Olivares, A. E. Duarte, E. A. Saravia, and F. J. Duarte, “Lithium Isotope Separation With Tunable Diode Lasers,” *Appl. Opt.*, vol. 41, no. 15, p. 2973, May 2002.

[29] L. Vegard, “Die Konstitution der Mischkristalle und die Raumfüllung der Atome,” *Zeitschrift für Phys.*, vol. 5, no. 1, pp. 17–26, Jan. 1921.

[30] F. Widulle, T. Ruf, M. Konuma, I. Silier, M. Cardona, W. Kriegseis, and V. I. Ozhogin, “Isotope effects in elemental semiconductors: a Raman study of silicon,” *Solid State Commun.*, vol. 118, no. 1, pp. 1–22, Mar. 2001.

[31] H. D. Fuchs, C. H. Grein, M. Cardona, W. L. Hansen, K. Itoh, and E. E. Haller, “Isotopic disorder-effects on the phonons in germanium,” *Solid State Commun.*, vol. 82, no. 4, pp. 225–228, Apr. 1992.

[32] H. Fuchs, C. Grein, R. Devlen, J. Kuhl, and M. Cardona, “Anharmonic decay time, isotopic

scattering time, and inhomogeneous line broadening of optical phonons in Ge70, Ge76, and natural Ge crystals," *Phys. Rev. B*, vol. 44, no. 16, pp. 8633–8642, 1991.

[33] J. M. Zhang, M. Giehler, A. Göbel, T. Ruf, M. Cardona, E. E. Haller, and K. Itoh, "Optical phonons in isotopic Ge studied by Raman scattering," *Phys. Rev. B*, vol. 57, no. 3, pp. 1348–1351, Jan. 1998.

[34] H. D. Fuchs, C. H. Grein, C. Thomsen, M. Cardona, W. L. Hansen, E. E. Haller, and K. Itoh, "Comparison of the phonon spectra of Ge70 and natural Ge crystals: Effects of isotopic disorder," *Phys. Rev. B*, vol. 43, no. 6, pp. 4835–4842, Feb. 1991.

[35] S. Tamura, "Isotope scattering of dispersive phonons in Ge," *Phys. Rev. B*, vol. 27, no. 2, pp. 858–866, Jan. 1983.

[36] P. G. Klemens, "Anharmonic Decay of Optical Phonons," *Phys. Rev.*, vol. 148, no. 2, pp. 845–848, Aug. 1966.

[37] J. Menéndez and M. Cardona, "Temperature dependence of the first-order Raman scattering by phonons in Si, Ge, and $\alpha - Sn$: Anharmonic effects," *Phys. Rev. B*, vol. 29, no. 4, pp. 2051–2059, Feb. 1984.

[38] M. Balkanski, R. Wallis, and E. Haro, "Anharmonic effects in light scattering due to optical phonons in silicon," *Phys. Rev. B*, vol. 28, no. 4, pp. 1928–1934, 1983.

[39] J. Spitzer, T. Ruf, M. Cardona, W. Dondl, R. Schorer, G. Abstreiter, and E. E. Haller, "Raman scattering by optical phonons in isotopic $^{70}(Ge)_n$ $^{74}(Ge)_n$ superlattices," *Phys. Rev. Lett.*, vol. 72, no. 10, pp. 1565–1568, Mar. 1994.

[40] T. Kojima, R. Nebashi, K. M. Itoh, and Y. Shiraki, "Growth and characterization of $^{28}(Si)_n$ $^{30}(Si)_n$ isotope superlattices," *Appl. Phys. Lett.*, vol. 83, no. 12, p. 2318, 2003.

[41] M. Cardona, "Renormalization of the Optical Response of Semiconductors by Electron-Phonon Interaction," *Phys. status solidi*, vol. 188, no. 4, pp. 1209–1232, Dec. 2001.

[42] N. Garro, A. Cantarero, M. Cardona, A. Göbel, T. Ruf, and K. Eberl, "Dependence of the lattice parameters and the energy gap of zinc-blende-type semiconductors on isotopic masses," *Phys. Rev. B*, vol. 54, no. 7, pp. 4732–4740, Aug. 1996.

[43] S. Zollner, M. Cardona, and S. Gopalan, "Isotope and temperature shifts of direct and

indirect band gaps in diamond-type semiconductors," *Phys. Rev. B*, vol. 45, no. 7, pp. 3376–3385, Feb. 1992.

[44] G. Davies, J. Hartung, V. Ozhogin, K. Itoh, W. L. Hansen, and E. E. Haller, "Effects of isotope disorder on phonons in germanium determined from bound exciton luminescence," *Semicond. Sci. Technol.*, vol. 8, no. 1, pp. 127–130, Jan. 1993.

[45] G. Davies, E. C. Lightowlers, T. S. Hui, V. Ozhogin, K. M. Itoh, W. L. Hansen, and E. E. Haller, "Isotope dependence of the lowest direct energy gap in crystalline germanium," *Semicond. Sci. Technol.*, vol. 8, no. 12, pp. 2201–2204, Dec. 1993.

[46] C. Parks, A. K. Ramdas, S. Rodriguez, K. M. Itoh, and E. E. Haller, "Electronic band structure of isotopically pure germanium: Modulated transmission and reflectivity study," *Phys. Rev. B*, vol. 49, no. 20, pp. 14244–14250, May 1994.

[47] D. Ronnow, L. F. LastrasMartinez, and M. Cardona, "Isotope effects on the electronic critical points of germanium: Ellipsometric investigation of the E_1 and $E_1+\Delta_1$ transitions," *Eur. Phys. J. B*, vol. 5, no. 1, pp. 29–35, 1998.

[48] D. Karaiskaj, M. L. W. Thewalt, T. Ruf, M. Cardona, and M. Konuma, "Photoluminescence studies of isotopically enriched silicon: isotopic effects on the indirect electronic band gap and phonon energies," *Solid State Commun.*, vol. 123, no. 3–4, pp. 87–92, Jul. 2002.

[49] H. Watanabe, T. Koretsune, S. Nakashima, S. Saito, and S. Shikata, "Isotope composition dependence of the band-gap energy in diamond," *Phys. Rev. B*, vol. 88, no. 20, p. 205420, Nov. 2013.

[50] A. Debernardi and M. Cardona, "Isotopic effects on the lattice constant in compound semiconductors by perturbation theory: An ab initio calculation," *Phys. Rev. B*, vol. 54, no. 16, pp. 11305–11310, Oct. 1996.

[51] E. Sozontov, L. X. Cao, A. Kazimirov, V. Kohn, M. Konuma, M. Cardona, and J. Zegenhagen, "X-ray standing wave analysis of the effect of isotopic composition on the lattice constants of Si and Ge.," *Phys. Rev. Lett.*, vol. 86, no. 23, pp. 5329–32, Jun. 2001.

[52] H. Holloway, K. C. Hass, M. A. Tamor, T. R. Anthony, and W. F. Banholzer, "Isotopic dependence of the lattice constant of diamond," *Phys. Rev. B*, vol. 44, no. 13, pp. 7123–7126, Oct. 1991.

[53] I. Y. Pomeranchuk, “Thermal Conductivity of Dielectrics below Debye Temperatures,” *Zh. Eksp. Teor. Fiz*, vol. 12, p. 245, Dec. 1942.

[54] V. I. Ozhogin, A. V. Inyushkin, A. N. Taldenkov, A. V. Tikhomirov, G. É. Popov, E. Haller, and K. Itoh, “Isotope effect in the thermal conductivity of germanium single crystals,” *J. Exp. Theor. Phys. Lett.*, vol. 63, no. 6, pp. 490–494, Mar. 1996.

[55] M. Asen-Palmer, K. Bartkowski, E. Gmelin, M. Cardona, A. P. Zhernov, A. V. Inyushkin, A. Taldenkov, V. I. Ozhogin, K. M. Itoh, and E. E. Haller, “Thermal conductivity of germanium crystals with different isotopic compositions,” *Phys. Rev. B*, vol. 56, no. 15, pp. 9431–9447, Oct. 1997.

[56] H. B. G. Casimir, “Note on the conduction of heat in crystals,” *Physica*, vol. 5, no. 6, pp. 495–500, Jun. 1938.

[57] R. Peierls, “Kinetic theory of heat conduction in crystals,” *Ann. Phys.*, vol. 3, pp. 1055–1101, 1929.

[58] T. Ruf, R. W. Henn, M. Asen-Palmer, E. Gmelin, M. Cardona, H.-J. Pohl, G. G. Devyatych, and P. G. Sennikov, “Thermal conductivity of isotopically enriched silicon,” *Solid State Commun.*, vol. 115, no. 5, pp. 243–247, Jun. 2000.

[59] D. T. Morelli, J. P. Heremans, and G. A. Slack, “Estimation of the isotope effect on the lattice thermal conductivity of group IV and group III-V semiconductors,” *Phys. Rev. B*, vol. 66, no. 19, p. 195304, Nov. 2002.

[60] D. G. Onn, A. Witek, Y. Z. Qiu, T. R. Anthony, and W. F. Banholzer, “Some aspects of the thermal conductivity of isotopically enriched diamond single crystals,” *Phys. Rev. Lett.*, vol. 68, no. 18, pp. 2806–2809, May 1992.

[61] J. R. Olson, R. O. Pohl, J. W. Vandersande, A. Zoltan, T. R. Anthony, and W. F. Banholzer, “Thermal conductivity of diamond between 170 and 1200 K and the isotope effect,” *Phys. Rev. B*, vol. 47, no. 22, pp. 14850–14856, Jun. 1993.

[62] L. Wei, P. K. Kuo, R. L. Thomas, T. R. Anthony, and W. F. Banholzer, “Thermal conductivity of isotopically modified single crystal diamond,” *Phys. Rev. Lett.*, vol. 70, no. 24, pp. 3764–3767, Jun. 1993.

[63] H. Bracht, N. Wehmeier, S. Eon, A. Plech, D. Issenmann, J. Lundsgaard Hansen, A. Nylandsted Larsen, J. W. Ager, and E. E. Haller, "Reduced thermal conductivity of isotopically modulated silicon multilayer structures," *Appl. Phys. Lett.*, vol. 101, no. 6, p. 64103, Aug. 2012.

[64] H. Bracht, S. Eon, R. Frieling, A. Plech, D. Issenmann, D. Wolf, J. Lundsgaard Hansen, A. Nylandsted Larsen, J. W. Ager Iii, and E. E. Haller, "Thermal conductivity of isotopically controlled silicon nanostructures," *New J. Phys.*, vol. 16, no. 1, p. 15021, 2014.

[65] S. Chen, Q. Wu, C. Mishra, J. Kang, H. Zhang, K. Cho, W. Cai, A. A. Balandin, and R. S. Ruoff, "Thermal conductivity of isotopically modified graphene.," *Nat. Mater.*, vol. 11, no. 3, pp. 203–7, Mar. 2012.

[66] M. Cardona, "Isotopic Effects in the Phonon and Electron Dispersion Relations of Crystals," *Phys. status solidi*, vol. 220, no. 1, pp. 5–18, Jul. 2000.

[67] H. J. Hrostowski and R. H. Kaiser, "Infrared Absorption of Oxygen in Silicon," *Phys. Rev.*, vol. 107, no. 4, pp. 966–972, Aug. 1957.

[68] M. Gienger, M. Glaser, and K. Laβmann, "Phonon spectroscopy of the low energy vibrations of interstitial oxygen in germanium," *Solid State Commun.*, vol. 86, no. 5, pp. 285–289, May 1993.

[69] A. J. Mayur, M. D. Sciacca, M. K. Udo, A. K. Ramdas, K. Itoh, J. Wolk, and E. E. Haller, "Fine structure of the asymmetric stretching vibration of dispersed oxygen in monoisotopic germanium," *Phys. Rev. B*, vol. 49, no. 23, pp. 16293–16299, Jun. 1994.

[70] J. Kato, K. M. Itoh, H. Yamada-Kaneta, and H.-J. Pohl, "Host isotope effect on the localized vibrational modes of oxygen in isotopically enriched ^{28}Si , ^{29}Si , and ^{30}Si single crystals," *Phys. Rev. B*, vol. 68, no. 3, p. 35205, Jul. 2003.

[71] D. Karaiskaj, M. Thewalt, T. Ruf, M. Cardona, H.-J. Pohl, G. Deviatych, P. Sennikov, and H. Riemann, "Photoluminescence of Isotopically Purified Silicon: How Sharp are Bound Exciton Transitions?," *Phys. Rev. Lett.*, vol. 86, no. 26, pp. 6010–6013, Jun. 2001.

[72] D. Karaiskaj, M. L. W. Thewalt, T. Ruf, M. Cardona, and M. Konuma, "'Intrinsic' Acceptor Ground State Splitting in Silicon: An Isotopic Effect," *Phys. Rev. Lett.*, vol. 89, no. 1, p. 16401, Jun. 2002.

[73] Y. Shimizu, M. Uematsu, and K. M. Itoh, “Experimental evidence of the vacancy-mediated silicon self-diffusion in single-crystalline silicon.,” *Phys. Rev. Lett.*, vol. 98, no. 9, p. 95901, Mar. 2007.

[74] H. Bracht, E. Haller, and R. Clark-Phelps, “Silicon Self-Diffusion in Isotope Heterostructures,” *Phys. Rev. Lett.*, vol. 81, no. 2, pp. 393–396, Jul. 1998.

[75] D. Karaiskaj, T. A. Meyer, M. L. W. Thewalt, and M. Cardona, “Dependence of the ionization energy of shallow donors and acceptors in silicon on the host isotopic mass,” *Phys. Rev. B*, vol. 68, no. 12, p. 121201, Sep. 2003.

[76] B. Pajot, B. Clerjaud, and M. D. McCluskey, “Isotope effects in the electronic spectrum of S^+ and Se^+ in silicon,” *Phys. Rev. B*, vol. 69, no. 8, p. 85210, Feb. 2004.

[77] M. L. W. Thewalt, M. Steger, A. Yang, N. Stavrias, M. Cardona, H. Riemann, N. V. Abrosimov, M. F. Churbanov, A. V. Gusev, A. D. Bulanov, I. D. Kovalev, A. K. Kaliteevskii, O. N. Godisov, P. Becker, H.-J. Pohl, J. W. Ager, and E. E. Haller, “Can highly enriched ^{28}Si reveal new things about old defects?,” *Phys. B Condens. Matter*, vol. 401, pp. 587–592, 2007.

[78] M. Steger, A. Yang, N. Stavrias, M. L. W. Thewalt, H. Riemann, N. V. Abrosimov, M. F. Churbanov, A. V. Gusev, A. D. Bulanov, I. D. Kovalev, A. K. Kaliteevskii, O. N. Godisov, P. Becker, and H.-J. Pohl, “Reduction of the Linewidths of Deep Luminescence Centers in ^{28}Si Reveals Fingerprints of the Isotope Constituents,” *Phys. Rev. Lett.*, vol. 100, no. 17, p. 177402, Apr. 2008.

[79] M. Steger, A. Yang, T. Sekiguchi, K. Saeedi, M. L. W. Thewalt, M. O. Henry, K. Johnston, H. Riemann, N. V. Abrosimov, M. F. Churbanov, A. V. Gusev, A. D. Bulanov, I. D. Kaliteevski, O. N. Godisov, P. Becker, and H.-J. Pohl, “Isotopic fingerprints of gold-containing luminescence centers in ^{28}Si,” *Phys. B Condens. Matter*, vol. 404, no. 23, pp. 5050–5053, 2009.

[80] M. Steger, A. Yang, T. Sekiguchi, K. Saeedi, M. L. W. Thewalt, M. O. Henry, K. Johnston, E. Alves, U. Wahl, H. Riemann, N. V. Abrosimov, M. F. Churbanov, A. V. Gusev, A. K. Kaliteevskii, O. N. Godisov, P. Becker, and H.-J. Pohl, “Isotopic fingerprints of Pt-containing luminescence centers in highly enriched ^{28}Si,” *Phys. Rev. B*, vol. 81, no. 23, p.

235217, Jun. 2010.

[81] H. Fuchs, W. Walukiewicz, E. Haller, W. Dondl, R. Schorer, G. Abstreiter, A. Rudnev, A. Tikhomirov, and V. Ozhogin, "Germanium ^{70}Ge/^{74}Ge isotope heterostructures: An approach to self-diffusion studies," *Phys. Rev. B*, vol. 51, no. 23, pp. 16817–16821, Jun. 1995.

[82] E. Hüger, U. Tietze, D. Lott, H. Bracht, D. Bougeard, E. E. Haller, and H. Schmidt, "Self-diffusion in germanium isotope multilayers at low temperatures," *Appl. Phys. Lett.*, vol. 93, no. 16, p. 162104, Oct. 2008.

[83] O. Moutanabbir, S. Miyamoto, E. E. Haller, and K. M. Itoh, "Transport of Deposited Atoms throughout Strain-Mediated Self-Assembly," *Phys. Rev. Lett.*, vol. 105, no. 2, p. 26101, Jul. 2010.

[84] B. E. Kane, "A silicon-based nuclear spin quantum computer," *Nature*, vol. 393, pp. 133–137, 1998.

[85] K. M. Itoh, "An all-silicon linear chain NMR quantum computer," *Solid State Commun.*, vol. 133, no. 11, pp. 747–752, 2005.

[86] M. Steger, T. Sekiguchi, A. Yang, K. Saeedi, M. E. Hayden, M. L. W. Thewalt, K. M. Itoh, H. Riemann, N. V. Abrosimov, P. Becker, and H.-J. Pohl, "Optically-detected NMR of optically-hyperpolarized ^{31}P neutral donors in ^{28}Si," *J. Appl. Phys.*, vol. 109, no. 10, p. 102411, May 2011.

[87] A. Yang, M. Steger, T. Sekiguchi, M. L. W. Thewalt, T. D. Ladd, K. M. Itoh, H. Riemann, N. V. Abrosimov, P. Becker, and H.-J. Pohl, "Simultaneous Subsecond Hyperpolarization of the Nuclear and Electron Spins of Phosphorus in Silicon by Optical Pumping of Exciton Transitions," *Phys. Rev. Lett.*, vol. 102, no. 25, p. 257401, Jun. 2009.

[88] H. Hayashi, T. Itahashi, K. M. Itoh, L. S. Vlasenko, and M. P. Vlasenko, "Dynamic nuclear polarization of ^{29}Si nuclei in isotopically controlled phosphorus doped silicon," *Phys. Rev. B*, vol. 80, no. 4, p. 45201, Jul. 2009.

[89] W. Akhtar, V. Filidou, T. Sekiguchi, E. Kawakami, T. Itahashi, L. Vlasenko, J. J. L. Morton, and K. M. Itoh, "Coherent Storage of Photoexcited Triplet States Using ^{29}Si Nuclear Spins in Silicon," *Phys. Rev. Lett.*, vol. 108, no. 9, p. 97601, Feb. 2012.

[90] J. T. Muhonen, J. P. Dehollain, A. Laucht, F. E. Hudson, R. Kalra, T. Sekiguchi, K. M. Itoh, D. N. Jamieson, J. C. McCallum, A. S. Dzurak, and A. Morello, "Storing quantum information for 30 seconds in a nanoelectronic device," *Nat. Nanotechnol.*, vol. 9, no. 12, pp. 986–991, Oct. 2014.

[91] M. Steger, K. Saeedi, M. L. Thewalt, J. J. Morton, H. Riemann, N. V Abrosimov, P. Becker, and H. J. Pohl, "Quantum information storage for over 180 s using donor spins in a ^{28}Si 'semiconductor vacuum,'" *Science*, vol. 336, no. 6086, pp. 1280–1283, 2012.

[92] M. Veldhorst, J. C. C. Hwang, C. H. Yang, A. W. Leenstra, B. de Ronde, J. P. Dehollain, J. T. Muhonen, F. E. Hudson, K. M. Itoh, A. Morello, and A. S. Dzurak, "An addressable quantum dot qubit with fault-tolerant control-fidelity," *Nat. Nanotechnol.*, vol. 9, no. 12, pp. 981–985, Oct. 2014.

[93] F. Dolde, I. Jakobi, B. Naydenov, N. Zhao, S. Pezzagna, C. Trautmann, J. Meijer, P. Neumann, F. Jelezko, and J. Wrachtrup, "Room-temperature entanglement between single defect spins in diamond," *Nat. Phys.*, vol. 9, no. 3, pp. 139–143, Feb. 2013.

[94] G. Balasubramanian, P. Neumann, D. Twitchen, M. Markham, R. Kolesov, N. Mizuochi, J. Isoya, J. Achard, J. Beck, J. Tissler, V. Jacques, P. R. Hemmer, F. Jelezko, and J. Wrachtrup, "Ultralong spin coherence time in isotopically engineered diamond," *Nat. Mater.*, vol. 8, no. 5, pp. 383–387, May 2009.

[95] E. W. Müller, "Das Feldionenmikroskop," *Zeitschrift für Phys.*, vol. 131, no. 1, pp. 136–142, Mar. 1951.

[96] E. W. Müller, "Study of Atomic Structure of Metal Surfaces in the Field Ion Microscope," *J. Appl. Phys.*, vol. 28, no. 1, p. 1, 1957.

[97] E. W. Müller, J. A. Panitz, and S. B. McLane, "The Atom-Probe Field Ion Microscope," *Rev. Sci. Instrum.*, vol. 39, no. 1, p. 83, Nov. 1968.

[98] J. A. Panitz, "The 10 cm Atom Probe," *Rev. Sci. Instrum.*, vol. 44, no. 8, p. 1034, Nov. 1973.

[99] A. Cerezo, T. J. Godfrey, and G. D. W. Smith, "Application of a position-sensitive detector to atom probe microanalysis," *Rev. Sci. Instrum.*, vol. 59, no. 6, p. 862, Jun. 1988.

[100] O. Nishikawa, M. Kimoto, M. Iwatsuki, and Y. Ishikawa, "Development of a scanning atom

probe," *J. Vac. Sci. Technol. B*, vol. 13, no. 2, p. 599, Mar. 1995.

[101] T. F. Kelly, P. P. Camus, D. J. Larson, L. M. Holzman, and S. S. Bajikar, "On the many advantages of local-electrode atom probes," *Ultramicroscopy*, vol. 62, no. 1–2, pp. 29–42, Jan. 1996.

[102] B. Gault, M. P. Moody, J. M. Cairney, and S. P. Ringer, *Atom Probe Microscopy*. New York: Springer, 2012.

[103] A. J. Melmed, "The art and science and other aspects of making sharp tips," *J. Vac. Sci. Technol. B Microelectron. Nanom. Struct.*, vol. 9, no. 2, p. 601, Mar. 1991.

[104] T. T. Tsong, "Formation of multiatomic cluster ions of silicon in pulsed-laser stimulated field desorption," *Appl. Phys. Lett.*, vol. 45, no. 10, pp. 1149–1151, Nov. 1984.

[105] M. K. Miller, K. F. Russell, and G. B. Thompson, "Strategies for fabricating atom probe specimens with a dual beam FIB.," *Ultramicroscopy*, vol. 102, no. 4, pp. 287–98, Mar. 2005.

[106] A. Devaraj, C. Szymanski, P. Yan, C. M. Wang, V. Murgesan, J. M. Zheng, J. Zhang, T. Tyliszczak, and S. Thevuthasan, "Nanoscale Characterization of Li-ion Battery Cathode Nanoparticles by Atom Probe Tomography Correlated with Transmission Electron Microscopy and Scanning Transmission X-Ray Microscopy," *Microsc. Microanal.*, vol. 21, no. S3, pp. 685–686, Aug. 2015.

[107] N. A. Sanford, P. T. Blanchard, M. Brubaker, K. A. Bertness, A. Roshko, J. B. Schlager, R. Kirchhofer, D. R. Diercks, and B. Gorman, "Laser-assisted atom probe tomography of MBE grown GaN nanowire heterostructures," *Phys. status solidi*, vol. 11, no. 3–4, pp. 608–612, Feb. 2014.

[108] D. E. Perea, J. L. Lensch, S. J. May, B. W. Wessels, and L. J. Lauhon, "Composition analysis of single semiconductor nanowires using pulsed-laser atom probe tomography," *Appl. Phys. A*, vol. 85, no. 3, pp. 271–275, Sep. 2006.

[109] R. Agrawal, R. A. Bernal, D. Isheim, and H. D. Espinosa, "Characterizing Atomic Composition and Dopant Distribution in Wide Band Gap Semiconductor Nanowires Using Laser-Assisted Atom Probe Tomography," *J. Phys. Chem. C*, vol. 115, no. 36, pp. 17688–17694, Sep. 2011.

[110] S. Koelling, A. Li, A. Cavalli, S. Assali, D. Car, S. Gazibegovic, E. P. A. M. Bakkers, and P. M. Koenraad, "Atom-by-Atom Analysis of Semiconductor Nanowires with Parts Per Million Sensitivity," *Nano Lett.*, vol. 17, no. 2, pp. 599–605, Feb. 2017.

[111] H. Blumtritt, D. Isheim, S. Senz, D. N. Seidman, and O. Moutanabbir, "Preparation of nanowire specimens for laser-assisted atom probe tomography.," *Nanotechnology*, vol. 25, no. 43, p. 435704, Oct. 2014.

[112] A. Devaraj, D. E. Perea, J. Liu, L. M. Gordon, T. J. Prosa, P. Parikh, D. R. Diercks, S. Meher, R. P. Kolli, Y. S. Meng, and S. Thevuthasan, "Three-dimensional nanoscale characterisation of materials by atom probe tomography," *Int. Mater. Rev.*, pp. 1–34, Jan. 2017.

[113] C. B. Ene, G. Schmitz, R. Kirchheim, and A. Hütten, "Stability and thermal reaction of GMR NiFe/Cu thin films," *Acta Mater.*, vol. 53, no. 12, pp. 3383–3393, 2005.

[114] C. K. Sudbrack, K. E. Yoon, R. D. Noebe, and D. N. Seidman, "Temporal evolution of the nanostructure and phase compositions in a model Ni–Al–Cr alloy," *Acta Mater.*, vol. 54, no. 12, pp. 3199–3210, 2006.

[115] F. Yang, D. R. Coughlin, P. J. Phillips, L. Yang, A. Devaraj, L. Kovarik, R. D. Noebe, and M. J. Mills, "Structure analysis of a precipitate phase in an Ni-rich high-temperature NiTiHf shape memory alloy," *Acta Mater.*, vol. 61, no. 9, pp. 3335–3346, May 2013.

[116] R. Prakash Kolli and D. N. Seidman, "The temporal evolution of the decomposition of a concentrated multicomponent Fe–Cu-based steel," *Acta Mater.*, vol. 56, no. 9, pp. 2073–2088, May 2008.

[117] K. E. Yoon, C. K. Sudbrack, R. D. Noebe, and D. N. Seidman, "The temporal evolution of the nanostructures of model Ni – Al – Cr and Ni – Al – Cr – Re superalloys," *Zeitschrift für Met.*, vol. 96, no. 5, pp. 481–485, 2005.

[118] O. Moutanabbir, D. Isheim, D. N. Seidman, Y. Kawamura, and K. M. Itoh, "Ultraviolet-laser atom-probe tomographic three-dimensional atom-by-atom mapping of isotopically modulated Si nanoscopic layers," *Appl. Phys. Lett.*, vol. 98, no. 1, p. 13111, 2011.

[119] Y. Shimizu, H. Takamizawa, Y. Kawamura, M. Uematsu, T. Toyama, K. Inoue, E. E. Haller, K. M. Itoh, and Y. Nagai, "Atomic-scale characterization of germanium isotopic multilayers by atom probe tomography," *J. Appl. Phys.*, vol. 113, no. 2, p. 26101, Jan. 2013.

[120] K. Thompson, J. H. Bunton, J. S. Moore, and K. S. Jones, "Compositional analysis of Si nanostructures: SIMS–3D tomographic atom probe comparison," *Semicond. Sci. Technol.*, vol. 22, no. 1, pp. S127–S131, Jan. 2007.

[121] M. J. Galtrey, R. A. Oliver, M. J. Kappers, C. J. Humphreys, D. J. Stokes, P. H. Clifton, and A. Cerezo, "Three-dimensional atom probe studies of an $In_xGa_{1-x}N$/GaN multiple quantum well structure: Assessment of possible indium clustering," *Appl. Phys. Lett.*, vol. 90, no. 6, p. 61903, Feb. 2007.

[122] A. G. Norman, M. C. Hanna, P. Dippo, D. H. Levi, R. C. Reedy, J. S. Ward, and M. M. Al-Jassim, "InGaAs/GaAs QD superlattices: MOVPE growth, structural and optical characterization, and application in intermediate-band solar cells," in *Conference Record of the Thirty-first IEEE Photovoltaic Specialists Conference, 2005.*, pp. 43–48.

[123] K. Inoue, H. Takamizawa, K. Kitamoto, J. Kato, T. Miyagi, Y. Nakagawa, N. Kawasaki, N. Sugiyama, H. Hashimoto, Y. Shimizu, T. Toyama, Y. Nagai, and A. Karen, "Three-Dimensional Elemental Analysis of Commercial 45 nm Node Device with High-k/Metal Gate Stack by Atom Probe Tomography," *Appl. Phys. Express*, vol. 4, no. 11, p. 116601, Oct. 2011.

[124] K. Thompson, J. H. Booske, D. J. Larson, and T. F. Kelly, "Three-dimensional atom mapping of dopants in Si nanostructures," *Appl. Phys. Lett.*, vol. 87, no. 5, p. 52108, Aug. 2005.

[125] K. Hoummada, E. Cadel, D. Mangelinck, C. Perrin-Pellegrino, D. Blavette, and B. Deconihout, "First stages of the formation of Ni silicide by atom probe tomography," *Appl. Phys. Lett.*, vol. 89, no. 18, p. 181905, Oct. 2006.

[126] B. Imbert, R. Pantel, S. Zoll, M. Gregoire, R. Beneyton, S. del Medico, and O. Thomas, "Nickel silicide encroachment formation and characterization," *Microelectron. Eng.*, vol. 87, no. 3, pp. 245–248, Mar. 2010.

[127] H. Takamizawa, Y. Shimizu, Y. Nozawa, T. Toyama, H. Morita, Y. Yabuuchi, M. Ogura, and Y. Nagai, "Dopant characterization in self-regulatory plasma doped fin field-effect transistors by atom probe tomography," *Appl. Phys. Lett.*, vol. 100, no. 9, p. 93502, Feb. 2012.

[128] M. S. Hatzistergos, M. Hopstaken, E. Kim, L. Vanamurthy, and J. F. Shaffer, "Characterization of 3D Dopant Distribution in State of the Art FinFET Structures," *Microsc. Microanal.*, vol. 19, no. S2, pp. 960–961, Aug. 2013.

[129] F. Panciera, K. Hoummada, M. Gregoire, M. Juhel, F. Lorut, N. Bicais, and D. Mangelinck, "Atom probe tomography of SRAM transistors: Specimen preparation methods and analysis," *Microelectron. Eng.*, vol. 107, pp. 167–172, Jul. 2013.

[130] B. P. Gorman, A. G. Norman, and Y. Yan, "Atom Probe Analysis of III–V and Si-Based Semiconductor Photovoltaic Structures," *Microsc. Microanal.*, vol. 13, no. 6, pp. 493–502, Dec. 2007.

[131] D. E. Perea, J. E. Allen, S. J. May, B. W. Wessels, D. N. Seidman, and L. J. Lauhon, "Three-dimensional nanoscale composition mapping of semiconductor nanowires.," *Nano Lett.*, vol. 6, no. 2, pp. 181–185, Feb. 2006.

[132] S. Assali, A. Dijkstra, A. Li, S. Koelling, M. A. Verheijen, L. Gagliano, N. von den Driesch, D. Buca, P. M. Koenraad, J. E. M. Haverkort, and E. P. A. M. Bakkers, "Growth and Optical Properties of Direct Band Gap Ge/$Ge_{0.87}Sn_{0.13}$ Core/Shell Nanowire Arrays," *Nano Lett.*, vol. 17, no. 3, pp. 1538–1544, Mar. 2017.

[133] N. Dawahre, G. Shen, S. Balci, W. Baughman, D. S. Wilbert, N. Harris, L. Butler, R. Martens, S. M. Kim, and P. Kung, "Atom Probe Tomography of Zinc Oxide Nanowires," *J. Electron. Mater.*, vol. 41, no. 5, pp. 801–808, May 2012.

[134] M. Roussel, W. Chen, E. Talbot, R. Lardé, E. Cadel, F. Gourbilleau, B. Grandidier, D. Stiévenard, and P. Pareige, "Atomic scale investigation of silicon nanowires and nanoclusters.," *Nanoscale Res. Lett.*, vol. 6, no. 1, p. 271, Jan. 2011.

[135] D. E. Perea, E. R. Hemesath, E. J. Schwalbach, J. L. Lensch-Falk, P. W. Voorhees, and L. J. Lauhon, "Direct measurement of dopant distribution in an individual vapour–liquid–solid nanowire," *Nat. Nanotechnol.*, vol. 4, no. 5, pp. 315–319, May 2009.

[136] S. Du, T. Burgess, B. Gault, Q. Gao, P. Bao, L. Li, X. Cui, W. Kong Yeoh, H. Liu, L. Yao, A. V. Ceguerra, H. Hoe Tan, C. Jagadish, S. P. Ringer, and R. Zheng, "Quantitative dopant distributions in GaAs nanowires using atom probe tomography," *Ultramicroscopy*, vol. 132, pp. 186–192, Sep. 2013.

[137] J. E. Allen, E. R. Hemesath, D. E. Perea, J. L. Lensch-Falk, Z. Y. Li, F. Yin, M. H. Gass, P. Wang, A. L. Bleloch, R. E. Palmer, and L. J. Lauhon, "High-resolution detection of Au catalyst atoms in Si nanowires," *Nat. Nanotechnol.*, vol. 3, no. 3, pp. 168–173, Mar. 2008.

[138] O. Moutanabbir, D. Isheim, H. Blumtritt, S. Senz, E. Pippel, and D. N. Seidman, "Colossal injection of catalyst atoms into silicon nanowires," *Nature*, vol. 496, no. 7443, pp. 78–82, 2013.

[139] J. R. Riley, S. Padalkar, Q. Li, P. Lu, D. D. Koleske, J. J. Wierer, G. T. Wang, and L. J. Lauhon, "Three-Dimensional Mapping of Quantum Wells in a GaN/InGaN Core–Shell Nanowire Light-Emitting Diode Array," *Nano Lett.*, vol. 13, no. 9, pp. 4317–4325, Sep. 2013.

[140] A. Devaraj, R. Colby, F. Vurpillot, and S. Thevuthasan, "Understanding Atom Probe Tomography of Oxide-Supported Metal Nanoparticles by Correlation with Atomic-Resolution Electron Microscopy and Field Evaporation Simulation," *J. Phys. Chem. Lett.*, vol. 5, no. 8, pp. 1361–1367, Apr. 2014.

[141] D. J. Larson, T. J. Prosa, R. M. Ulfig, B. P. Geiser, and T. F. Kelly, *Local Electrode Atom Probe Tomography*. New York: Springer, 2013.

[142] S. V. Krishnaswamy and E. W. Müller, "Premature field evaporation in the atom probe," *Rev. Sci. Instrum.*, vol. 45, no. 9, pp. 1049–1052, Sep. 1974.

[143] F. Vurpillot, J. Houard, A. Vella, and B. Deconihout, "Thermal response of a field emitter subjected to ultra-fast laser illumination," *J. Phys. D. Appl. Phys.*, vol. 42, no. 12, p. 125502, Jun. 2009.

[144] T. F. Kelly and D. J. Larson, "Atom Probe Tomography 2012," *Annu. Rev. Mater. Res.*, vol. 42, no. 1, pp. 1–31, Aug. 2012.

[145] E. W. Müller, "Field Desorption," *Phys. Rev.*, vol. 102, no. 3, pp. 618–624, May 1956.

[146] R. Gomer, "Field Desorption," *J. Chem. Phys.*, vol. 31, no. 2, pp. 341–345, Aug. 1959.

[147] T. T. Tsong, *Atom-Probe Field Ion Microscopy*. Cambridge, UK: Cambridge University Press, 1990.

[148] G. L. Kellogg, "Measurement of activation energies for field evaporation of tungsten ions

as a function of electric field," *Phys. Rev. B*, vol. 29, no. 8, pp. 4304–4312, Apr. 1984.

[149] M. Wada, "On the thermally activated field evaporation of surface atoms," *Surf. Sci.*, vol. 145, no. 2–3, pp. 451–465, Oct. 1984.

[150] M. Gilbert, F. Vurpillot, A. Vella, H. Bernas, and B. Deconihout, "Some aspects of the silicon behaviour under femtosecond pulsed laser field evaporation.," *Ultramicroscopy*, vol. 107, no. 9, pp. 767–72, Sep. 2007.

[151] G. E. H. Reuter and E. H. Sondheimer, "The Theory of the Anomalous Skin Effect in Metals," *Proc. R. Soc. London A Math. Phys. Eng. Sci.*, vol. 195, no. 1042, 1948.

[152] B. Gault, A. Vella, F. Vurpillot, A. Menand, D. Blavette, and B. Deconihout, "Optical and thermal processes involved in ultrafast laser pulse interaction with a field emitter," *Ultramicroscopy*, vol. 107, no. 9, pp. 713–719, 2007.

[153] A. Vella, F. Vurpillot, B. Gault, A. Menand, and B. Deconihout, "Evidence of field evaporation assisted by nonlinear optical rectification induced by ultrafast laser," *Phys. Rev. B*, vol. 73, no. 16, p. 165416, Apr. 2006.

[154] J. Houard, A. Vella, F. Vurpillot, and B. Deconihout, "Optical near-field absorption at a metal tip far from plasmonic resonance," *Phys. Rev. B*, vol. 81, no. 12, p. 125411, Mar. 2010.

[155] E. P. Silaeva, A. Vella, N. Sevelin-Radiguet, G. Martel, B. Deconihout, and T. E. Itina, "Ultrafast laser-triggered field ion emission from semiconductor tips," *New J. Phys.*, vol. 14, no. 11, p. 113026, Nov. 2012.

[156] E. P. Silaeva, N. S. Shcheblanov, T. E. Itina, A. Vella, J. Houard, N. Sévelin-Radiguet, F. Vurpillot, and B. Deconihout, "Numerical study of femtosecond laser-assisted atom probe tomography," *Appl. Phys. A*, vol. 110, no. 3, pp. 703–707, Sep. 2012.

[157] H. Tamura, M. Tsukada, K. P. McKenna, A. L. Shluger, T. Ohkubo, and K. Hono, "Laser-assisted field evaporation from insulators triggered by photoinduced hole accumulation," *Phys. Rev. B*, vol. 86, no. 19, p. 195430, Nov. 2012.

[158] E. P. Silaeva, L. Arnoldi, M. L. Karahka, B. Deconihout, A. Menand, H. J. Kreuzer, and A. Vella, "Do dielectric nanostructures turn metallic in high-electric dc fields?," *Nano Lett.*, vol. 14, no. 11, pp. 6066–72, Nov. 2014.

[159] D. A. Long, *The Raman Effect: A Unified Treatment of the Theory of Raman Scattering by Molecules*. New York: John Wiley & Sons Ltd, 2002.

[160] C. V. Raman, "A Change of Wave-length in Light Scattering," *Nature*, vol. 121, no. 3051, pp. 619–619, Apr. 1928.

[161] R. Loudon, "The Raman effect in crystals," *Adv. Phys.*, vol. 13, no. 52, pp. 423–482, Oct. 1964.

[162] R. F. Egerton, *Physical Principles of Electron Microscopy*. New York: Springer US, 2005.

[163] D. B. Williams and C. B. Carter, *The Transmission Electron Microscope-I*. New York: Plenum Publishing Corporation, 2009.

[164] H. Umezawa, M. Nagase, Y. Kato, and S. Shikata, "High temperature application of diamond power device," *Diam. Relat. Mater.*, vol. 24, pp. 201–205, Apr. 2012.

[165] V. Goyal, A. V. Sumant, D. Teweldebrhan, and A. a. Balandin, "Direct Low-Temperature Integration of Nanocrystalline Diamond with GaN Substrates for Improved Thermal Management of High-Power Electronics," *Adv. Funct. Mater.*, vol. 22, no. 7, pp. 1525–1530, Apr. 2012.

[166] T. Ishikawa, K.-M. C. Fu, C. Santori, V. M. Acosta, R. G. Beausoleil, H. Watanabe, S. Shikata, and K. M. Itoh, "Optical and spin coherence properties of nitrogen-vacancy centers placed in a 100 nm thick isotopically purified diamond layer.," *Nano Lett.*, vol. 12, no. 4, pp. 2083–7, Apr. 2012.

[167] C. Hepp, T. Müller, V. Waselowski, J. N. Becker, B. Pingault, H. Sternschulte, D. Steinmüller-Nethl, A. Gali, J. R. Maze, M. Atatüre, and C. Becher, "Electronic Structure of the Silicon Vacancy Color Center in Diamond," *Phys. Rev. Lett.*, vol. 112, no. 3, p. 36405, Jan. 2014.

[168] N. Mizuochi, T. Makino, H. Kato, D. Takeuchi, M. Ogura, H. Okushi, M. Nothaft, P. Neumann, A. Gali, F. Jelezko, J. Wrachtrup, and S. Yamasaki, "Electrically driven single-photon source at room temperature in diamond," *Nat. Photonics*, vol. 6, no. 5, pp. 299–303, Apr. 2012.

[169] G. Balasubramanian, I. Y. Chan, R. Kolesov, M. Al-Hmoud, J. Tisler, C. Shin, C. Kim, A.

Wojcik, P. R. Hemmer, A. Krueger, T. Hanke, A. Leitenstorfer, R. Bratschitsch, F. Jelezko, and J. Wrachtrup, “Nanoscale imaging magnetometry with diamond spins under ambient conditions.,” *Nature*, vol. 455, no. 7213, pp. 648–51, Oct. 2008.

[170] J. R. Maze, P. L. Stanwix, J. S. Hodges, S. Hong, J. M. Taylor, P. Cappellaro, L. Jiang, M. V. G. Dutt, E. Togan, A. S. Zibrov, A. Yacoby, R. L. Walsworth, and M. D. Lukin, “Nanoscale magnetic sensing with an individual electronic spin in diamond.,” *Nature*, vol. 455, no. 7213, pp. 644–7, Oct. 2008.

[171] A. Fiori, F. Jomard, T. Teraji, S. Koizumi, J. Isoya, E. Gheeraert, and E. Bustarret, “Synchronized B and ^{13}C Diamond Delta Structures for an Ultimate In-Depth Chemical Characterization,” *Appl. Phys. Express*, vol. 6, no. 4, p. 45801, Apr. 2013.

[172] E. P. Silaeva, M. Karahka, and H. J. Kreuzer, “Atom Probe Tomography and field evaporation of insulators and semiconductors: Theoretical issues,” *Curr. Opin. Solid State Mater. Sci.*, vol. 17, no. 5, pp. 211–216, Oct. 2013.

[173] D. Larson, R. Alvis, D. Lawrence, T. Prosa, R. Ulfig, D. Reinhard, P. Clifton, S. Gerstl, J. Bunton, D. Lenz, T. Kelly, and K. Stiller, “Analysis of Bulk Dielectrics with Atom Probe Tomography,” *Microsc. Microanal.*, vol. 14, no. S2, pp. 1254–1255, Aug. 2008.

[174] H. N. Southworth and B. Ralph, “Image formation from alloys in the field-ion microscope,” *J. Microsc.*, vol. 90, no. 3, pp. 167–197, Dec. 1969.

[175] B. Gault, F. Vurpillot, A. Bostel, A. Menand, and B. Deconihout, “Estimation of the tip field enhancement on a field emitter under laser illumination,” *Appl. Phys. Lett.*, vol. 86, no. 9, p. 94101, Feb. 2005.

[176] C. Zener, “A Theory of the Electrical Breakdown of Solid Dielectrics,” *Proc. R. Soc. A Math. Phys. Eng. Sci.*, vol. 145, no. 855, pp. 523–529, Jul. 1934.

[177] R. J. Trew, J.-B. Yan, and P. M. Mock, “The potential of diamond and SiC electronic devices for microwave and millimeter-wave power applications,” *Proc. IEEE*, vol. 79, no. 5, pp. 598–620, May 1991.

[178] S. Koelling, N. Innocenti, A. Schulze, M. Gilbert, A. K. Kambham, and W. Vandervorst, “In-situ observation of non-hemispherical tip shape formation during laser-assisted atom probe tomography,” *J. Appl. Phys.*, vol. 109, no. 10, p. 104909, May 2011.

[179] F. Vurpillot, B. Gault, A. Vella, M. Bouet, and B. Deconihout, “Estimation of the cooling times for a metallic tip under laser illumination,” *Appl. Phys. Lett.*, vol. 88, no. 9, p. 94105, Mar. 2006.

[180] G. P. Srivastava, J. L. Martins, and A. Zunger, “Atomic structure and ordering in semiconductor alloys,” *Phys. Rev. B*, vol. 31, no. 4, pp. 2561–2564, Feb. 1985.

[181] M. Ichimura and A. Sasaki, “Short-range order in III-V ternary alloy semiconductors,” *J. Appl. Phys.*, vol. 60, no. 11, p. 3850, Dec. 1986.

[182] L. Alagna, T. Prosperi, S. Turchini, C. Ferrari, L. Francesio, and P. Franzosi, “Diffraction anomalous near-edge structure in ordered GaInP,” *J. Appl. Phys.*, vol. 83, no. 7, p. 3552, 1998.

[183] C. Bocchi, P. Franzosi, and C. Ghezzi, “X-ray diffuse scattering by composition waves in GaAlAs,” *J. Appl. Phys.*, vol. 57, no. 10, p. 4533, May 1985.

[184] T. Kuan, T. Kuech, W. Wang, and E. Wilkie, “Long-range order in $Al_xGa_{1-x}As$.,” *Phys. Rev. Lett.*, vol. 54, no. 3, pp. 201–204, Jan. 1985.

[185] A. Attiaoui and O. Moutanabbir, “Indirect-to-direct band gap transition in relaxed and strained $Ge_{1-x-y}Si_xSn_y$ ternary alloys,” *J. Appl. Phys.*, vol. 116, no. 6, p. 63712, Aug. 2014.

[186] S. Wirths, A. T. Tiedemann, Z. Ikonic, P. Harrison, B. Holländer, T. Stoica, G. Mussler, M. Myronov, J. M. Hartmann, D. Grützmacher, D. Buca, and S. Mantl, “Band engineering and growth of tensile strained Ge/(Si)GeSn heterostructures for tunnel field effect transistors,” *Appl. Phys. Lett.*, vol. 102, no. 19, p. 192103, May 2013.

[187] G. Sun, H. H. Cheng, J. Menéndez, J. B. Khurgin, and R. A. Soref, “Strain-free Ge⁄GeSiSn quantum cascade lasers based on L-valley intersubband transitions,” *Appl. Phys. Lett.*, vol. 90, no. 25, p. 251105, Jun. 2007.

[188] J. D. Gallagher, C. Xu, L. Jiang, J. Kouvetakis, and J. Menéndez, “Fundamental band gap and direct-indirect crossover in $Ge_{1-x-y}Si_xSn_y$ alloys,” *Appl. Phys. Lett.*, vol. 103, no. 20, p. 202104, Nov. 2013.

[189] J. Kouvetakis, J. Menendez, and A. V. G. Chizmeshya, “TIN-BASED GROUP IV SEMICONDUCTORS: New Platforms for Opto- and Microelectronics on Silicon,” *Annu.*

Rev. Mater. Res., vol. 36, no. 1, pp. 497–554, Aug. 2006.

[190] P. Moontragoon, R. A. Soref, and Z. Ikonic, "The direct and indirect bandgaps of unstrained $Si_xGe_{1-x-y}Sn_y$ and their photonic device applications," *J. Appl. Phys.*, vol. 112, no. 7, p. 73106, Oct. 2012.

[191] K. Lu Low, Y. Yang, G. Han, W. Fan, and Y.-C. Yeo, "Electronic band structure and effective mass parameters of $Ge_{1-x}Sn_x$ alloys," *J. Appl. Phys.*, vol. 112, no. 10, p. 103715, Nov. 2012.

[192] S. Gupta, B. Magyari-Köpe, Y. Nishi, and K. C. Saraswat, "Achieving direct band gap in germanium through integration of Sn alloying and external strain," *J. Appl. Phys.*, vol. 113, no. 7, p. 73707, Feb. 2013.

[193] R. Kotlyar, U. E. Avci, S. Cea, R. Rios, T. D. Linton, K. J. Kuhn, and I. A. Young, "Bandgap engineering of group IV materials for complementary n and p tunneling field effect transistors," *Appl. Phys. Lett.*, vol. 102, no. 11, p. 113106, Mar. 2013.

[194] M. Oehme, D. Widmann, K. Kostecki, P. Zaumseil, B. Schwartz, M. Gollhofer, R. Koerner, S. Bechler, M. Kittler, E. Kasper, and J. Schulze, "GeSn/Ge multiquantum well photodetectors on Si substrates.," *Opt. Lett.*, vol. 39, no. 16, pp. 4711–4, Aug. 2014.

[195] S. Takeuchi, A. Sakai, K. Yamamoto, O. Nakatsuka, M. Ogawa, and S. Zaima, "Growth and structure evaluation of strain-relaxed $Ge_{1-x}Sn_x$ buffer layers grown on various types of substrates," *Semicond. Sci. Technol.*, vol. 22, no. 1, pp. S231–S235, Jan. 2007.

[196] R. Chen, S. Gupta, Y.-C. Huang, Y. Huo, C. W. Rudy, E. Sanchez, Y. Kim, T. I. Kamins, K. C. Saraswat, and J. S. Harris, "Demonstration of a Ge/GeSn/Ge Quantum-Well Microdisk Resonator on Silicon: Enabling High-Quality Ge(Sn) Materials for Micro- and Nanophotonics," *Nano Lett.*, vol. 14, no. 1, pp. 37–43, Jan. 2014.

[197] S. Mukherjee, H. Watanabe, D. Isheim, D. N. Seidman, and O. Moutanabbir, "Laser-Assisted Field Evaporation and Three-Dimensional Atom-by-Atom Mapping of Diamond Isotopic Homojunctions.," *Nano Lett.*, vol. 16, no. 2, pp. 1335–1344, Jan. 2016.

[198] D. E. Perea, I. Arslan, J. Liu, Z. Ristanović, L. Kovarik, B. W. Arey, J. A. Lercher, S. R. Bare, and B. M. Weckhuysen, "Determining the location and nearest neighbours of aluminium in zeolites with atom probe tomography," *Nat. Commun.*, vol. 6, p. 7589, Jul.

2015.

[199] W. Chen, L. Yu, S. Misra, Z. Fan, P. Pareige, G. Patriarche, S. Bouchoule, and P. R. I. Cabarrocas, “Incorporation and redistribution of impurities into silicon nanowires during metal-particle-assisted growth.,” *Nat. Commun.*, vol. 5, p. 4134, Jan. 2014.

[200] J.-H. Fournier-Lupien, S. Mukherjee, S. Wirths, E. Pippel, N. Hayazawa, G. Mussler, J. M. Hartmann, P. Desjardins, D. Buca, and O. Moutanabbir, “Strain and composition effects on Raman vibrational modes of silicon-germanium-tin ternary alloys,” *Appl. Phys. Lett.*, vol. 103, no. 26, p. 263103, Dec. 2013.

[201] S. Wirths, D. Buca, and S. Mantl, “Si–Ge–Sn alloys: From growth to applications,” *Prog. Cryst. Growth Charact. Mater.*, vol. 62, no. 1, pp. 1–39, Jan. 2016.

[202] F. Gencarelli, D. Grandjean, Y. Shimura, B. Vincent, D. Banerjee, A. Vantomme, W. Vandervorst, R. Loo, M. Heyns, and K. Temst, “Extended X-ray absorption fine structure investigation of Sn local environment in strained and relaxed epitaxial $Ge_{1-x}Sn_x$ films,” *J. Appl. Phys.*, vol. 117, no. 9, p. 95702, Mar. 2015.

[203] R. K. W. Marceau, L. T. Stephenson, C. R. Hutchinson, and S. P. Ringer, “Quantitative atom probe analysis of nanostructure containing clusters and precipitates with multiple length scales.,” *Ultramicroscopy*, vol. 111, no. 6, pp. 738–42, May 2011.

[204] F. De Geuser, W. Lefebvre, and D. Blavette, “3D atom probe study of solute atoms clustering during natural ageing and pre-ageing of an Al-Mg-Si alloy,” *Philos. Mag. Lett.*, vol. 86, no. 4, pp. 227–234, Apr. 2006.

[205] Y. Shimura, T. Asano, T. Yamaha, M. Fukuda, W. Takeuchi, O. Nakatsuka, and S. Zaima, “EXAFS study of local structure contributing to Sn stability in $Si_yGe_{1-y-z}Sn_z$,” *Mater. Sci. Semicond. Process.*, 2016.

[206] J. Martins and A. Zunger, “Stability of ordered bulk and epitaxial semiconductor alloys.,” *Phys. Rev. Lett.*, vol. 56, no. 13, pp. 1400–1403, Mar. 1986.

[207] M. Cardona and M. L. W. Thewalt, “Isotope effect on the optical spectra of semiconductors,” *Rev. Moden Phys.*, vol. 77, no. 4, pp. 1173–1224, 2005.

[208] E. E. Haller, “Isotopically Controlled Semiconductors,” *MRS Bull.*, vol. 31, no. 7, pp. 547–

553, Jan. 2006.

[209] G. Davies, E. C. Lightowlers, K. Itoh, W. L. Hansen, E. E. Haller, and V. Ozhogin, “Isotope dependence of the indirect energy gap of germanium,” *Semicond. Sci. Technol.*, vol. 7, no. 10, pp. 1271–1273, Oct. 1992.

[210] A. M. Tyryshkin, S. Tojo, J. J. Morton, H. Riemann, N. V Abrosimov, P. Becker, H. J. Pohl, T. Schenkel, M. L. Thewalt, K. M. Itoh, and S. A. Lyon, “Electron spin coherence exceeding seconds in high-purity silicon,” *Nat Mater*, vol. 11, no. 2, pp. 143–147, 2012.

[211] D. R. McCamey, J. Van Tol, G. W. Morley, and C. Boehme, “Electronic spin storage in an electrically readable nuclear spin memory with a lifetime >100 seconds.,” *Science*, vol. 330, no. 6011, pp. 1652–6, Dec. 2010.

[212] K. M. Itoh, “An all-silicon linear chain NMR quantum computer,” *Solid State Commun.*, vol. 133, no. 11, pp. 747–752, Mar. 2005.

[213] R. K. Kremer, K. Graf, M. Cardona, G. G. Devyatykh, A. V Gusev, A. M. Gibin, A. V Inyushkin, A. N. Taldenkov, and H. J. Pohl, “Thermal conductivity of isotopically enriched ^{28}Si: revisited,” *Solid State Commun.*, vol. 131, no. 8, pp. 499–503, 2004.

[214] M. Nakajima, H. Harima, K. Morita, K. Itoh, K. Mizoguchi, and E. Haller, “Coherent confined LO phonons in ^{70}Ge/^{74}Ge isotope superlattices generated by ultrafast laser pulses,” *Phys. Rev. B*, vol. 63, no. 16, p. 161304, Apr. 2001.

[215] D. Morelli, J. Heremans, and G. Slack, “Estimation of the isotope effect on the lattice thermal conductivity of group IV and group III-V semiconductors,” *Phys. Rev. B*, vol. 66, no. 19, p. 195304, Nov. 2002.

[216] O. Moutanabbir, S. Senz, Z. Zhang, and U. Gösele, “Synthesis of isotopically controlled metal-catalyzed silicon nanowires,” *Nano Today*, vol. 4, no. 5, pp. 393–398, 2009.

[217] J. B. Hannon, S. Kodambaka, F. M. Ross, and R. M. Tromp, “The influence of the surface migration of gold on the growth of silicon nanowires,” *Nature*, vol. 440, no. 7080, pp. 69–71, 2006.

[218] O. R. A. Bailly N. Barrett, L. F. Zagonel, P. Gentile, N. Pauc, F. Dhalluin, T. Baron, A. Chabli, J. C. Cezar, and N. B. Brookes, “Direct Quantification of Gold along along a single

Si Nanowire," *Nano Lett*, vol. 8, no. 11, pp. 3709–3714, 2008.

[219] K. Adu, H. Gutiérrez, U. Kim, and P. Eklund, "Inhomogeneous laser heating and phonon confinement in silicon nanowires: A micro-Raman scattering study," *Phys. Rev. B*, vol. 73, no. 15, 2006.

[220] H. Scheel, S. Reich, A. C. Ferrari, M. Cantoro, A. Colli, and C. Thomsen, "Raman scattering on silicon nanowires: The thermal conductivity of the environment determines the optical phonon frequency," *Appl. Phys. Lett.*, vol. 88, no. 23, p. 233114, Jun. 2006.

[221] M. Soini, I. Zardo, E. Uccelli, S. Funk, G. Koblmüller, A. Fontcuberta i Morral, and G. Abstreiter, "Thermal conductivity of GaAs nanowires studied by micro-Raman spectroscopy combined with laser heating," *Appl. Phys. Lett.*, vol. 97, no. 26, p. 263107, 2010.

[222] R. Frieling, M. Radek, S. Eon, H. Bracht, and D. E. Wolf, "Phonon coherence in isotopic silicon superlattices," *Appl. Phys. Lett.*, vol. 105, no. 13, p. 132104, Sep. 2014.

[223] S. Piscanec, A. C. Ferrari, M. Cantoro, S. Hofmann, J. A. Zapien, Y. Lifshitz, S. T. Lee, and J. Robertson, "Raman Spectrum of silicon nanowires," *Mater. Sci. Eng. C*, vol. 23, no. 6–8, pp. 931–934, 2003.

[224] C. Kittel, *Introduction to Solid State Physics*, 8th ed. New York: Wiley, 2005.

[225] J. Callaway, "Model for Lattice Thermal Conductivity at Low Temperatures," *Phys. Rev. Lett.*, vol. 113, no. 4, pp. 1046–1051, Feb. 1959.

[226] R. Gupta, Q. Xiong, C. K. Adu, U. J. Kim, and P. C. Eklund, "Laser-Induced Fano Resonance Scattering in Silicon Nanowires," *Nano Lett.*, vol. 3, no. 5, pp. 627–631, May 2003.

[227] From Ref [30], $\Delta_{\text{Anhrm}}^{\text{Nat-Si Bulk}}(\text{T} = 6\text{K}) \approx 1.21\text{cm}^{-1}$ and $\Delta_{\text{Isotope}}^{\text{Nat-Si Bulk}}$ is negligible. This makes the anharmonic contribution equal to the total line broadening from bulk $^{\text{Nat}}$Si sample. The anharmonic contribution was extrapolated to 300K using equation (4.3), giving $\Delta_{\text{Anhrm}}^{\text{Nat-Si Bulk}}(\text{T} = 300\text{K}) \approx \text{FWHM}^{\text{Nat-Si}}(\text{T} = 300\text{K}) \approx 2.154\ \text{cm}^{-1}$. Next a $^{\text{Nat}}$Si bulk sample was measured using the InVia RM 3000 setup using 488nm at an incident power density of 0.08 mW/μm^2 and the FWHM was found to be around 5.2 cm^{-1}. We attributed

this excess line broadening (of about $3cm^{-1}$) to instrumental resolution. We did not calculate the contribution of instrumental broadening for the other setup (used for high power measurements) because the entire analysis concerning the FWHM of the NWs was done using the quasi-harmonic approximation, based on the data at the lowest recorded power density which was measured using the InVia RM 3000 setup

[228] S. H. Oh, M. F. Chisholm, Y. Kauffmann, W. D. Kaplan, W. Luo, M. Rühle, and C. Scheu, "Oscillatory Mass Transport in Vapor-Liquid-Solid Growth of Sapphire Nanowires," *Science*, vol. 330, no. 6003, 2010.

[229] A. D. Gamalski, C. Ducati, and S. Hofmann, "Cyclic Supersaturation and Triple Phase Boundary Dynamics in Germanium Nanowire Growth," *J. Phys. Chem. C*, vol. 115, no. 11, pp. 4413–4417, Mar. 2011.

[230] C.-Y. Wen, J. Tersoff, K. Hillerich, M. C. Reuter, J. H. Park, S. Kodambaka, E. A. Stach, and F. M. Ross, "Periodically Changing Morphology of the Growth Interface in Si, Ge, and GaP Nanowires," *Phys. Rev. Lett.*, vol. 107, no. 2, p. 25503, Jul. 2011.

[231] H. Wang, L. A. Zepeda-Ruiz, G. H. Gilmer, and M. Upmanyu, "Atomistics of vapour-liquid-solid nanowire growth.," *Nat. Commun.*, vol. 4, p. 1956, Jan. 2013.

[232] T. Haxhimali, D. Buta, M. Asta, P. W. Voorhees, and J. J. Hoyt, "Size-dependent nucleation kinetics at nonplanar nanowire growth interfaces," *Phys. Rev. E*, vol. 80, no. 5, p. 50601, Nov. 2009.

[233] E. Sutter and P. Sutter, "Phase Diagram of Nanoscale Alloy Particles Used for Vapor−Liquid−Solid Growth of Semiconductor Nanowires," *Nano Lett.*, vol. 8, no. 2, pp. 411–414, Jan.2008.

[234] J. G. Connell, K. Yoon, D. E. Perea, E. J. Schwalbach, P. W. Voorhees, and L. J. Lauhon, "Identification of an Intrinsic Source of Doping Inhomogeneity in Vapor–Liquid–Solid-Grown Nanowires," *Nano Lett.*, vol. 13, no. 1, pp. 199–206, Jan. 2013.

[235] S. Mukherjee, U. Givan, S. Senz, A. Bergeron, S. Francoeur, M. de la Mata, J. Arbiol, T. Sekiguchi, K. M. Itoh, D. Isheim, D. N. Seidman, and O. Moutanabbir, "Phonon Engineering in Isotopically Disordered Silicon Nanowires.," *Nano Lett.*, vol. 15, no. 6, pp. 3885–3893, May 2015.

[236] C. Persson and E. Janzén, “Electronic band structure in hexagonal close-packed Si polytypes,” *J. Phys. Condens. Matter*, vol. 10, no. 47, pp. 10549–10555, Nov. 1998.

[237] J. Arbiol, A. Fontcuberta i Morral, S. Estradé, F. Peiró, B. Kalache, P. Roca i Cabarrocas, and J. R. Morante, “Influence of the (111) twinning on the formation of diamond cubic/diamond hexagonal heterostructures in Cu-catalyzed Si nanowires,” *J. Appl. Phys.*, vol. 104, no. 6, p. 64312, 2008.

[238] I. Forrest M. Davidson, Doh C. Lee, A. Dayne D. Fanfair, and B. A. Korgel, “Lamellar Twinning in Semiconductor Nanowires,” *J.Phys. Chem.C*, vol. 111, no. 7, pp. 2929–2935, 2007.

[239] F. J. Lopez, E. R. Hemesath, and L. J. Lauhon, “Ordered Stacking Fault Arrays in Silicon Nanowires,” *Nano Lett.*, vol. 9, no. 7, pp. 2774–2779, Jul. 2009.

[240] Z. He, H. T. Nguyen, L. Duc Toan, and D. Pribat, “A detailed study of kinking in indium-catalyzed silicon nanowires,” *CrystEngComm*, vol. 17, no. 33, pp. 6286–6296, 2015.

[241] N. Jeon, S. A. Dayeh, and L. J. Lauhon, “Origin of Polytype Formation in VLS-Grown Ge Nanowires through Defect Generation and Nanowire Kinking,” *Nano Lett.*, vol. 13, no. 8, pp. 3947–3952, Aug. 2013.

[242] H. F. Zhan, Y. Y. Zhang, J. M. Bell, and Y. T. Gu, “Thermal conductivity of Si nanowires with faulted stacking layers,” *J. Phys. D. Appl. Phys.*, vol. 47, no. 1, p. 15303, 2014.

[243] M. Royo and R. Rurali, “Tuning thermal transport in Si nanowires by isotope engineering,” *Phys. Chem. Chem. Phys.*, vol. 18, no. 37, pp. 26262–26267, 2016.

[244] C. Barroo, A. P. Magyar, A. J. Akey, and D. C. Bell, “Preparation and Characterization of Eu-Doped Diamond Samples by Atom Probe Tomography,” *Microsc. Microanal.*, vol. 22, no. S3, pp. 694–695, Jul. 2016.

[245] C. W. Chang, D. Okawa, A. Majumdar, and A. Zettl, “Solid-State Thermal Rectifier,” *Science*, vol. 314, no. 5802, pp. 1121–1124, 2006.

[246] S. Chesi and W. A. Coish, “Theory of box-model hyperfine couplings and transport signatures of long-range nuclear-spin coherence in a quantum-dot spin valve,” *Phys. Rev. B*, vol. 91, no. 24, p. 245306, Jun. 2015.

APPENDIX A: SUPPLEMENTARY MATERIAL FOR THE ARTICLE 1: LASER-ASSISTED FIELD EVAPORATION AND THREE-DIMENSIONAL ATOM-BY-ATOM MAPPING OF DIAMOND ISOTOPIC HOMOJUNCTIONS

Samik Mukherjee[†], Hideyuki Watanabe,[§] Dieter Isheim[¥], David N. Seidman[¥], and Oussama Moutanabbir[†]

[†]*Department of Engineering Physics, École Polytechnique de Montréal, Montréal, C. P. 6079, Succ. Centre-Ville, Montréal, Québec, H3C 3A7 Canada*

[§] *Correlated Electronics Group, Electronics and Photonics Research Institute, National Institute of Advanced Industrial Science and Technology (AIST), Tsukuba Central 4, 1-1-1, Higashi, Tsukuba, Ibaraki 305-8562, Japan*

[¥]*Department of Materials Science and Engineering and Northwestern University Center for Atom-Probe Tomography (NUCAPT), Northwestern University, Evanston, IL 60208-3108, USA*

Growth of samples:

The sample investigated in this research work is a $^{12}C/^{13}C$ diamond homojunctions grown in a 1.5 kW ASTeX 2.45 GHz microwave plasma assisted chemical vapor deposition (CVD) reactor using isotopically enriched methane ($^{j}CH_4$ with j=12 or 13) as precursor. The isotopically enriched precursors were obtained from Tokyo Gas Chemicals Co. and had an isotopic purity better than 99.9% and 98.7% for $^{12}CH_4$ and $^{13}CH_4$ respectively. The substrate used for the homoepitaxial growth of the diamond films was HPHT (high pressure high temperature) synthetic-type Ib (100) crystalline diamond plates. The reactor pressure was 25 Torr and the total gas ($^{j}CH_4$+H_2) flow was 400 sccm. with the gas mixture containing 0.15% of $^{j}CH_4$. A microwave power of 750W was applied and the measured substrate temperature for the growth was 800°C. The two isotopically enriched precursors were alternated during the growth process leading to the growth of $^{12}C/^{13}C$ superlattice, as schematically illustrated in Figure 4.1(a) of the main article. The thickness of each layer is about 30 nm.

Nanotip fabrication and atom probe tomography:

A small piece of the as-grown samples were placed in an ion beam sputtering system. About 70nm of Ni was deposited on top of the samples for protection. The chamber pressure, ion current and the Ni deposition rate was 10^{-4} Torr, 7mA, and 1.5nm/min, respectively. The Ni-coated sample was then inserted in a Helios dual beam focused ion beam (Dual FIB) microscope. The sequential steps involved in the fabrication of the nanotip are shown in Figure 4.2 of the main article. A patch of Pt (0.15μm) thick was first deposited on a selected region for additional protection during Ga^+ ion FIB milling. The section was lifted out using an Omniprobe after milling trenches on its four sides (using Ga^+ ion accelerated through 30 kV) and then attached to an APT micro-post cold Pt welding. Finally, the sample was milled into a needle-like shape (using Ga^+ ion, initially a pyramidal shape was given at 30 kV and final polishing was done at 5 kV). After the final polishing, the typical apex of a nanotip is ~100nm as confirmed by electron beam images from the Dual FIB microscope. The APT analysis was performed utilizing a UV laser-assisted Local Electrode Atom Probe (LEAP). Evaporation of individual atoms was assisted by focusing a UV laser (355 nm), with a spot diameter of ~5 μm and a pulse duration of ~15 ps. The evaporation rate (ion $pulse^{-1}$), the laser pulse repetition-rate, and energy per pulse (E_{Pulse}) were 0.03, 250 kHz, and 1000 pJ respectively. The base temperature and base pressure within the APT chamber was 85 K and 2×10^{-10} Torr, respectively. On a different run, we used a lower pulse energy of 500 pJ and all other parameters were kept the same. The reason for chosing a fixed base temperature of 85 K is the fact that diamond has a maximum thermal conductivity at this temprature [1] and the heat generated from the pulsed laser should quickly dissipate away. The 3-D reconstructions were performed using Cameca's IVAS program.

Estimate of nanotip surface temperature:

We assumed that the free hole concentration at the surface of the diamond nanotip (n_h) can reach any value between semi-metallic and metallic free carrier concentrations ($n_h \sim 10^{19}\text{cm}^{-3} - 10^{22}\text{cm}^{-3}$). We can then define a hole plasma frequency (ω_P) according to Drude's model as [2]:

$$\omega_P = \sqrt{\frac{n_h e^2}{\varepsilon_0 m_h^*}} \quad (A1)$$

where m_h^* is the optical effective mass of holes in diamond, e is electronic charge, n_h is concentration of surface free holes and ε_0 is free space permittivity. The change in the complex dielectric constant function as a result of the free holes is defined as [2]

$$\Delta\varepsilon_{free-holes} = -\left(\frac{\omega_P}{\omega}\right)^2 \frac{1}{1+{}^{i}/_{\omega\tau_D}} = -\frac{n_h e^2}{\varepsilon_0 m_h^* \omega^2}\frac{(\omega\tau_D)^2}{1+(\omega\tau_D)^2} + i\,\frac{n_h e^2}{\varepsilon_0 m_h^* \omega^2}\frac{(\omega\tau_D)}{1+(\omega\tau_D)^2} \qquad (A2)$$

where τ_D is the Drude damping time and ω is the incident angular frequency. The free holes absorption coefficient is given by [2]

$$\alpha_{free-hole} = \frac{4\pi}{\lambda\sqrt{2}}\left[\sqrt{Re^2\Delta\varepsilon_{free-holes}+Im^2\Delta\varepsilon_{free-holes}} - Re^2\Delta\varepsilon_{free-holes}\right]^{\frac{1}{2}} \qquad (A3)$$

where $\mathrm{Re}\,\Delta\varepsilon_{\mathrm{free-holes}}$ and and $\mathrm{Im}\Delta\varepsilon_{\mathrm{free-holes}}$ are the real and imaginary parts of equation (A2) respectively and $\lambda = 355\mathrm{nm}$. Taking into account both light holes $(m_{lh}^* = 0.26m_0)$ and heavy holes $(m_{hh}^* = 0.66m_0)$ [3] we obtain from (A1), (A2), and (A3), the values of $\alpha_{\mathrm{free-light\ hole}}$ and $\alpha_{\mathrm{free-heavy\ hole}}$ respectively. We take $\alpha_{\mathrm{free-\ hole}}$ as an average of the two values. Within the specified range of n_h, $\alpha_{\mathrm{free-\ hole}}$ can vary from $9.14\times10^4\mathrm{cm}^{-1}$ for $n_h = 10^{19}\mathrm{cm}^{-3}$ to $1.45\times10^6\mathrm{cm}^{-1}$ for $n_h = 10^{22}\mathrm{cm}^{-3}$. A rough estimate of the surface temperature can be made using the conservation law:

$$\int_{T_{Base}}^{T'_{max}} C(T)\,dT = \alpha_{free-hole}(1-R)J\tau_{Pulse} \qquad (A4)$$

where $C(T)$ is the temperature dependent heat capacity, T_{Base} and T'_{max} are the base temperature of the APT and the maximum temperature of the surface respectively, R is the reflectivity, J is the intensity of the laser light and τ_{Pulse} is the duration of a UV laser pulse. At high frequency, the Drude contribution to the refractive index becomes insignificant. Hence we calculated the reflectivity using the refractive index (η) of diamond at UV $(\lambda = 355\mathrm{nm})$ and the Fresnel's equation for normal incidence as $R = \frac{(\eta-1)^2}{(\eta+1)^2} \approx 0.18$.

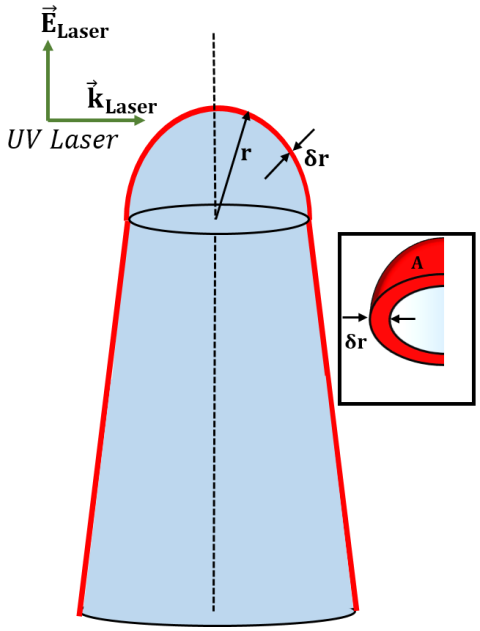

Figure S-A1: *Schematic of the diamond nanotip with a conic shape and a hemishperical cap having a radius 'r'. There is a thin shell of width 'δr' (shown in red) where the free holes are located. The E-field is strong in this region and a steady state of free holes is maintained by impact ionization. The entire blue region is where the E-field is essentially zero with no impact ionization. The concentration of carriers (electrons and holes) in this region are orders of magnitude lower than the free hole concentration at the surface. The UV pulsed laser is shown to be incident normally from left. Inset: 3-D bottom view of the half the hemispherical cap of the diamond nanotip. The parameters 'A' considered in equation (A5) is one quarter the surface area of a sphere of radius 'r'. The free holes absorb the incident laser light leading to a rise in temperature of the surface (details in text) assisting in evaporation of atoms. The blue region is transparent to UV laser light and remains around the APT base temperature of 85K*

We assume the nanotip to be in form of a long tapered cylinder with a hemispherical cap of radius r as shown in Figure S-A1. We consider a thin shell of thickness δr at the surface (shown in red) where the free holes are located and the electric field is high enough to keep impact ionization going. The UV laser is taken to be incident normally from left. First we consider the left half of the hemisphere (inset on Figure S-A1) on which the laser is incident and analyze the temperature rise of this thin shell. $C(T)$ appearing in equation (A4) is approximated as the heat capacity of a 2D phonon gas. The contribution of free holes within this 2-D shell to $C(T)$ is neglected. The phononic heat capacity taking into account the total 2-D phonon density of states

for a surface area 'A' (curved surface area of the half the hemispherical shell shown in inset of Figure S-A1):

$$C(T) = \frac{3Ak_B^3T^2}{2\pi v_D^2\hbar^2}\left\{\int_0^{x_D}\frac{x^3e^x}{(e^x-1)^2}dx\right\} \quad with\ x = \frac{\hbar\omega'}{k_BT}\ and\ x_D = \frac{T_D}{T} \qquad (A5)$$

where T_D is the Debye temperature of diamond, v_D is the Debye velocity which we shall approximate as the velocity of sound in diamond and ω' is the phonon frequency, and $\hbar$ is the reduced Planck's constant. We get a T^2 dependence of heat capacity due to the 2-D density of states rather than a T^3 dependence normally observed for bulk materials. Taking $v_D \approx 17.5\times10^5$ cm/s, $T_D = 1860$ K [4], $\delta r = 2$ nm, $\tau_{Pulse} = 15$ ps, and $r = 15$ nm (Note that the apex diameter of the nanotip, ~100 nm as mentioned in the tip fabrication section, is the diameter considering the diamond nanotip as well as the Ni capping layer. The actual diamond radius is 15nm taken from the APT reconstruction in Figure 4.1(c) of the main article). We deduce from equation (A4) and (A5) that the maximum surface temperature (T'_{max}) on the illuminated side can vary from ~152 K to ~306 K. Since we have a high free carrier absorption coefficient at the surface we have to take into account the loss in intensity of the incident laser as it crosses the thin layer of thickness δr. The amount of laser power absorbed $\{e^{-\alpha_{free-hole}\times\delta r}\}$ can vary from as low as 2% for $\alpha_{free-hole} = 9.14\times10^4$ cm^{-1} to as high as 26% for $\alpha_{free-hole} = 1.45\times10^6$ cm^{-1}. Next, the laser passes through the core {blue region in Figure S-B1}, where the free carrier density is orders of magnitude smaller than the surface. The free carrier contribution at the core of the nanotip being small we take the bulk absorption coefficient of diamond to UV laser light which is negligible. This means the laser light crosses the core of the nanotip virtually unabsorbed. From equation (A4) we get the maximum surface temperature on the dark side to vary from ~147 to ~274 K in the hole concentration range considered ($10^{19}-10^{22}$cm^{-3}).

APT reconstruction for $E_{Pulse} = 500pJ$:

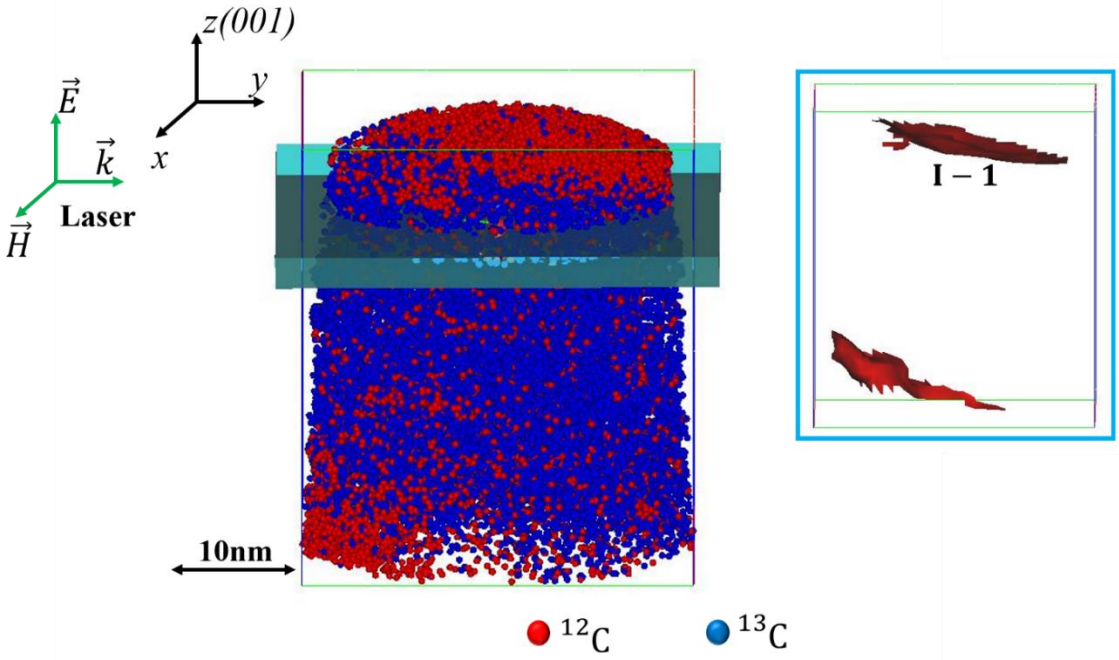

Figure S-A2: *3D atom-by-atom reconstruction of the nanotip evaporated at E_{Pulse} =500 pJ. ^{12}C atoms are shown in red spheres and ^{13}C atoms in blue spheres. Both the growth and analysis direction was (001). Atoms within the cuboid was extracted and used in the analysis shown in Figure S-A3. Inset: The ^{12}C / ^{13}C slanted interface drawn as iso-concentration surfaces (in brown) at 50 at.% ^{13}C concentration. The direction of the upward slant tells us that the laser was incident along the +y direction.*

Extraction of core and surface atoms:

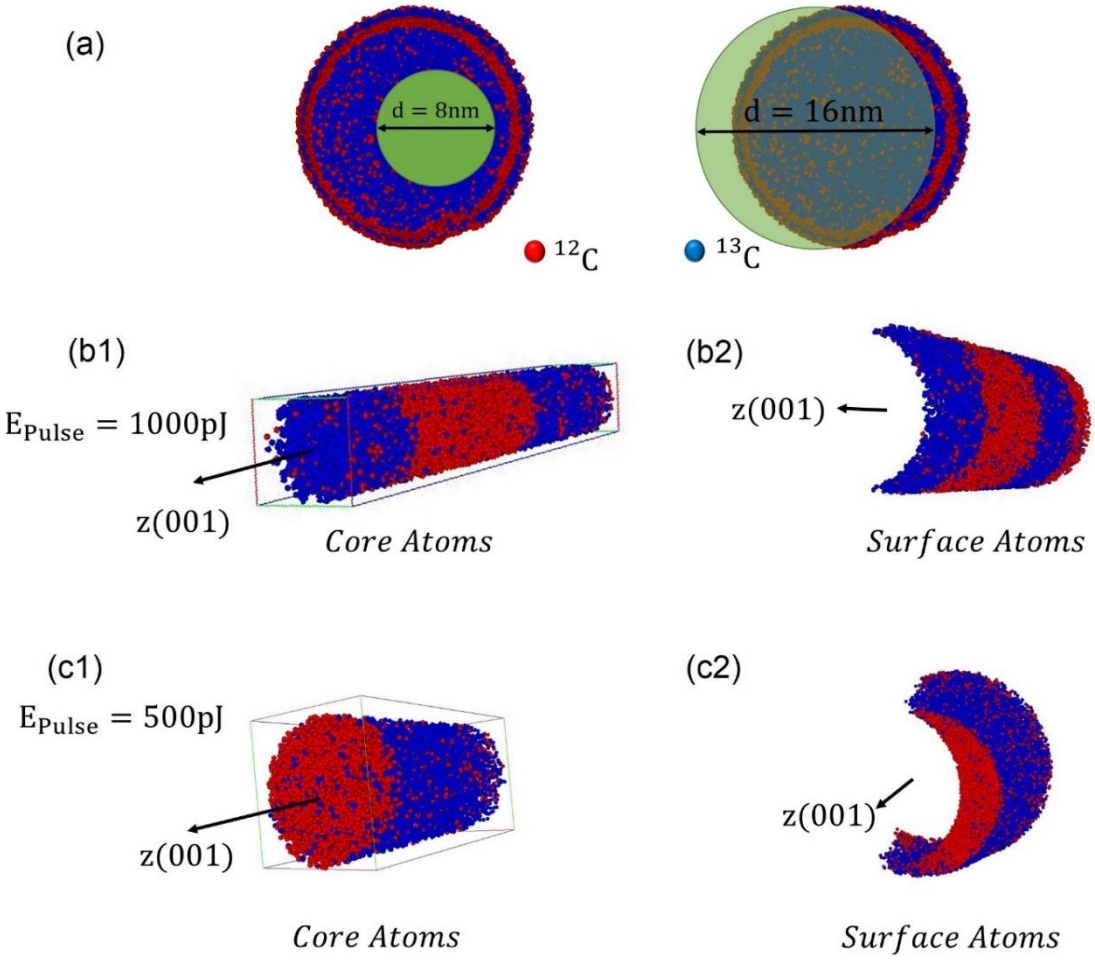

Figure S-A3: *(a) The technique implemented for extracting the core and surface atoms of the diamond nanotip. For the core region, a cylinder with diameter 8nm (in green) was considered along the z axis and atoms only within this cylinder were taken into account. For the surface region, a larger cylinder of diameter 16 nm was considered and atoms outside this cylinder were taken into account. (b) The atom-by-atom reconstruction of the core (b1) and surface atoms (b2) for* E_{Pulse} *=1000 pJ (c) The atom-by-atom reconstruction of the core (c1) and surface atoms (c2) for* E_{Pulse} *=500 pJ. The surface atoms in both (b2) and (c2) are those from the dark (non-illuminated) side of the respective nanotips.*

First, the entire reconstruction region was divided into two separate regions: a core region and a surface region as shown in Figure S-A3(a). Here, we demonstrate the technique using the reconstruction for $E_{Pulse} = 1000$ pJ (Figure 4.1(c) of the main article). For $E_{Pulse} = 500$ pJ the same technique was used. For the core region, a cylinder with diameter 8nm was considered along the z axis and atoms only within this cylinder were taken into account. For the surface region, a larger cylinder of diameter 16nm was considered. All atoms within this larger cylinder were removed and only those lying outside it were taken into account. In Figure S-A3(a) we have shown the cylinders placed in such a way that both the core atoms and the surface atoms from only the non-illuminated (or dark side) side of the nanotip are captured. If the surface atoms from the illuminated side needs capturing (as was required for extracting the mass spectra in Figure 4.3(d) of the main article) the cylinders had to be placed accordingly. Figure S-A3(b) and A3(c) shows the reconstruction of the core and surface atoms for E_{Pulse} =1000 pJ and 500 pJ respectively.

Analysis of atomic diffusion:

We considered three separate diffusion processes as shown in Figure 4.4(a) of the main article process (1), process (2), and process (3) each of which are described in the text of the main article. What comes out from our systematic study is that diffusion is a combined effect of the rise in temperature as well as the number of laser pulses (equivalent to a time factor) the atoms encountered before evaporating. The proximity histogram showing the concentration profile of ^{13}C atoms extracted from the surface (on the non-illuminated or dark side of the nanotip. See Figure S-A3 b(2) and c(2) for corresponding reconstructions) across the interface I-1 of the respective nanotips evaporated at $E_{Pulse} = 1000$ pJ and 500 pJ is displayed in Figure 4.4(b) of the main article. The data has been fitted with the solution of Fick's second law $c(x) = c_0 + c_1\{1 - erf(x/2\sqrt{D\tau_{Diff}})\}$ or $c(x) = c_0 + c_1\{erf(x/2\sqrt{D\tau_{Diff}})\}$ (shown in continuous black lines) where x is the distance, $c(x)$ is the concentration at a given x, D is the self-diffusion coefficient of carbon atoms, c_0 and c_1 are constants, and τ_{Diff} is the diffusion time. The parameter $\sqrt{D\tau_{Diff}}$ is the diffusion length ℓ. The value of ℓ extracted from Figure 4.4(b) of the main article is thus the diffusion length for process (2) which at I-1 for $E_{Pulse} = 1000$ pJ and 500 pJ is 1.63 ± 0.01 nm and 1.46 ± 0.01 nm respectively ($\sim$11.5% increase for $E_{Pulse} = 1000$ pJ). This increase can be attributed to the increase in surface temperature induced by doubling the pulse energy.

In the main article, it has been discussed that the proximity histogram in Figure 4.3(b) shows an apparent broadening due to the difference in the evaporation rate between the illuminated and the dark side of the tip. However, this phenomenon of non-uniform evaporation rate should have the same effect on $\mathcal{L}$ at all the interfaces. From Figure 4.3(b) of the main article we calculated the relative interface width between the different interfaces $\left\{\mathcal{L}_{\mathrm{I}-2}^{13-\mathrm{C}} - \mathcal{L}_{\mathrm{I}-1}^{13-\mathrm{C}} = 1.06 \pm 0.01 \text{ nm and } \mathcal{L}_{\mathrm{I}-3}^{13-\mathrm{C}} - \mathcal{L}_{\mathrm{I}-1}^{13-\mathrm{C}} = 1.49 \pm 0.01 \text{ nm}\right\}$ which cancels the contribution coming from the broadening. The increasing value of the relative interface width suggest that some diffusive component is increasing from I-1 to I-2 to I-3 as we go deeper within the nanotip (along –z axis in Figure 4.1(c) of the main article) from the apex. The root cause of this effect can be attributed to the more number of atoms undergoing diffusion across I-3 than those at I-2 and I-1. This might simply come from the fact that the I-3 encountered more laser pulses than I-2 and I-1. The evaporation can be assumed to be taking place essentially from the surface of the hemisphere in Figure S-A1 because the maximum accumulation of the free holes is at the curved surface. This presents the atoms at the surface of the hemisphere with the greatest chance of field evaporation due to the lowest $\mathrm{Q}_n(\mathrm{F})$. But the size of the heated zone is larger than the size of the hemisphere and encompasses a part of the tapered cylindrical portion of the nanotip as well. While the evaporation is going on from the surface of the hemisphere, the atoms at the surface of the tapered cylinder are just experiencing the periodic heating and rapid cooling process with every pulse without any evaporation. This gives more time to atoms in the vicinity of I-3 to diffuse across the interface as compared to I-2 and I-1.

In Figure 4.4(c) of the main article we have plotted the $^{13}\mathrm{C}$ concentration profile at I-1 and I-2 at the surface atoms of the nanotip evaporated at $\mathrm{E}_{\mathrm{Pulse}} = 1000$ pJ. The inset shows only the Fick's law fits of the raw data. For convenience of display the x-coordinate of the fitting equation for I-2 has been negated before plotting. The value of ℓ extracted from Figure 4.4(c) of the main article is also the diffusion length for process (2). The Fick's law fits give the value of ℓ for process (2) at I-1 and I-2 to be 1.63 ± 0.01 nm and 1.94 ± 0.01 nm respectively ($\sim$19% increase at I-2). With 'D' the same at both interfaces, the result suggests that atoms at the vicinity of I-2 encountered more laser pulses and thus had more time to diffuse than the atoms in vicinity of I-1. In Figure 4.4(d) of the main article we plotted the concentration profile of $^{13}\mathrm{C}$ atoms at I-1 and I-2 extracted from the core of the nanotips evaporated at $\mathrm{E}_{\mathrm{Pulse}} = 1000$ pJ. The inset shows only the Fick's law

fits of the raw data. Similar to Figure 4.4(c) of the main article, the x-coordinate of the fitting equation for I-2 was negated before plotting. The value of ℓ extracted from this figure is thus the diffusion length for process (3) which at I-1 and I-2 are 0.31 ± 0.01 nm and 0.35 ± 0.01 nm respectively ($\sim 13\%$ increase at I-2). Just like process (2), the bulk diffusion length increases as we go deeper from the apex of the nanotip. This too can be attributed to the fact that the core atoms in the vicinity of I-2 had more time to undergo bulk diffusion that those in the vicinity of I-1. The other important thing to note here is that at each interface the axial bulk diffusion length is much less that the axial surface diffusion length (a similar statement can be made regarding the corresponding orthogonal counterparts). This is because the surface and the bulk of the nanotip are heated by two different mechanisms. The free holes (generated by impact ionization) at the surface first absorb the laser and raise the temperature of the surface as they relax by colliding with lattice vibrations. During this entire process core essentially remains at the base temperature (negligible free carrier absorption at the core due to orders of magnitude less number of free carriers at the core of the nanotip). Its only when the heat from the surface starts dissipating (the two step heat dissipation process was proposed in the main article) the temperature of the core increases from the base temperature but in principle it should never increase as much as the surface. This is possibly the reason that ℓ for process (3) at I-1 or I-2 for $\mathrm{E_{Pulse}} = 1000$ pJ is less by a factor of ~ 5 compared to ℓ for process (2). The interface width ($\mathcal{L}$) at the core and the surface (dark side) at I-1 of the nanotip evaporated at $\mathrm{E_{Pulse}} = 1000$ pJ showed a similar effect. $\mathcal{L}$ was estimated from the cubic spline interpolation of the raw data (red dashed lines in Figure 4.4(c) and (d) of the main article) using the separation between 10% and 90% concentration points of $^{13}\mathrm{C}$ atoms. For the core region $\mathcal{L}_{\mathrm{I-1}}^{^{13}\mathrm{C}}$is $\sim 0.58 \pm 0.01$ nm while for the surface it is $\sim 2.03 \pm 0.01$ nm demonstrating a decrease of $\mathcal{L}$ by a factor of ~ 3.5 at the core of the nanotip than at the surface. Note that figures similar to Figure 4.4(c) and (d) of the main article could not be generated for the nanotip evaporated at $\mathrm{E_{Pulse}} = 500$ pJ because as Figure S-A2 reveals, the nanotip fractured while crossing I-2, hence the reconstruction has only one complete interface which is I-1.

Distributions of various cations and clusters:

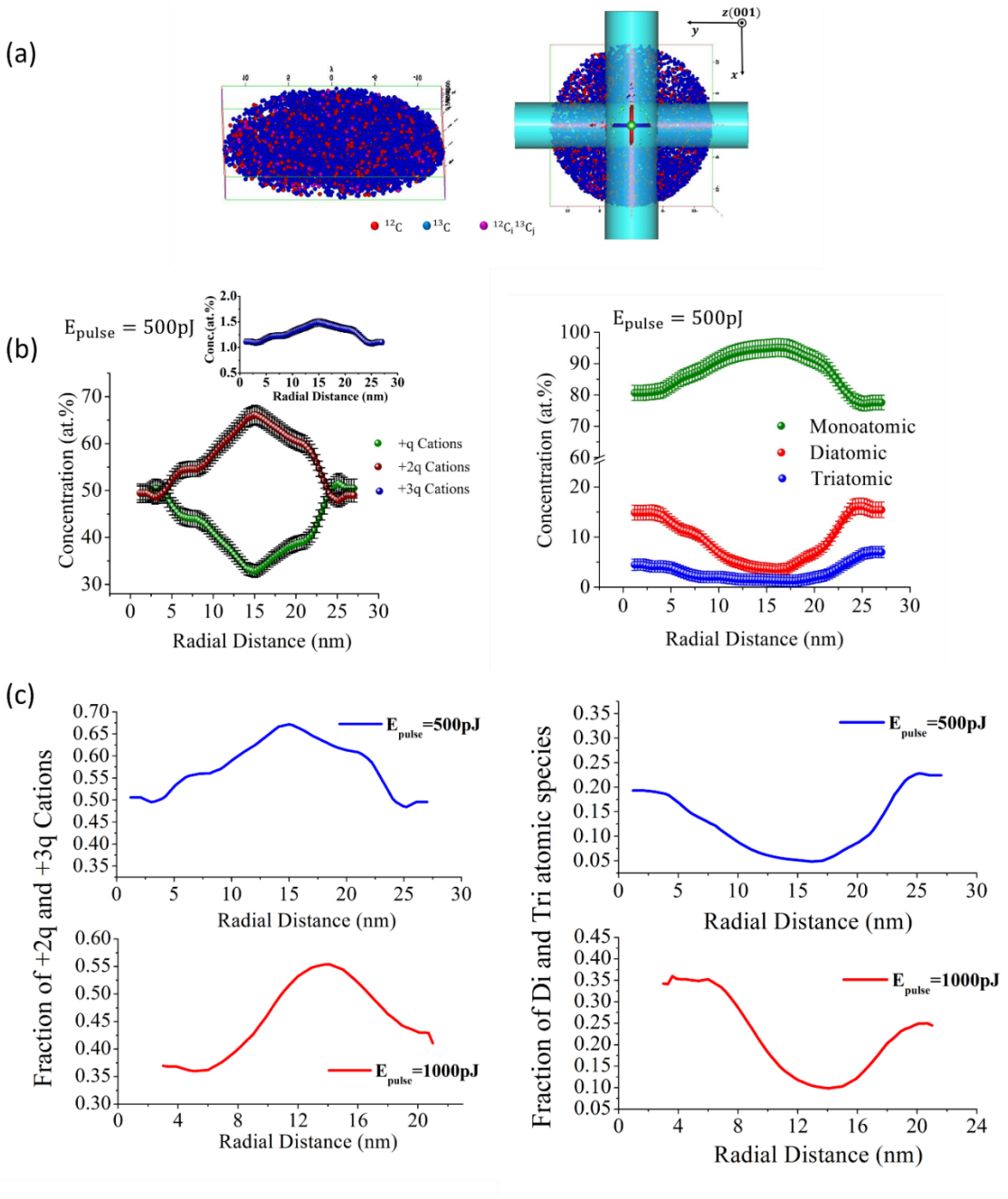

Figure S-A4: *(a) Left: 3-D mapping of atoms within the cuboid shown in Figure S-A2. Right: Two perpendicular cylinders were considered and the average normalized concentrations of various cations and atomic clusters along the length of these two cylinders were used in Figure S-A4(b) and (c). Left: Plot of normalized concentration of +q, +2q and +3q (inset) cations with radial distance for* E_{pulse} *=500 pJ. Right: Plot of normalized concentration of mono, di, and tri atomic*

species with radial distance for E_{pulse} =500 pJ.(c) Left: Fractional composition of +2q and +3q cations with radial distance for E_{pulse} =500 pJ (top) and for E_{pulse} =1000 pJ (bottom). Right: Fractional composition of di and tri atomic clusters with radial distance for E_{pulse} =500 pJ (top) and for E_{pulse} =1000 pJ (bottom).

We extracted a thin slice of atoms from within the cuboid shown in Figure S-A2. (For Figure 4.5 of the main article we used the same technique to extract a thin slice of atoms from the first ^{13}C layer of the reconstruction shown in Figure 4.1(c)). A tilted front view of the slice is shown in Figure S-A4(a) on the left. To the right, the top view of the slice is displayed. Also displayed are two perpendicular cylinders of same length and diameter. The concentration of a perticular cation or cluster was measured along the length of these two cylinders, averaged and normalized data was used for analysis.

[1] Wei, L.; Kuo, P. K.; Thomas, R. L.; Anthony, T. R.; Banholzer, W. F. *Phys. Rev. Lett.* **1993**, *70* (24), 3764–3767.

[2] Sokolowski-Tinten, K.; von der Linde, D. *Phys. Rev. B* **2000**, *61* (4), 2643–2650.

[3] Naka, N.; Fukai, K.; Handa, Y.; Akimoto, I. *Phys. Rev. B* **2013**, *88* (3), 035205.

[4] Wild, C.; Worner, E. The CVD Diamond Booklet.

APPENDIX B : SUPPLEMENTARY MATERIAL FOR THE ARTICLE 2: SHORT-RANGE ATOMIC ORDERING IN NON-EQUILIBRIUM SILICON-GERMANIUM-TIN SEMICONDUCTORS

S. Mukherjee[1], N. Kodali[1], D. Isheim[2], S. Wirths[3], J. M. Hartmann[4], D. Buca[3],

D. N. Seidman[2], and O. Moutanabbir[1,*]

[1] *Department of Engineering Physics, École Polytechnique de Montréal, Montréal, C. P. 6079, Succ. Centre-Ville, Montréal, Québec H3C 3A7, Canada.*

[2] *Department of Materials Science and Engineering and Northwestern University Center for Atom-Probe Tomography, Northwestern University, Evanston, IL 60208-3108, USA.*

[3] *Peter Grünberg Institute 9 and JARA - FIT, Forschungszentrum Juelich, Juelich 52425, Germany.*

[4] *CEA, LETI, Minatec Campus, 17 rue des Martyrs, Grenoble 38054, France*.

Details of growth of the ternary alloys: The growth was carried out on low-defect density Ge/Si(100) virtual substrates developed in Ref [1]. The thickness of the Ge layer atop the Si(001) was ~ 2.7 µm. Si_2H_6, Ge_2H_6 (10% diluted in H_2), and $SnCl_4$ were used as precursors and N_2 as carrier gas. Relatively low growth temperatures (350 - 475°C) were used to avoid segregation, phase separation, and epitaxial breakdown thus ensuring the growth of high crystalline quality $Si_xGe_{1-x-y}Sn_y$ with an Sn content above the equilibrium composition (>1 at.%). The general approach to obtain these non-equilibrium alloy is to deposit the material one atomic layer at a time, under growth conditions in which the surface mobility of atoms is limited to such an extent that the nucleation of separated phases on the surface is prevented. Then, with the deposition of the next layer, these atoms become buried and freeze in a mixed state. The thickness of the investigated layers is ~ 50 nm.

Atom Probe Tomography Investigation. The APT sample preparation was done using the standard lift-out technique [2]. The APT experiment was carried out using a UV laser-assisted Local Electrode Atom Probe (LEAP). Field evaporation of individual atoms was assisted by focusing a UV laser (355 nm), with a beam waist smaller than 5 µm, on the apex of the needle-shaped specimen. The evaporation rate (ion/pulse), the laser pulse repetition-rate, and energy per

pulse were 0.01, 500 kHz, and 25 pJ respectively. The base temperature and base pressure within the APT chamber were maintained at $50\,\mathrm{K}$ and 3.2×10^{-11} Torr respectively. The 3-D reconstructions were performed using Cameca's IVAS program.

Statistical Formalism.

i) The frequency distribution analysis: In the frequency distribution analysis, the ROI is broken down into N' blocks each containing equal number of atoms, n_b. The total number of atoms of a particular element is then counted in each block and frequency at which a particular atom occurs is then compared with a binomial distribution. For example, if n is the number of atoms of a particular element which is randomly distributed throughout the ROI and has a bulk normalized concentration of C then its frequency of occurrence must follow the binomial distribution [3]:

$$f(n) = \frac{N' n_b!}{n!\,(n_b - n)!} C^n (1 - C)^{(n_b - n)} \qquad (B1)$$

ii) The partial radial distribution function (p-RDF) analysis: In (p-RDF) analysis the k^{th} atom of an element X (which could be Si, Ge, or Sn) is chosen as the central atom. Then a spherical shell of radius r and thickness dr is defined around this central atom and the number of atoms of the i^{th} element (Si, Ge, or Sn) positioned within the volume $4\pi r^2 dr$ is calculated. Next, r is incremented by small steps and the number of atoms are computed after each step. This continues till r reaches the pre-assigned maximum radius. If the atoms are ideally random (completely uncorrelated), then the exact number of atoms at r within the shell of thickness dr is the average number of atoms per unit volume times $4\pi r^2 dr$. Thus, $C_i^0 = \rho_i 4\pi r^2 dr$, where ρ_i is the density of the i^{th} element assuming it is randomly distributed, that is $\rho_i = {}^{N_i}/_{V}$. To quantify atomic ordering in a given material, the (p-RDF) is defined as [4]:

$$p - RDF = \frac{1}{C_i^0} \sum_{k=1}^{N_X} \frac{N_i^k(r)}{N_{tot}^k(r)} \qquad (B2)$$

with $N_i^k(r)$ as the actual number of atoms of the i^{th} element within the shell of thickness dr around the k^{th} atom of element X at the center, $N_{tot}^k(r)$ is the total number of atoms of all atomic species

within the shell around the k^{th} atom of element X at the center, and N_X is the total number of X atoms within the ROI. It is clear from the expression of (p-RDF) that if the i^{th} element is randomly distributed or completely uncorrelated with respect to (wrt.) an element X, its (p-RDF) should be unity. (p-RDF) greater than unity symbolized positive correlation or a concentration greater than the bulk normalized concentration. Conversely, a (p-RDF) less than unity symbolized negative correlation indicating a concentration below the bulk normalized concentration.

iii) The nearest neighbor (NN) distribution analysis: For an ABC-type ternary alloy various combinations of NN distribution can be calculated like NN_{A-A}, NN_{A-B}, NN_{B-C} and so on. Here, we have analyzed only the NN_{A-A} type but for different order. The NN distribution analysis calculates the distance between an A atom and its closest neighboring 'A' atoms. This gives the first nearest neighbor distance or $NN_{A-A} - 1$. This is then extended to calculate the distance between the A atom and its higher k^{th} order neighbors, giving $NN_{A-A} - k$. The process is then repeated until the entire ROI is processed. For an ideal solid solution, where the atoms of an element are randomly distributed with a bulk normalized concentration of *C*, the probability of its k^{th} nearest neighbor of a given atom being at a distance r is given by the following distribution function [5]:

$$P_k(r, C) = \frac{3}{(k-1)!}\left(\frac{4\pi}{3}C\right)^k r^{3k-1} e^{-(4\pi/3)Cr^3} \qquad (B3)$$

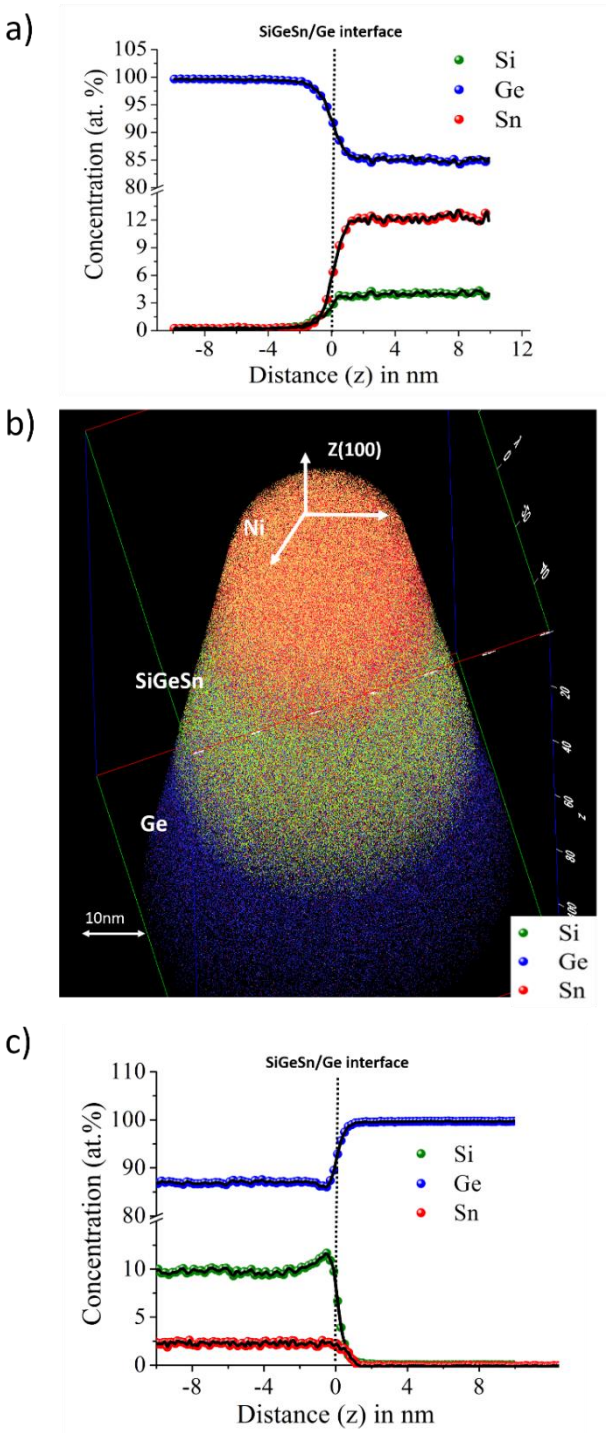

Figure. S-B1: *(a) 1D proximity histogram of the alloy with high Sn content ($Si_{0.04}Ge_{0.84}Sn_{0.12}$) across the SiGeSn/Ge interface (b) 3-D reconstruction and (c) 1D proximity histogram across the SiGeSn/Ge interface of the ternary alloy with lowest Sn content ($Si_{0.04}Ge_{0.84}Sn_{0.12}$).*

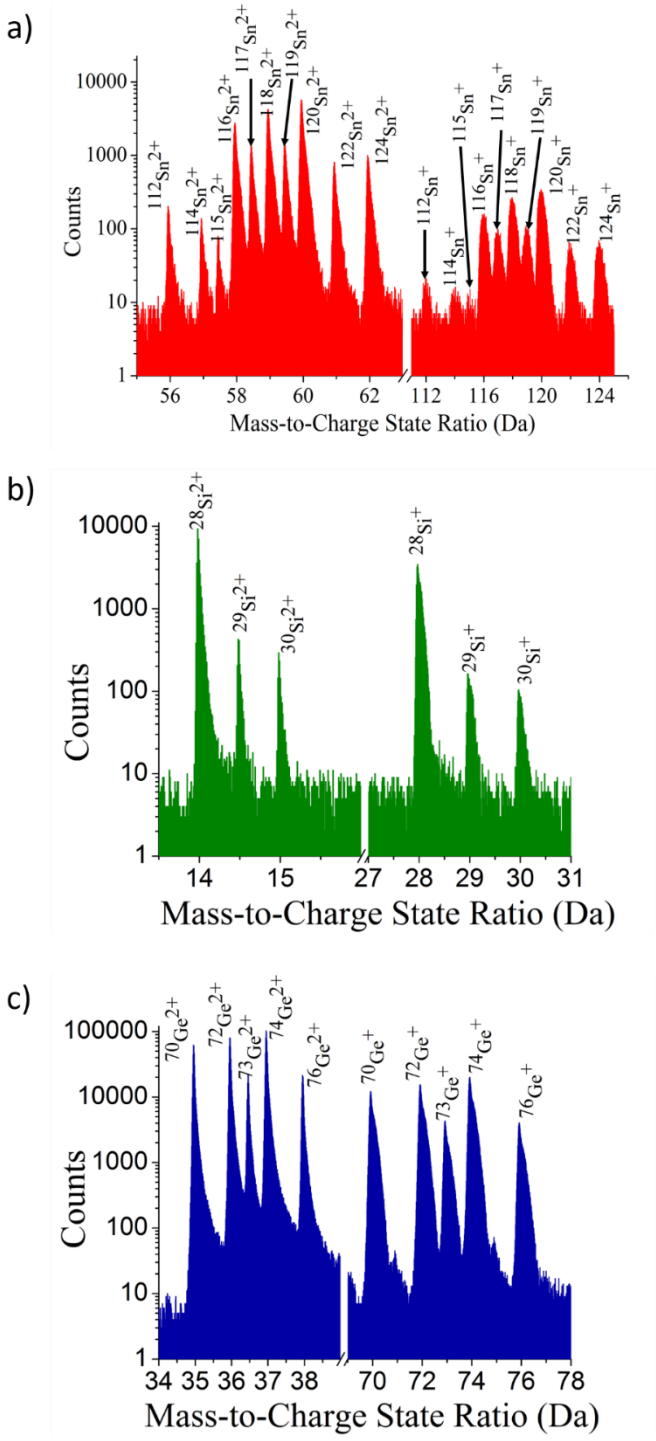

Figure. S-B2: *Mass spectra of (a) Sn, (b) Si, and (c) Ge respectively in the* $Si_{0.04}Ge_{0.84}Sn_{0.12}$ *alloy. Both single and doubly charged states of all the isotopes are shown. The y-axis of the figures is in log scale and the x-axis has been broken to include both charge states in a single graph.*

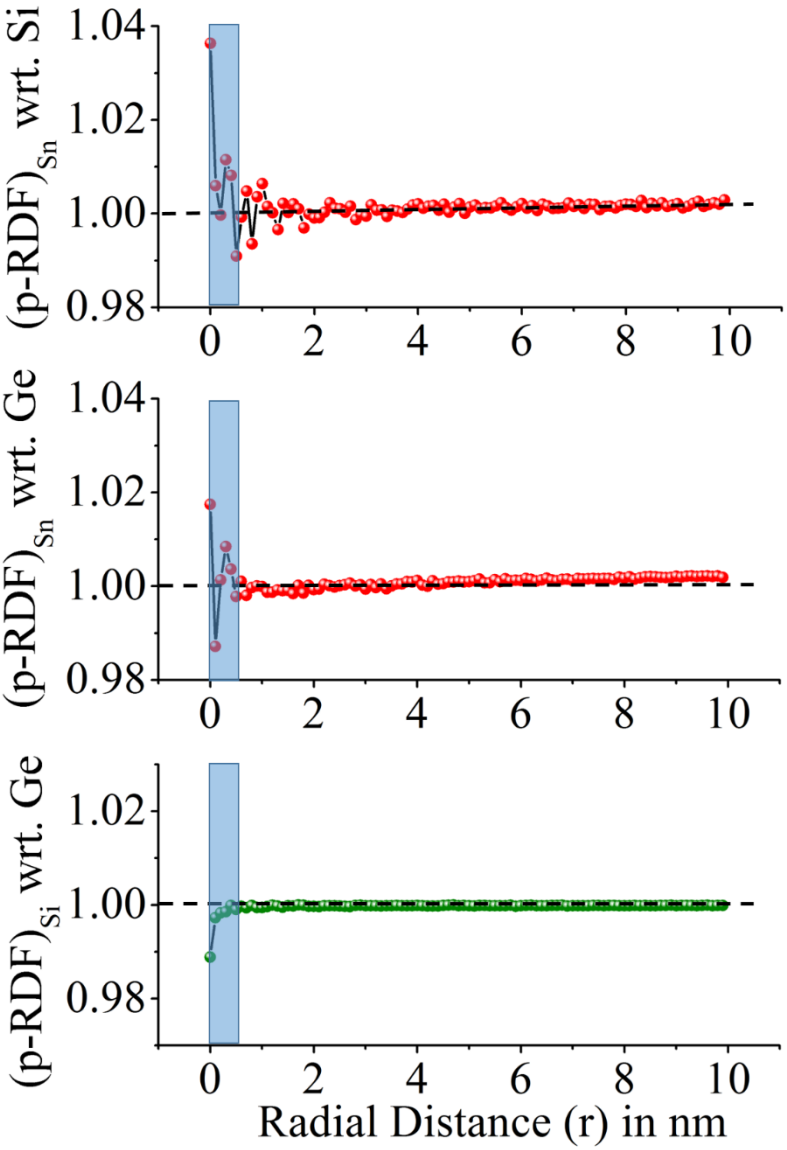

Figure S-B3: *The partial radial distribution function (p-RDF) of Sn wrt. Si (top). Sn wrt. Ge (middle), and Si wrt. Ge (bottom) atoms in the alloy with lowest Sn content ($Si_{0.04}Ge_{0.84}Sn_{0.12}$) for r =10 nm. The IVAS computed error bars are smaller than the data symbols. The black dotted line represents $p - RDF$ =1.*

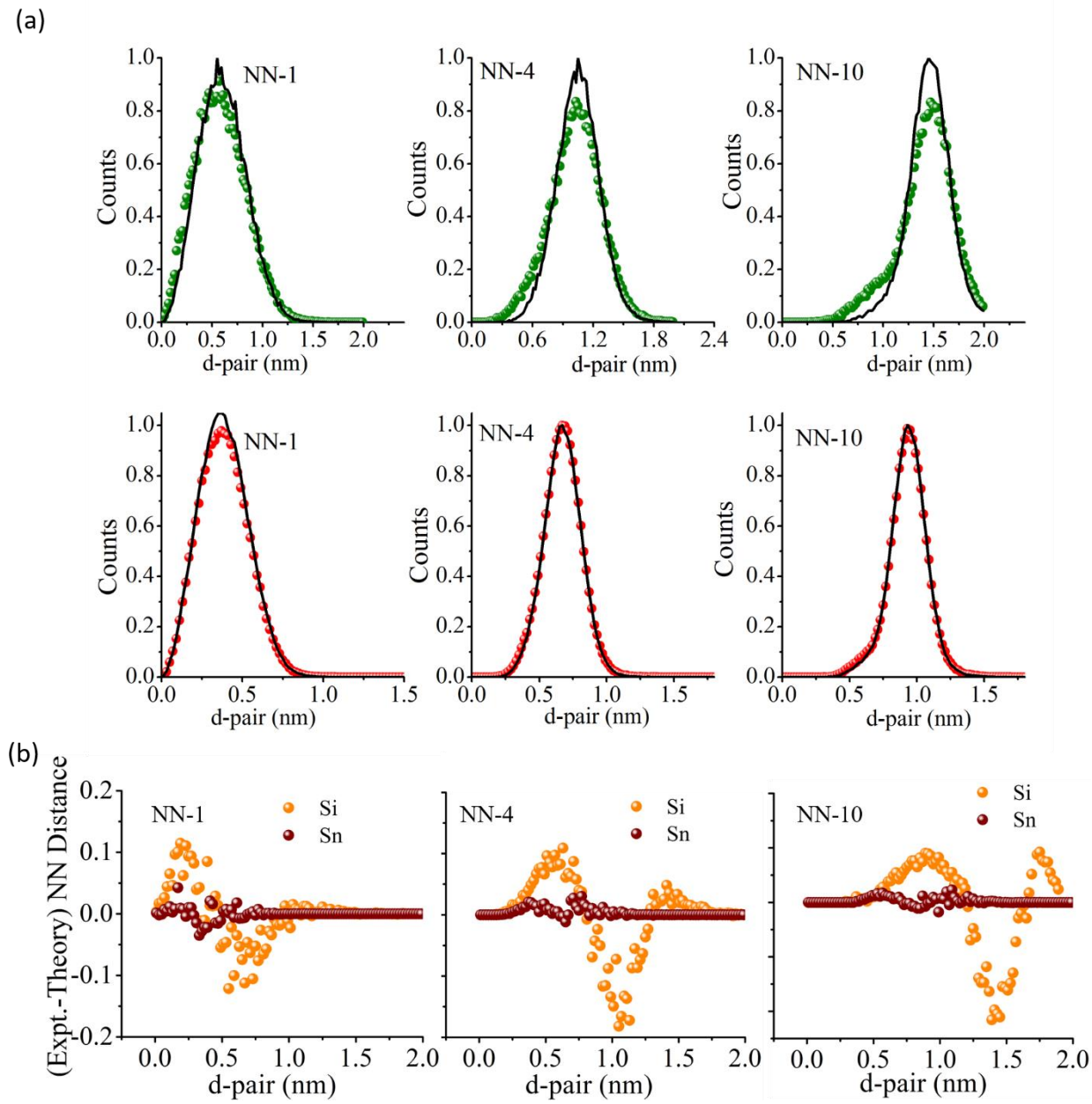

Figure S-B4: *(a) The NN-1, 4, and 10 distribution of Si (green) and Sn (red) in* $Si_{0.04}Ge_{0.84}Sn_{0.12}$*. In both the plots, the distribution determined from APT reconstruction are shown in solid spheres and the corresponding theoretical distribution considering a perfect random alloy are shown in black continuous lines. (b) Departure of the observed Si-Si and Sn-Sn NN 1, 4, and 10 distributions from the binomial distribution in* $Si_{0.04}Ge_{0.84}Sn_{0.12}$*. The y-axis in all the three figures are the same.*

(a)

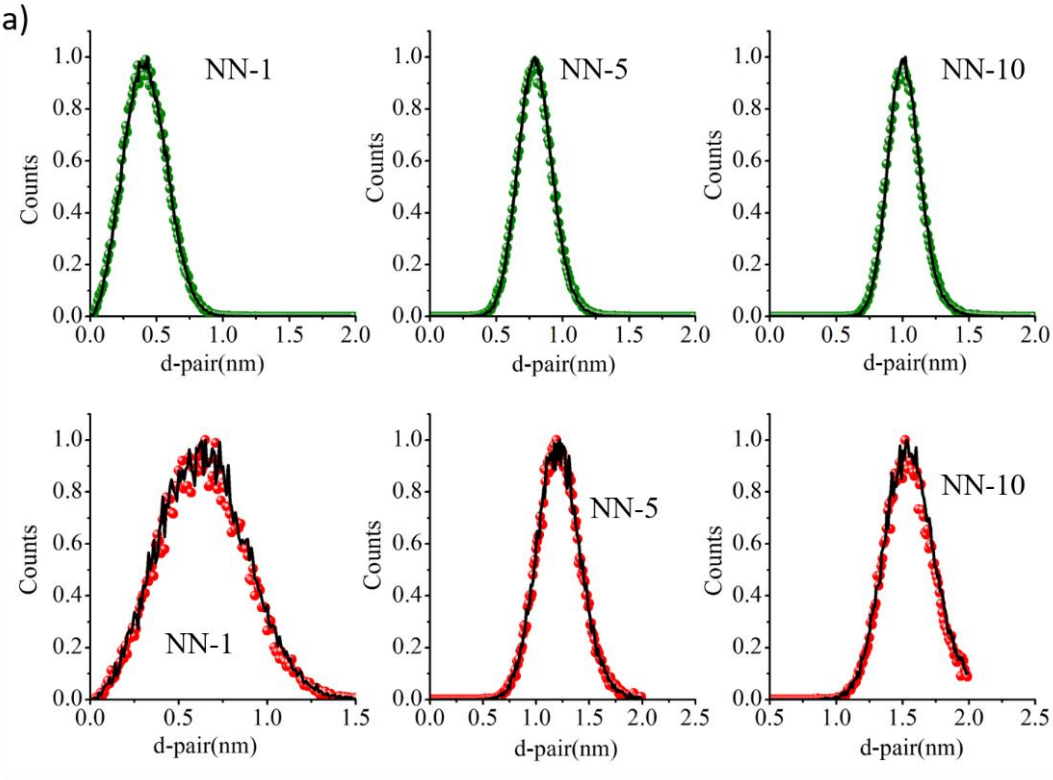
NN-1
NN-5
NN-10
NN-1
NN-5
NN-10
Counts
d-pair(nm)

(b)

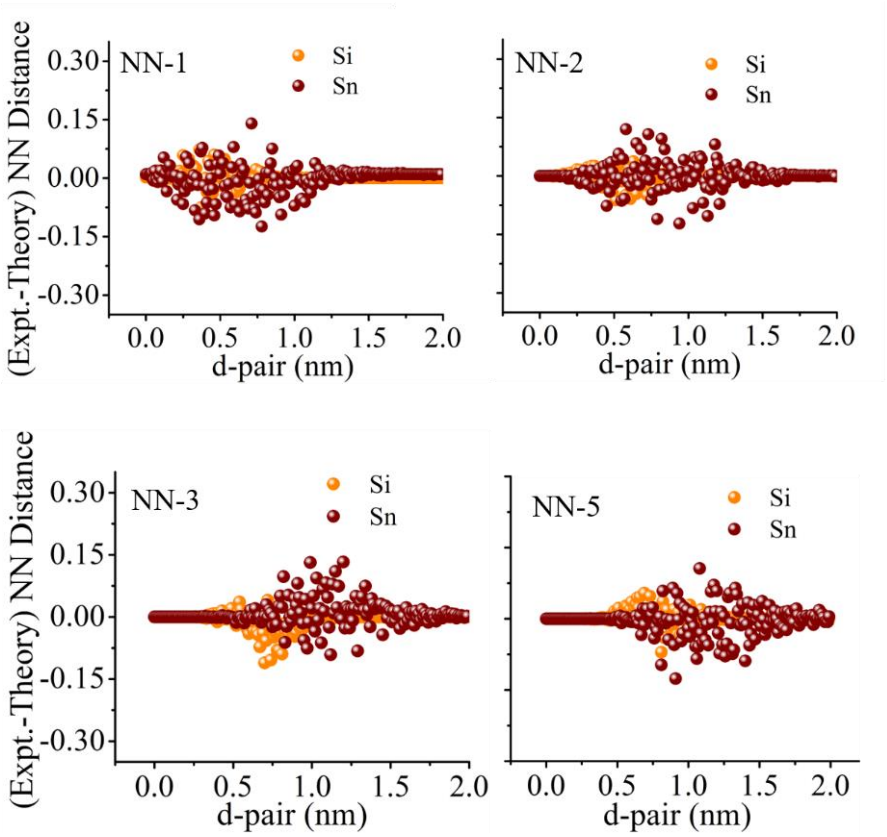
NN-1
NN-2
NN-3
NN-5
Si
Sn
(Expt.-Theory) NN Distance
d-pair (nm)

Figure S-B5: *(a) The NN-1, 5, and 10 distribution of Si (green) and Sn (red) in $Si_{0.10}Ge_{0.875}Sn_{0.025}$. In both the plots, the distribution determined from APT reconstruction are shown in solid spheres and the corresponding theoretical distribution considering a perfect random alloy are shown in black continuous lines. (b) Departure of the observed Si-Si and Sn-Sn NN 1, 2, 3, and 5 distributions from the binomial distribution in $Si_{0.10}Ge_{0.875}Sn_{0.025}$.*

DFT Calculations: The density-functional theory (DFT) calculations were done using the Quantum Espresso code [6], with a plane-wave energy cutoff of 60 R_y (R_y is the Rydberg constant equaling 13.6 eV). The pseudopotentials used were a combination of ultrasoft [7] and PAW [8] pseudopotentials with the Perdew-Burke-Ernzerhof functional [9]. These pseudopotentials were taken from the Pslibrary project [10] and the GBRV project [11]. The reciprocal space has been sampled using a Monkhorst-Pack mesh [12] of 9 K-points. We have analyzed the (100) layer of Ge lattice by considering a supercell with 32 Ge atoms (4×4 Germanium unit cells with interlayer spacing of about 17Å) and 32 H atoms which were added to avoid surface reconstruction and remove dangling bonds. Finally, we have replaced Ge atoms with Sn and/or Si atoms as necessary to study the interactions between Sn and Si atoms in Ge lattice. We performed variable cell relaxation calculations considering the x component of the first lattice vector, the y component of the second lattice vector and all the atomic positions as variables. The BFGS quasi-Newton algorithm was used for both Ion and Cell dynamics.

There are obviously a very large number of configurations in which the Sn and Si atoms can be arranged within the ternary alloy lattice. Herein, without losing the sense of generality, we present the result obtained for a few cases. The Sn atom is always placed at the second layer from the top and the Si atom is either placed at the outermost layers of the unit cell (case 1, Figure S-B6(a)) or at the inner layers of the unit cell (case 2, Figure S-B6(b)). The energy of the unit cell for both the cases for different Sn-Si distance was calculated and the difference in energy per unit cell relative to the lowest energy configuration was plotted as a function of Si-Sn distance in Figure S-B7 (case 1 on top and case 2 at the bottom). The nearest neighbor configurations are mentioned alongside each data point in Figure S-B7 and corresponds to the schematic representation shown in Figures S-B6(a) and (b). The lowest energy was found to be the $(NN3)_a$ configuration for case 1 and the $(NN4)_b$ configuration for case 2. Interestingly, we found that a Si-Sn bond (NN-1

configuration) is indeed energetically not favorable in all cases (∼+50meV/unit cell for case 1) and (∼+250meV/unit cell for case 2), supporting the hypothesized repulsive interaction between Si and Sn atoms.

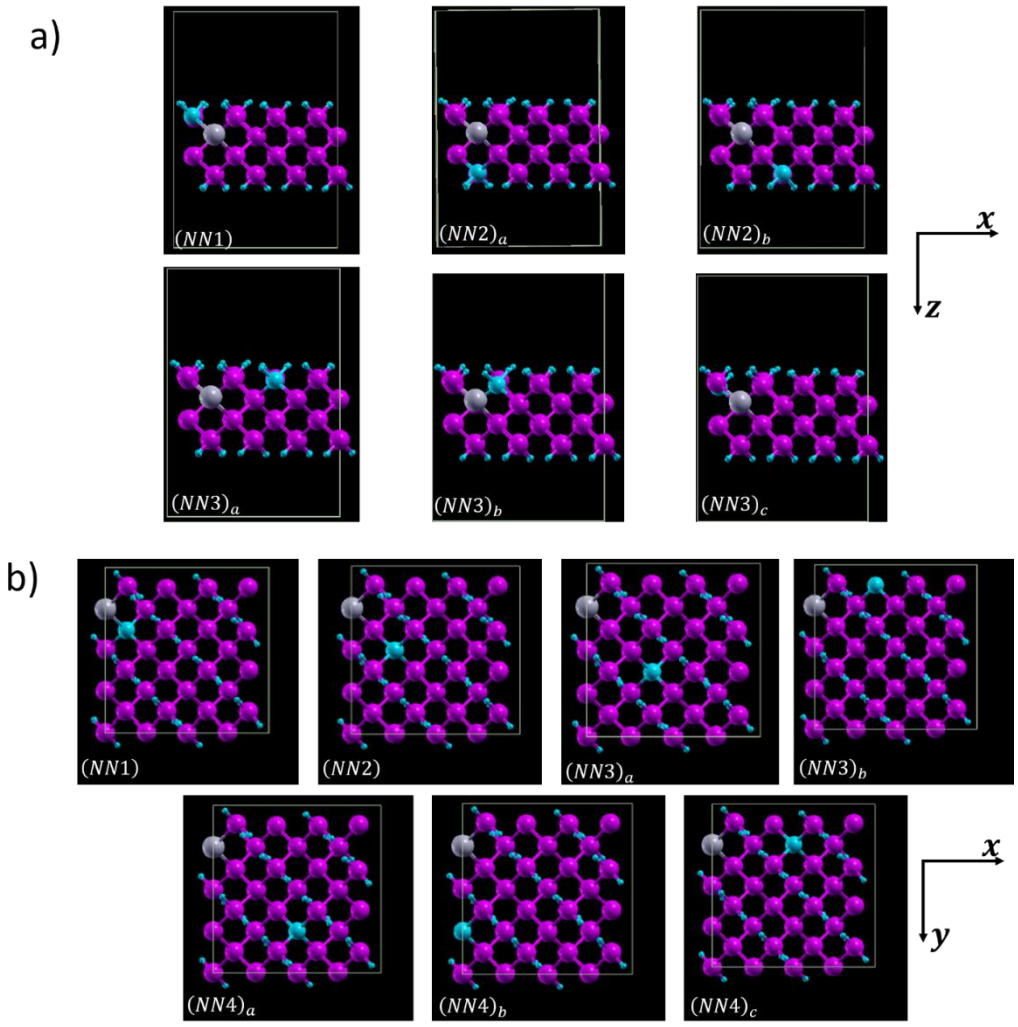

Figure S-B6: *The Si-Sn NN configurations considered for the DFT calculations. The Ge atoms are shown in purple, Sn in grey and Si in light blue. The Sn atom is always placed at the second layer from top. (a) Case 1: The Si atoms are placed in the outermost layers. (b) Case 2: The Si atoms are placed in the inner two layers.*

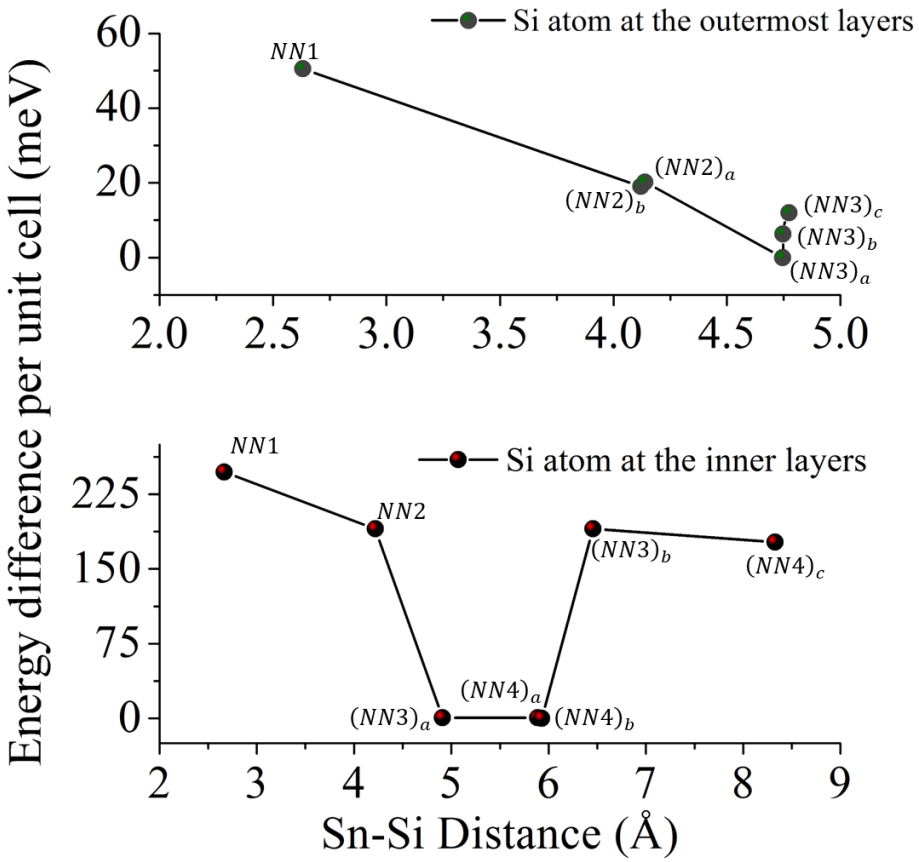

Figure S-B7: *DFT results plotting the energy difference per unit cell as a function of the Sn-Si distance. The Sn atom was always placed at the second layer from top. In the top graph, the Si atom are located only in the outermost layers of the 4×4 unit cell while in the bottom graph the Si atom was placed in the inner layers of the unit cell. The NN configurations has also been mentioned alongside each data point. The lowest energy configurations were the* $(NN3)_a$ *in the top graph and the* $(NN4)_b$ *in the bottom graph. The energy difference has been plotted relative to these lowest energy configurations. The solid black line is for the guide to the eye.*

[1] J. M. Hartmann, A. Abbadie, N. Cherkashin, H. Grampeix, and L. Clavelier, Semicond. Sci. Technol. **24**, 55002 (2009).

[2] M. K. Miller, K. F. Russell, and G. B. Thompson, Ultramicroscopy **102**, 287 (2005).

[3] M. P. Moody, L. T. Stephenson, A. V Ceguerra, and S. P. Ringer, Microsc. Res. Tech. **71**, 542 (2008)

[4] C. Sudbrack, R. Noebe, and D. Seidman, Phys. Rev. B **73**, 212101 (2006).

[5] B. Gault, M. P. Moody, J. M. Cairney, and S. P. Ringer, *Atom Probe Microscopy* (Springer, New York, 2012).

[6] P. Giannozzi *et al.*, J. Phys. Condens. Matter **21**, 395502 (2009).

[7] D. Vanderbilt, Phys. Rev. B **41**, 7892 (1990).

[8] P. E. Blöchl, Phys. Rev. B **50**, 17953 (1994).

[9] J. P. Perdew, K. Burke, and M. Ernzerhof, Phys. Rev. Lett. **77**, 3865 (1996).

[10] A. Dal Corso, Comput. Mater. Sci. **95**, 337 (2014).

[11] K. F. Garrity, J. W. Bennett, K. M. Rabe, and D. Vanderbilt, Comput. Mater. Sci. **81**, 446 (2014).

[12] H. J. Monkhorst and J. D. Pack, Phys. Rev. B **13**, 5188 (1976).

APPENDIX C – SUPPLEMENTARY MATERIAL FOR THE ARTICLE 3: PHONON ENGINEERING IN ISOTOPICALLY DISORDERED SILICON NANOWIRES

S. Mukherjee,[†] U. Givan,[‡] S. Senz,[‡] A. Bergeron,[†] S. Francoeur,[†] M. de la Mata,[§] J. Arbiol,[§,#] T. Sekiguchi,[‖] K. M. Itoh,[‖] D. Isheim,[¥] D. N. Seidman,[¥] and O. Moutanabbir,[†]

[†] *Department of Engineering Physics, Polytechnique Montréal, C. P. 6079, Succ. Centre-Ville, Montréal, Québec H3C 3A7, Canada*

[‡] *Max Planck Institute of Microstructure Physics, Weinberg 2, D 06120 Halle (Saale), Germany*

[§] *Institut de Ciencia de Materials de Barcelona, ICMAB-CSIC, Campus de la UAB, 08193 Bellaterra, Catalonia, Spain*

[#] *Institució Catalana de Recerca i Estudis Avançats (ICREA), 08010 Barcelona, Catalonia, Spain*

[‖] *Department of Applied Physics and Physico-Informatics, Keio University, Hiyoshi, Yokohama, Japan*

[¥] *Department of Materials Science and Engineering Northwestern University Center for Atom-Probe Tomography, Northwestern University, Evanston, IL 60208-3108, USA*

Experimental Details.

Growth of Isotopically Engineered Nanowires: The growth of the NWs was achieved using the classical gold (Au)-catalyzed vapor phase epitaxy in an Ultra High Vacuum Chemical Vapor Deposition (UHV-CVD) chamber having a background pressure of ~ 10^{-10} mbar. A Si (111) wafer was cleaned by standard RCA process prior to dipping in 1% HF to achieve H-terminated surface. Next the wafer was coated with 1 nm Au film by employing E-beam evaporator and then transferred into the UHV-CVD reactor. A pre-calibrated annealing step (450 ^{0}C, 20 min) was carried out in order to break the Au film into Au-Si eutectic droplets which served, in turn, as catalysts for the following VLS growth process. The precursors used for the growth were monoisotopic silane $^{28}SiH_4$, $^{29}SiH_4$, and $^{30}SiH_4$ with isotopic purity higher than 99.9%. These precursors were synthesized by hydrogenation of isotopically enriched SiF_4. The growth of the

nanowires was carried out at a temperature of 480 ºC, and a reactor pressure of 1.5 Torr. The samples consist of isotopically pure ^{29}Si NWs and isotopically mixed $^{28}Si_x{}^{30}Si_{1-x}$ NWs. The former were grown by injecting the monoisotopic $^{29}SiH_4$ precursor, whereas for the latter $^{28}SiH_4$ and $^{30}SiH_4$ were simultaneously introduced in the growth chamber. The control of the content of each isotope in the growing isotopically mixed NWs was achieved through the control of the partial pressures of the two precursors. The growths lasted for 16 min resulting in the growth of around 5 μm long NWs.

Raman Spectroscopy: Raman spectroscopy was employed to investigate the vibrational properties of these NWs. To enable the analysis of individual NWs, the as-grown NWs were first transferred onto gold-capped Si to suppress the background signal from the underlying substrate during subsequent Raman analysis. A suspension of NWs in acetone was made by first scratching a small piece of an as-grown sample using a sharp blade and then agitating it in an ultrasonic bath for 10 min at room temperature. Next 2-3 drops of the suspension were deposited on a 5 mm × 5 mm gold-capped Si and left alone in air at room temperature for the acetone to evaporate. Backscattering micro-Raman experiment was carried out in a Renishaw InVia RM 3000 setup using a 488nm CW laser and a 100× Olympus objective of numerical aperture 0.9 (spot area at laser waist ~ 0.36 μm^2) at incident power densities in the range of 0.08–1.94 mW/μm^2. Higher power measurements were performed in a separate Raman setup using a 532nm CW laser and a 100× objective of numerical aperture 0.8 (spot area at laser waist ~ 0.5 μm^2) at incident power densities in the range of 3.87–11.76 mW/μm^2 (high power regime). Using an optical microscope, we focused the laser on NWs that are isolated to avoid NWs in clusters. The average length of the NWs after dispersion was found to be 2-3 μm. The reason for analyzing only single isolated NWs is that they are in good thermal contact with the gold in contrast to the case of clusters where several NWs may remain suspended leading to a poor thermal contact with the substrate. These NWs heat up faster when exposed to laser beam, which influences their Raman modes. Also, based on the optical microscope observation we ensured that all the individual NWs investigated in this work had comparable lengths. The laser power incident on a NW was recorded prior to each measurement by a miniature hand held power meter.

All calculations involving the quasi-harmonic approximation were carried out on data sets recorded at the lowest incident power density of 0.08 mW/μm^2 at which the local temperature of the NWs

is confirmed to be equal to the ambient temperature of 300K. Indeed, all measured Raman spectra below this power were found to be insensitive to laser power indicating the absence of any significant heating.

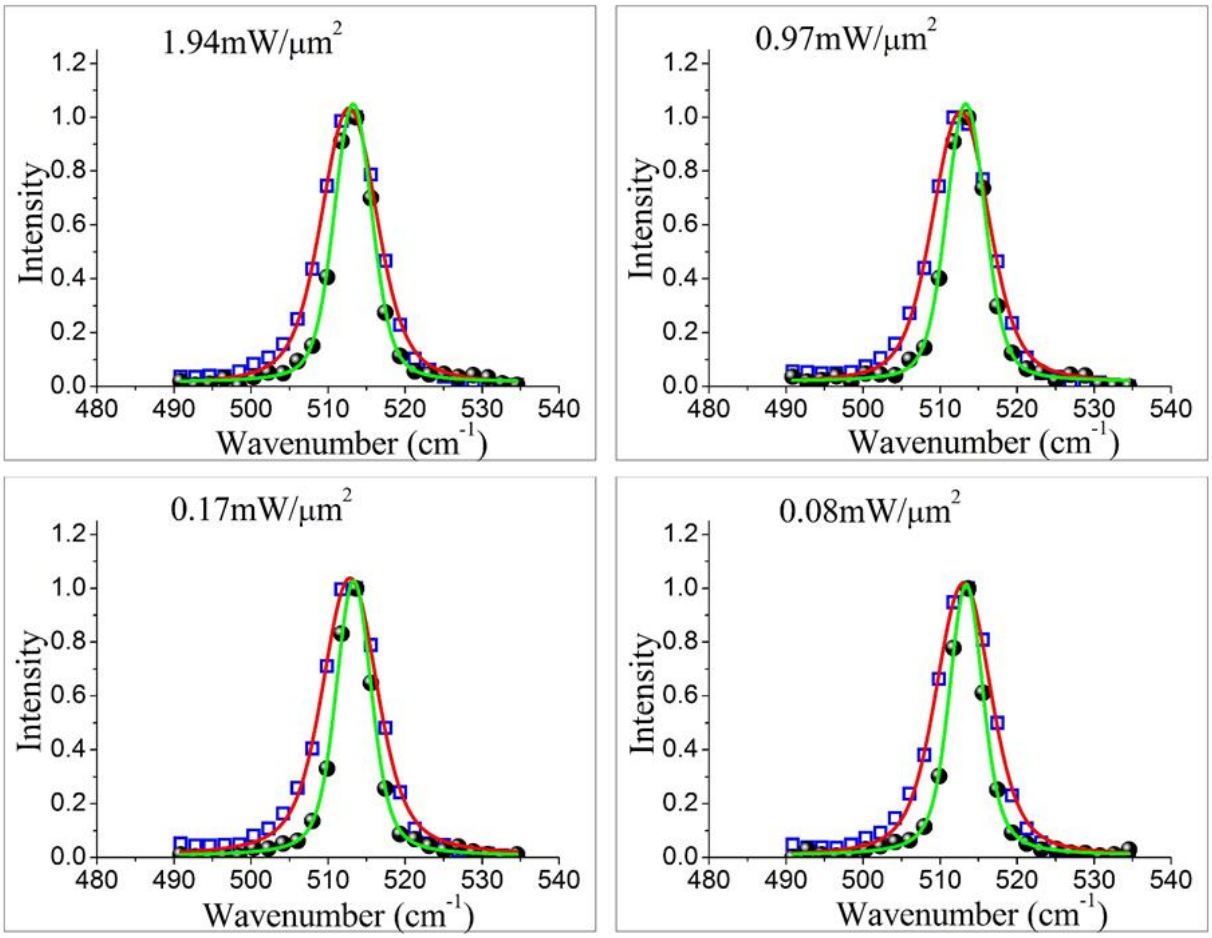

Figure S-C1: *Si-Si LO normalized phonon spectra of $^{28}Si_x{}^{30}Si_{1-x}$ NW and ^{29}Si NW at different incident laser power densities of 1.94 mW/μm², 0.97 mW/μm², 0.17 mW/μm², and 0.08 mW/μm². The low power measurements were done using the 488nm laser. All the data points corresponding to the $^{28}Si_x{}^{30}Si_{1-x}$ NWs are shown in empty blue squares and that of ^{29}Si NWs are shown in filled black circles. The red and the green curves correspond to the Voigt fit for $^{28}Si_x{}^{30}Si_{1-x}$ NWs and ^{29}Si NWs respectively.*

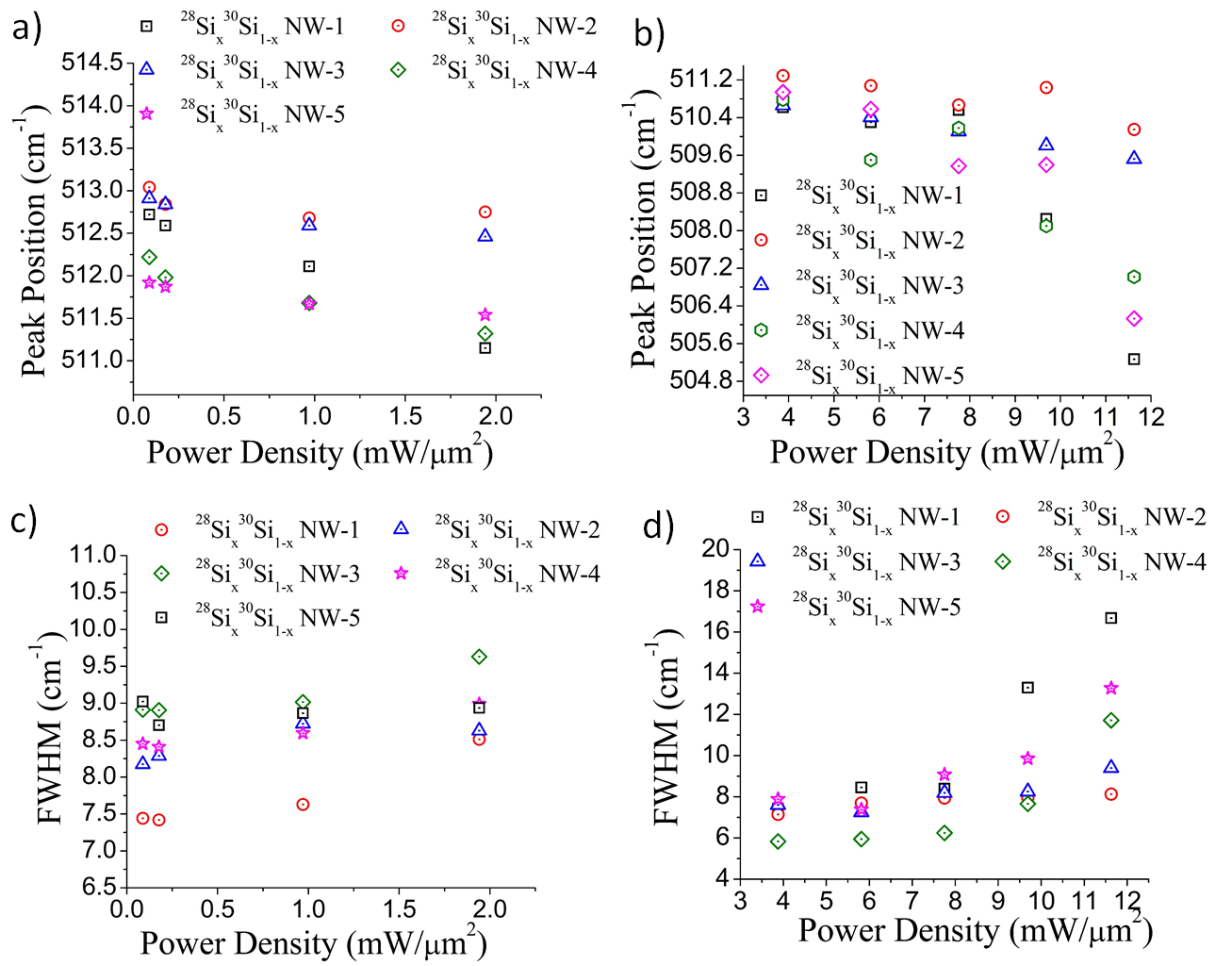

Figure S-C2: *Evolution of peak position and FWHM for individual $^{28}Si_x{}^{30}Si_{1-x}$ NWs at low power regime (Figure (a) and (c)) and at high power regime (Figure (b) and (d)). The data symbols $^{28}Si_x{}^{30}Si_{1-x}$ NW -1 to $^{28}Si_x{}^{30}Si_{1-x}$ NW -5 in Figure (a) and(c) represent the same NWs. Similarly, for (b) and (d). But $^{28}Si_x{}^{30}Si_{1-x}$ NW -1 to $^{28}Si_x{}^{30}Si_{1-x}$ NW -5 in (b) and (d) are not the same NWs as those measured in (a) and (c). For convenience, we have displayed the data for only 4-5 NWs and omitted the rest. But the average peak position and FWHM were calculated on all the measured NWs (>10 for low power measurements and 7 for high power measurements).*

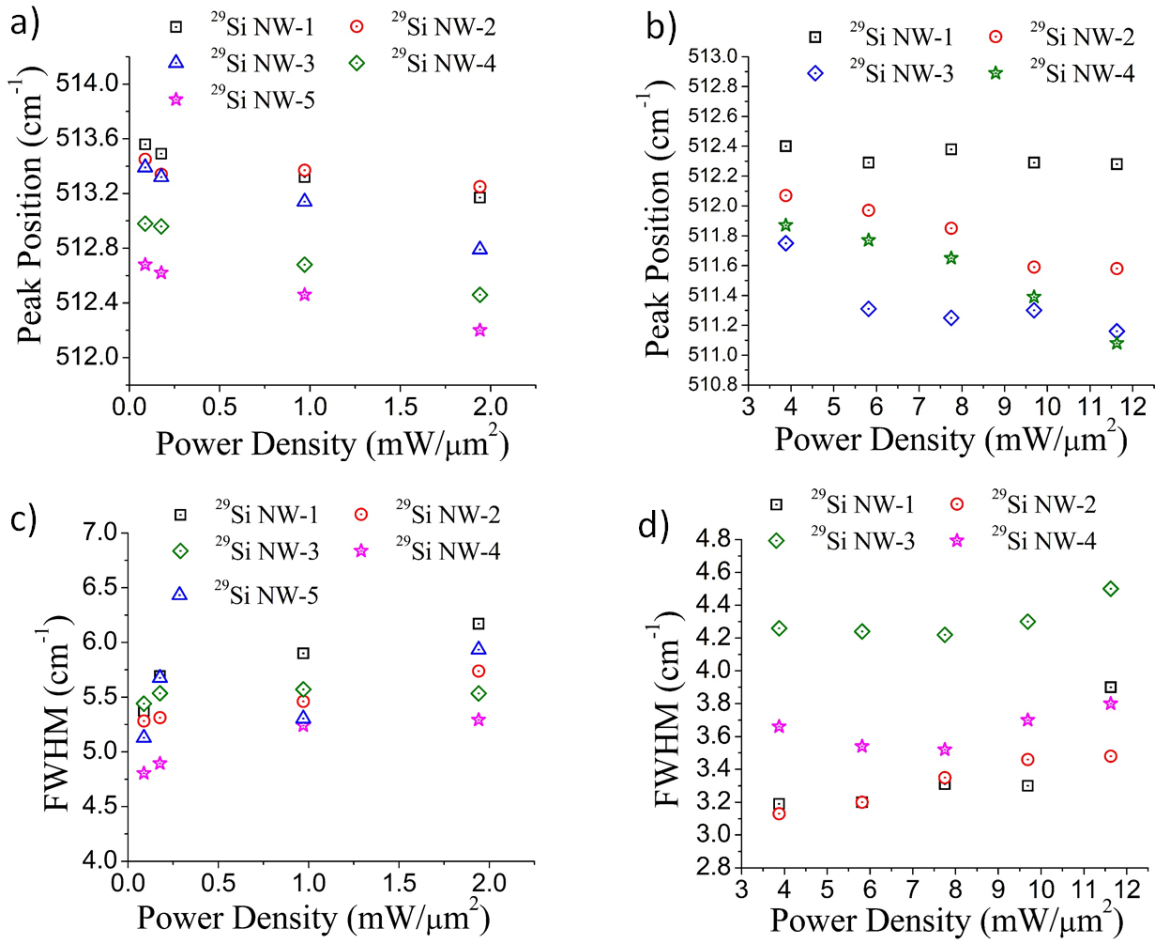

Figure S-C3: *Evolution of peak position and FWHM for different individual ^{29}Si NWs at low power regime {Figure (a) and (c)} and at high power regime {Figure (b) and (d)}. The data symbols ^{29}Si NW-1 to ^{29}Si NW-5 in Figure (a) and(c) represents the same NWs. Similarly, for (b) and (d). But ^{29}Si NW-1 to ^{29}Si NW-4 in (b) and (d) are not the same NWs as those measured in (a) and (c). For convenience we have displayed the data for only 4-5 NWs and omitted the rest. But the average peak position and FWHM was calculated on all the measured NWs (>10 for low power measurements and 7 for high power measurements).*

Estimate of the ratio of thermal conductivities of $^{28}Si_x{}^{30}Si_{1-x}$ NWs to ^{29}Si NWs at around 300K

In a material with a temperature difference of ΔT across its length L, the temperature gradient of $\Delta T/L$ leads to a flow of heat. If A is the area of the cross section of this material, then the rate of this heat flow can be expressed as:

$$Q' = A\kappa\frac{\Delta T}{L} \quad (C1)$$

where κ is the thermal conductivity of the material and Q' is the rate of the heat flow. Herein, Q' corresponds to a fraction of the measured laser power. Note that the laser spot diameter (for both λ=488nm and 532nm) is much larger than the diameter of the NWs investigated (the entire laser beam does not irradiate the NW). The power intercepted (P_i) by a NW is thus the measured power density (PD) times the surface area of a NW (Ω) exposed to the incident laser beam. A portion of the intercepted laser is reflected at the air-NW interface and the rest is transmitted. The transmitted power (P_t) is thus $(1-R)P_i$, where R is the reflectance at air-NW interface. Only a certain fraction of the transmitted power is actually absorbed. We can write the power absorbed as $P_a = C_a \times P_t$ where C_a is a constant. C_a depends on the absorbance of the NW at a particular wavelength and distance the light travels within a NW. The calculation of the exact path of a photon within a NW can be quite complicated. The laser after crossing the entire diameter of the NW reaches the NW-Au interface. It might be reflected / scattered from the interface and a certain fraction of the reflected /scattered light might re-enter the NW leading to further absorption. We do not need the precise details of C_a because it is the same for both $^{28}Si_x{}^{30}Si_{1-x}$ NWs and ^{29}Si NWs. Next a fraction of the absorbed power is converted to heat. The remaining fraction can be absorbed through other processes such as photo generating charge carriers. If there is no accumulation of heat at any point within a NW then the rate at which heat is absorbed by a NW must equal the rate at which heat is dissipated. Under such an assumption of a steady-state, the expression $C_h \times C_a \times (1-R) \times (\Omega \times PD)$ represents the rate at which heat flows through a NW (Q'), where C_h is the fraction of the absorbed power converted to heat. Since C_h, C_a, R, Ω are all the same for both $^{28}Si_x{}^{30}Si_{1-x}$ NWs and ^{29}Si NWs, Q' can be written as a certain constant K times the measured power density PD

$$Q' = K \times PD \quad (C2)$$

where $K = C_h \times C_a \times (1-R) \times \Omega$

Combining equation (C1) and (C2) we see that the rate at which the temperature changes with incident power density becomes inversely proportional to the thermal conductivity of the medium through which the heat is flowing. This technique has been implemented previously to measure the thermal conductivity of the environment surrounding Si NWs which were sonicated on Ag coated Cu substrates [1]. In that work, since the NWs were extremely thin (average diameter of 15 nm) the authors neglected conduction of heat through the NW itself. Rather they assumed the entire NW (heated by laser) to be acting as a source of heat and the dissipation to take place mainly through the surrounding gases. In our experiments, the NWs being much thicker (50-100nm), we assume a non-negligible conduction of heat through the NW itself. As shown in Figure S-C4, we assume that the laser of spot diameter d_{Laser} is incident on a NW lying on Au capped Si substrate. It heats up a cylindrical volume (the blue inner cylinder in Figure S-C4). This acts as a source of heat. We assume that a large portion of this generated heat flows axially to the end faces (long red arrows in Figure S-C4), which we assume are at ambient temperature of 300 K. Ideally for a cylinder lying on a flat surface, the contact area is zero. But neither the NW is a perfect cylinder (sidewalls are faceted) nor the surface is perfectly flat due to oughness. Hence, we assume some amount of heat will flow across the NW-Au interface (short red arrows in Figure S-C4) into the Au layer, which is also at 300 K and acts as a sink.

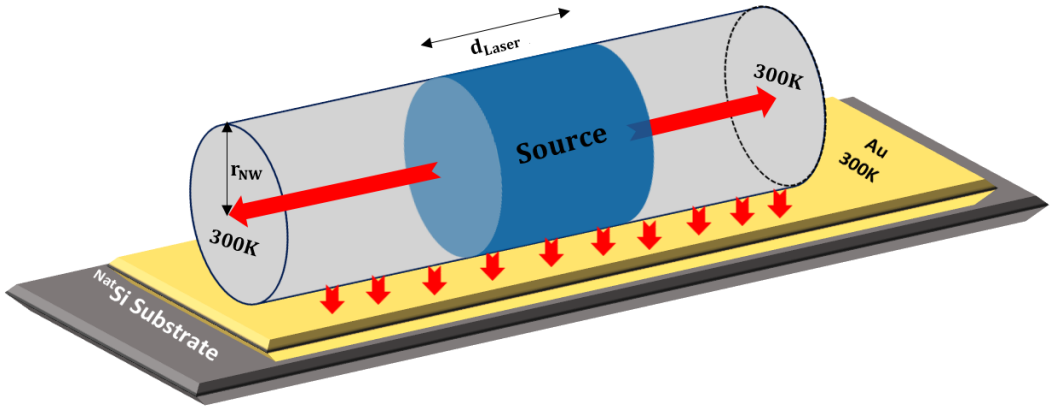

Figure S-C4: *Schematics of heat flow within a NW lying on a gold capped (in golden yellow)* ^{Nat}Si *substrate (in deep grey). The NW is depicted as a light grey cylinder. The blue cylinder (inside the NW) is where the laser (of spot diameter* d_{Laser}*) is incident and absorbed. The red arrows represent the heat flow.The end faces of the NW are assumed to be at ambient temperature of 300 K. The Au substrate is also assumed to be at ambient temperature of 300 K.*

In our analysis we neglect dissipation of heat from a NW through the surrounding air. This is a reasonable approximation because the amount of heat dissipated through the surrounding air is very small. This approximation is also at the basis of early analysis of the thermal conductivity of suspended GaAs NWs [2] and carbon nanotubes [3]. To sum up the discussion above:

1) A certain fraction of the incident laser power is converted to heat and that fraction is taken to be the same for both $^{28}Si_x{}^{30}Si_{1-x}$ NWs and ^{29}Si NWs because it depends on the NW morphology.
2) The volume within a NW that directly absorbs the laser heats up and acts as a heat source.
3) Neglecting dissipation through air, the major portion of the generated heat is dissipated by conduction, up to the end faces of the NW along its growth axis and the remaining through the NW-Au interface into the gold layer.
4) The local temperature which we estimated from the shift in Raman peak position is actually the temperature of the blue region. Since the rate of heat generation is assumed to be same in a $^{28}Si_x{}^{30}Si_{1-x}$ NW and ^{29}Si NW, the shift in Raman peak and consequently the effective temperature depends on how easily the heat is able to flow away from the source. This depends on two major factors: the thermal conductivity of the NW material and the nature of the contact of a NW with the Au substrate (which determines the interface thermal resistance). There is no physical reason that suggests that the nature of a $^{28}Si_x{}^{30}Si_{1-x}$ NW-Au contact will be any different from a ^{29}Si NW-Au contact. Thus, the whole thing boils down to the difference in thermal conductivity of the NW material. For a NW with lower thermal conductivity the temperature of the blue cylinder will be higher than a NW with higher thermal conductivity at the same incident laser power density.

Thus the difference in the rate at which the effective local temperature rises with incident power density gives a measure of the thermal conductivity of the material of the NW. From Figure 6.3(c), the slope of the dotted lines $(\Delta T/\Delta P)$ in the low power regime is found to be 14.09 $\text{Kelvin} - \mu\text{m}^2/\text{mW}$ for the $^{28}Si_x{}^{30}Si_{1-x}$ NWs and 10.95 $\text{Kelvin} - \mu\text{m}^2/\text{mW}$ for the ^{29}Si NWs.

$$\text{Since } \frac{\left(\Delta T/\Delta P\right)_{Iso-Mix\ NW}}{\left(\Delta T/\Delta P\right)_{Si-29\ NW}} \propto \frac{\kappa_{Si-29\ NW}}{\kappa_{Iso-Mix\ NW}} \qquad (C3)$$

We estimate that $\kappa_{Si-29\,NW}/\kappa_{Iso-Mix\,NW} = 1.286$ thus suggesting ~30% reduction of the thermal conductivity of $^{28}Si_x{}^{30}Si_{1-x}$ NWs around 300 K as compared to that of ^{29}Si NWs.

As discussed earlier, the nature of the contact between the NW and Au shall determine which of the two conduction processes shall dominate – the conduction along the long axis of a NW up to the end faces or the conduction across the interface into the Au substrate. Thus for more precise thermal conductivity measurements the NWs needs to be suspended. The other source of error which we speculate could have affected the ratio is the very nature by which the temperature was extracted. Normally two techniques are implemented to calculate the temperature of a material using Raman spectroscopy – the ratio of Stokes to Antistokes intensity and the shift in Raman peak position [4]. Both techniques present only a rough estimate of the local temperature. Also the temperature estimated by the two techniques often don't converge to the same value [1], [4]. We have chosen to use the latter technique, but the temperature extracted here is a gross estimate. This approach nonetheless provides a reasonable estimate of the temperature and a reliable indicator of the relative temperature.

[1] Scheel, H.; Reich, S.; Ferrari, A. C.; Cantoro, M.; Colli, A.; Thomsen, C. *Appl. Phys. Lett.* **2006**, *88*, 233114.

[2] Soini, M.; Zardo, I.; Uccelli, E.; Funk, S.; Koblmüller, G.; Fontcuberta i Morral, A.; Abstreiter, G. *Appl. Phys. Lett.* **2010**, *97*, 263107.

[3] Soini, M.; Zardo, I.; Uccelli, E.; Funk, S.; Koblmüller, G.; Fontcuberta i Morral, A.; Abstreiter, G. *Appl. Phys. Lett.* **2010**, *97*, 263107.

[4] Gupta, R.; Xiong, Q.; Adu, C. K.; Kim, U. J.; Eklund, P. C. *Nano Lett.* **2003**, *3*, 627–631.

APPENDIX D - ATOM PROBE TIP FABRICATION ON A $^{28}Si_x{}^{30}Si_{1-x}$ NANOWIRE, IN A DUAL-FIB

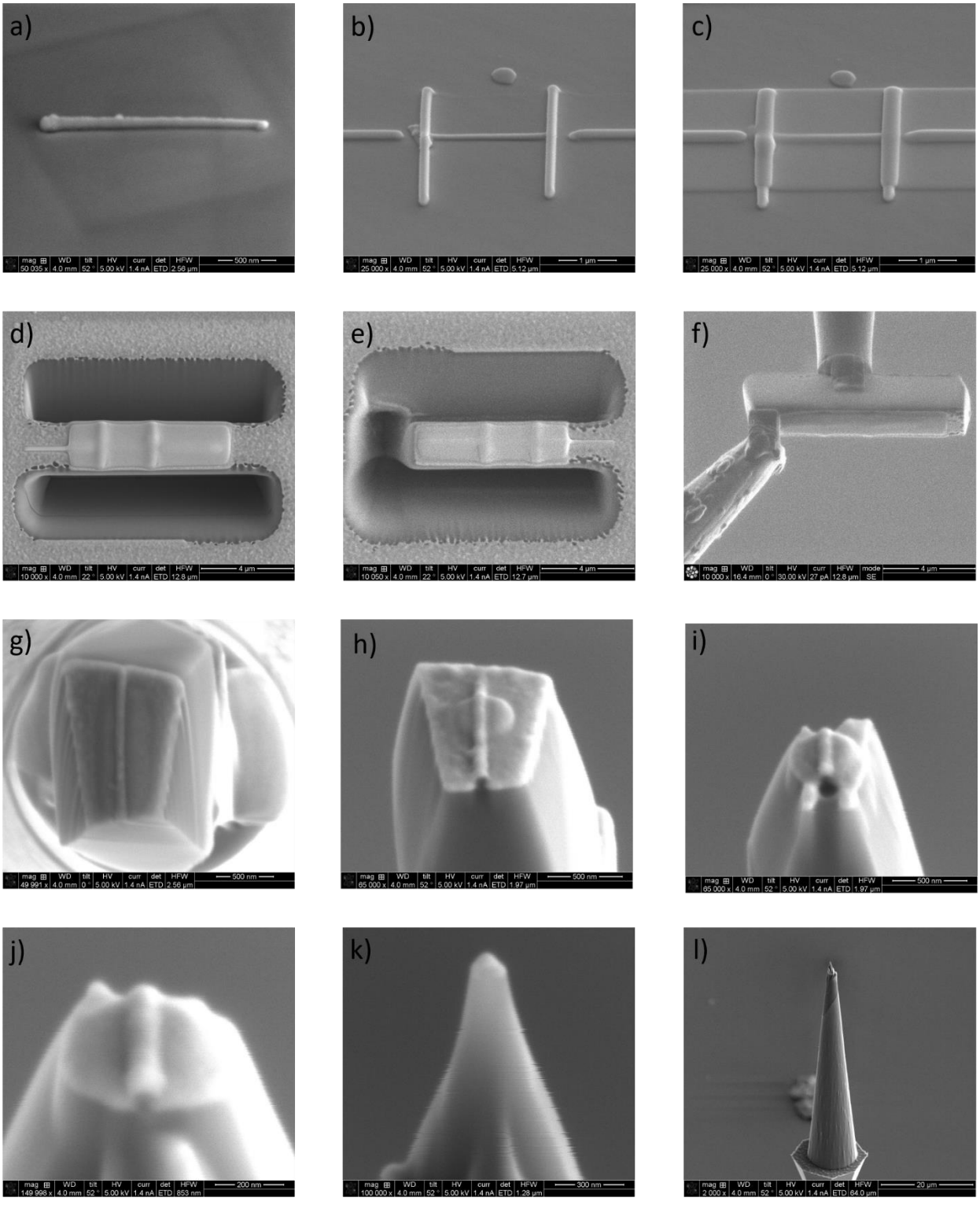

Figure S-D1: *Electron beam and ion beam images obtained from a Dual-FIB microscope, demonstrating the sequential steps of fabrication of an atom probe tip using a* $^{28}Si_x{}^{30}Si_{1-x}$ *NW. (a) An isolated NW dispersed on* ^{Nat}Si *substrate. (b) Markers are laid using cold Pt deposition to identify the exact position of the NW during later stages of tip fabrication. (c) The NW was coated with 0.15 µm thick Pt layer, to protect the NW during FIB milling. (d) and (e) Trenches were milled on 3 sides, surrounding the NW, by* Ga^+ *ion (30 kV) FIB milling. (f) After milling off the* 4^{th} *side, the section was lifted out using a micromanipulator needle and attached to an APT micro-post using cold Pt welding. (g) To initiate the tip sharpening process, first a pyramidal shape was given to the attached sample using rectangular milling patterns. (h), (i), and (g) Circular milling patterns of varying diameter were used to give the tip it's characteristics needle like shape. (k) Final polishing of the tip was done using low energy* Ga^+ *ions (5 kV) (l) Final shape of the APT nanotip before inserting into the APT chamber.*

APPENDIX E – OTHER PUBLICATIONS AND CONFERENCES

Journal Publications

1) S. Mukherjee, U.Givan, A.Tarun, S.Senz, M. de la Mata, J.Arbiol, and O.Moutanabbir; *Tuning heat transport in nanowires by combining mass disorder and ordered defect engineering*; (to be submitted to Nano Letters).

2) S. Mukherjee, U. Givan, S.Senz, D.Isheim, D.Seidman, and O. Moutanabbir; *Atomistics of metal-catalyzed nanowire growth unraveled by stable isotope tracing*; (to be submitted to Nano Letters).

3) M. Fortin-Deschênes, O. Waller, T. Mentes, A. Locatelli, S. Mukherjee, F. Genuzio, P. Levesque, A. Hebert, R. Martel, and O. Moutanabbir; *Synthesis of Antimonene on Germanium*; (under review Nano Letters)

4) S. Mukherjee, N. Nateghi, R.M. Jacobberger, E. Bouthillier, M. de la Mata, J. Arbiol, T. Coenen, D. Cardinal, P. Levesque, P. Desjardins, R. Martel, M. S. Arnold, and O. Moutanabbir; *Growth and luminescence of polytypic InP on epitaxial graphene*; (under review Advanced Functional Materials).

5) D. Jung, J. Faucher, S. Mukherjee, A. Akey, D. J. Ironside, M. Cabral, X. Sang, J. Lebeau, S. R. Bank, T. Buonassisi, O. Moutanabbir, and M. L. Lee; *Highly tensile-strained Ge/InAlAs nanocomposites*, Nature Communication, vol. 8, no. 14204, Dec. 2016.

6) S. Mukherjee, H. Watanabe, D. Isheim, D. N. Seidman, and O. Moutanabbir, *Mapping isotopes in nanoscale and quantum materials using atom probe tomography*; Microscopy and Microanalysis, vol 22, supplement S3, pp.652-653, July 2016.

7) J.-H. Fournier-Lupien, S. Mukherjee, S. Wirths, E. Pippel, N. Hayazawa, G. Mussler, J. M. Hartmann, P. Desjardins, D. Buca, and O. Moutanabbir; *Strain and composition effects on Raman vibrational modes of silicon-germanium-tin ternary alloys, Appl. Phys. Lett.*, vol. 103, no. 26, pp. 263103, Dec. 2013.

Conferences

1) S. Mukherjee and O. Moutanabbir; Heat Transport in Isotopically Engineered Nanowires; Contributed talk at the Materials Research Society Spring Meeting and Exhibit 2017; Phoenix (USA).

2) S. Mukherjee and O. Moutanabbir; Atomistic Insights into Novel Group IV Semiconductors – From Isotopically Engineered Materials to Non-Equilibrium Alloys; Invited talk at the International Union of Materials Research Society, International Conference of Young Researchers on Advanced Materials (IUMRS-ICYRAM) 2016; Bangalore (India).

3) S. Mukherjee, H. Watanabe, D. Isheim, D. N. Seidman, and O. Moutanabbir, Mapping isotopes in nanoscale and qunatum materials using atom probe tomography; Contributed talk at the Microscopy and Microanalysis Conference 2016; Columbus (USA).

4) S. Mukherjee, D. Isheim, D. N. Seidman, and O. Moutanabbir; Isotope mapping in nanosctructures using atom probe tomography; Contributed talk at the Atom Probe Tomography and Microscopy Conference 2016; Gyeongju (South Korea)

5) S. Mukherjee and O. Moutanabbir; Dynamics of the nanowire VLS growth unravelled by isotope tracing; Poster at the 9th Nanowire Growth Workshop Nanowires 2015; Barcelona (Spain)

6) S. Mukherjee, D. Isheim, D. N. Seidman, and O. Moutanabbir; Effect of isotope disorder on phonon scattering and thermal conductivity of silicon nanowires; Contributed talk at the 9th International Conference on Silicon Epitaxy and Heterostructures (ICSI-9) 2015, Montreal (Canada).

7) S**.** Mukherjee and O. Moutanabbir; Phonon engineering in silicon nanowires using stable isotopes; Contributed talk at the Canadian Association of Physicists Congress 2013; Montreal (Canada).

8) S. Mukherjee, N. Duchene and O. Moutanabbir; Phonon properties in isotopically engineered silicon nanowires using vibrational spectroscopy; Contributed talk at the Materials Science & Technology Conference & Exhibition 2013; Montréal (Canada).